Title

Decadal, Millennial, and Million-Year Erosion Rates in the Easternmost Himalaya

Author

Shao, Kevin

Publication Date

2023

Peer reviewed|Thesis/dissertation

UNIVERSITY OF CALIFORNIA

Los Angeles

Decadal, Millennial, and Million-Year Erosion Rates in the Easternmost Himalaya

A dissertation submitted in partial satisfaction of the requirements for the degree Doctor of Philosophy in Geology

by

Kevin Shao

2023

ABSTRACT OF THE DISSERTATION

Decadal, Millennial, and Million-Year Erosion Rates in the Easternmost Himalaya

by

Kevin Shao

Doctor of Philosophy in Geology

University of California, Los Angeles, 2023

Professor Seulgi Moon, Chair

Quantifying tectonic uplift and erosion rates on various timescales is essential for understanding how tectonic and climate forcings interact to produce the landscape we see today. My dissertation is centered around three topics related to the erosion rates of the easternmost Himalaya in the Indian state of Arunachal Pradesh at decadal, millennial, and million-year timescales to better understand present-day natural hazards to long-term landscape evolution. In my dissertation, I quantify 1) landslide susceptibility, 2) landslide-derived decadal and ^{10}Be-derived millennial erosion rates, and 3) plausible million-year timescale exhumation rates in the easternmost Himalaya to better understand climatic, topographic, and tectonic controls on surface processes and erosion over different timescales.

In the second chapter, I mapped landslide occurrences using satellite images, quantified landslide susceptibility using statistical and machine learning methods, and assessed the dominant controls of landslide occurrences in the easternmost Himalaya. Recently, deep neural networks (DNN) have been used in the application of estimating landslide susceptibility alongside physical and statistical models. However, DNNs are uninterpretable, making it difficult to determine mechanistic information about landslide controls in the modeled region. My landslide inventory was ultimately used to train an interpretable superposable neural network (SNN), developed and applied by my colleague, to model

landslide susceptibility in the easternmost Himalaya. The SNN performed similarly to a state-of-the-art deep neural network, outperforming commonly used physically and statistically based models while revealing the relative importance of contributing controls. The analyses reveal that both strong slope-climate coupling and microclimates are dominant contributors to landslide occurrences in the region.

In the third chapter, I quantified landslide-derived decadal erosion rates over a 20-year interval from satellite images and determined millennial erosion using cosmogenic ^{10}Be. Previous studies generally report a tectonic control on millennial erosion rates across the Himalaya. However, there exist well-understood and well-defined patterns of climate variation, tectonic deformation, and lithologic distribution along-strike of the Himalaya that allows for their disentanglement. In this chapter, I measured cosmogenic ^{10}Be-derived millennial erosion rates of 12 basins from the range front to the hinterland of the Dibang and Lohit valleys. In addition, I compiled 161 ^{10}Be-derived erosion rates from the Garhwal, Nepal, and Bhutan Himalaya and grouped basins by dominant metasedimentary or crystalline lithology. I observe a clear correlation between climate metrics and erosion rates for basins dominated by metasedimentary lithology that is absent those dominated by crystalline lithology. Additionally, we find that the response of fluvial and hillslope erosional efficiency to climate differs between lithologies in the Himalaya. Furthermore, the high erosion rates and efficiencies observed in the easternmost Himalayan range front are likely facilitated by rainfall-induced landslides and efficient fluvial erosion and transport in metasedimentary lithology. Future studies may incorporate more extensive datasets including low-temperature thermochronometers, which may further elucidate the links among tectonics, erosion, and climate.

In the fourth chapter, I inferred the magnitude and spatial pattern of million-year timescale exhumation rates using five newly measured apatite (U-Th)/He sample ages from the Dibang Valley in the easternmost Himalaya. Fault activity along the active easternmost Himalayan range front is largely unconstrained over recent million-year timescales that are more relevant to our landslide and erosion rate analyses. Additionally, although the persistence of out-of-sequence faulting over recent million-year timescales has been proposed, little is known about the timing and magnitude of exhumation rates over

this period. I determine plausible cooling histories using HeFTy inverse thermal modeling for two samples in both the range front and hinterland and infer exhumation rates over the last ~2-1 Ma assuming a simplified geothermal gradient. I observe that exhumation along the range front is highest along the Lalpani thrust and concentrated near the Lohit thrust in the hinterland. My findings potentially support persistent out-of-sequence faulting of the Lohit thrust that continues until the present though at a slower rate than that of the range front. Future studies might include additional thermochronology measurements in the range front to better constrain the spatial extent of high exhumation rates. Additionally, an improved understanding of the geothermal gradient would yield more accurate and reliable exhumation rate estimates.

The dissertation of Kevin Shao is approved.

Timothy Mark Harrison

Gilles F. Peltzer

An Yin

Seulgi Moon, Committee Chair

TABLE OF CONTENTS

Chapter 1: Introduction 1
1.1 The role of tectonic-climate-erosion interactions in global landscape evolution 1
1.2 Assessing the controls of erosion rates in mountain ranges over varying timescales 3
1.2.1 Decadal erosion rates 3
1.2.2 Millennial erosion rates 5
1.3 The easternmost Himalaya as an important and ideal natural laboratory 6
1.4 Dissertation structure 7
1.5 References 9
Chapter 2: Landslide Susceptibility Modeling by Interpretable Neural Network 20
2.1 Introduction 20
2.2 Superposable neural networks 24
2.3 Landslides in the easternmost Himalaya 26
2.4 Results and Discussion 27
2.4.1 SNN Implementation 27
2.4.2 Comparison with traditional landslide susceptibility modeling 27
2.4.3 SNN model explainability 29
2.4.4 Accurate and interpretable landslide susceptibility from the SNN 31
2.4.5 Implications, limitations, and future directions 35
2.5 Methods 39
2.5.1 Study Area 39
2.5.2 Landslide Inventory 41
2.5.3 Model Input Feature Descriptions 44
2.6 Figures 47
2.7 References 52
Chapter 3: Climate-driven erosional efficiency varies with lithology across the Himalaya 62
3.1 Introduction 62
3.2 Millennial erosion rate compilation and measurements 64
3.3 Quantification of environmental controls 65
3.4 Quantifying erosional efficiency from fluvial and landslide processes 66
3.5 Millennial erosion rate and efficiency from the Himalaya 67
3.6 Linking climate, erosional efficiency, and lithological variability across the Himalaya 69
3.7 Rapid and efficient erosion from extreme rainfall and weak lithology 70
3.8 Connection among tectonics, climate, and erosion for the Himalaya 72

3.9 Figures 75
3.10 References 80
Chapter 4: Patterns of low-temperature thermochronologic ages 89
4.1 Introduction 89
4.2 Methods 90
4.3 Results: Measured (U-Th)/He ages and inferred T-t histories 92
4.4 Discussion 94
4.4.1 Inferred exhumation of the easternmost Himalayan range front and hinterland 94
4.4.2 Comparison of exhumation with other Himalayan regions 95
4.4.3 Comparison between spatial patterns of exhumation and millennial erosion rates in the easternmost Himalaya 96
4.5 Limitations and Future Work 97
4.6 Figures 99
4.7 References 104
Chapter 5: Synthesis 109
5.1 Summary of findings 109
Appendix A: Landslide Susceptibility Modeling by Interpretable Neural Network 112
A.1 Appendix Note A1: Construction and Performance Assessments of Models 112
A.2 Appendix Note A2: Explanation of Aspect as a Microclimate Control 117
A.3 Appendix Figures and Tables 120
A.4 Appendix References 135
Appendix B: Climate-driven erosional efficiency varies with lithology 138
B.1 Appendix Note B1: Description of sample preparation 138
B.2 Appendix Note B2: Accelerator Mass Spectrometry analysis 139
B.3 Appendix Note B3: ^{10}Be-derived erosion rate calculation 140
B.4 Appendix Note B4: Compilation of ^{10}Be-derived erosion rates 140
B.5 Appendix Note B5: Quantification of topographic, climatic, lithologic, and geologic controls 141
B.6 Appendix Note B6: Description of ^{10}Be-derived erosion rates and quantified controls 144
B.7 Appendix Note B7: Landslide mapping and analysis 145
B.8 Appendix Note B8: Topographic steady-state in the easternmost Himalaya 149
B.9 Appendix Figures and Tables 150
B.10 Appendix References 177
Appendix C: Patterns of low-temperature thermochronologic ages from the easternmost Himalaya 182
C.1 Appendix Note C1: Apatite (U-Th)/He preparation and analytical methods 182
C.2 Appendix Note C2: HeFTy thermal model assumptions, constraints, and parameters 183

C.3 Appendix Figures and Tables 186
C.4 Appendix References 189

LIST OF FIGURES

Fig. 2.1: Study area in the easternmost Himalaya 47
Fig. 2.2: Mapped landslides and modeled susceptibility 48
Fig. 2.3: Individual feature contributions to total susceptibility 49
Fig. 2.4: Feature contributions to total susceptibility 50
Fig. 2.5: Important controls for landslides 51

Fig. 3.1: Maps of our study area 75
Fig. 3.2: Comparison between ^{10}Be-derived erosion rates and topographic and climatic metrics 76
Fig. 3.3: Comparison between climatic metric and erosional efficiency coefficients 77
Fig. 3.4: Variations of erosion rates and efficiencies with proximity to major faults 78
Fig. 3.5: Comparison among landslides, erosion rates, and environmental metrics 79

Fig. 4.1: Apatite (U-Th)/He (AHe) sample locations and mean ages 99
Fig. 4.2: Apatite (U-Th)/He (AHe) sample locations and grain ages in cross-sectional view 100
Fig. 4.3: Relationship between single grain apatite and zircon (U-Th)/He ages and eU and R_S 101
Fig. 4.4: HeFTy inverse-modeled T-t histories for our four apatite (U-Th)/He samples 102
Fig. 4.5: Spatial trends of ^{10}Be-derived millennial erosion rates, inferred exhumation rates, and NEE with $Dist_{MFT}$ 103

Fig. A1: Conventional DNN architecture vs SNN architecture 120
Fig. A2: Superposable neural network training flow diagram 121
Fig. A3: Comparison among the feature ranges of our three study regions 122
Fig. A4: Flowchart detailing the semi-automatic landslide mapping procedure 123
Fig. A5: Examples of semi-automatically detected landslides 124
Fig. A6: Landslide area versus probability density 125
Fig. A7: Spatial distribution of 15 features used in the superposable neural network model 126
Fig. A8: Illustration of spatial data partitioning using Pythagorean tiling 127
Fig. A9: The relationship among aspect, normalized difference vegetation index, and S_{Asp} 127
Fig. A10: Bar charts representing ΔSnj from different methods 128

Fig. B1: Along-strike variations of climate metrics in the Himalaya 150
Fig. B2: Spatial patterns of erosion and low-temperature thermochronology ages in the easternmost Himalaya 151

Fig. B3a: Simplified lithologic maps of the study areas in our compilation 153
Fig. B3b: Simplified lithologic map of the Garhwal Himalaya study area 153
Fig. B4: Comparison between ^{10}Be-derived erosion rates and topographic metrics 154
Fig. B5a: Comparison between topographic and climatic metrics across the Himalaya 155
Fig. B5b: Comparison between geologic and climatic metrics across the Himalaya 156
Fig. B6: Variations of erosional efficiencies with proximity to major faults 157
Fig. B7: Field photos of detrital sand sample locations at basin outlets 158
Fig. B8: Map of χ for the easternmost Himalaya 159
Fig. B9: Relationship between χ and elevation for our study basins in the easternmost Himalaya 160
Fig. B10: Hillslope positions of landslides from in the easternmost Himalaya 161
Fig. B11: ^{10}Be-derived erosion rates calculated using different blank scenarios 162
Fig. B12: Maps of landslides across studied basins in the easternmost Himalaya 163
Fig. B13: Probability density as a function of landslide area 164

Fig. C1: HeFTy inverse-modeled sensitivity tests 186

LIST OF TABLES

Table A1: Description of Landslide Inventory 129
Table A2: Description and Ranges of 15 Features 129
Table A3: AUROC of Models and Single Features 130
Table A4: Artificial Neural Network and Statistical Model Confidence Intervals 131
Table A5: Performance Metrics for Models 132
Table A6: Correlation Metrics Between Features (R-value) 133
Table A7: Logistic Regression Control Coefficients 134

Table B1: Basin-averaged topographic, climatic, and erosional variables 165
Table B2: Erosion rates and cosmogenic concentrations 173
Table B3: Landslide-derived erosion rates and characteristics 174
Table B4: Compilation statistics of erosion rate and controls 175
Table B5: Model Coefficients and RMSE for relationships between erosion rates and controls 176

Table C1: Apatite grain properties and ages 187

Acknowledgments

To begin, I would like to thank Seulgi Moon. Over our many years working together, I believe that I have grown not only in my understanding of geomorphology but also as a critical thinker, communicator, and scientist under her guidance and mentorship. Additionally, I am grateful for the opportunities I have had to travel to numerous conferences across the country to meet and engage with the amazing geomorphology community that I have had the privilege to be involved in. I am grateful for the once-in-a-lifetime opportunity to travel to the Himalaya and see it in a way that very few people ever have the chance to. But most of all, I am grateful for the long hours, late nights, and nonstop grind that she puts in to ensure her students' success. Thank you for guiding me on this journey.

Next, thank you to my committee of remarkable scientists, each of whom I have taken courses with and learned so much from. Although Mark Harrison's course on low-temperature thermochronometry proved too insightful for me to grasp at the time, his direction has guided me in my efforts to become a more prudent and circumspect scientist and his teachings have been important to my research involving thermochronometry. Gilles Peltzer's course on remote sensing introduced me to a new perspective of geology that I love and has been integral to each of my research projects. A special thank you to An Yin who I have taken the most courses and had the craziest field memories with. I will do my best to continue to be curious and THINK(!) wherever I go. Thank you for the unforgettable stories that I will tell for years to come.

Many other members of the UCLA department deserve my utmost gratitude as well. Through Jonathan Aurnou's course using MATLAB, I discovered my interest and love for quantitative analysis through coding, which I will take with me in my future endeavors. Tina Treude's course on academic writing provided initial guidelines on how to formulate academic papers and taught me how to be a more effective communicator as a scientist. A very special thank you to Rod O'Connor and Anthony Sansone

for miraculously recovering all my data from my dying computer in my second year. You guys are magicians.

A huge thank you to my many collaborators from UCLA, the University of Vermont, the University of Connecticut, and the University of Nevada Las Vegas for sharing your expertise with me. Your constructive input has made me a more well-rounded and curious scientist.

Thank you to my fellow UCLA graduate students for being with me on this arduous journey. Akash Gupta, Yufan Xu, Tyler Powell, Rob Ulrich, Will Misener, and Leslie Insixiengmay, I always looked forward to grabbing lunch or talking in the hallways whenever we could. I can't wait to hear how you are doing in the next chapter of your journeys.

I owe an enormously special thanks to the Seulgi Squad of past and present. Justin Higa, Marina Argueta, Christina Kitamikado, Josh Lee, Boontigan Kuhasubpasin, Amanda Hunt, Gen Li, Heather Kirkpatrick, and Jessica Lin, thank you for the hilarious memories in and out of the office that kept me sane.

Last, I am deeply grateful to my family and long-time friends for reminding me that I am more than just my research. I am lucky to be able to surround myself with friends that I am proud to know, who constantly encourage me in my endeavors and listen to my troubles. To my Mom and Dad, my sister Stephanie, Yooliana, and the Fruit Family: thank you for your unwavering support and love all these years, for being my safe space, and for always reminding me that I am more than enough. I am blessed to have you in my life.

CURRICULUM VITAE

Kevin Shao

EDUCATION

University of California, Los Angeles — Fall 2017 – Spring 2023
Ph.D. Candidate, Geology
Candidacy Exam, February 2022 (C.Phil. awarded)
Qualifying Exam, October 2019 (M.S. awarded)

Cornell University — Fall 2011 – Spring 2015
B.A., Science of Earth Systems – Geosciences

HONORS AND AWARDS

Geological Society of America Graduate Student Research Grant — Spring 2019
Teaching Award — Fall 2021

PAPERS

Youssef, K., **Shao, K.**, Moon, S., & Bouchard, L.S. (2023). Landslide Susceptibility Modeling by Interpretable Neural Network. *Communications Earth & Environment*.

Shao, K., Moon, S., Li, G.K., Haproff, P.J., Yin, A., Corbett, L.B., Bierman, P.R., Argueta, M.O., Hidy, A.J. (2023). Climate-driven erosion varies with lithology across the Himalaya. *In review at Nature Communications*.

PLANNED PAPER

Shao, K., Moon, S., Fosdick, J.C., Haproff, P.J., Odlum, M.L., Yin, A (in prep). Patterns of low-temperature thermochronologic ages from the easternmost Himalaya.

PUBLISHED ABSTRACTS AND PRESENTATIONS

K.Shao, S. Moon, J. C. Fosdick, P. J. Haproff, A. Yin (2021) Controls of tectonic and climate forcing on long-term exhumation rates in the eastern end of Himalaya. American Geophysical Union Fall Meeting. New Orleans, LA (oral)

K. Shao, S. Moon, G. Li, P. J. Haproff, A. Yin, L. B. Corbett, P. R. Bierman, M. O. Argueta (2020) Assessing climatic controls of millennial erosion in the eastern end of Himalaya. American Geophysical Union Fall Meeting. Virtual Conference (poster)

K. Shao, K. Youssef, S. Moon, L.-S. Bouchard (2019) Explainable AI Landslide Susceptibility Modeling by Superposable Neural Networks. American Geophysical Union Fall Meeting. San Francisco, CA (poster)

K. Shao, S. Moon, G. Li (2019) Climatic controls of landslides in the eastern end of Himalaya. Annual Southern California Geomorphology Symposium. Pasadena, CA (poster)

K. Shao, S. Moon, G. Li (2018) Climatic controls of landslides in the eastern end of Himalaya. Annual Southern California Geomorphology Symposium. Pasadena, CA (poster)

K. Shao, S. Moon, G. Li (2018) Climatic and tectonic controls of erosion in the eastern end of Himalaya. American Geophysical Union Fall Meeting. Washington, D.C. (poster)

TEACHING EXPERIENCE (*6 quarters*)

Graduate Teaching Assistant, EPSS, UCLA — Fall 2017, 2018, 2019, 2020, 2021, 2022
EPSS 1, Introduction to Earth Science

INDUSTRY EXPERIENCE

Geologist I, Golder Associates, Inc., Richmond, VA — May 2016 – June 2017
Business Development Researcher, Integral Consulting Inc. — June 2015 – January 2016
Syracuse, NY

Chapter 1:

Introduction

1.1 The role of tectonic-climate-erosion interactions in global landscape evolution

Geologists have long debated the relationship between tectonics, climate, and erosion in the evolution of landscapes over geologic timescales. Previous studies investigating the competing forces of tectonic and climate forcings on erosion estimated a substantial and abrupt increase in global terrigenous sediment accumulation in the world's oceans over the last 5 Ma (Hay et al., 1988, 1989; Métivier et al., 1999; Peizhen et al., 2001; Herman et al., 2013). This increase in sediment accumulation was initially attributed to rapid changes in sea level associated with the cycle of continental glaciation and potentially the influence of late-Cenozoic tectonic activity (Hays et al., 1976; Hay et al., 1988, 1989; Ruddiman and Raymo, 1988; Ruddiman et al., 1989; Molnar and England, 1990; Raymo, 1994). However, subsequent studies determined that the increase in sediment accumulation and coarsening could also be explained by global climate change towards lower temperatures, further motivating the discussion of competing tectonic and climate forcings on erosion (Donnelly, 1982; Frostick and Reid, 1989; Molnar and England, 1990; Peizhen et al., 2001; Herman et al., 2013). In this case, increased erosion over the last 5 Ma would be the result of a more variable, stormier climate and glacial erosion rather than steep topography related to increased tectonic activity. Additionally, the late-Cenozoic increase in sediment accumulation appears independent of a shift in global tectonic rates or their effects (Donnelly, 1982; Molnar and England, 1990; Krijgsman et al., 1999).

Further evidence challenges the observation and control of the increase in sedimentation over this period (Willenbring and von Blanckenburg, 2010; Lenard et al., 2020). The abrupt increase in late-Cenozoic sedimentation rates likely drives an increased drawdown of CO_2 if they amplify silicate weathering and subsequent burial of carbonate sediments. However, inferred atmospheric CO_2 concentrations calculated from multiple proxies display relatively constant levels over the observed

period of increased sedimentation (Willenbring and von Blanckenburg, 2010; Caves Rugenstein et al., 2019). Alternatively, the increase may be an artifact in part related to observation and measurement biases. Furthermore, $^{10}Be/^{9}Be$ ratio weathering proxies from Pacific and Atlantic Ocean marine cores indicate relatively constant ratios over the last 12 Ma (von Blanckenburg and O'Nions, 1999; Willenbring and von Blanckenburg, 2010). This consistency suggests that if chemical weathering and physical erosion rates are directly linked, large increases in late-Cenozoic global sedimentation are unlikely. Although global controls on erosion and sedimentation offer important insights into Earth's conditions over geologic timescales, they are limited in furthering our understanding of the nuanced and dynamic nature of tectonics, climate, and erosion in mountain belts.

As major contributors to global sediment flux, orogenic belts have been frequently investigated to determine the link between climate, erosion, and tectonics. A better understanding of fold-and-thrust belt mechanics has paved the way for further investigation into the possibility of erosion influencing the evolution of mountain belts (Davis, 1983; Dahlen et al., 1984; Beaumont et al., 1992; Willett, 1999; Willett and Brandon, 2002; Hilley and Strecker, 2004; Hilley et al., 2004; Grujic et al., 2006; Cruz et al., 2010). Studies demonstrated that orogenic wedges deform internally to a critical taper and topographic slope (Davis, 1983; Stockmal, 1983; Dahlen et al., 1984; Whipple, 2009). The dimensions and growth rate of the wedge taper and slope are influenced by the material properties and erosional processes of the wedge (Leturmy et al., 2000; Koyi et al., 2000; Hoth et al., 2006; Whipple, 2009; Cruz et al., 2010). Conversely, erosion transports sediment away from the wedge, which adjusts the stress field near the surface and potentially incurs a tectonic response. Previous studies demonstrated through sandbox and numerical experiments that greater erosional efficiencies, conventionally assumed to be influenced by lithology, climate, and sediment load, are directly linked to fewer fore-shear bands in the orogenic wedge, but larger shear strain magnitudes along these bands (Cruz et al., 2010). Thus, high erosional magnitude and efficiency driven by climate may influence tectonic activity and deformation in orogenic wedges.

Previous studies have used numerical models to investigate the coupling between deformation and erosion for real-world observations in mountain belts. Willett (1999) showed that the direction and

localization of enhanced precipitation can potentially result in a broadened or focused zone of exhumation depending on a consistent or opposing wind direction to the direction of the subducting plate, respectively. Exhumational asymmetry was observed in the Southern Alps of New Zealand supporting model results in cases of winds that oppose subducting plate motion while domal patterns of exhumation observed in Cascadia were consistent with those of winds in the direction of subducting plate motion. Additionally, numerical experiments of Himalayan-Tibetan tectonics suggest that efficient erosion, possibly related to the spatial distribution of rainfall, can be associated with channel flow or extrusion dependent on the location of the erosional front (Beaumont et al., 2001; Koons et al., 2002). However, though these models may provide an explanation for certain features of the Himalaya, field evidence, such as inconsistent spatial distributions of sustained, enhanced erosion and zones of crystalline rock, appear at odds with these experiments (Harrison, 2006). The lack of clear field evidence displaying a coupling between deformation and erosion in mountain belts hinders the support for climate-driven erosion spurring tectonic activity over million-year timescales in mountain belts.

1.2 Assessing the controls of erosion rates in mountain ranges over varying timescales

Although ascertaining tectonic-climate-erosion interactions on million-year timescales has large implications on landscape evolution, these connections may vary depending on the timescale of interest. Furthermore, gaining a better understanding of these connections at different timescales can have important implications for addressing issues including natural hazard mitigation and the individual processes involved in the long-term evolution of landscapes.

1.2.1 Decadal erosion rates

Understanding the controls of erosion on modern decadal timescales, especially in landslide-prone mountain belts, can improve natural hazard mitigation efforts. Landslides contribute to sediment flux denuding mountain belts and can impact erosion rates and landscape evolution over millennial timescales (Bookhagen et al., 2005; Bookhagen, 2010; Jones et al., 2021). Additionally, landslides are responsible

for hundreds of human losses globally each year and major economic and infrastructure costs (Petley, 2012; Froude and Petley, 2018). Evidence indicates an order-of-magnitude intensification of geomorphic processes over the last century, expanding the need for a better understanding of vulnerable areas (Cendrero et al., 2020). With projected increases in annual wettest day precipitation across nearly all continental regions at global warming levels of 1.5°C and above (Lee et al., 2023), the occurrence of climate-driven geomorphic processes, such as landslides, is expected to increase further. Thus, quantifying the link between climate and landslide occurrence is critical for modern society and understanding decadal timescale processes involved in landscape evolution.

Current models accurately quantifying landslide susceptibility are resource intensive or lack interpretability, limiting their use in determining landslide triggering factors. Since the year 2000, the number of studies investigating landslide susceptibility and their triggering factors increased substantially (Reichenbach et al., 2018). These studies utilized physically-based models (e.g. SHALSTAB, TRIGRS) (Montgomery and Dietrich, 1994; Dietrich et al., 1995, 2001; Montgomery et al., 1998; Baum et al., 2002, 2010) or data-driven models (e.g. likelihood ratios, logistic regression, machine learning algorithms, deep neural networks) (Lee, 2004, 2005; Lee and Sambath, 2006; Tien Bui et al., 2012, 2020; Pradhan, 2013; Regmi et al., 2014; Reichenbach et al., 2018; Stanley et al., 2020) with varying degrees of success. However, each type of model has its shortcomings. Physically-based landslide susceptibility models have limited incorporation of triggering factors, simplified assumptions of failure plane geometry, and the high cost of model calibration using field measurements (Guzzetti et al., 1999). On the other hand, data-driven models are limited in their reliance on experts' choices and handling of input features (Reichenbach et al., 2018). Although data-driven models can achieve high performance, especially with the use of deep neural networks, they lack interpretability and generally cannot display the relative contributions of each input feature to landslide susceptibility. Although current explainable methods can explain the local behavior of a model (Lundberg and Lee, 2017), current methods do not incorporate globally interpretable architecture. Evidently, determining the controls of landslide susceptibility and decadal erosion on a regional basis with high accuracy and low cost poses a great challenge.

1.2.2 Millennial erosion rates

Million-year timescale erosion measurements provide profound insights into long-term landscape evolution but may represent the cumulative result of individual processes driven by different controls operating over millennial timescales (e.g., glaciation, monsoonal rainfall). Similar to how episodic, decadal erosional processes (e.g., landslides, earthquakes, glacial outburst floods) are mechanisms that accumulate sediment flux over millennial timescales, so too can millennial processes collectively offer detailed insight into long-term landscape evolution. Geomorphologists often compare modern topographic and climatic metrics with millennial erosion rates, such as those measured by cosmogenic radionuclide dating (Brown et al., 1995; Kirchner et al., 2001; von Blanckenburg, 2005; DiBiase et al., 2010; Moon et al., 2011; Portenga and Bierman, 2011; Scherler et al., 2014; Godard et al., 2014; Adams et al., 2020). Although these correlations directly represent erosional processes over millennial timescales, these same forces may be at work in shaping landscapes over longer timescales. Consistent erosional processes are expected in steady-state landscapes where tectonically driven accretionary flux is balanced with erosion flux (Willett and Brandon, 2002). In this case, global erosion rates on millennial timescales exhibit little or no correlation between climate and erosion rates, supporting tectonic activity as a main driver of erosion over this timescale (von Blanckenburg, 2005; Portenga and Bierman, 2011; Godard et al., 2014). Instead, climate forcings are reflected in landscape morphology rather than erosion rates. However, studies examining erosion rates from transient systems responding to changes in environmental conditions, such as deglaciated landscapes, reported a correlation between erosion rate and efficiency and precipitation magnitude or variability (Reiners et al., 2003; Moon et al., 2011; Ferrier et al., 2013). Similarly, landscapes undergoing a feedback between climate, erosion, and tectonics over millennial timescales would also display a correlation between erosion rates and climate, but field evidence supporting such a link and potential processes in active mountain belts is lacking (Whipple, 2009). Understanding the temporal extent of observed erosional processes requires careful attention. Nevertheless, correlations between modern environmental conditions and millennial erosion rates can

bridge short and long-term landscape evolution processes, which can then be inferred using globally available datasets (Kirby and Whipple, 2001, 2012; Adams et al., 2020).

1.3 The easternmost Himalaya as an important and ideal natural laboratory

As one of the most dynamic mountain belts in the world, the Himalaya span a diverse range of well-defined environmental conditions, allowing for the quantification and disentanglement of precipitation, topography, lithology, and tectonic deformation, and their influence on decadal, millennial, and million-year timescale erosion rates. Modern orographic precipitation trends across the Himalaya display a general increase eastward along-strike of the mountain belt related to moisture originating from the Bay of Bengal (Bookhagen and Burbank, 2006, 2010; Bookhagen, 2010; Andermann et al., 2011; Yatagai et al., 2012; Mukherjee et al., 2015; Yang et al., 2018; Varikoden and Revadekar, 2020; Jamshadali et al., 2021). Because rainfall in the region is directly related to the Indian Summer Monsoon, a majority of annual precipitation predictably falls during the summer. Across-strike spatial distributions of precipitation are associated with topography where increases in elevation spatially coincide with bands of high rainfall (Bookhagen and Burbank, 2006, 2010). For example, the two-step rise in topography from south to north of the central Himalaya spatially coincides with two distinct peaks in rainfall while the one-step rise in topography of the western and eastern Himalaya experiences one especially strong peak in rainfall. Additionally, lithology has been mapped across the Himalaya indicating well-defined, laterally continuous units separated by orogen-scale thrust faults (Yin, 2006). Furthermore, numerous studies have quantified tectonic activity along these thrust faults in the Himalaya using a variety of techniques, such as low-temperature thermochronology, river incision measurements, cosmogenic radionuclide dating, topographic analyses, and GPS velocities (Lavé and Avouac, 2000; Kirby and Whipple, 2001; Banerjee et al., 2008; Burgess et al., 2012; Thiede and Ehlers, 2013; Berthet et al., 2014; Le Roux-Mallouf et al., 2015; Ge et al., 2015; Stevens and Avouac, 2015). These studies suggest high degrees of slip and exhumation near the Main Frontal and Central thrusts. Additionally, Holocene shortening rates appear to

increase along-strike eastward (Lavé and Avouac, 2000; Kumar et al., 2006; Burgess et al., 2012; Stevens and Avouac, 2015).

The easternmost Himalaya, located in the Indian state of Arunachal Pradesh, are characterized by especially extreme environmental conditions relative to other Himalayan regions that make it an ideal site to study the various factors influencing erosion rates. As previously mentioned, the eastward increase in precipitation magnitude and crustal shortening results in intense rainfall on consistently steep slopes throughout the region. Additionally, a decrease in thrust belt width and missing lithologic units compared to other Himalayan regions (i.e., Greater and Tethyan Himalayan Sequences and southern Gangdese batholith) may suggest especially high degrees of shortening, underthrusting, or erosion (Yin, 2006; Haproff et al., 2019, 2020). A high degree of erosion is supported by previous studies examining millennial erosion rates from eastern Himalayan catchments that found especially high erosion rates in the Dibang and Lohit valleys of the easternmost Himalaya (Lupker et al., 2017). Furthermore, between 2004 to 2016, 75% of landslides globally occurred in Asia with a substantial amount located in the Himalaya (Froude and Petley, 2018). Thus, the Himalaya provides ample opportunities to examine environmental triggering factors fundamental to driving landslide occurrence. Substantiating these findings, satellite imagery from the easternmost Himalaya reveals a high frequency of rainfall-induced landslides located in the range front of the region. These landslides are not only indicative of a rapidly eroding landscape but also pose a significant hazard to local communities. However, despite extensive research on the controls of erosion in other Himalayan regions, there is still a lack of studies that quantify and assess the factors influencing the spatial distribution of millennial erosion and landslide occurrence in the easternmost Himalaya.

1.4 Dissertation structure

This dissertation serves to investigate the dominant influences on erosion over decadal, millennial, and million-year timescales in the easternmost Himalaya. The remaining chapters are organized as follows:

The second chapter describes the geological implications of the first application of an interpretable neural network to quantify and understand the factors that contribute to landslide susceptibility. I manually mapped landslides in the easternmost Himalaya using satellite imagery. This inventory was used to generate a semi-automatically mapped inventory that trained a superposable neural network (SNN), both designed and developed by our collaborator, along with various environmental controls. I compare the performance between the SNN model output and that of other commonly used physical and statistical models. Additionally, by exploiting the SNN's interpretable architecture, I quantify each feature's contribution to landslide susceptibility and determine a primary landslide control in the easternmost Himalaya. This chapter is published in *Nature Communications Earth & Environment*.

The third chapter investigates the influence of climate, lithology, topography, and tectonics on millennial erosion rates and erosional efficiency across the Himalaya. I measured ^{10}Be and decadal landslide erosion rates in 12 new basins along the Dibang and Lohit valleys and compiled an additional 161 previously reported ^{10}Be-derived erosion rates from the Garhwal, Nepal, and Bhutan Himalaya and landslide inventories from 13 basins in Nepal. We separate erosion rates and efficiency by lithologic group and assess their correlations with examined environmental metrics, which were used to determine potential controls. Additionally, we investigate rainfall-induced landslide occurrences as an important mechanism linking erosional efficiency and climate metrics. This chapter is in review at *Nature Communications*.

The fourth chapter explores plausible cooling histories of five newly measured apatite (U-Th)/He ages and the inferred magnitude and spatial distribution of exhumation rates over recent million-year timescales in the Dibang Valley. These cooling histories offer insight into the persistence of out-of-sequence faulting proposed by Haproff et al. (2020) and were used to estimate exhumation rates on more recent timescales. We compare the magnitude and spatial distribution of exhumation rates with those of different Himalayan regions and my previously measured ^{10}Be-derived millennial erosion rates. This chapter is in prep to be submitted to *Geology* by Fall 2023.

1.5 References

Adams, B.A., Whipple, K.X., Forte, A.M., Heimsath, A.M., and Hodges, K. V, 2020, Climate controls on erosion in tectonically active landscapes: Science Advances, v. 6, p. 3166–3182.

Andermann, C., Bonnet, S., and Gloaguen, R., 2011, Evaluation of precipitation data sets along the Himalayan front: Geochemistry, Geophysics, Geosystems, v. 12, doi:10.1029/2011GC003513.

Banerjee, P., Bürgmann, R., Nagarajan, B., and Apel, E., 2008, Intraplate deformation of the Indian subcontinent: Geophysical Research Letters, v. 35, doi:10.1029/2008GL035468.

Baum, R.L., Godt, J.W., and Savage, W.Z., 2010, Estimating the timing and location of shallow rainfall-induced landslides using a model for transient, unsaturated infiltration: Journal of Geophysical Research: Earth Surface, v. 115, doi:10.1029/2009JF001321.

Baum, R.L., Savage, W.Z., and Godt, J.W., 2002, TRIGRS-A Fortran Program for Transient Rainfall Infiltration and Grid-Based Regional Slope-Stability Analysis.:

Beaumont, C., Fullsack, P., and Hamilton, J., 1992, Erosional control of active compressional orogens: Thrust Tectonics, p. 1–18.

Beaumont, C., Jamieson, R.A., Nguyen, M.H., and Lee, B., 2001, Himalayan tectonics explained by extrusion of a low-viscosity crustal channel coupled to focused surface denudation: Nature, v. 414, p. 738–742.

Berthet, T., Ritz, J.F., Ferry, M., Pelgay, P., Cattin, R., Drukpa, D., Braucher, R., and Hetényi, G., 2014, Active tectonics of the eastern Himalaya: New constraints from the first tectonic geomorphology study in southern Bhutan: Geology, v. 42, p. 427–430, doi:10.1130/G35162.1.

von Blanckenburg, F., 2005, The control mechanisms of erosion and weathering at basin scale from cosmogenic nuclides in river sediment: Earth and Planetary Science Letters, v. 237, p. 462–479, doi:10.1016/j.epsl.2005.06.030.

von Blanckenburg, F., and O'Nions, R.K., 1999, Response of beryllium and radiogenic isotope ratios in Northern Atlantic Deep Water to the onset of northern hemisphere glaciation: Earth and Planetary Science Letters, v. 167, p. 175–182.

Bookhagen, B., 2010, Appearance of extreme monsoonal rainfall events and their impact on erosion in the Himalaya: Geomatics, Natural Hazards and Risk, v. 1, p. 37–50, doi:10.1080/19475701003625737.

Bookhagen, B., and Burbank, D.W., 2006, Topography, relief, and TRMM-derived rainfall variations along the Himalaya: Geophysical Research Letters, v. 33, doi:10.1029/2006GL026037.

Bookhagen, B., and Burbank, D.W., 2010, Toward a complete Himalayan hydrological budget: Spatiotemporal distribution of snowmelt and rainfall and their impact on river discharge: Journal of Geophysical Research: Earth Surface, v. 115, doi:10.1029/2009JF001426.

Bookhagen, B., Thiede, R.C., and Strecker, M.R., 2005, Abnormal monsoon years and their control on erosion and sediment flux in the high, arid northwest Himalaya: Earth and Planetary Science Letters, v. 231, p. 131–146, doi:10.1016/j.epsl.2004.11.014.

Brown, E.T., Stallard, R.F., Larsen, M.C., Raisbeck, G.M., and Yiou, F., 1995, Denudation rates determined from the accumulation of in situ-produced ^{10}Be in the luquillo experimental forest, Puerto Rico: Earth and Planetary Science Letters, v. 129, p. 193–202, doi:10.1016/0012-821X(94)00249-X.

Burgess, W.P., Yin, A., Dubey, C.S., Shen, Z.K., and Kelty, T.K., 2012, Holocene shortening across the main frontal thrust zone in the eastern Himalaya: Earth and Planetary Science Letters, v. 357–358, p. 152–167, doi:10.1016/j.epsl.2012.09.040.

Caves Rugenstein, J.K., Ibarra, D.E., and von Blanckenburg, F., 2019, Neogene cooling driven by land surface reactivity rather than increased weathering fluxes: Nature, v. 571, p. 99–102, doi:10.1038/s41586-019-1332-y.

Cendrero, A., Forte, L.M., Remondo, J., and Cuesta-Albertos, J.A., 2020, Anthropocene Geomorphic Change. Climate or Human Activities? Earth's Future, v. 8, doi:10.1029/2019EF001305.

Cruz, L., Malinski, J., Wilson, A., Take, W.A., and Hilley, G., 2010, Erosional control of the kinematics and geometry of fold-and-thrust belts imaged in a physical and numerical sandbox: Journal of Geophysical Research: Solid Earth, v. 115, doi:10.1029/2010JB007472.

Dahlen, F.A., Suppe, J., and Davis, D., 1984, Mechanics of Fold-and-Thrust Belts and Accretionary Wedges: Cohesive Coulomb Theory: Journal of Geophysical Research, v. 89, p. 10087–10101, doi:10.1029/JB089iB12p10087.

Davis, G.H., 1983, Shear-zone model for the origin of metamorphic core complexes: Geology, v. 11, p. 342–347, http://pubs.geoscienceworld.org/gsa/geology/article-pdf/11/6/342/3506833/i0091-7613-11-6-342.pdf.

DiBiase, R.A., Whipple, K.X., Heimsath, A.M., and Ouimet, W.B., 2010, Landscape form and millennial erosion rates in the San Gabriel Mountains, CA: Earth and Planetary Science Letters, v. 289, p. 134–144, doi:10.1016/j.epsl.2009.10.036.

Dietrich, W.E., Bellugi, D., and Real de Asua, R., 2001, Validation of the Shallow Landslide Model, SHALSTAB, for forest management, *in* Land use and watersheds: human influence on hydrology and geomorphology in urban and forest areas, v. 2, p. 195–227, doi:10.1029/ws002p0195.

Dietrich, W.E., Reiss, R., Hsu, M.-L., and Montgomery, D.R., 1995, A Process-Based Model For Colluvial Soil Depth and Shallow Landsliding Using Digital Elevation Data: Hydrological Processes, v. 9, p. 383–400.

Donnelly, T.W., 1982, Worldwide continental denudation and climatic deterioration during the late Tertiary: Evidence from deep-sea sediments: Geology, v. 10, p. 451–454, http://pubs.geoscienceworld.org/gsa/geology/article-pdf/10/9/451/3506350/i0091-7613-10-9-451.pdf.

Ferrier, K.L., Taylor Perron, J., Mukhopadhyay, S., Rosener, M., Stock, J.D., Huppert, K.L., and Slosberg, M., 2013, Covariation of climate and long-term erosion rates across a steep rainfall gradient on the Hawaiian island of Kaua'i: Bulletin of the Geological Society of America, v. 125, p. 1146–1163, doi:10.1130/B30726.1.

Frostick, L.E., and Reid, I., 1989, Climatic versus tectonic controls of fan sequences: lessons from the Dead Sea, Israel: Journal of the Geological Society, v. 146, p. 527–538, https://www.lyellcollection.org.

Froude, M.J., and Petley, D.N., 2018, Global fatal landslide occurrence from 2004 to 2016: Natural Hazards and Earth System Sciences, v. 18, p. 2161–2181, doi:10.5194/nhess-18-2161-2018.

Ge, W.P., Molnar, P., Shen, Z.K., and Li, Q., 2015, Present-day crustal thinning in the southern and northern Tibetan Plateau revealed by GPS measurements: Geophysical Research Letters, v. 42, p. 5227–5235, doi:10.1002/2015GL064347.

Godard, V., Bourlès, D.L., Spinabella, F., Burbank, D.W., Bookhagen, B., Fisher, G.B., Moulin, A., and Léanni, L., 2014, Dominance of tectonics over climate in Himalayan denudation: Geology, v. 42, p. 243–246, doi:10.1130/G35342.1.

Grujic, D., Coutand, I., Bookhagen, B., Bonnet, S., Blythe, A., and Duncan, C., 2006, Climatic forcing of erosion, landscape, and tectonics in the Bhutan Himalayas: Geology, v. 34, p. 801–804, doi:10.1130/G22648.1.

Guzzetti, F., Carrara, A., Cardinali, M., and Reichenbach, P., 1999, Landslide hazard evaluation: a review of current techniques and their application in a multi-scale study, Central Italy: Geomorphology, v. 31, p. 181–216.

Haproff, P.J., Odlum, M.L., Zuza, A. V., Yin, A., and Stockli, D.F., 2020, Structural and Thermochronologic Constraints on the Cenozoic Tectonic Development of the Northern Indo-Burma Ranges: Tectonics, v. 39, doi:10.1029/2020TC006231.

Haproff, P.J., Zuza, A. V., Yin, A., Harrison, T.M., Manning, C.E., Dubey, C.S., Ding, L., Wu, C., and Chen, J., 2019, Geologic framework of the northern Indo-Burma Ranges and lateral correlation of Himalayan-Tibetan lithologic units across the eastern Himalayan syntaxis: Geosphere, v. 15, p. 856–881, doi:10.1130/GES02054.1.

Harrison, T.M., 2006, Did the Himalayan Crystallines extrude partially molten from beneath the Tibetan Plateau? Geological Society, London, Special Publications, v. 268, p. 237–254, https://www.lyellcollection.org.

Hay, W.W., Shaw, C.A., and Wold, C.N., 1989, Mass-balanced paleogeographic reconstructions: Geologische Rundschau, p. 207–242.

Hay, W.W., Sloan, J.L., and Wold, C.N., 1988, Mass/age distribution and composition of sediments on the ocean floor and the global rate of sediment subduction: Journal of Geophysical Research, v. 93, doi:10.1029/jb093ib12p14933.

Hays, J.D., Imbrie, J., and Shackleton, N.J., 1976, Variations in the Earth's Orbit: Pacemaker of the Ice Ages Author:, http://www.jstor.orgURL:http://www.jstor.org/stable/1743620.

Herman, F., Seward, D., Valla, P.G., Carter, A., Kohn, B., Willett, S.D., and Ehlers, T.A., 2013, Worldwide acceleration of mountain erosion under a cooling climate: Nature, v. 504, p. 423–426, doi:10.1038/nature12877.

Hilley, G.E., and Strecker, M.R., 2004, Steady state erosion of critical Coulomb wedges with applications to Taiwan and the Himalaya: Journal of Geophysical Research: Solid Earth, v. 109, doi:10.1029/2002jb002284.

Hilley, G.E., Strecker, M.R., and Ramos, V.A., 2004, Growth and erosion of fold-and-thrust belts with an application to the Aconcagua fold-and-thrust belt, Argentina: Journal of Geophysical Research: Solid Earth, v. 109, doi:10.1029/2002jb002282.

Hoth, S., Adam, J., Kukowski, N., and Oncken, O., 2006, Influence of erosion on the kinematics of bivergent orogens: Results from scaled sandbox simulations: Special Paper of the Geological Society of America, v. 398, p. 201–225, doi:10.1130/2006.2398(12).

Jamshadali, V.H., Reji, M.J.K., Varikoden, H., and Vishnu, R., 2021, Spatial variability of south Asian summer monsoon extreme rainfall events and their association with global climate indices: Journal of Atmospheric and Solar-Terrestrial Physics, v. 221, p. 105708, doi:10.1016/j.jastp.2021.105708.

Jones, J.N., Boulton, S.J., Stokes, M., Bennett, G.L., and Whitworth, M.R.Z., 2021, 30-year record of Himalaya mass-wasting reveals landscape perturbations by extreme events: Nature Communications, v. 12, doi:10.1038/s41467-021-26964-8.

Kirby, E., and Whipple, K.X., 2012, Expression of active tectonics in erosional landscapes: Journal of Structural Geology, v. 44, p. 54–75, doi:10.1016/j.jsg.2012.07.009.

Kirby, E., and Whipple, K., 2001, Quantifying differential rock-uplift rates via stream profile analysis:, https://pubs.geoscienceworld.org/gsa/geology/article-pdf/29/5/415/3521633/i0091-7613-29-5-415.pdf.

Kirchner, J.W., Finkel, R.C., Riebe, C.S., Granger, D.E., Clayton, J.L., King, J.G., and Megahan, W.F., 2001, Mountain erosion over 10 yr, 10 k.y., and 10 m.y. time scales:, www.copyright.com.

Koons, P.O., Zeitler, P.K., Chamberlain, C.P., Craw, D., and Meltzer, A.S., 2002, MECHANICAL LINKS BETWEEN EROSION AND METAMORPHISM IN NANGA PARBAT, PAKISTAN HIMALAYA: American Journal of Science, v. 302, p. 749–773.

Koyi, H.A., Hessami, K., and Teixell, A., 2000, Epicenter distribution and magnitude of earthquakes in fold-thrust belts: Insights from sandbox models: Geophysical Research Letters, v. 27, p. 273–276, doi:10.1029/1999GL010833.

Krijgsman, W., Langereis, C.G., Zachariasse, W.J., Boccaletti, M., Moratti, G., Gelati, R., Iaccarino, S., Papani, G., and Villa, G., 1999, Late Neogene evolution of the Taza-Guercif Basin (Rifian Corridor, Morocco) and implications for the Messinian salinity crisis.:

Kumar, S., Wesnousky, S.G., Rockwell, T.K., Briggs, R.W., Thakur, V.C., and Jayangondaperumal, R., 2006, Paleoseismic evidence of great surface rupture earthquakes along the Indian Himalaya: Journal of Geophysical Research: Solid Earth, v. 111, p. 3304, doi:10.1029/2004JB003309.

Lavé, J., and Avouac, J.P., 2000, Active folding of fluvial terraces across the Siwaliks Hills, Himalayas of central Nepal: Journal of Geophysical Research: Solid Earth, v. 105, p. 5735–5770, doi:10.1029/1999JB900292.

Lee, S., 2005, Application of logistic regression model and its validation for landslide susceptibility mapping using GIS and remote sensing data: International Journal of Remote Sensing, v. 26, p. 1477–1491, doi:10.1080/01431160412331331012.

Lee, S., 2004, Soil erosion assessment and its verification using the Universal Soil Loss Equation and Geographic Information System: A case study at Boun, Korea: Environmental Geology, v. 45, p. 457–465, doi:10.1007/s00254-003-0897-8.

Lee, H., Calvin, K., Dasgupta, D., Krinner, G., and Mukherji, A., 2023, Synthesis Report of the IPCC Sixth Assessment Report: Panmao Zhai.

Lee, S., and Sambath, T., 2006, Landslide susceptibility mapping in the Damrei Romel area, Cambodia using frequency ratio and logistic regression models: Environmental Geology, v. 50, p. 847–855, doi:10.1007/s00254-006-0256-7.

Lenard, S.J.P., Lavé, J., France-Lanord, C., Aumaître, G., Bourlès, D.L., and Keddadouche, K., 2020, Steady erosion rates in the Himalayas through late Cenozoic climatic changes: Nature Geoscience, v. 13, p. 448–452, doi:10.1038/s41561-020-0585-2.

Leturmy, P., Mugnier, J.L., Vinour, P., Baby, P., Colletta, B., and Chabron, E., 2000, Piggyback basin development above a thin-skinned thrust belt with two detachment levels as a function of interactions between tectonic and superficial mass transfer: the case of the Subandean Zone (Bolivia):, www.elsevier.com/locate/tecto.

Lundberg, S.M., and Lee, S.-I., 2017, A Unified Approach to Interpreting Model Predictions: Advances in neural information processing systems, https://github.com/slundberg/shap.

Lupker, M. et al., 2017, ^{10}Be systematics in the Tsangpo-Brahmaputra catchment: The cosmogenic nuclide legacy of the eastern Himalayan syntaxis ETH Library Be systematics in the Tsangpo-Brahmaputra catchment: the cosmogenic nuclide legacy of the eastern Himalayan syntaxis: Earth Surf. Dynam, v. 5, p. 429–449, doi:10.3929/ethz-b-000192411.

Métivier, F., Gaudemer, Y., Tapponnier, P., and Klein, M., 1999, Mass accumulation rates in Asia during the Cenozoic: Geophysical Journal International, v. 137, p. 280–318, doi:10.1046/j.1365-246X.1999.00802.x.

Molnar, P., and England, P., 1990, Late Cenozoic uplift of mountain ranges and global climate change: chicken or egg? Nature, v. 346, p. 29–34.

Montgomery, D.R., and Dietrich, W.E., 1994, A physically based model for the topographic control on shallow landsliding: Water Resources Research, v. 30.

Montgomery, D.R., Sullivan, K., and Greenberg, H.M., 1998, Regional test of a model for shallow landsliding: Hydrological Processes, v. 12, p. 943–955.

Moon, S., Page Chamberlain, C., Blisniuk, K., Levine, N., Rood, D.H., and Hilley, G.E., 2011, Climatic control of denudation in the deglaciated landscape of the Washington Cascades: Nature Geoscience, v. 4, p. 469–473, doi:10.1038/ngeo1159.

Mukherjee, S., Joshi, R., Prasad, R.C., Vishvakarma, S.C.R., and Kumar, K., 2015, Summer monsoon rainfall trends in the Indian Himalayan region: Theoretical and Applied Climatology, v. 121, p. 789–802, doi:10.1007/s00704-014-1273-1.

Peizhen, Z., Molnar, P., and Downs, W.R., 2001, Increased sedimentation rates and grain sizes 2-4 Myr ago due to the influence of climate change on erosion rates: Nature, v. 410, p. 891–897, www.nature.com.

Petley, D., 2012, Global patterns of loss of life from landslides: Geology, v. 40, p. 927–930, doi:10.1130/G33217.1.

Portenga, E.W., and Bierman, P.R., 2011, Understanding Earth's eroding surface with ^{10}Be: GSA Today, v. 21, p. 4–10, doi:10.1130/G111A.1.

Pradhan, B., 2013, A comparative study on the predictive ability of the decision tree, support vector machine and neuro-fuzzy models in landslide susceptibility mapping using GIS: Computers and Geosciences, v. 51, p. 350–365, doi:10.1016/j.cageo.2012.08.023.

Raymo, M.E., 1994, The Initiation of Northern Hemisphere Glaciation: Annual Review of Earth and Planetary Sciences, v. 22, p. 353–383, www.annualreviews.org.

Regmi, A.D., Devkota, K.C., Yoshida, K., Pradhan, B., Pourghasemi, H.R., Kumamoto, T., and Akgun, A., 2014, Application of frequency ratio, statistical index, and weights-of-evidence models and their comparison in landslide susceptibility mapping in Central Nepal Himalaya: Arabian Journal of Geosciences, v. 7, p. 725–742, doi:10.1007/s12517-012-0807-z.

Reichenbach, P., Rossi, M., Malamud, B.D., Mihir, M., and Guzzetti, F., 2018, A review of statistically-based landslide susceptibility models: Earth-Science Reviews, v. 180, p. 60–91, doi:10.1016/j.earscirev.2018.03.001.

Reiners, P.W., Ehlers, T.A., Mitchell, S.G., and Montgomery, D.R., 2003, Coupled spatial variations in precipitation and long-term erosion rates across the Washington Cascades: Nature, v. 426, p. 645–647, doi:10.1038/nature02111.

Le Roux-Mallouf, R. et al., 2015, Evidence for a wide and gently dipping Main Himalayan Thrust in western Bhutan: Geophysical Research Letters, v. 42, p. 3257–3265, doi:10.1002/2015GL063767.

Ruddiman, W.F., Prell, W.L., and Raymo, M.E., 1989, Late Cenozoic uplift in southern Asia and the American west: rationale for general circulation modeling experiments: Journal of Geophysical Research, v. 94, doi:10.1029/jd094id15p18379.

Ruddiman, W.F., and Raymo, M.E., 1988, Northern Hemisphere climate regimes during the past 3 Ma: possible tectonic connections: Philosophical Transactions of the Royal Society of London. B, Biological Sciences, v. 318, p. 411–430, https://royalsocietypublishing.org/.

Scherler, D., Bookhagen, B., and Strecker, M.R., 2014, Tectonic control on ^{10}Be-derived erosion rates in the Garhwal Himalaya, India: Journal of Geophysical Research: Earth Surface, v. 119, p. 83–105, doi:10.1002/2013JF002955.

Stanley, T.A., Kirschbaum, D.B., Sobieszczyk, S., Jasinski, M.F., Borak, J.S., and Slaughter, S.L., 2020, Building a landslide hazard indicator with machine learning and land surface models: Environmental Modelling and Software, v. 129, doi:10.1016/j.envsoft.2020.104692.

Stevens, V.L., and Avouac, J.P., 2015, Interseismic coupling on the main Himalayan thrust: Geophysical Research Letters, v. 42, p. 5828–5837, doi:10.1002/2015GL064845.

Stockmal, G.S., 1983, Modeling of large-scale accretionary wedge deformation: Journal of Geophysical Research, v. 88, p. 8271–8287, doi:10.1029/JB088iB10p08271.

Thiede, R.C., and Ehlers, T.A., 2013, Large spatial and temporal variations in Himalayan denudation: Earth and Planetary Science Letters, v. 371–372, p. 278–293, doi:10.1016/j.epsl.2013.03.004.

Tien Bui, D., Pradhan, B., Lofman, O., Revhaug, I., and Dick, O.B., 2012, Landslide susceptibility assessment in the Hoa Binh province of Vietnam: A comparison of the Levenberg-Marquardt and Bayesian regularized neural networks: Geomorphology, v. 171–172, p. 12–29, doi:10.1016/j.geomorph.2012.04.023.

Tien Bui, D., Tsangaratos, P., Nguyen, V.T., Liem, N. Van, and Trinh, P.T., 2020, Comparing the prediction performance of a Deep Learning Neural Network model with conventional machine learning models in landslide susceptibility assessment: Catena, v. 188, doi:10.1016/j.catena.2019.104426.

Varikoden, H., and Revadekar, J. V., 2020, On the extreme rainfall events during the southwest monsoon season in northeast regions of the Indian subcontinent: Meteorological Applications, v. 27, doi:10.1002/met.1822.

Whipple, K.X., 2009, The influence of climate on the tectonic evolution of mountain belts: Nature Geoscience, v. 2, p. 97–104, doi:10.1038/ngeo413.

Willenbring, J.K., and von Blanckenburg, F., 2010, Long-term stability of global erosion rates and weathering during late-Cenozoic cooling: Nature, v. 465, p. 211–214, doi:10.1038/nature09044.

Willett, S.D., 1999, Orogeny and orography: The effects of erosion on the structure of mountain belts: Journal of Geophysical Research: Solid Earth, v. 104, p. 28957–28981, doi:10.1029/1999jb900248.

Willett, S.D., and Brandon, M.T., 2002, On steady states in mountain belts: Geology, v. 3, p. 175, http://pubs.geoscienceworld.org/gsa/geology/article-pdf/30/2/175/3524227/i0091-7613-30-2-175.pdf.

Yang, Y., Zhao, T., Ni, G., and Sun, T., 2018, Atmospheric rivers over the Bay of Bengal lead to northern Indian extreme rainfall: International Journal of Climatology, v. 38, p. 1010–1021, doi:10.1002/joc.5229.

Yatagai, A., Kamiguchi, K., Arakawa, O., Hamada, A., Yasutomi, N., and Kitoh, A., 2012, Aphrodite constructing a long-term daily gridded precipitation dataset for Asia based on a dense network of

rain gauges: Bulletin of the American Meteorological Society, v. 93, p. 1401–1415, doi:10.1175/BAMS-D-11-00122.1.

Yin, A., 2006, Cenozoic tectonic evolution of the Himalayan orogen as constrained by along-strike variation of structural geometry, exhumation history, and foreland sedimentation: Earth-Science Reviews, v. 76, p. 1–131, doi:10.1016/j.earscirev.2005.05.004.

Chapter 2:

Landslide Susceptibility Modeling by Interpretable Neural Network

Note: This chapter is modified from Youssef, K.*, Shao, K.*, Moon, S., & Bouchard, L. S. (2023). Landslide susceptibility modeling by interpretable neural network. *Communications Earth & Environment*, 4(1), 162. (* co-first authors). This chapter contains my primary contributions to this work.

2.1 Introduction

Landslides are a major natural hazard that cause billions of dollars in direct damages and thousands of deaths globally each year (Petley, 2012; Froude and Petley, 2018). Landslides can also cause various secondary hazards, such as damming and flooding, which often leave a region prone to subsequent damage following the initial event (Huang and Fan, 2013). Additionally, landslide debris may cause instability by perturbing river sedimentation and disrupting ecosystems (Huang and Fan, 2013; Fan et al., 2019). As landslide hazards are expected to increase due to climate change, scientists have sought to more accurately assess landslide susceptibility (Tien Bui et al., 2012, 2019; Stanley and Kirschbaum, 2017; Phong et al., 2019; Kirschbaum et al., 2020; Dikshit et al., 2021), an estimate of the probability that a landslide may occur in a specific area, with the goal of mitigating the impact of landslides on the economy, public safety, and local ecosystems.

Landslide occurrences are influenced by various factors including physical attributes of the terrain, such as slope, relief, and drainage areas, and material properties such as the density and strength of soil and bedrock (Radbruch-Hall et al., 1982; Montgomery and Dietrich, 1994; Dietrich et al., 1995; Montgomery et al., 1998). Also, environmental conditions such as climate, hydrology, ecology, and ground motion due to earthquakes may contribute to slope instability (Guzzetti et al., 1999; Baum et al.,

2002; Meunier et al., 2008). Landslide susceptibility is calculated from these various controlling factors either through physically-based models (Montgomery and Dietrich, 1994; Montgomery et al., 1998; Baum et al., 2002, 2010), data-driven approaches utilizing statistical analysis (Lee and Sambath, 2006; Regmi et al., 2014), or machine learning techniques (ML), including random forest, support vector machines, and deep neural networks (DNN) (Lee et al., 2004; Gómez and Kavzoglu, 2005; Conforti et al., 2014; Tien Bui et al., 2019, 2020; Van Dao et al., 2020; Stanley et al., 2020).

While substantial work has been devoted to assessing susceptibility, each model has shortcomings. Physically- or mechanistically-based approaches, based on the equilibrium between driving and resisting forces, have been widely applied to assess slope stability (Montgomery and Dietrich, 1994; Dietrich et al., 1995, 2001; Montgomery et al., 1998). However, mechanistic models have limitations, including a limited number of variables, simplified assumptions of landslide geometry and certain environmental conditions (e.g., antecedent moisture, bedrock structure), and the high cost of geotechnical exploration necessary to estimate and calibrate for accurate subsurface properties (e.g., cohesive strength, pore pressure, weathering profile) (Guzzetti et al., 1999). Alternatively, data-driven approaches, including statistical and ML methods, can handle a large number of controls to assess susceptibility. Statistical methods such as logistic regression and likelihood ratios (Lee and Sambath, 2006; Regmi et al., 2014; Reichenbach et al., 2018) can utilize a multitude of landslide controls as inputs. Scientists using these data-driven approaches have obtained a measurable degree of success in determining areas susceptible to landslides (Lee and Sambath, 2006; Regmi et al., 2014; Tien Bui et al., 2019). However, these data-driven models also rely on the expert's choices, preconditions, and classifications of input variables. The outcome of these models' results, the landslide susceptibility map, does not decouple individual feature contributions to landslide susceptibility nor account for their interdependencies due to the limited computational capabilities in conventional approaches (Reichenbach et al., 2018).

Machine learning approaches, such as fuzzy logic algorithms, support vector machines, and DNNs, have been applied to landslide studies for mapping landslide susceptibility (Gómez and Kavzoglu, 2005;

Pradhan, 2013; Tien Bui et al., 2020). DNNs have achieved improved performance compared to both statistical methods and other ML approaches due to their use of nonlinearities, complex interdependencies of interlayer connections, as well as internal representations of data (Gómez and Kavzoglu, 2005; Conforti et al., 2014; Adadi and Berrada, 2018; Rudin, 2019; Gunning et al., 2019; Tien Bui et al., 2020; Van Dao et al., 2020). However, the black-box nature of DNNs has been a major hurdle for their adoption in practice and research, making it difficult for experts to understand and trust their outcomes. With DNNs, it is nearly impossible to determine the exact relation between individual inputs and outputs (Adadi and Berrada, 2018; Rudin, 2019; Gunning et al., 2019). Lack of interpretability is a weakness of DNNs and a fundamental drawback for high-stakes applications such as landslide mitigation where decisions impact lives and result in untold costs of insurance and reconstruction (Huang and Fan, 2013; Froude and Petley, 2018; Cui et al., 2019). Interpretability would ideally provide decision-makers with a list of contributing factors ranked in order of importance, as well as any possible interplay between these factors.

The DNN's lack of interpretability has prompted the Defense Advanced Research Projects Agency's (DARPA) third wave of AI call in 2017 and the European Union's 2018 General Data Protection Regulation, which grants a right to an explanation, for algorithmic decisions that are made. Next-generation AI systems refer to the so-called explainable or interpretable AI (XAI) models. The latter must be able to construct explanatory models for classes of real-world phenomena that can be communicated to humans (Adadi and Berrada, 2018). Various XAI categories have since been defined in the literature based on factors such as application and methodology, where each category is further divided into subclasses (Li et al., 2020). Although the use of XAI in research is expanding, existing approaches aimed at explaining black box models exhibit a trade-off between accuracy and interpretability, resulting in a large performance gap (e.g., Leiva et al., 2019). Recently, Rudin (2018) showed that with proper feature engineering, and a shift from explaining existing black box models to creating methods with inherently interpretable models, the trade-off between accuracy and interpretability can be circumvented.

To this end, we propose a framework that bridges the gap between explainability and accuracy for landslide susceptibility models. This framework utilizes a hybrid of model extraction methods and feature-based methods to generate a fully interpretable additive ANN model while simultaneously pruning features and feature interdependencies that are redundant or suboptimal to model performance and generalizability. Additive ANN are a type of generalized additive model (GAM) that has been recently gaining popularity (Friedman, 2001; Hastie, 2017; Agarwal et al., 2020). They combine separate ANNs, each specializing in a single feature, to optimize a common outcome. Unlike other additive XAI methods such as Shapley additive explanations (SHAP) that aim to explain the local behavior of a black box model (Lundberg et al., 2017), additive neural networks are inherently interpretable models with both local and global interpretability. Model extraction methods aim to train an explainable "student" model to mimic the behavior of a "teacher" model, and feature-based methods aim to analyze and quantify the influence or the importance of each input feature (Li et al., 2020). Our optimization framework possesses full interpretability, high accuracy, high generalizability, and low model complexity. Most notably, toy problems provided by Youssef et al. (2023) demonstrate the capability of our framework to generate fully interpretable additive ANNs with controlled complexity and accuracy that can match state-of-the-art DNNs, as well as find globally optimal unique solutions. Furthermore, we utilize dataset division and outcome interpretation techniques uniquely suitable for landslide susceptibility modeling applications with spatially dependent data structures. We refer to the approach as superposable neural network (SNN) optimization in reference to the automated way of incrementally generating the additive ANN model and determining the contributing features. Our approach is different from the more commonly followed approach of designing a fixed network architecture with a fixed set of manually selected input features where the entire network is jointly trained in an end-to-end fashion (Agarwal et al., 2020).

In this study, we model three different regions of the easternmost Himalaya using SNNs. For comparison, we include results from a physically-based slope stability model (SHALSTAB), two statistical methods (logistic regression and likelihood ratios), in addition to state-of-the-art DNN teacher

models. Finally, we examine the SNN-determined relationship and relative importance of each feature's contribution to landslide susceptibility and discuss how information extracted from the SNN can provide insights into the physical controls of landslides in our studied regions. Our results highlight underappreciated, important controls such as the product of slope and precipitation and hillslope aspect in the studied region. Controls that consist of products of input features can help unveil the influences from feature interactions.

2.2 Superposable neural networks

Our collaborator, Dr. Khalid Youssef, designed and developed the architecture of the SNN presented here. SNNs are an additive ANN architecture that enforces no interconnections between inputs (Fig. A1). The lack of interconnections between features is the key to explainability. Unlike DNNs where interdependencies between features are embedded in layers of network connections, interdependencies in SNNs are explicitly created as a product function of more than one original input feature. We refer to these products as "composite features" (see Methods for details). Important interdependencies between features are automatically determined by isolating composite features contributing to the desired outcome. Contributing composite features are explicitly added as independent inputs to the model, while non-contributing composite features are discarded (see SNN training flow diagram in Fig. A2 as well as Methods). Furthermore, we label SNNs according to the highest level of composite features used in training the model, which refers to the maximum number of features allowed in multivariate interactions. For example, a Level-3 SNN can include Level-1, Level-2 and Level-3 composite features. Using composite features, SNNs can approximate any continuous function for inputs within a specific range as a polynomial expansion to any desired precision. This ability allows SNNs to retain a level of accuracy on par with state-of-the-art DNNs.

The SNN is represented mathematically by the function (Eq. 1):

$$S_t(\{\chi_j\}) = \sum_j \left(\sum_k w_{j,k} e^{-\left(a_{j,k}\chi_j + b_{j,k}\right)^2} + c_j \right) \qquad \textit{Eq. 1}$$

It contains only two hidden layers of neurons with radial basis activation functions in the first layer and linear activation functions in the second layer. The choice of radial basis activation functions allows the user to minimize the number of neurons in the model, maximizing the efficiency of our method. Each input χ_j is exclusively connected to a group of neurons to form an independent function $S_j = \sum_k w_{j,k} e^{-\left(a_{j,k}\chi_j + b_{j,k}\right)^2} + c_j$ and the SNN output $S_t = \sum_j S_j$ is the sum of all independent functions, where j = 1:number of features (M), k = 1:number of neurons per feature (v), and χ_j is the j^{th} composite feature. In addition to determining the features and interdependencies between features that contribute to the outcome, the SNN architecture enables the quantification of their exact contributions to the output.

The model simplicity and lack of connections between neurons associated with different features makes our model fully interpretable and mathematically analyzable. However, this aspect also makes the model highly constrained, which poses challenges on its training. Jointly training the model with commonly used gradient descent-based optimizers proved to be extremely difficult to converge, especially as the number of features increases. Our optimization approach enables the separate training of individual neural networks by utilizing several state-of-the-art ML techniques (multi-stage training, knowledge distillation, second order optimization (Hinton et al., 2015; Youssef et al., 2015, 2018; Tan et al., 2018)) to deliver a model that is optimal in terms of performance and remarkably simple in terms of architecture. The reduction in model complexity, while maintaining an accuracy that rivals that of DNNs, which are orders of magnitude more complex in terms of number of parameters and redundancies in interconnectivities, presents a substantial advance.

A validation of our approach using toy models is provided by Youssef et al. (2023). In the first application, we create a synthetic dataset by adding known functions of composite features and test the ability of the SNN to find the contributing features and extract their functions from the data. The second application incorporates up to Level-4 feature interactions and demonstrates the impressive ability to

extract boolean relationships from synthetic data. Boolean inference tasks are notoriously difficult because of the high degree of stiffness and nonlinearity between input and output. The SNN optimization algorithm is described in Methods.

2.3 Landslides in the easternmost Himalaya

Asia holds the majority of human losses due to landslides globally, with a high concentration in the Himalayan Arc (Petley, 2012; Froude and Petley, 2018). In particular, the easternmost Himalaya has a high susceptibility to numerous landslides from steep slopes, extreme precipitation events, flooding, and frequent earthquakes (Ben-Menahem et al., 1974; Barros et al., 2004; Bookhagen and Burbank, 2010; Larsen and Montgomery, 2012; Yang et al., 2018) (Fig. 2.1 and Fig. A3). We generated a landslide inventory of the easternmost Himalaya by combining the manual delineation of landslide areas with a semi-automatic detection algorithm (Ghorbanzadeh et al., 2019; Prakash et al., 2020) (Fig. 2.2a-c; a flowchart diagram in Fig. A4, exemplary landslides in Fig. A5). Within the entire study area of 4.19×10^9 m^2, the total number of mapped landslides is 2,289, and their areas range from 900 to 1.96×10^6 m^2 (Fig. A6, Table A1). Landslide densities calculated over a 2.25 km^2 window are generally high in the range front (max 0.121) and low in the hinterland (~0.039).

Within the easternmost Himalaya, we selected three regions (the Dibang, Lohit, and range front regions) with varying ranges of landslide controls to test the performance and application of the SNN model (Fig. 2.1). Hereafter, we refer to Dibang, Lohit, and range front regions as the N-S, E-W, and NW-SE regions, respectively. Testing the SNN over these three regions with varying environmental conditions will allow us to examine the following: 1) whether the SNN can identify universal or distinctly different controls of landslides, and 2) whether SNN-determined functions of feature contributions to susceptibility, S_j, are similar or different across these three regions. We used 15 single features in the SNN model (Fig. A7, Table A2). The 15 single features include aspect (*Asp*), mean curvature ($Curv_M$), planform curvature, profile curvature, total curvature, discharge, distance to channel ($Dist_C$), distance to

faults ($Dist_F$), distance to the Main Frontal Thrust and suture zone ($Dist_{MFT}$), drainage area, elevation (*Elev*), local relief (Relief), mean annual precipitation (*MAP*), number of extreme rainfall events (*NEE*) and slope. The inclusion of these variables is based on previous studies that examined landslide controls in the Himalayan region (Devkota et al., 2013; Regmi et al., 2014; Mandal and Mandal, 2018; Chowdhuri et al., 2021). The details of study area, landslide inventory, input data sources and calculation are presented in Methods.

2.4 Results and Discussion

2.4.1 SNN Implementation

We modeled landslide susceptibility of the easternmost Himalaya using Level-1, 2, and 3 SNN models. We find that the Level-3 SNN can achieve over 99% of the accuracy of the state-of-the-art teacher DNN, and the Level-2 SNN is able to achieve over 98%. Given the small difference, we assume the explainability of the Level-2 SNN to be sufficient for our analysis. Due to the nature of this application, a special data partitioning method was devised to partition each region into roughly 70% for training and 30% for validation, which utilizes Pythagorean tiling to partition the regions in a spatially representative manner (Fig. A8) (see Methods for details).

A threshold value of S_t is used as a binary classifier to predict landslides and compare them with observed landslides from our inventory. We selected a threshold susceptibility corresponding to the closest point to a perfect classifying model with 100% true positive rate and 0% false positive rate on a receiver operating characteristic (ROC) curve. Areas with S_t greater and lower than this threshold are classified as landslide (*ld*) and non-landslide (*nld*) areas, respectively, in the model (Fig. 2.2d-f).

2.4.2 Comparison with traditional landslide susceptibility modeling

In addition to the comparison against the state-of-the-art DNN teacher model, we provide comparisons of Level-1 and Level-2 SNN performance to a number of traditional methods, all applied to

the same regions and using the same inventory data. Comparison of different models on the same area is needed since model performance cannot be directly compared to model performance published in other papers, since those papers focused on different regions.

First, we investigated each of the 15 single features as individual classifiers for landslide occurrences. Second, we applied a physically-based slope stability model (SHALSTAB) for soil landslides (Montgomery and Dietrich, 1994; Dietrich et al., 2001; Moon et al., 2011) that couples infinite slope stability and steady-state hydrology for cohesionless material. Considering that most landslides in our inventory are soil landslides (Methods), SHALSTAB was assumed to be suitable for our analysis. We modified SHALSTAB and calculated a metric called the failure index (*FI*), as the ratio of driving to resisting forces on a hillslope. *FI* is equivalent to the inverse of the factor-of-safety, which represents the propensity for landslide occurrence. Third, we used two commonly used statistical models, logistic regression and likelihood ratios, to model landslide susceptibility (Lee, 2005; Akgun, 2012; Reichenbach et al., 2018). Logistic regression (hereafter, LogR) is based on a multivariate regression between a binary response of landslide occurrence and a set of predicting features that are continuous, discrete, or a combination of both types (Lee, 2005). Likelihood ratios (LR) are calculated as the ratio of the percentage of landslide pixels relative to total landslide pixels divided by the percentage of pixels relative to the total area within a specific range of feature values (Lee, 2005; Akgun, 2012). Previous studies have quantified the ratio of the probability of landslide occurrences to the probability of non-occurrences or all-occurrences within a range of feature values and referred to it as the likelihood ratio, frequency ratio, or probability ratio (Lee, 2005; Akgun, 2012; Reichenbach et al., 2018). A ratio of 1, >1, or <1 indicates an average, above-average, or below-average likelihood of landslide occurrence, respectively, within the feature range compared to that of the study area. Landslide susceptibility for each pixel is calculated as the sum of the corresponding LR from each feature's value. A threshold value of modeled landslide susceptibility from LogR and LR can be used as a binary classifier to predict landslides following a similar procedure that we used for the SNN.

We assessed model performance based on various metrics including area under the receiver operating characteristic curve (AUROC). In addition, we calculated the statistical measures of accuracy, sensitivity (probability of detection, POD), specificity (probability of false detection, POFD), and POD-POFD. We also calculated the 95% confidence interval of mean AUROC from the statistical and neural network model outputs based on a 10-fold cross validation. The 95% confidence intervals of mean AUROC can be used to determine whether model performances are statistically different (model and method details in Appendix Note A1).

We show that the SNN model's performance is comparable to that of the teacher, second-order-optimized DNN, while providing a statistically significant improvement over commonly used physically-based and statistical models. AUROCs of Level-1 and Level-2 SNNs are 0.856 and 0.890, respectively, calculated as the averages from the three study regions. The value for each region is presented in Table A3. The Level-2 SNNs captured over 98% of the teacher model (MST) performance across all three study regions. The Level-2 SNN is optimal in the sense that it provides high accuracy (comparable to deep nets) and relatively simple model complexity (hereafter, SNN refers to Level-2 SNN).

The SNN achieved ~21% average improvement in AUROC over the top performing single original features (i.e., MAP or slope, AUROC = 0.737), ~22% over a physically-based model (SHALSTAB) (AUROC = 0.727), and ~5-8% over logistic regression (AUROC = 0.848) and likelihood ratios (AUROC = 0.823) in our three study regions. The 95% confidence intervals of the mean AUROC of the SNN lie above and do not overlap with those of the statistical models (Table A4). In addition, the vast majority of other performance metrics such as accuracy, POD, POFD, and POD-POFD from the SNN are improved over these other methods as well (Table A5).

2.4.3 SNN model explainability

The SNN-determined independent functions S_j show varying relationships between both features and feature interdependencies, and their absolute susceptibility contribution (Fig. 2.4). $S_{MAP*Slope}$ and $S_{NEE*Slope}$

generally exhibit steep increases with feature value, followed by asymptotic behavior (Fig. 2.4a, d, g). These nonlinear relationships between landslide susceptibility and the product of slope and climatic features of MAP and NEE are similar in all three regions. In addition, S_{Asp} shows a peak around 145◦ to 180◦, which indicates a preference for south-facing slopes, likely due to moisture from the Bay of Bengal (Bookhagen and Burbank, 2010) (Fig. A9, Appendix Note A2). These functional relationships are similar to those deduced by the LR statistical method that represent the likelihood of landslide occurrence. However, unlike LR, which assume the same, average likelihood (LR = 1) for each feature, S_j corresponding to LR = 1 varies depending on a feature's absolute, decoupled contribution to landslide susceptibility.

The SNN provides the exact contribution of each individual feature to the total susceptibility outcome, which allows us to quantify the relative importance of landslide controls in different localities and across varying spatial scales (Fig. 2.5d-f). Causal rankings of individual features that drive landslides can be obtained by calculating the susceptibility difference between *ld* v.s. *nld* pixels, $\Delta\bar{S}_j$, within a region of interest for each individual feature. This is demonstrated both globally (Fig. 2.5a-c), where the region of interest is the entire region of study, and locally (Fig. 2.6a-c), where the region of study is divided into hundreds of smaller regions of interest, each consisting of a 2.25 km^2 window. For comparison, we also identified the primary controls of landslides and their relative contributions from the Level-1 SNN and weights determined by the logistic regression model (Appendix Note A1, Fig. A10).

Composite features involving topographic and climate features are identified as important landslide controls for our study area. Namely, the product of slope and *NEE* or *MAP*, *Asp*, and the product of *Asp* and *Relief* tend to have large $\Delta\bar{S}_j$ across all three regions (Fig. 2.5a-c). In addition, those features are identified as locally important, primary features when analyzing using a 2.25 km^2 window throughout the area (Fig. 2.6a-c). The primary features of *MAP*Slope* and *NEE*Slope* are consistent among our three study regions in the easternmost Himalaya, despite differences in the spatial distribution and magnitude of precipitation and proximity to a major fault with a history of earthquakes (Fig. A3). In the N-S region,

localities where *Asp*Relief* is a primary feature are spatially consistent with areas with lower *MAP* and particularly high *Relief*. Although these composite features may not be the largest contributor for total susceptibility (Fig. 2.5d-f), they tend to have different contributions for *ld* and *nld* areas and lead to a large $\Delta\bar{S}_j$ (Fig. 2.5a-c).

SNN-derived individual feature contributions are used to assess the relative importance between climate and slope features. The feature independence in the SNN additive architecture and the use of composite features allows us to isolate the effect of slope or climate in the model. (1) The exact marginal contribution is calculated for Level-2 features involving slope or climate (i.e., *Asp*, *NEE*, and *MAP*). (2) Level-1 slope and Level-2 slope marginal contributions are added together to produce the total susceptibility contribution from slope, $S_{t,Slope}$. (3) Level-1 climate and Level-2 climate marginal contributions are added together to produce total susceptibility contribution from climate features, $S_{t,Climate}$. In Fig. 2.6d-f, we compare the relative importance of slope and climate features using our approach that separates their contributions between *ld* and *nld* pixels throughout the region. Then, we calculate the difference between $\Delta\bar{S}_{t,Slope}$ and $\Delta\bar{S}_{t,Climate}$, divided by the threshold susceptibility value, $S_{t,threshold}$, for each respective region. Localities with greater climate than slope susceptibility contributions are generally consistent with spatial patterns of high *MAP* or *NEE* across all study regions. However, localities in the hinterland of the N-S region with large climate contributions reflect susceptibility contributions from *Asp* and generally coincide with areas where *Asp*Relief* is a primary feature (Fig. 2.6a). Additionally, although most of the NW-SE region experiences high NEE (Fig. A7n), localities in the NW-SE region with higher slope than climate susceptibility contributions coincide with areas of especially high slope (Fig. A7o). Overall, we find that ~74%, 54%, and 54% of localities have a larger contribution from climate features than that of slope for the N-S, NW-SE, and E-W regions, respectively, emphasizing the importance of climatic features in driving landslides.

2.4.4 Accurate and interpretable landslide susceptibility from the SNN

Whereas many XAI efforts involve a trade-off between accuracy and interpretability, our SNN does not compromise accuracy. Given the SNN's inherent and unique ability to decouple individual feature contributions and select feature interdependencies, we can easily isolate local contributions from primary controls discovered by the SNN (Fig. 2.6). Our local analyses for assessing landslide controls indicate that the contribution of climate features, such as *NEE*, *MAP*, and *Asp*, to landslide susceptibility tends to surpass that of slope for a majority of landslide occurrences in this area. These results highlight a prevalent climatic control on landslide occurrences in the easternmost Himalayan region. Due to the eastward increasing trends of precipitation rate and variability along the Himalaya, the easternmost Himalaya contains one of the largest strike-perpendicular climatic variations across the steep mountain range (Bookhagen and Burbank, 2010). This considerable climate gradient from the range front to the hinterland likely impacts landslide susceptibility in the easternmost Himalaya.

The transparency of our SNN model offers insight into potential mechanisms of landslides and the relative importance of controlling factors. First, the SNN highlights the important, yet underappreciated controls of *NEE*Slope*, *MAP*Slope*, *Asp*, and *Asp*Relief* (Fig. 2.6), which implies a dominant occurrence of precipitation-induced landslides in our study site. However, these topography-climate composite features reveal the importance of both incorporated features. These features comprising the product between slope and precipitation rates and intensity as well as that of aspect and relief suggest that landslides are affected by strong slope-climate couplings and aspect-related microclimates.

The nonlinear asymptotic function of $S_{MAP*Slope}$ and $S_{NEE*Slope}$ (Fig. 2.4a, d, g) can be explained by a physical mechanism of rainfall-induced landslides that induces slope failure due to an increase in pore-water pressure and subsurface saturation (Iverson, 2000). The modeled total landslide susceptibility (S_t) is analogous to the physically-derived failure index (*FI*), which is equivalent to the inverse of the factor-of-safety. *FI* is formulated from equilibrium on an infinite, cohesionless slope considering a pore pressure effect based on SHALSTAB (Montgomery and Dietrich, 1994; Moon et al., 2011) as:

$$FI = \frac{S}{S_0}\left(1 - W\frac{\rho_w}{\rho_s}\right)^{-1} \qquad Eq.\ 2$$

where S_0 is the threshold slope, S is the local slope, ρ_s is the wet bulk density of soil (2.0 g/cm^3), ρ_w is the bulk density of water (1.0 g/cm^3), and W is wetness. W is calculated as a ratio between local hydraulic flux from a given steady-state precipitation rate relative to that of soil profile saturation (Montgomery and Dietrich, 1994):

$$W = \frac{h}{z} = \frac{qA}{bTsin\theta} \qquad Eq.\ 3$$

where h is the saturated height of the soil column (L), z is the total height of the soil column (L), q is the steady-state precipitation during a storm event (L/T), A is the drainage area (L^2) draining across the contour length b (L), T is the soil transmissivity when saturated (L^2/T), and θ is the local slope in degrees. W varies from 0 (unsaturated) to 1 (fully saturated). See Appendix Note A1 for model details.

Expansion of the denominator in a geometric series gives:

$$FI = \frac{S}{S_0}\left(1 + W\frac{\rho_w}{\rho_s} + W^2\left(\frac{\rho_w}{\rho_s}\right)^2 + O(W^3)\right) \equiv \frac{S}{S_0}k(W) \qquad Eq.\ 4$$

The approximated FI has three components: local slope S, threshold slope S_0, and $k(W)$, which represents the degrees that landslides are promoted by subsurface saturation. $k(W)$ varies from 1 (unsaturated) to 2 (fully saturated). The multiplication of local slope and $k(W)$, which has an upper bound, mimics the nonlinear asymptotic function of $S_{MAP*Slope}$ and $S_{NEE*Slope}$. This asymptotic increase in susceptibility is similar to observations of other precipitation-induced landslides, but different from earthquake-induced landslides whose occurrences increase nonlinearly with increasing slope (Meunier et al., 2008; Huang and Montgomery, 2014).

Second, the identified controls of *MAP*, *NEE*, and *Asp* imply that local precipitation infiltration on steep slopes may be the dominant contributors to subsurface saturation in the easternmost Himalaya. A change in climatic conditions can raise volumetric water content and porewater pressure. This rise leads

to an increased degree of subsurface saturation (i.e., *W*) and subsequently induces slope failure. Previous physically-based slope stability models consider various climatic factors (e.g., rainfall amount and intensity, subsurface convergence flow) to deduce the degree of subsurface saturation to model rainfall-induced landslide occurrences (Montgomery and Dietrich, 1994; Baum et al., 2002, 2010). For example, SHALSTAB (Montgomery and Dietrich, 1994; Dietrich et al., 2001) uses the topographic wetness index, proposed by Beven and Kirkby (1979), to calculate subsurface saturation considering the convergence of shallow subsurface flow from up-slope drainage areas for a given steady-state precipitation. On the other hand, the Transient Rainfall Infiltration and Grid based Regional Slope stability model (TRIGRS) (Baum et al., 2002, 2010) calculates transient pore pressure development due to vertical rainfall infiltration from rainfall intensity. In reality, both subsurface convergence and rainfall infiltration are essential contributors to subsurface saturation and need to be implemented in physically-based slope stability models. However, measuring precipitation intensity, moisture availability, or subsurface convergence and saturation in the field is difficult, especially in rural mountainous areas with limited accessibility.

According to our SNN model results, the most important, controlling features for landslides in this area are the product of slope and *MAP* (N-S region) or that of slope and *NEE* (NW-SE and E-W regions). This result implies that local precipitation infiltration influenced by precipitation rate and intensity, represented by *MAP* and *NEE*, may serve as a first-order control on *W* or *k(W)* in eq. (4). The absence of drainage area or discharge as a dominant contributing feature to susceptibility may suggest that subsurface flow convergence may be a second-order contributor to landslides in the easternmost Himalaya. However, we cannot rule out the possibility that the importance of topographic convergence was masked due to the low-resolution of our input topographic and rainfall data (Leonarduzzi et al., 2021). These factors can be further examined in future studies using high-resolution topographic and climate data in SNN models.

Nonetheless, identifying the exact trigger for a landslide requires dense field measurements and historic records of soil, hydrologic, and climatic conditions (e.g., soil moisture, antecedent rainfall,

rainfall intensity) (Kirschbaum et al., 2020; Orland et al., 2020), which are often difficult to obtain, especially in rural mountainous areas with limited accessibility. We have shown that our SNN model can identify key controls and quantify their potential contributions to susceptibility, highlighting the essence of strong slope-climate coupled controls on landslide occurrences. The composite features identified by the SNN such as *NEE*Slope* or *MAP*Slope* are consistent with previous understandings of landslide mechanisms. However, they were not explicitly implemented in previous data-driven statistical models. In DNNs, such couplings would likely be identified, but if that were the case, the information would be implicitly contained in the network weights and not readily available to the user. By incorporating climatic composite features including *MAP*Slope*, *NEE*Slope*, and *Asp*Relief*, the performance of the SNN improved, increasing average AUROC by 5-22% compared to those of statistical or physically-based models (Montgomery and Dietrich, 1994; Dietrich et al., 2001; Lee, 2005; Akgun, 2012) (Appendix Note A1, Table A3). This performance enhancement is statistically significant according to our confidence interval estimates from a 10-fold cross validation.

2.4.5 Implications, limitations, and future directions

Our work presents a substantial advance in XAI applications to natural hazards and circumvents the "black box" nature of common AI models. SNNs provide quantitative analyses of controlling factors and further highlight the important, mechanistic interpretations of landslides. Our AI-based decision-making approach provides a comprehensive framework that allows for the examination of numerous composite features and identification of key controls while retaining high accuracy. As natural perturbations increase due to urban development and climate change, the SNN may provide a promising, data-driven predictive tool that will enable communities to confidently tailor plans for hazard mitigation.

While a variety of explainable AI methods are available today, our proposed SNN method offers unique advantages that are not simultaneously present in any other method. SNN is a fully explainable model that achieves a level of explainability comparable to linear regression, while delivering state-of-

the-art performance that matches that of black box models like deep neural networks. Furthermore, unlike other additive models, SNN can incorporate multivariate functions without compromising full explainability. Additionally, the model features adaptive optimization of both feature selection and network architecture during training. A comprehensive comparison of SNN with other explainable AI methods must take all of these factors into account. This requires an in-depth study beyond the scope of this paper. For instance, other additive model methods generally rely on fixed architectures and preselected feature sets that lack feature interactions beyond bivariate interactions. On the other hand, decision trees utilize highly nonlinear interactions between multiple features through a different approach that theoretically offers full explainability but is often difficult to interpret for large number of features or complex problems requiring numerous branches. It is also worth noting that SNN is not restricted to MST as the teacher model, and its accuracy can be further improved when more accurate teacher models are found. A viable alternative to MST for applications with small datasets is random forest, which is an ensemble of decision trees trained on randomly selected feature and dataset subsets using bootstrapping. While decision trees are explainable, random forest is considered a black box since its outcome is an aggregate of multiple trees. In such cases, SNN can leverage random forest as a teacher model to achieve similar accuracy while maintaining full explainability.

We acknowledge that the overall importance of slope and climatic features and their functional relationships with susceptibility revealed by the SNN are qualitatively similar to those inferred from statistical models. However, the SNN is more useful for landslide susceptibility assessment because it decouples individual feature contributions and quantifies absolute contributions from features and feature interdependencies. For example, the relative and absolute importance of SNN decoupled features are different from those determined by the weights set by logistic regression. In addition, our analysis shows that S_j corresponding to LR=1 differs depending on a feature's absolute, decoupled contribution to landslide susceptibility. The SNN approach reveals the important coupling between slope and climatic factors (e.g., *MAP*Slope*, *NEE*Slope*) as a primary driver for landslide occurrence. Accounting for these

underappreciated features and feature interdependencies that are not generally implemented in statistical methods or physically-based models can lead to a substantial increase in performance. We note that these results are specific to the region analyzed herein (easternmost Himalaya), and other regions may feature a different set of dominant factors.

We acknowledge there are limitations of our method in the easternmost Himalaya. Our input features are averaged over time and space, making it impossible to relate them directly to specific events (e.g., intense rainstorms or earthquakes) inducing landslides in our inventories. In addition, our inventory is based on optical satellite images acquired at a specific time (e.g., 2017 Landsat) and post-failure spectral signatures. Thus, our model lacks information about the precise timing or types of landslides (e.g., fast- or slow-moving landslides, soil or bedrock landslides). This makes it difficult to assess the timescales and spatial dependencies of landslide-triggering events (e.g., rainfall intensity or duration) for specific landslides or landslide types. Previous studies from the Nepal Himalaya suggest that the spatial distribution of landslides can vary with triggering events such as cloud outbursts, flooding and large-magnitude earthquake (Jones et al., 2021a, 2021b).

However, for this study region, our method properly captures the first-order climatic controls of landslide occurrences. Our primary feature datasets may capture a representative, spatial distribution of landslide-triggering events such as intense precipitation and rock damage over the decadal timescale of concern. In the easternmost Himalaya, both *MAP* and *NEE* from TRMM and APHRODITE datasets covering 12 and 50 years show similar southward increasing trends (Bookhagen and Burbank, 2010; Yatagai et al., 2012). This spatial pattern likely emerges from the aggregation of intense precipitation events influenced by orographic precipitation (Bookhagen and Burbank, 2010). In the 30 years prior to the mapped inventory, there were no earthquakes with a magnitude larger than M_W 5.0 (Incorporated Research Institutions for Seismology, www.iris.edu), which can induce abundant landslides. In future studies, a time-series landslide inventory from multiple years and information on nonrepresentative or

infrequent extreme events can be used to assess the spatial and temporal correspondence between triggering events and landslides (Jones et al., 2021a).

Additionally, landslide and input feature data have relatively coarse spatial resolutions and are based on limited temporal information (e.g., 30 m resolution Landsat satellite images from 2017, 90 m resolution SRTM DEM, and ~5 km resolution TRMM data over 12 years (Bookhagen and Burbank, 2010)). We do not have access to high-quality, high-resolution data of topography, surface materials (e.g., soil depth, bedrock structures, lithology), and climatic and ecohydrologic conditions (e.g., landslide-triggering storm intensity, time-series precipitation intensity, vegetation types). Due to the extremely rugged mountains in the Himalaya, the highest available DEM resolution without extensive data gaps, suitable for regional-scale landslide susceptibility analysis, is 90 m (Stanley and Kirschbaum, 2017; Kirschbaum et al., 2020). Also, there are no readily available time-series precipitation data with a resolution <5 km in this area. We used relatively coarse 30 m resolution Landsat images to map landslides even though limited high-resolution satellite imagery is available (e.g., PlanetScope Scene). This is because: 1) Landsat images are globally available, open-source satellite images with a ~40-year historic archive, 2) reliable topographic, climatic, and geologic feature data have coarser resolutions than 30 m, and 3) we cover a large region of the easternmost Himalaya (a total area of 4.19×10^9 m^2, 4.66×10^6 pixels at 30 m). When applying a regional-scale model covering a large area with limited input data resolution and high computational costs, the use of 30 m resolution imagery for our model was inevitable. Although our inventory is based on coarse 30 m resolution Landsat images, our landslide inventory adequately captures the regional-scale spatial distributions of landslide occurrences and provides essential information for regional-scale landslide susceptibility models (see Methods). However, it is possible that our results from both physically-based or data-driven models may be biased due to the inherited uncertainties and limitations of our input data that are resolution-sensitive (e.g., topographic metrics, mapped landslides).

Despite data limitations and uncertainties, our method is general and adaptable to other regions as well as sets and formats of contributing factors and available datasets. Our SNN analysis of the easternmost Himalaya alone presents an important contribution to landslide hazard studies. High mountains in Asia hold the majority of human losses due to landslides globally, according to a global analysis conducted using 2004 - 2016 data (Petley, 2012; Froude and Petley, 2018). Due to the associated high risks, there have been efforts to model landslide susceptibility in the Himalayan regions based on currently available data with limited resolutions (Devkota et al., 2013; Regmi et al., 2014; Mandal and Mandal, 2018; Kirschbaum et al., 2020; Chowdhuri et al., 2021). Our work aims to capture the regional-scale spatial distributions of landslide susceptibility, differentiate controls of landslide occurrences, and provide interpretable, empirical functional relationships between landslide controls and susceptibility. The decoupled SNN-identified functions combined with future changes in environmental conditions (e.g., extreme precipitation) (Kirschbaum et al., 2020; Stanley et al., 2020) may provide a promising tool for assessing potential landslide hazards in this area. Additionally, a modified version of the semi-automatic detection algorithm can be extended further to incorporate InSAR data from sources such as Copernicus Sentinel-1 satellites alongside time-scale optical satellite imagery (Bekaert et al., 2020; Singh et al., 2022) to specifically detect slow-moving landslides in future studies. With these datasets, we can apply SNN methods to slow-moving landslides and assess the controls of surface deformation while accounting for temporal changes in environmental conditions (Finnegan et al., 2021). Our method is easily applicable to other locations, different datasets, and other physical hazards, such as earthquakes and wildfires. The SNN is remarkably simple consisting of only two hidden layers, yet its performance rivals that of DNNs. Our SNN can also be easily updated and improved when global, open-source, high-resolution datasets and high-performance computational resources become more available in the future.

2.5 Methods

2.5.1 Study Area

Numerous landslides in the Himalayan region come from steep topography, intense rainfall and flood events, and seismic activities (Kent and Dasgupta, 2004; Bookhagen and Burbank, 2010; Larsen and Montgomery, 2012; Coudurier-Curveur et al., 2020; Chowdhuri et al., 2021). In particular, the easternmost Himalaya (Fig. 2.1) has a high susceptibility to landslides due to the following reasons. First, this area exhibits a dramatic precipitation gradient due to moisture originating from the Bay of Bengal in the south (Barros et al., 2004; Bookhagen and Burbank, 2010; Yang et al., 2018) (Fig. 2.1). Previous studies have calculated daily and mean annual precipitation rates based on 90-min measurements from the Tropical Rainfall Measuring Mission (TRMM) 2B31 over 12 years (January 1998 to December 2009), with a spatial resolution of ~5 km (Bookhagen and Burbank, 2010). According to these datasets, our region has mean annual precipitation rates (*MAP*) varying from ~7000 mm/yr in the range front to ~200 mm/yr in the hinterland (Bookhagen and Burbank, 2010) with the number of extreme rainfall events (*NEE*), calculated as the number of days that exceed the 90th percentile of daily rainfall rates, reaching ~13 and ~2 events/yr in the range front and hinterland, respectively (Bookhagen and Burbank, 2010). The dramatic orographic patterns of precipitation magnitude and variability are also observed in the 57-yr Asian Precipitation–Highly Resolved Observational Data Integration Towards Evaluation of Water Resources project (APHRODITE) (Yatagai et al., 2012). Second, this area has consistently steep slopes from the range front, where Holocene Himalayan shortening is concentrated near and along the Main Frontal Thrust, into the hinterland, which is affected by deglaciations from the last glacial maximum (Burgess et al., 2012; Haproff et al., 2019, 2020; Salvi et al., 2020). Third, this area is prone to active seismicity. The 1950 M_W 8.6 Assam earthquake, one of the largest earthquakes in the Himalayan range, struck the nearby Namche Barwa region (Ben-Menahem et al., 1974). Since 1973, this region has experienced >450 earthquakes with M_W >4 according to the Incorporated Research Institutions for Seismology data archive (www.iris.edu, accessed on 10/01/2020). Many of these factors contribute to landslide occurrences in our study site.

Within the easternmost Himalaya, we selected three regions (the Dibang, Lohit, and range front regions) with varying ranges of landslide controls to test the performance and application of the SNN model (Fig. 2.1; Fig. A3). Both Dibang and Lohit regions extend from the active range front to the hinterland, from north to south and east to west, respectively. The Dibang region consists of metasedimentary rocks in the range front and crystalline rocks in the hinterland. The Lohit region is mainly composed of crystalline rocks. The active range front region is oriented in a northwest-southeast direction and mainly composed of metasedimentary rocks.

2.5.2 Landslide Inventory

We generated a landslide inventory of the easternmost Himalaya using a semi-automatic detection algorithm that combines manual delineation of landslide areas with an automatic detection algorithm based on convolutional neural networks (CNN) (Ghorbanzadeh et al., 2019; Prakash et al., 2020) (Fig. 2.2a-c; the method illustrated using a flowchart diagram in Fig. A4). The basic procedure is as follows. We initially mapped landslides using 30 m resolution Landsat 8 imagery from November 2017 with bands 2, 3, 4, 5, and 7. These satellite images were used to generate natural and false color imagery to show information of landcover types. High degrees of vegetation in the area allow for the easy detection of vegetation removal due to landslides and clear delineation of a landslide polygon. Most landslides are mapped as a combination of source and deposit, which are difficult to distinguish in coarse-resolution Landsat bands. Whenever possible, we excluded debris transport or deposits and only mapped landslide scars associated with source areas. Because our landslide mapping is based on spectral signatures of post failures, our inventory likely includes both shallow, soil landslides and deep, bedrock landslides. We only assessed regions where landslides generally have the potential to occur or be detectable. Thus, areas of topographic slope less than 0.06 and alpine areas without vegetation cover were excluded from our landslide mapping and analysis. A slope threshold of 0.06 was determined to be the minimum slope along which landslides occur based on a cumulative distribution function of slope from observed landslides in the easternmost Himalaya. Similar criteria based on terrain characteristics such as slope or local relief

have been used in previous studies to constrain the area of landslide analysis (Parker et al., 2011). Alpine areas were classified using spectral signatures representing snow cover in Landsat 8 imagery from February 2018.

Then, we used a CNN to detect landslides automatically, following previous works (Ghorbanzadeh et al., 2019; Prakash et al., 2020) (Fig. A4). The CNN is used as a segmentation model for identifying landslides from 5 Landsat 8 bands and 7 input features (i.e., mean curvature, elevation, local relief, mean annual precipitation, slope, failure index, and wetness). The model takes a 32×32×12 patch as an input, where 12 represents the sum of 5 satellite bands and 7 input features. The model produces a 32×32 binary patch as an output, where landslide pixels are given a value of 1, and non-landslide pixels are given a value of 0. The model segments a full region by dividing the region into 32×32 patches, segmenting each patch individually, then stitching the model outputs back together to obtain a fully segmented region. The training dataset was prepared by manually annotating a small percentage of each studied region to be used as the ground truth targets for training the CNN. The manually annotated areas were selected as a number of randomly distributed 50×50 pixel square sections throughout the studied regions. The manually annotated sections were selected such that half of them include landslides and half of them do not. Hundreds of 32×32 patches were extracted from each 50×50 square section to augment the size of the training dataset. Once the CNN model is trained and used to segment the full region, the result is reviewed manually by an expert and modifications are made.

We manually corrected landslides from the automatic detection method using Landsat 8 images, high-resolution satellite images from Google Earth, and a 4-band PlanetScope Scene with a 3 m resolution. Manual correction is necessary because of potentially inaccurate representations of landslide areas in automatically mapped inventories. Common issues include large, detected features aggregated from multiple, adjacent landslides and small detected features that are not related to landslides (Parker et al., 2011; Marc and Hovius, 2015). We divided aggregated features into multiple landslides following suggestions from a previous study (Marc and Hovius, 2015). Most landslide polygons in all study regions

were checked for aggregated features, which were divided based on the spectral signatures of recent scars and debris flows shown in high-resolution imagery. We used the manually corrected, automatically mapped landslides for our final landslide inventory (referred to as semi-automated landslides). The spatial distributions and extents of landslides from our inventory are shown in Fig. 2.2a-c.

The manually and semi-automatically detected landslides show a good correspondence (>90% match for landslides >4 pixels (3,600 m^2)) based on object identification that examines the existence of overlapping areas. Generally, most landslides missing from the manually detected inventory are objects with a small number of pixels that are not easily and objectively detected by humans. Semi-automated landslides with ≤4 pixels comprise ~7.5% of total landslide areas. When comparing these pixels with 3 m resolution Planetscope Scene satellite images during the post-processing procedure, we found that many of these pixels are indeed small landslides showing different spectral signatures (e.g., Fig. A5). Thus, we included these semi-automatic landslides with ≤4 pixels in our final inventory. Areas commissioned by semi-automatic detection, but not manual mapping, were ~0.1, ~0.4, and ~0.1%, while areas omitted by semi-automated detection were ~0.2, ~0.6, and ~0.1% of the N-S, NW-SE, and E-W study areas, respectively.

The area frequency distribution of our landslides from manual and semi-automatic mappings before 2017 shows a similar distribution to that of pre-2007 landslides from a nearby eastern Himalayan region that was manually mapped using 15-30 m resolution ASTER and Landsat images (Larsen et al., 2010; Larsen and Montgomery, 2012) (Fig. A6). According to a global compilation of geometrical measurements and types of 4,231 landslides (Larsen et al., 2010), soil landslides from all examined regions including the Himalayan region do not appear to exceed an area of 100,000 m^2. Below this threshold, soil landslides tend to be dominant (Larsen et al., 2010; Larsen and Montgomery, 2012). In our landslide inventory, <1% of individual landslides and <20% of total landslide area are greater than 100,000 m^2 (Table A1). Thus, we assume that most mapped landslides are likely soil landslides. In addition, we find that more abundant small landslides detected using the semi-automated method are

similar to those observed in the landslide area-frequency distribution based on high-resolution imagery (~4-15 m) from an eastern Himalayan region nearby (Fig. A6) (Larsen and Montgomery, 2012). This supports that our semi-automatically mapped landslide inventory likely includes many small landslides missed by humans that were detected by a CNN-based automatic detection algorithm.

The total number of semi-automatically mapped landslides in our inventory is 2,289, whose areas range from 900 to 1.96×10^6 m^2 (Fig. 2.2a-c). The total mapped landslide area is 2.83×107 m^2, which produces a landslide density of 0.007 within the entire study area of 4.19×10^9 m^2 (Table A1). Landslide density is also calculated within a 2.25 km^2 window, which is greater than the largest landslide size (1.96 km^2). Landslide densities calculated over a 2.25 km^2 window are high in the range front (maximum of 0.121) and low in the hinterland (maximum of 0.039).

2.5.3 Model Input Feature Descriptions

We quantified the spatial distribution of 15 topographic, climatic, and geologic controls and used them as input features for the SNN (Fig. A7, Table A2). Topographic controls include aspect (the direction of topographic slope face; *Asp*), mean curvature (*CurvM*), planform curvature, profile curvature, total curvature, distance to channel (*DistC*), drainage area, elevation (*Elev*), local relief calculated as an elevation range within a 2.5 km radius circular window (*Relief*), and slope. Climatic or hydrologic controls include discharge, mean annual precipitation (*MAP*), and number of extreme rainfall events (*NEE*). Last, geologic controls include the distance to lithologic boundaries (i.e., mostly faults) ($Dist_F$) and distance to the Main Frontal Thrust and suture zone ($Dist_{MFT}$). These features were selected from literatures that examined landslide occurrences in the Himalayan region (Devkota et al., 2013; Regmi et al., 2014; Mandal and Mandal, 2018; Chowdhuri et al., 2021). We mostly used features directly measured through satellite data including a 90 m digital elevation model from the Shuttle Radar Topography Mission (SRTM) and rainfall magnitude and variability from TRMM (Bookhagen and Burbank, 2010), as well as published regional geologic maps (Taylor and Yin, 2009; Haproff et al., 2019). Utilizing open-

source satellite data with a long-term historic archive allows anyone to easily implement our approach in other regions (e.g., Himalayan Arc) with limited accessibility, high landslide potential, and a long landslide history (Petley, 2012; Froude and Petley, 2018; Zhu et al., 2019; Kirschbaum et al., 2020).

Below are the details of our data sources and methods of calculation. First, topographic variables such as slope, aspect, local relief, curvature, distance to channel, and drainage area were calculated from a 90 m SRTM digital elevation model (DEM). Although a higher-resolution 30 m DEM is available, it contains missing values within our study area. Thus, we used a 90 m DEM for calculating topographic variables. Slope was calculated as the steepest descent gradient using an 8-direction (D8) flow routing method (Schwanghart and Scherler, 2014). We calculated aspect, the direction of slope face, as the angle in degrees clockwise from north given by the components of the 3-D surface normal. The surface normal was calculated using the x, y, and z components of each pixel. Local relief was calculated as the range in elevation within a 2.5 km radius circular window. We used a 2.5 km radius window because it is similar to the length scale of across-valley widths in the range front where most landslides are. Local relief at this scale allowed us to quantify the spatial variation of topographic relief relevant to landslides on these fluvial valleys. Curvature was calculated as the second derivative of the 90 m SRTM DEM. We calculated mean, planform, profile, and total curvatures using TopoToolbox 2 (Schmidt et al., 2003; Schwanghart and Scherler, 2014). To calculate distance from channel, we first determined flow direction using D8 flow routing. The flow direction was carved through topographic depressions and flat areas to avoid sinks and generate a continuous drainage system. We then imposed a minimum drainage area of 1 km^2 needed to initiate a stream before extracting a stream network based on the flow direction. Using the stream network, we calculated the distance of each pixel in the DEM to the nearest location in the stream network.

We acquired *MAP* and *NEE* from a previous study (Bookhagen and Burbank, 2010) that analyzed the Tropical Rainfall Measuring Mission (TRMM) 2B31 datasets from January 1998 to December 2009. Daily rainfall and *MAP* values were integrated from 90-min measurements over 12 years. To calculate

NEE, the 90th percentile of daily rainfall total for each pixel was determined for the 12-year measurement period (Bookhagen and Burbank, 2010). Only days with measured rainfall were included in calculating the probability density function. The number of days per year with a daily rainfall total above the 90th percentile was counted as NEE (Bookhagen, 2010; Bookhagen and Burbank, 2010). The resolution of the original *MAP* and *NEE* datasets in our study area is ~5 km, which we resampled to 30 m resolution to be consistent with the resolution of our landslide inventory. To calculate the drainage area, we first calculated D8 flow directions of stream networks and calculated the number of upstream cells that contribute to each pixel. The number of cells can then be converted into a drainage area. Discharge was calculated by summing upstream contributing cells weighted by their *MAP* to account for spatially varying precipitation patterns. Using these weights, cells with higher *MAP* values will contribute more to total discharge than cells with lower precipitation values.

Previous studies (Parker et al., 2011; Xu et al., 2014) have shown that distance to fault ruptures is a good predictor for the occurrence of earthquake-induced landslides. We do not have information on active fault planes at depth and ground peak acceleration patterns for past earthquakes in these regions. Thus, we calculated $Dist_{MFT}$ for our study regions as each pixel's Euclidean distance from the closest point on traces of the Main Frontal Thrust (MFT) and suture zones mapped by Taylor and Yin (2009). These faults represent potentially active faults in our study area (Haproff et al., 2019, 2020). Because the suture zone is located far to the north, $Dist_{MFT}$ largely reflects the distance to the MFT. In addition, we calculated $Dist_F$ as the Euclidean distance of each pixel from boundaries separating all lithologic units reported in (Haproff et al., 2019). We included $Dist_F$ because bedrock tends to be more damaged near major lithologic boundaries due to faulting, which may influence landslide occurrences. The Euclidean distance was calculated using ArcGIS 10.6.

2.6 Figures

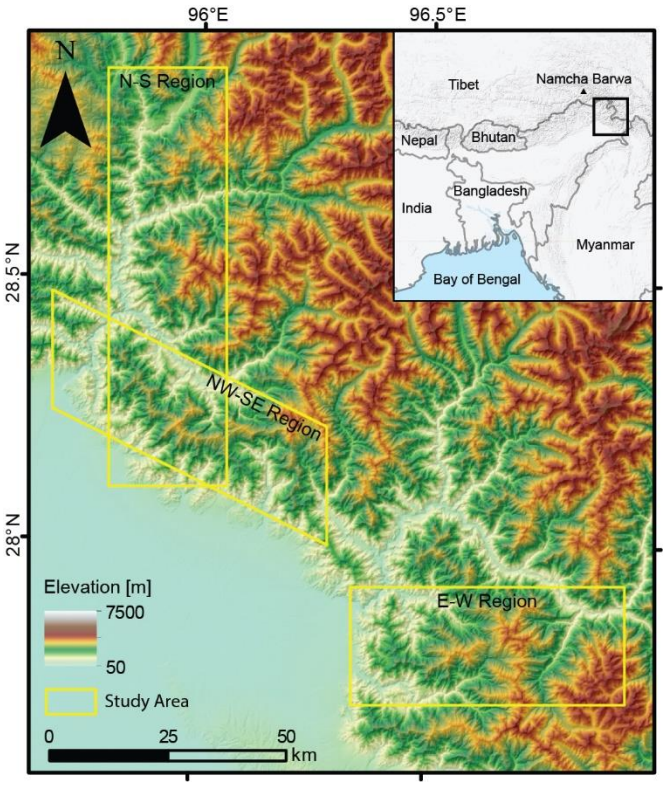

Fig. 2.1: Study area in the easternmost Himalaya. Colors represent the elevation, and yellow boxes indicate our N-S (Dibang), NW-SE (range front), and E-W (Lohit) oriented study regions. The inset map shows the eastern Himalayan region with our study area shown in a yellow box and national borders shown in dark gray lines.

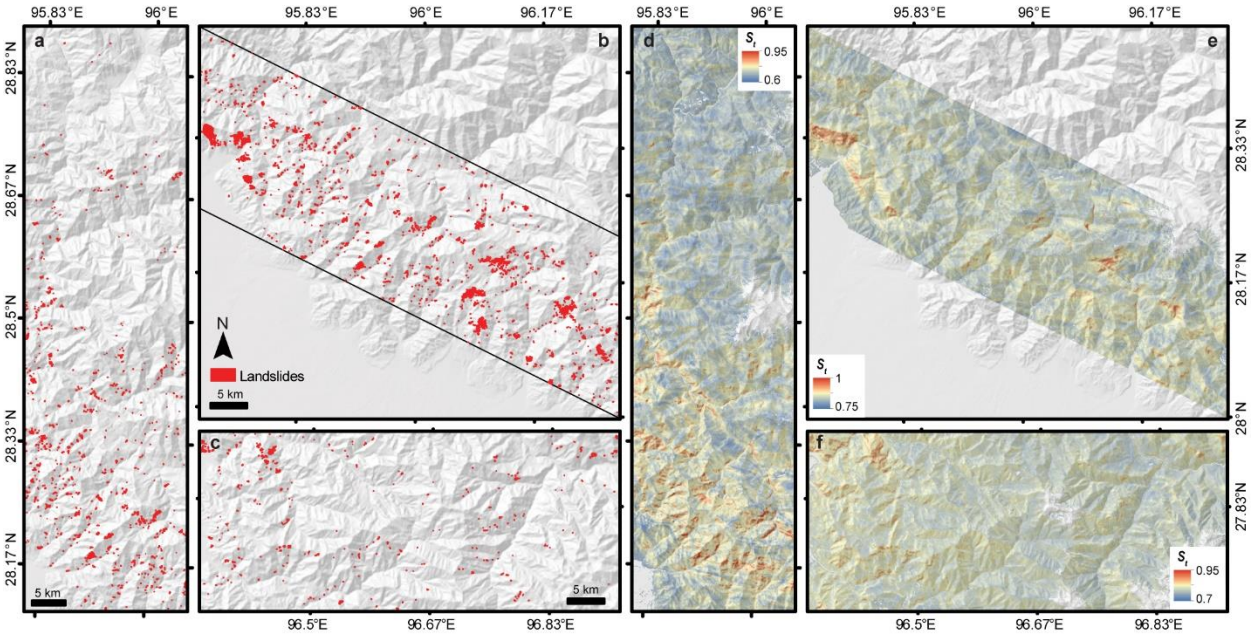

Fig. 2.2: Mapped landslides and modeled susceptibility. Spatial distribution of (a-c) mapped landslides and (d-f) modeled landslide susceptibility for the (a,d) N-S, (b,e) NW-SE, and (c,f) E-W study regions. (a) 959, (b) 1536, and (c) 386 landslides are shown in red polygons in (a-c). Total susceptibility at the pixel scale (S_t) from the Level-2 superposable neural network is shown in (d-f). The threshold S_t values that are used to classify landslide and non-landslide pixels in the model are (d) 0.767, (e) 0.861, and (f) 0.816, respectively.

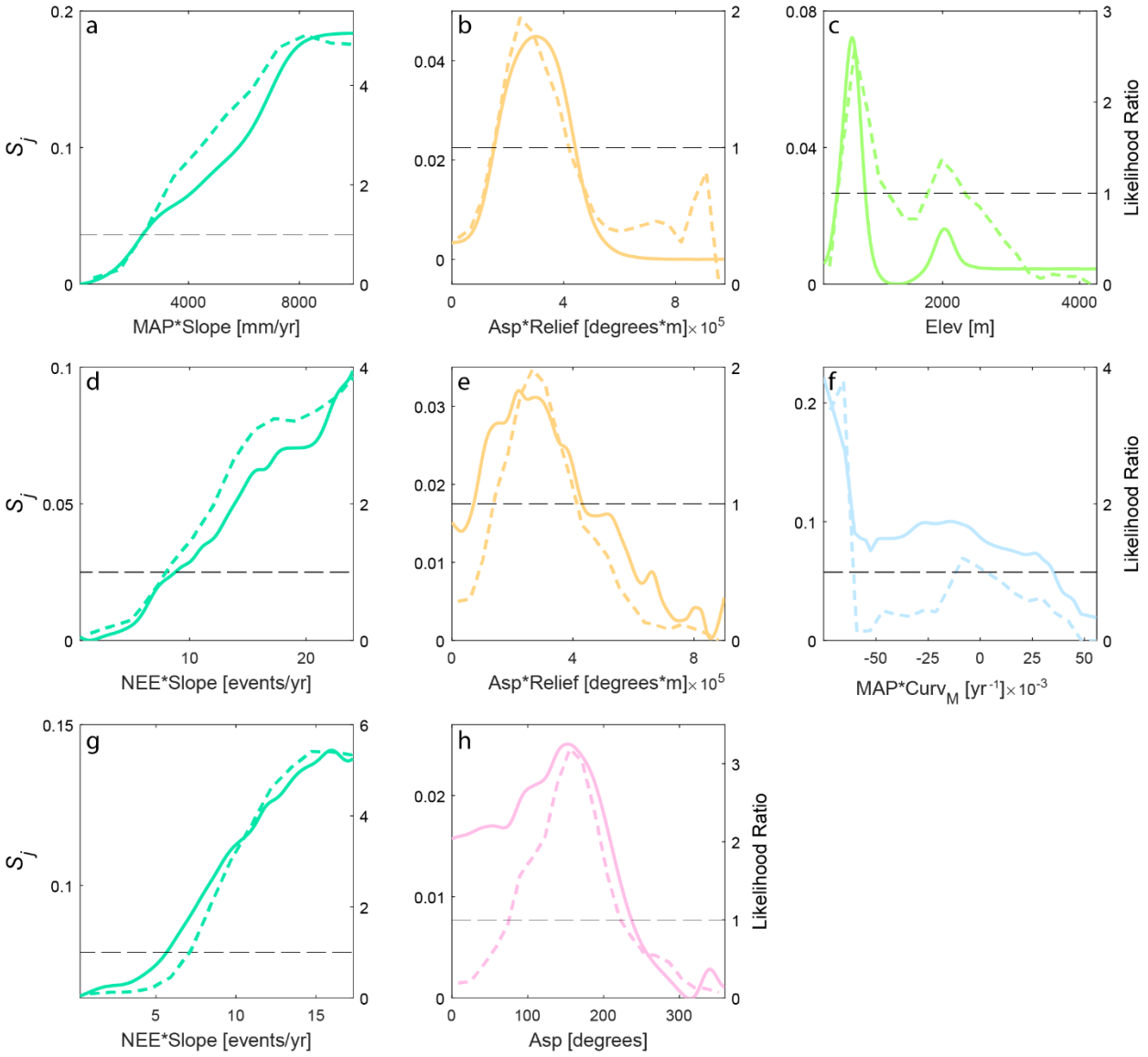

Fig. 2.3: Individual feature contributions to total susceptibility. Independent functions of *Sj* identified as primary landslide controls are shown for the (a-c) N-S, (d-f) NW-SE, and (g, h) E-W study regions. Likelihood ratios (LR), representing the likelihood of landslide occurrence for a specific range of feature values, are shown as short, dashed, colored lines with corresponding right-side y-axes for reference. LR = 1 and LR>1 represent the average and above-average likelihood of landslide occurrence, respectively. Note that S_j corresponding to LR=1, shown as long-dashed black lines, differ between features because the SNN quantifies the absolute contributions of S_j decoupled from other features. Features related to topography, aspect, climate, and geology are shown in green, pink, blue, and brown or combinations thereof, respectively. Mean annual precipitation (*MAP*), number of extreme rainfall events (*NEE*), aspect (*Asp*), elevation (*Elev*), mean curvature ($Curv_M$), and local relief (*Relief*). The asterisk * indicates the algebraic multiplication of two features.

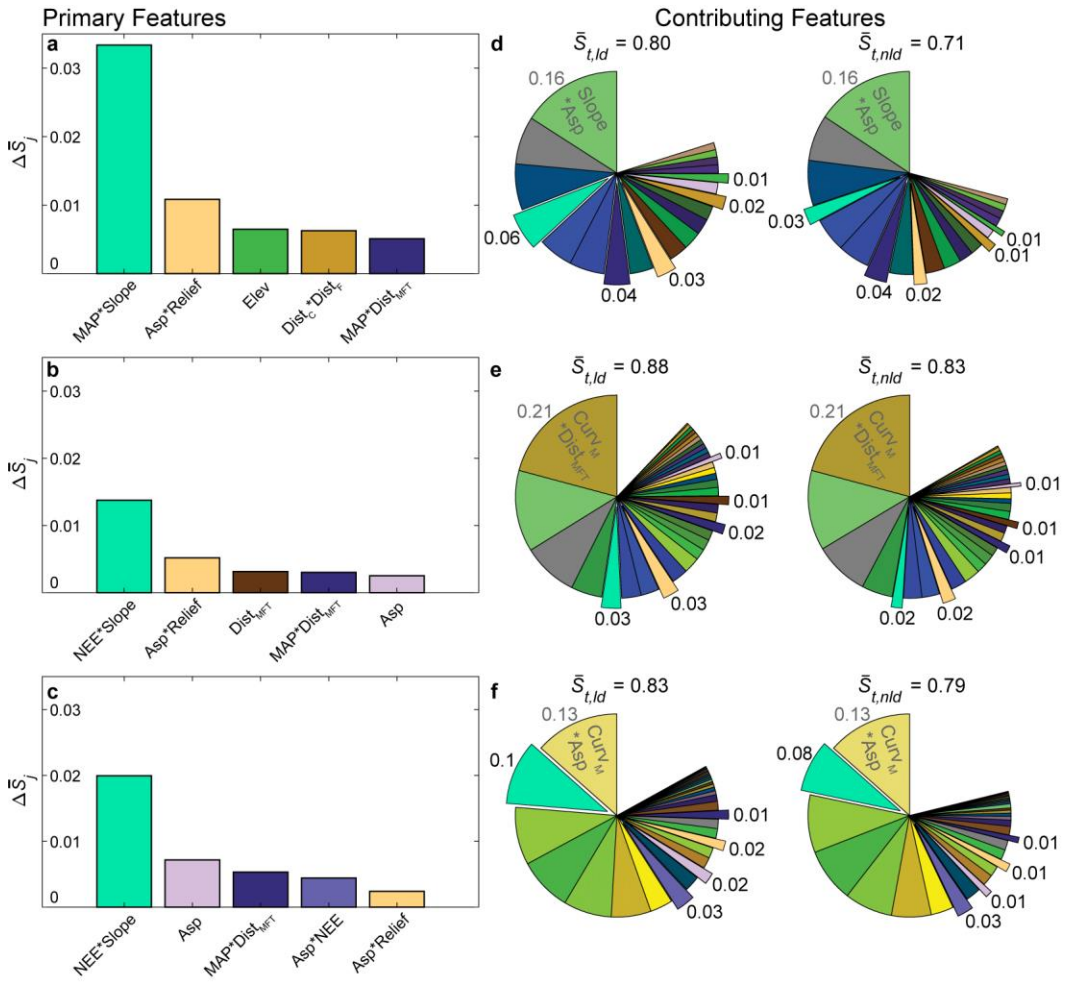

Fig. 2.4: Feature contributions to total susceptibility for the (a,d) N-S, (b,e) NW-SE, and (c,f) E-W study regions. Bar charts in (a-c) represent $\Delta\bar{S}_j$ in descending order, and pie charts in (d-f) represent average S_j ($\bar{S}_j$) contributions to landslide (*ld*) and non-landslide (*nld*) areas. $\Delta\bar{S}_j$ represents the difference in average contribution between areas of *ld* and *nld* in each region. Extruding pie chart features are features with large $\Delta\bar{S}_j$) found in the corresponding bar chart on the left. Features related to topography, aspect, climate, and geology are shown in green, pink, blue, and brown or combinations thereof, respectively. Mean annual precipitation (*MAP*), number of extreme rainfall events (*NEE*), aspect (*Asp*), elevation (*Elev*), mean curvature ($Curv_M$), distances to channel ($Dist_C$), all faults ($Dist_F$), and the Main Frontal Thrust and suture zone ($Dist_{MFT}$), and local relief (*Relief*). The asterisk * indicates the algebraic multiplication of two features. Information regarding features is provided in Methods.

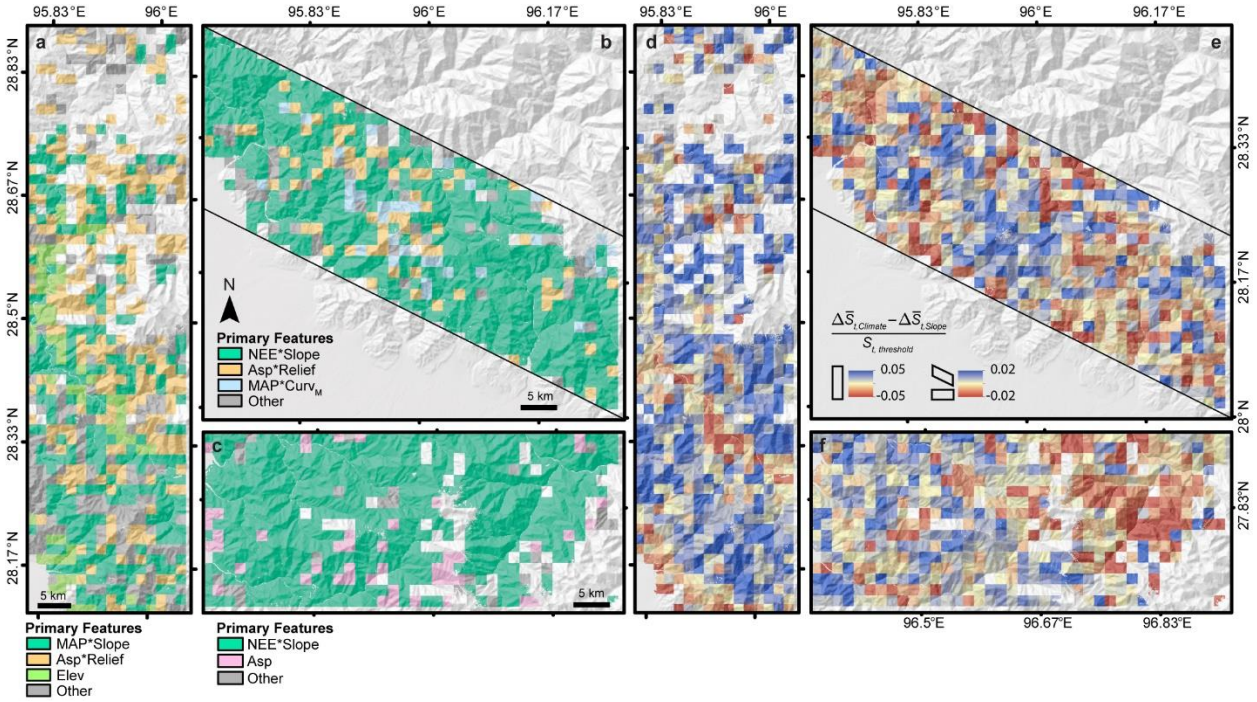

Fig. 2.5: Important controls for landslides. Spatial distribution of (a-c) primary features identified as locally important controls of landslides and (d-f) relative climate vs slope susceptibility contributions for the (a,d) N-S, (b,e) NW-SE, and (c,f) E-W study regions. The locally important control in (a-c) is identified as the feature with the largest difference in average contribution ($\Delta\bar{S}_j$) between areas of landslides (*ld*) and non-landslides (*nld*) within a 2.25 km^2 window. The contribution from climate features ($\Delta\bar{S}_{t,Climate}, j$ = *Asp*, *NEE*, *MAP*) relative to that of slope ($\Delta\bar{S}_{t,Slope}$) normalized by the corresponding threshold S_t is shown in (d-f). Windows with a higher climate contribution are colored blue while those with a greater slope contribution are colored red. Windows with no data contain a majority of unmapped areas or indicate a lack of modeled landslides. Features related to topography, aspect, climate, and geology are shown in green, pink, blue, and brown or combinations thereof, respectively. Mean annual precipitation (*MAP*), number of extreme rainfall events (*NEE*), aspect (*Asp*), elevation (*Elev*), mean curvature ($Curv_M$), and local relief (*Relief*). The asterisk * indicates the algebraic multiplication of two features.

2.7 References

Adadi, A., and Berrada, M., 2018, Peeking Inside the Black-Box: A Survey on Explainable Artificial Intelligence (XAI): IEEE Access, v. 6, p. 52138–52160, doi:10.1109/ACCESS.2018.2870052.

Agarwal, R., Melnick, L., Frosst, N., Zhang, X., Lengerich, B., Caruana, R., and Hinton, G.E., 2020, Neural Additive Models: Interpretable Machine Learning with Neural Nets: arXiv preprint.

Akgun, A., 2012, A comparison of landslide susceptibility maps produced by logistic regression, multi-criteria decision, and likelihood ratio methods: A case study at İzmir, Turkey: Landslides, v. 9, p. 93–106, doi:10.1007/s10346-011-0283-7.

Barros, A.P., Kim, G., Williams, E., and Nesbitt, S.W., 2004, Probing orographic controls in the Himalayas during the monsoon using satellite imagery: Natural Hazards and Earth System Sciences, v. 4, p. 29–51.

Baum, R.L., Godt, J.W., and Savage, W.Z., 2010, Estimating the timing and location of shallow rainfall-induced landslides using a model for transient, unsaturated infiltration: Journal of Geophysical Research: Earth Surface, v. 115, doi:10.1029/2009JF001321.

Baum, R.L., Savage, W.Z., and Godt, J.W., 2002, TRIGRS-A Fortran Program for Transient Rainfall Infiltration and Grid-Based Regional Slope-Stability Analysis.:

Bekaert, D.P.S., Handwerger, A.L., Agram, P., and Kirschbaum, D.B., 2020, InSAR-based detection method for mapping and monitoring slow-moving landslides in remote regions with steep and mountainous terrain: An application to Nepal: Remote Sensing of Environment, v. 249, doi:10.1016/j.rse.2020.111983.

Ben-Menahem, A., Aboodi, E., and Schild, R., 1974, The Source of the Great Assam Earthquake - An Interplate Wedge Motion: Physics of the Earth and Planetary Interiors, v. 9, p. 265–289.

Beven, K.J., and Kirkby, M.J., 1979, A physically based, variable contributing area model of basin hydrology: Hydrological Sciences Bulletin, v. 24, p. 43–69, doi:10.1080/02626667909491834.

Bookhagen, B., 2010, Appearance of extreme monsoonal rainfall events and their impact on erosion in the Himalaya: Geomatics, Natural Hazards and Risk, v. 1, p. 37–50, doi:10.1080/19475701003625737.

Bookhagen, B., and Burbank, D.W., 2010, Toward a complete Himalayan hydrological budget: Spatiotemporal distribution of snowmelt and rainfall and their impact on river discharge: Journal of Geophysical Research: Earth Surface, v. 115, doi:10.1029/2009JF001426.

Burgess, W.P., Yin, A., Dubey, C.S., Shen, Z.K., and Kelty, T.K., 2012, Holocene shortening across the main frontal thrust zone in the eastern Himalaya: Earth and Planetary Science Letters, v. 357–358, p. 152–167, doi:10.1016/j.epsl.2012.09.040.

Chowdhuri, I., Pal, S.C., Chakrabortty, R., Malik, S., Das, B., and Roy, P., 2021, Torrential rainfall-induced landslide susceptibility assessment using machine learning and statistical methods of eastern Himalaya: Natural Hazards, v. 107, p. 697–722, doi:10.1007/s11069-021-04601-3.

Conforti, M., Pascale, S., Robustelli, G., and Sdao, F., 2014, Evaluation of prediction capability of the artificial neural networks for mapping landslide susceptibility in the Turbolo River catchment (northern Calabria, Italy): Catena, v. 113, p. 236–250, doi:10.1016/j.catena.2013.08.006.

Coudurier-Curveur, A., Tapponnier, P., Okal, E., Van der Woerd, J., Kali, E., Choudhury, S., Baruah, S., Etchebes, M., and Karakaş, C., 2020, A composite rupture model for the great 1950 Assam earthquake across the cusp of the East Himalayan Syntaxis: Earth and Planetary Science Letters, v. 531, doi:10.1016/j.epsl.2019.115928.

Cui, Y., Cheng, D., Choi, C.E., Jin, W., Lei, Y., and Kargel, J.S., 2019, The cost of rapid and haphazard urbanization: lessons learned from the Freetown landslide disaster: Landslides, doi:10.1007/s10346-019-01167-x.

Van Dao, D. et al., 2020, A spatially explicit deep learning neural network model for the prediction of landslide susceptibility: Catena, v. 188, doi:10.1016/j.catena.2019.104451.

Devkota, K.C., Regmi, A.D., Pourghasemi, H.R., Yoshida, K., Pradhan, B., Ryu, I.C., Dhital, M.R., and Althuwaynee, O.F., 2013, Landslide susceptibility mapping using certainty factor, index of

entropy and logistic regression models in GIS and their comparison at Mugling-Narayanghat road section in Nepal Himalaya: Natural Hazards, v. 65, p. 135–165, doi:10.1007/s11069-012-0347-6.

Dietrich, W.E., Bellugi, D., and Real de Asua, R., 2001, Validation of the Shallow Landslide Model, SHALSTAB, for forest management, *in* Land use and watersheds: human influence on hydrology and geomorphology in urban and forest areas, v. 2, p. 195–227, doi:10.1029/ws002p0195.

Dietrich, W.E., Reiss, R., Hsu, M.-L., and Montgomery, D.R., 1995, A Process-Based Model For Colluvial Soil Depth and Shallow Landsliding Using Digital Elevation Data: Hydrological Processes, v. 9, p. 383–400.

Dikshit, A., Pradhan, B., and Alamri, A.M., 2021, Pathways and challenges of the application of artificial intelligence to geohazards modelling: Gondwana Research, v. 100, p. 290–301, doi:10.1016/j.gr.2020.08.007.

Fan, X. et al., 2019, Earthquake-Induced Chains of Geologic Hazards: Patterns, Mechanisms, and Impacts: Reviews of Geophysics, v. 57, p. 421–503, doi:10.1029/2018RG000626.

Finnegan, N.J., Perkins, J.P., Nereson, A.L., and Handwerger, A.L., 2021, Unsaturated Flow Processes and the Onset of Seasonal Deformation in Slow-Moving Landslides: Journal of Geophysical Research: Earth Surface, v. 126, doi:10.1029/2020JF005758.

Friedman, J.H., 2001, Greedy Function Approximation: A Gradient Boosting Machine: The Annals of Statistics, v. 29, p. 1189–1232.

Froude, M.J., and Petley, D.N., 2018, Global fatal landslide occurrence from 2004 to 2016: Natural Hazards and Earth System Sciences, v. 18, p. 2161–2181, doi:10.5194/nhess-18-2161-2018.

Ghorbanzadeh, O., Blaschke, T., Gholamnia, K., Meena, S.R., Tiede, D., and Aryal, J., 2019, Evaluation of different machine learning methods and deep-learning convolutional neural networks for landslide detection: Remote Sensing, v. 11, doi:10.3390/rs11020196.

Gómez, H., and Kavzoglu, T., 2005, Assessment of shallow landslide susceptibility using artificial neural networks in Jabonosa River Basin, Venezuela: Engineering Geology, v. 78, p. 11–27, doi:10.1016/j.enggeo.2004.10.004.

Gunning, D., Stefik, M., Choi, J., Miller, T., Stumpf, S., and Yang, G.Z., 2019, XAI-Explainable artificial intelligence: Science Robotics, v. 4, doi:10.1126/scirobotics.aay7120.

Guzzetti, F., Carrara, A., Cardinali, M., and Reichenbach, P., 1999, Landslide hazard evaluation: a review of current techniques and their application in a multi-scale study, Central Italy: Geomorphology, v. 31, p. 181–216.

Haproff, P.J., Odlum, M.L., Zuza, A. V., Yin, A., and Stockli, D.F., 2020, Structural and Thermochronologic Constraints on the Cenozoic Tectonic Development of the Northern Indo-Burma Ranges: Tectonics, v. 39, doi:10.1029/2020TC006231.

Haproff, P.J., Zuza, A. V., Yin, A., Harrison, T.M., Manning, C.E., Dubey, C.S., Ding, L., Wu, C., and Chen, J., 2019, Geologic framework of the northern Indo-Burma Ranges and lateral correlation of Himalayan-Tibetan lithologic units across the eastern Himalayan syntaxis: Geosphere, v. 15, p. 856–881, doi:10.1130/GES02054.1.

Hastie, T.J.*, 2017, Generalized Additive Models: Statistical models in S, p. 249–307.

Hinton, G., Vinyals, O., and Dean, J., 2015, Distilling the Knowledge in a Neural Network: arXiv preprint, http://arxiv.org/abs/1503.02531.

Huang, R., and Fan, X., 2013, The landslide story: Nature Geoscience, v. 6, p. 325–326, doi:10.1038/ngeo1806.

Huang, A.Y.L., and Montgomery, D.R., 2014, Topographic locations and size of earthquake- and typhoon-generated landslides, Tachia River, Taiwan: Earth Surface Processes and Landforms, v. 39, p. 414–418, doi:10.1002/esp.3510.

Iverson, R.M., 2000, Landslide triggering by rain infiltration: Water Resources Research, v. 36, p. 1897–1910, doi:10.1029/2000WR900090.

Jones, J.N., Boulton, S.J., Bennett, G.L., Stokes, M., and Whitworth, M.R.Z., 2021a, Temporal Variations in Landslide Distributions Following Extreme Events: Implications for Landslide Susceptibility Modeling: Journal of Geophysical Research: Earth Surface, v. 126, doi:10.1029/2021JF006067.

Jones, J.N., Boulton, S.J., Stokes, M., Bennett, G.L., and Whitworth, M.R.Z., 2021b, 30-year record of Himalaya mass-wasting reveals landscape perturbations by extreme events: Nature Communications, v. 12, doi:10.1038/s41467-021-26964-8.

Kent, W.N., and Dasgupta, U., 2004, Structural evolution in response to fold and thrust belt tectonics in northern Assam. A key to hydrocarbon exploration in the Jaipur anticline area: Marine and Petroleum Geology, v. 21, p. 785–803, doi:10.1016/j.marpetgeo.2003.12.006.

Kirschbaum, D., Kapnick, S.B., Stanley, T., and Pascale, S., 2020, Changes in Extreme Precipitation and Landslides Over High Mountain Asia: Geophysical Research Letters, v. 47, doi:10.1029/2019GL085347.

Larsen, I.J., and Montgomery, D.R., 2012, Landslide erosion coupled to tectonics and river incision: Nature Geoscience, v. 5, p. 468–473, doi:10.1038/ngeo1479.

Larsen, I.J., Montgomery, D.R., and Korup, O., 2010, Landslide erosion controlled by hillslope material: Nature Geoscience, v. 3, p. 247–251, doi:10.1038/ngeo776.

Lee, S., 2005, Application of logistic regression model and its validation for landslide susceptibility mapping using GIS and remote sensing data: International Journal of Remote Sensing, v. 26, p. 1477–1491, doi:10.1080/01431160412331331012.

Lee, S., Ryu, J.H., Won, J.S., and Park, H.J., 2004, Determination and application of the weights for landslide susceptibility mapping using an artificial neural network: Engineering Geology, v. 71, p. 289–302, doi:10.1016/S0013-7952(03)00142-X.

Lee, S., and Sambath, T., 2006, Landslide susceptibility mapping in the Damrei Romel area, Cambodia using frequency ratio and logistic regression models: Environmental Geology, v. 50, p. 847–855, doi:10.1007/s00254-006-0256-7.

Leiva, R.G., Anta, A.F., Mancuso, V., and Casari, P., 2019, A novel hyperparameter-free approach to decision tree construction that avoids overfitting by design: IEEE Access, v. 7, p. 99978–99987, doi:10.1109/ACCESS.2019.2930235.

Leonarduzzi, E., Maxwell, R.M., Mirus, B.B., and Molnar, P., 2021, Numerical Analysis of the Effect of Subgrid Variability in a Physically Based Hydrological Model on Runoff, Soil Moisture, and Slope Stability: Water Resources Research, v. 57, doi:10.1029/2020WR027326.

Li, X.-H. et al., 2020, A Survey of Data-driven and Knowledge-aware eXplainable AI: IEEE Transactions on Knowledge and Data Engineering, p. 1–1, doi:10.1109/tkde.2020.2983930.

Lundberg, S.M., Allen, P.G., and Lee, S.-I., 2017, A Unified Approach to Interpreting Model Predictions: Advances in neural information processing systems, https://github.com/slundberg/shap.

Mandal, S., and Mandal, K., 2018, Modeling and mapping landslide susceptibility zones using GIS based multivariate binary logistic regression (LR) model in the Rorachu river basin of eastern Sikkim Himalaya, India: Modeling Earth Systems and Environment, v. 4, p. 69–88, doi:10.1007/s40808-018-0426-0.

Marc, O., and Hovius, N., 2015, Amalgamation in landslide maps: Effects and automatic detection: Natural Hazards and Earth System Sciences, v. 15, p. 723–733, doi:10.5194/nhess-15-723-2015.

Meunier, P., Hovius, N., and Haines, J.A., 2008, Topographic site effects and the location of earthquake induced landslides: Earth and Planetary Science Letters, v. 275, p. 221–232, doi:10.1016/j.epsl.2008.07.020.

Montgomery, D.R., and Dietrich, W.E., 1994, A physically based model for the topographic control on shallow landsliding: Water Resources Research, v. 30.

Montgomery, D.R., Sullivan, K., and Greenberg, H.M., 1998, Regional test of a model for shallow landsliding: Hydrological Processes, v. 12, p. 943–955.

Moon, S., Page Chamberlain, C., Blisniuk, K., Levine, N., Rood, D.H., and Hilley, G.E., 2011, Climatic control of denudation in the deglaciated landscape of the Washington Cascades: Nature Geoscience, v. 4, p. 469–473, doi:10.1038/ngeo1159.

Orland, E., Roering, J.J., Thomas, M.A., and Mirus, B.B., 2020, Deep Learning as a Tool to Forecast Hydrologic Response for Landslide-Prone Hillslopes: Geophysical Research Letters, v. 47, doi:10.1029/2020GL088731.

Parker, R.N., Densmore, A.L., Rosser, N.J., De Michele, M., Li, Y., Huang, R., Whadcoat, S., and Petley, D.N., 2011, Mass wasting triggered by the 2008 Wenchuan earthquake is greater than orogenic growth: Nature Geoscience, v. 4, p. 449–452, doi:10.1038/ngeo1154.

Petley, D., 2012, Global patterns of loss of life from landslides: Geology, v. 40, p. 927–930, doi:10.1130/G33217.1.

Phong, T. Van, Phan, T.T., Prakash, I., Singh, S.K., Shirzadi, A., Chapi, K., Ly, H.B., Ho, L.S., Quoc, N.K., and Pham, B.T., 2019, Landslide susceptibility modeling using different artificial intelligence methods: a case study at Muong Lay district, Vietnam: Geocarto International, v. 36, p. 1685–1708, doi:10.1080/10106049.2019.1665715.

Pradhan, B., 2013, A comparative study on the predictive ability of the decision tree, support vector machine and neuro-fuzzy models in landslide susceptibility mapping using GIS: Computers and Geosciences, v. 51, p. 350–365, doi:10.1016/j.cageo.2012.08.023.

Prakash, N., Manconi, A., and Loew, S., 2020, Mapping landslides on EO data: Performance of deep learning models vs. Traditional machine learning models: Remote Sensing, v. 12, doi:10.3390/rs12030346.

Radbruch-Hall, D.H., Colton, R.B., Davies, W.E., Lucchitta, I., Skipp, B.A., and Varnes, D.J., 1982, Landslide Overview Map of the Conterminous United States:, https://books.google.com/books?hl=en&lr=&id=MVdq1sXZFyQC&oi=fnd&pg=PA25&ots=F6bnQDr_0n&sig=xa2iSr_rbNkKgSdmfLJfqSupmwY#v=onepage&q&f=false (accessed January 2022).

Regmi, A.D., Devkota, K.C., Yoshida, K., Pradhan, B., Pourghasemi, H.R., Kumamoto, T., and Akgun, A., 2014, Application of frequency ratio, statistical index, and weights-of-evidence models and

their comparison in landslide susceptibility mapping in Central Nepal Himalaya: Arabian Journal of Geosciences, v. 7, p. 725–742, doi:10.1007/s12517-012-0807-z.

Reichenbach, P., Rossi, M., Malamud, B.D., Mihir, M., and Guzzetti, F., 2018, A review of statistically-based landslide susceptibility models: Earth-Science Reviews, v. 180, p. 60–91, doi:10.1016/j.earscirev.2018.03.001.

Rudin, C., 2019, Stop Explaining Black Box Machine Learning Models for High Stakes Decisions and Use Interpretable Models Instead: Nature machine intelligence, v. 1, p. 206–215, http://arxiv.org/abs/1811.10154.

Salvi, D., Mathew, G., Kohn, B., Pande, K., and Borgohain, B., 2020, Thermochronological insights into the thermotectonic evolution of Mishmi hills across the Dibang Valley, NE Himalayan Syntaxis: Journal of Asian Earth Sciences, v. 190, doi:10.1016/j.jseaes.2019.104158.

Schmidt, J., Evans, I.S., and Brinkmann, J., 2003, Comparison of polynomial models for land surface curvature calculation: International Journal of Geographical Information Science, v. 17, p. 797–814, doi:10.1080/13658810310001596058.

Schwanghart, W., and Scherler, D., 2014, Short Communication: TopoToolbox 2 - MATLAB-based software for topographic analysis and modeling in Earth surface sciences: Earth Surface Dynamics, v. 2, p. 1–7, doi:10.5194/esurf-2-1-2014.

Singh, S., Raju, A., and Banerjee, S., 2022, Detecting slow-moving landslides in parts of Darjeeling–Sikkim Himalaya, NE India: quantitative constraints from PSInSAR and its relation to the structural discontinuities: Landslides, v. 19, p. 2347–2365, doi:10.1007/s10346-022-01900-z.

Stanley, T., and Kirschbaum, D.B., 2017, A heuristic approach to global landslide susceptibility mapping: Natural Hazards, v. 87, p. 145–164, doi:10.1007/s11069-017-2757-y.

Stanley, T.A., Kirschbaum, D.B., Sobieszczyk, S., Jasinski, M.F., Borak, J.S., and Slaughter, S.L., 2020, Building a landslide hazard indicator with machine learning and land surface models: Environmental Modelling and Software, v. 129, doi:10.1016/j.envsoft.2020.104692.

Tan, S., Caruana, R., Hooker, G., and Lou, Y., 2018, Distill-and-Compare: Auditing Black-Box Models Using Transparent Model Distillation, *in* AIES 2018 - Proceedings of the 2018 AAAI/ACM Conference on AI, Ethics, and Society, Association for Computing Machinery, Inc, p. 303–310, doi:10.1145/3278721.3278725.

Taylor, M., and Yin, A., 2009, Active structures of the Himalayan-Tibetan orogen and their relationships to earthquake distribution, contemporary strain field, and Cenozoic volcanism: Geosphere, v. 5, p. 199–214, doi:10.1130/GES00217.1.

Tien Bui, D. et al., 2019, Shallow Landslide Prediction Using a Novel Hybrid Functional Machine Learning Algorithm: Remote Sensing, v. 11, p. 931, doi:10.3390/rs11080931.

Tien Bui, D., Pradhan, B., Lofman, O., Revhaug, I., and Dick, O.B., 2012, Landslide susceptibility assessment in the Hoa Binh province of Vietnam: A comparison of the Levenberg-Marquardt and Bayesian regularized neural networks: Geomorphology, v. 171–172, p. 12–29, doi:10.1016/j.geomorph.2012.04.023.

Tien Bui, D., Tsangaratos, P., Nguyen, V.T., Liem, N. Van, and Trinh, P.T., 2020, Comparing the prediction performance of a Deep Learning Neural Network model with conventional machine learning models in landslide susceptibility assessment: Catena, v. 188, doi:10.1016/j.catena.2019.104426.

Xu, C., Xu, X., Yao, X., and Dai, F., 2014, Three (nearly) complete inventories of landslides triggered by the May 12, 2008 Wenchuan Mw 7.9 earthquake of China and their spatial distribution statistical analysis: Landslides, v. 11, p. 441–461, doi:10.1007/s10346-013-0404-6.

Yang, Y., Zhao, T., Ni, G., and Sun, T., 2018, Atmospheric rivers over the Bay of Bengal lead to northern Indian extreme rainfall: International Journal of Climatology, v. 38, p. 1010–1021, doi:10.1002/joc.5229.

Yatagai, A., Kamiguchi, K., Arakawa, O., Hamada, A., Yasutomi, N., and Kitoh, A., 2012, Aphrodite constructing a long-term daily gridded precipitation dataset for Asia based on a dense network of

rain gauges: Bulletin of the American Meteorological Society, v. 93, p. 1401–1415, doi:10.1175/BAMS-D-11-00122.1.

Youssef, K., Bouchard, L., Haigh, K., Silovsky, J., Thapa, B., and Valk, C. Vander, 2018, Machine learning approach to RF transmitter identification: IEEE Journal of Radio Frequency Identification, v. 2, p. 197–205, doi:10.1109/JRFID.2018.2880457.

Youssef, K., Jarenwattananon, N.N., and Bouchard, L.S., 2015, Feature-Preserving Noise Removal: IEEE Transactions on Medical Imaging, v. 34, p. 1822–1829, doi:10.1109/TMI.2015.2409265.

Youssef, K., Shao, K., Moon, S., and Bouchard, L.S., 2023, Landslide susceptibility modeling by interpretable neural network: Communications Earth and Environment, v. 4, doi:10.1038/s43247-023-00806-5.

Zhu, Z. et al., 2019, Benefits of the free and open Landsat data policy: Remote Sensing of Environment, v. 224, p. 382–385, doi:10.1016/j.rse.2019.02.016.

Chapter 3:

Climate-driven erosional efficiency varies with lithology across the Himalaya

Note: This chapter is modified from Shao, K., Moon, S., Li, G.K., Haproff, P.J., Yin, A., Corbett, L.B., Bierman, P.R., Argueta, M.O., Hidy, A.J. (2023). Climate-driven erosion varies with lithology across the Himalaya. *In review at Nature Communications*.

3.1 Introduction

Theoretical and numerical studies have shown that climate-driven erosion can significantly impact the dynamics of orogenic development (Dahlen et al., 1984; Molnar and England, 1990; Beaumont et al., 2001; Hilley and Strecker, 2004; Whipple, 2009; Graveleau et al., 2012). However, observing a climatic control on long-time erosion rate or erosional efficiency (i.e., the rate of erosion for a given topography) through field studies has been difficult. For example, basin-averaged erosion rates from in-situ cosmogenic ^{10}Be measured in river sand (hereafter, ^{10}Be-derived erosion rates) generally correlated with fluvial relief, hillslope gradient, or channel steepness, which reflect the underlying tectonic uplift rates in quasi-steady-state landscapes (Scherler et al., 2014; Godard et al., 2014; Le Roux-Mallouf et al., 2015; Olen et al., 2015; Adams et al., 2016). In this case, ^{10}Be-derived erosion rates often showed limited or weaker correlations with climatic controls compared to topographic controls (e.g., von Blanckenburg (2005); Portenga and Bierman (2011)). Recent studies have shown that the controls of climate and lithology affect the functional relationships between ^{10}Be-derived erosion rates and topographic metrics, which implies their influence on erosional efficiency (Kirby and Whipple, 2012; Hilley et al., 2019; Adams et al., 2020; Leonard et al., 2023; Marder and Gallen, 2023).

An ideal site to examine climatic and lithologic influences on erosion rate and efficiency is the Himalayan orogen, which has well-defined and well-understood patterns of tectonic deformation,

topography, precipitation, and rock distribution (Burbank et al., 1996, 2003; Vance et al., 2003; Yin, 2006; Grujic et al., 2006). Mean annual precipitation and the number of extreme rainfall events in the orogen generally increase eastward due to moisture originating from the Bay of Bengal during the summer (Fig. 3.1; Fig. B1) (Bookhagen and Burbank, 2010; Mukherjee et al., 2015; Varikoden and Revadekar, 2020; Jamshadali et al., 2021). Finally, Holocene shortening rates of the Himalayan orogen increase eastward (Lavé and Avouac, 2000; Kumar et al., 2006; Burgess et al., 2012; Stevens and Avouac, 2015). Specifically, orogen-scale thrusts divide the orogen into laterally continuous belts of sedimentary, metasedimentary, and crystalline rocks (Yin, 2006).

However, there are ongoing debates about the extent of climatic and lithologic controls on erosion rate and efficiency across the Himalaya. Although several studies have shown strong topographic controls on ^{10}Be-derived erosion rates, few studies demonstrated clear influences from climate or lithology. Field and laboratory studies showed that different lithologic units from the Nepal Himalaya may have different bedrock erodibility and abrasion rates (Attal and Lavé, 2006; Godard et al., 2006). A compilation study by Adams et al. (2020) analyzed the controls of topography, climate, and lithology on ^{10}Be-derived erosion rates and erosional efficiencies from the Himalaya. They showed an improved fit between ^{10}Be-derived erosion rates with topographic metric, k_{sn}-q, which combines channel steepness, k_{sn}, and mean annual precipitation, suggesting a substantial influence of climate on erosional efficiency. However, no clear differences between lithologic units were observed. These inconclusive findings may imply that complex interplay among tectonic, lithology, and climate can influence surface erosion and landscape evolution in the Himalaya.

Here, we hypothesize that the degree to which climate influences erosional efficiency may differ depending on lithology across the Himalaya. To test this, we analyzed nearly 200 ^{10}Be-derived erosion rates from the orogen, including 12 newly measured rates from along the Dibang and Lohit valleys with high precipitation rates and variabilities. We separated the datasets into two different lithologies, sedimentary/metasedimentary and crystalline rocks, separated by an orogen-scale thrust. We find a strong, positive correlation between erosion rates and efficiency and the number of extreme rainfall

events for basins dominated by sedimentary/metasedimentary rocks. Further analyses indicate that mechanically weak rocks and extreme precipitation enhance the efficiency of fluvial and landslide erosion. Our work highlights potential considerable variations in erosional efficiency as a result of extreme precipitation and weak lithology in the large-scale tectonic evolution of the Himalayan range.

3.2 Millennial erosion rate compilation and measurements

We compiled and analyzed existing ^{10}Be-derived erosion rates from 20, 32, 14, and 95 basins from the Garhwal, central Nepal, eastern Nepal, and Bhutan Himalaya, respectively (Godard et al., 2012, 2014; Scherler et al., 2014; Portenga et al., 2015; Le Roux-Mallouf et al., 2015; Olen et al., 2015; Adams et al., 2016, 2020) (Fig. 3.1a, Table B1; Appendix B). We incorporated a previous compilation by Adams et al. (2020), which considered basins with spatially uniform erosion rates (e.g., lack of obvious disequilibrium features), with drainage areas > 9 km^2, and without considerable impacts from glaciers. Additionally, we apply a drainage area limit of ~650 km^2, which is consistent with drainage areas of compiled basins from Adams et al. (2020). Erosion rates of basins with large areas may span regions of varying topographic, climatic, and geologic controls.

In addition, we measured ^{10}Be-derived erosion rates from 12 basins in the far eastern Indian state of Arunachal Pradesh on the northern Indo-Burma Ranges (hereafter, easternmost Himalaya) (Fig. 3.1b). Our newly sampled basins lie along the Dibang and Lohit rivers, the two main river networks in the region. As a result of the Indian Summer Monsoon originating from the Bay of Bengal, this site has higher mean annual precipitation rates and number of extreme rainfall events than those of other Himalayan regions (Fig. B1). Topography in this region is characterized by elevation and slope that increase near the range front and are consistently high into the hinterland (Fig. B2). The rapid increase in elevation is associated with a high peak in orographic precipitation at the range front (~13 extreme rainfall events/yr, ~7 m/yr) with a rapid decrease into the hinterland (~5 extreme rainfall events/yr, ~1 m/yr) (Bookhagen and Burbank, 2010). High magnitudes of extreme rainfall in the eastern Himalaya are observed not only in the TRMM dataset but also in the APHRODITE dataset based on rainfall gauge

measurements spanning 65 years (Andermann et al., 2011; Yatagai et al., 2012; Jamshadali et al., 2021). A previous study by Lupker et al. (2017) reported very high ^{10}Be-derived erosion rates for the entire Dibang and Lohit river catchments (2.0-3.4 mm/yr), but spatial distributions of erosion rate and efficiency throughout these catchments remain unconstrained.

We collected detrital sand samples from the active channel outlets of 12 basins (drainage areas of 23-527 km^2) in 2018. We sieved, magnetically separated, and etched samples to isolate and purify quartz at the cosmogenic preparatory laboratory at the University of California, Los Angeles. We isolated ^{10}Be at the National Science Foundation/University of Vermont Community Cosmogenic Facility (Corbett et al., 2016). We then measured ^{10}Be/^{9}Be ratios by Accelerator Mass Spectrometry at Lawrence Livermore National Laboratory (Nishiizumi et al., 2007) and determined millennial erosion rates (Balco et al., 2008) (Table B2).

3.3 Quantification of environmental controls

We quantified lithologic, topographic, geologic, and climatic controls for all examined basins (Table B1; Appendix B). We quantified lithologic controls as the areal fraction of a basin residing in a mapped lithologic unit and grouped basins based on whether >50% of the basin area lies south or north of the Main Central Thrust (MCT) (Fig. B3) or locally known as the Demwe thrust (Fig. B3a); the thrust generally juxtaposes sedimentary and metasedimentary units (hereafter, metasedimentary lithology) to the south and crystalline rocks to the north. Details regarding the delineation of the MFT and MCT fault traces are provided in Appendix B. We calculated the distance of each basin from these major faults (hereafter, $Dist_{MFT}$ and $Dist_{MCT}$). Topographic metrics including elevation, slope, local relief (2.5 and 5 km radii), channel steepness (k_{sn}), and discharge-based channel steepness (k_{sn}-q) were calculated using TopoToolbox v2 (Perron and Royden, 2013; Schwanghart and Scherler, 2014; Adams et al., 2020). We used a 90 m-resolution void-filled Shuttle Radar Topography Mission (SRTM) digital elevation model (DEM) for all study areas (Farr et al., 2007; de Ferranti, 2021). Climate metrics including mean annual precipitation (MAP) and the number of extreme rainfall events (NEE) were obtained from Bookhagen and

Burbank (2010) who analyzed NASA's ~5 km-resolution Tropical Rainfall Measuring Mission (TRMM) 2B31 dataset that spans 12 years from 1998-2009 with a 90-min interval. NEE was defined as the number of days with measured daily rainfall above the 90th percentile of rainy days over the 12-year period for each pixel.

3.4 Quantifying erosional efficiency from fluvial and landslide processes

Considering that our basins are from fluvially dominated landscapes, we apply the stream-power river incision model to connect erosion rates to topographic metrics and quantify erosional efficiency. Following Adams et al. (2020), we build the stream-power models as:

$$E = KA^m S^n = K{k_{sn}}^n \qquad Eq.\ 1$$

$$E = K_{lp} Q^m S^n = K_{lp}(k_{sn} - q)^n \qquad Eq.\ 2$$

where E is the erosion rate (mm/yr), A is the drainage area (m^2), Q is the stream discharge (m^3/yr), S is the channel slope, K and K_{lp} are the erosional efficiency coefficients calculated using channel steepness k_{sn} and discharge-based channel steepness k_{sn}-q, respectively, and m and n are dimensionless constants, which can be related to concavity θ (i.e., θ = m/n). k_{sn} is calculated based on topography alone, while k_{sn}-q incorporates climatic information, in terms of discharge based on mean annual precipitation. In theory, both K and K_{lp} will be independent of the influence of topography but reflect climatic and lithologic influences such as rock erodibility, channel geometry, incision process, and sediment flux. Furthermore, K_{lp} will be independent of the influence of mean annual precipitation in terms of discharge.

We examine landslide erosional processes by quantifying landslide abundances over a 20-year interval. Among our study areas, we focus our analysis on the easternmost Himalaya and central and eastern Nepal where abundant landslides are observed and mapped for similar time periods. For the easternmost Himalaya, we generated two landslide inventory maps over consecutive ~10-year intervals using 30-m resolution Landsat 5 and 8 images from December 1997, December 2006, and November 2017. For central and eastern Nepal, we utilized the existing datasets of monsoon-induced landslides

between 1989 and 2009 reported by Jones et al. (2021). Landslides from 1989-1999 and 2004-2009 were mapped using Landsat 4 and 5 imageries, respectively, while landslides from 2000-2003 were mapped using Landsat 7 imagery. Only basins with average slopes >0.5 were considered because landslides are likely the dominant hillslope transport processes in these areas (12 basins from the easternmost and 13 basins from the Nepal Himalaya).

Then, we calculate landslide density, landslide volumes, basin-averaged erosion rates from landslide-derived sediment fluxes (hereafter, landslide-derived erosion rate), and basin-averaged slope failure rate from landslides each year (hereafter, average failure rate) (Table B3) (Montgomery and Dietrich, 1994; Larsen et al., 2010; Moon et al., 2015). Landslide density is calculated as the cumulative landslide-affected area over 20 years normalized by basin area. Average failure rate is calculated as landslide density divided by the mapping time interval to obtain the likelihood of an area in a basin to experience a landslide each year. Details on landslide mapping and analysis are provided in Appendix B.

3.5 Millennial erosion rate and efficiency from the Himalaya

Across the Himalaya, ^{10}Be-derived erosion rates vary from 0.022 to 7.5 mm/yr for basins dominated by metasedimentary rocks (n = 61) and from 0.035 to 3.5 mm/yr for basins dominated by crystalline rocks (n = 112). When we examine ^{10}Be-derived erosion rates with respect to the distance from major fault structures (MFT/MCT), we observe large variations in magnitude for basins located at similar distances from these major faults. These variations likely reflect different local tectonic, climatic, and geologic settings along the Himalayan range. Examining the median and interquartile range of ^{10}Be-derived erosion rates for a given interval of $Dist_{MFT}$ or $Dist_{MCT}$ can provide insight into overall patterns. ^{10}Be-derived erosion rates tend to be higher close to major faults. Those of basins dominated by metasedimentary lithology are high near the MFT in the range front, become low, and elevated again in the hinterland near the MCT (Fig. 3.4a). Those of basins dominated by crystalline lithology appear to exhibit a general decrease with increasing distance from the MCT but show large variations in value (Fig. 3.4b). Basins from different lithologies span comparable ranges of erosion rates, k_{sn}, k_{sn}-q, local relief,

slope, NEE, and MAP (Fig. 3.2; Fig. B4; Table B4). Climate-influenced metrics (e.g., MAP, NEE, k_{sn}-q) and topographic metrics (e.g., k_{sn}, local relief, slope) do not appear to exhibit strong intercorrelations (e.g., variance inflation factor < 3) regardless of dominant lithology (more details on metric ranges, separability, and intercorrelations in Appendix B) (Fig. 3.2; Fig. B5; Table B4).

Depending on dominant lithology, ^{10}Be-derived erosion rates show statistically different relationships with topographic and climatic metrics. For basins dominated by metasedimentary lithology, ^{10}Be-derived erosion rates exhibit better correlations with metrics that incorporate the influence of climate (NEE, MAP, and k_{sn}-q) than those that do not (k_{sn}, slope, local relief) (Table B5). On the other hand, for basins dominated by crystalline lithology, metrics incorporating the influence of both topography and climate (i.e., k_{sn}-q) or topography (e.g., k_{sn}, slope, local relief) generally exhibit better correlations with ^{10}Be-derived erosion rates (Fig. 3.2c,f; Fig. B5) than NEE and MAP (Fig. 3.2i,l). These different controls on erosion rates depending on dominant lithology are consistent regardless of correlation methods (e.g., linear, power-law, and exponential RMSE, reduced chi-squared statistic MSWD, χ^2, and Spearman's ρ and Kendall's τ rank correlation coefficients shown in Table B5).

Erosional efficiency coefficients from stream power models also show varying correlations with climate metrics depending on dominant lithology. For basins dominated by metasedimentary lithology, we observe a clear, positive correlation between erosional coefficients K and K_{lp} and climate metrics NEE and MAP (Fig. 3.3a,c). Conversely, for basins dominated by crystalline lithology, K and K_{lp} display weak and no correlations with climatic metrics, respectively (Fig. 3.3a,c). The median and interquartile range of K and K_{lp} with respect to the distance to major faults show somewhat different trends (Fig. 3.4e,f; Fig. B6c,d). We find that K_{lp} appears to be relatively constant or invariant with distance to faults compared to erosion rates or K. However, K_{lp} in metasedimentary rocks within a 20 km interval of the MFT exhibit a ~3.5-6.9-fold increase in median K_{lp} relative to that of other intervals (Fig. 3.4e,f).

Landslide erosion rates and density from mapped regions exhibit a positive correlation with ^{10}Be-derived erosion rates and tend to have varying trends in average failure rate for different lithologies. Except for a few basins from central and eastern Nepal (ARU-11-12, ARU-12-13, TR-170311-02) (Fig.

3.5c,d) (Table B3), ^{10}Be-derived erosion rates exhibit a strong, positive correlation with landslide density that represents landslide-affected basin area over 20 years ($R_{metased}$ = 0.90, p < 0.01; R_{crys} = 0.80, p < 0.01; Fig. 3.5b). These rates show a positive and near one-to-one correlation with ^{10}Be-derived erosion rates ($R_{metased}$ = 0.96, p < 0.01; R_{crys} = 0.78, p < 0.01; Fig. 3.3a). For the easternmost Himalaya, landslide-derived erosion rates, averaged at a basin scale, systematically decrease from the range front (5.5 mm/yr, AH18-19) to the hinterland (0.09 mm/yr, AH18-27) (Table B3). We find that average failure rates from basins dominated by metasedimentary lithology are higher (3.3-6.4×10^{-4} yr^{-1}) for this region than those from basins dominated by crystalline rocks (0.2-2.3×10^{-4} yr^{-1}). Average failure rates display a positive correlation with NEE, but trends for different lithologies diverge at higher NEE values (>10 events/yr) (Figs. 3.5c). However, average failure rates appear invariant or negatively correlated with topographic metrics such as k_{sn}-q (Figs. 3.5d).

3.6 Linking climate, erosional efficiency, and lithological variability across the Himalaya

Our analysis reveals that the degree of climatic controls on erosional efficiency differs depending on lithology in the Himalaya (Fig. 3.2h, 3.3). We find a positive correlation between ^{10}Be-derived erosion rates and topographic metrics such as k_{sn}-q or k_{sn} in basins dominated by crystalline lithologies, which is consistent with other studies in the Himalaya (Scherler et al., 2014; Godard et al., 2014; Le Roux-Mallouf et al., 2015; Olen et al., 2015; Adams et al., 2016). However, similar to Adams et al. (2020), we find that ^{10}Be-derived erosion rates show an improved fit with k_{sn}-q than k_{sn} for basins dominated by either lithology (Fig. 3.2a-f). This improvement suggests that the influence of climatic controls on erosional efficiency may be embedded in steady-state topographies that reflect underlying rock uplift rates under variable precipitation (Kirby and Whipple, 2012; Hilley et al., 2019). Our observation that erosional coefficient K is correlated with climate factors such as MAP and NEE further supports this inference (Fig. 3.3). Thus, consideration of the spatial distribution of MAP and discharge is a necessary first step before trying to infer the spatial distribution of tectonic uplift rates from topographic metrics.

For basins dominated by metasedimentary lithology, we find positive, power-law correlations between erosion rates and efficiencies with climate metrics of NEE or MAP that are stronger than those of topographic metrics (Fig. 3.2, 3.3). Although K_{lp} from k_{sn}-q theoretically should be independent of mean annual precipitation, we still find a statistically significant, positive correlation with NEE. This correlation suggests that erosional efficiency in areas with relatively weaker metasedimentary lithology is more sensitive to the frequency of extreme rainfall events compared to those with crystalline lithology. The enhanced sensitivity is likely due to mechanisms not accounted for by average discharge. Our finding of strong climatic controls on erosion rate through increased erosional efficiency coefficient K_{lp} in metasedimentary lithology differs from previous studies utilizing ^{10}Be (Scherler et al., 2014; Godard et al., 2014; Le Roux-Mallouf et al., 2015; Olen et al., 2015, 2016; Adams et al., 2016, 2020). We attribute this difference to our separation of lithologic groups and 12 new samples collected from the easternmost Himalaya that provide a NEE range much higher than that of other Himalayan regions (NEE = ~8-13 events/yr vs ~1-9 events/yr, respectively) (Fig. 3.2g) (Bookhagen and Burbank, 2010). This high NEE range on steep thresholded landscapes (e.g. Hilley et al. (2019)) may elucidate the influence of extreme NEE on erosional efficiency lacking in previous studies.

3.7 Rapid and efficient erosion from extreme rainfall and weak lithology

According to our analysis, both fluvial and landslide erosion processes are enhanced near the range front with mechanically weak metasedimentary lithology, driving high sediment fluxes and rapid ^{10}Be-derived erosion rates (Fig. 3.5a). Basins dominated by metasedimentary lithology near the MFT exhibit significantly higher erosional efficiency coefficients K_{lp} relative to those located further away (Fig. 3.4e,f). We also find that basins dominated by metasedimentary lithology appear to have higher average failure rates compared to those in crystalline rocks (e.g., the Lohit Plutonic Complex) under similar degrees of climate variability (Fig. 3.5c). It is possible that extreme rainfall events on steep, mechanically weak, metasedimentary hillslopes likely trigger numerous and frequent landslides. Previous studies in the Himalaya have also shown a measurable influence of extreme climatic events on landslide activity and

enhanced past and present-day erosion (Bookhagen et al., 2005b, 2005a; Jones et al., 2021). We infer that metasedimentary lithologies are more susceptible to episodic mass movements from extreme climatic events than crystalline rocks due to bedding, lithologic heterogeneity, or climate-induced chemical and mechanical weathering (Clarke and Burbank, 2010; Eppes and Keanini, 2017; Eppes et al., 2020). This observation is consistent with previous studies that display lower landslide-triggering rainfall thresholds for mechanically weak rocks than for strong rocks (Peruccacci et al., 2012, 2017).

Extreme rainfall events not only induce abundant landslides on metasedimentary hillslopes but also may play a crucial role in enhancing fluvial incision or transporting debris flow sediments from catchments (Wang et al., 2015). Field observations of channels in the active easternmost Himalayan range front consistently display large boulders and cobbles likely derived from landslides and debris flows from hillslopes (Fig. B7). Previous studies highlight the increasing importance of extreme rainfall events that provide shear stress exceeding high thresholds for sediment entrainment for channels with coarse bedload material (Baker, 1977; Tucker and Bras, 2000; Sklar and Dietrich, 2004). The presence of coarse channel sediment from landslides may increase thresholds for sediment transport and contribute to high erosional sensitivity to extreme rainfall events and climatic variability. In addition, abundant debris from landslides in metasedimentary lithologies may influence the erosive power of streams by altering grain size distribution and sediment flux (Sklar and Dietrich, 2001, 2004). This influence may be reflected in the positive correlation between K_{lp} and NEE, which results in especially high ^{10}Be-derived erosion rates.

Although we favor the influence of climate such as extreme precipitation as the main driver of generating erosional efficiency that varies with lithologies, other factors such as earthquakes, the unique tectonic setting, fault kinematics, or changes in environmental conditions (e.g., deglaciation) may also contribute to our observations. For example, major earthquakes are known for triggering landslides across the Himalaya including our study region (M_w 8.6 1950 Assam Earthquakes) (Coudurier-Curveur et al., 2020), while post-glaciation landscapes with steep slopes also promote slope failures that increase millennial-scale erosion rates in other locations (e.g., Abrahami et al. (2016)). It is possible that seismic shaking and faulting induce extensive fracturing and speed chemical weathering, which may predispose

rocks to landsliding when extreme precipitation occurs. However, our mapped landslides from 1997 to 2017 occurred ~50 years after the last major earthquake event, which is longer than the typical timescale of hillslope revegetation (~10 years for the eastern Himalaya according to Larsen and Montgomery (2012)). During our mapping period, large magnitude earthquakes (> M_w 6.0) are absent (Incorporated Research Institutions for Seismology, www.iris.edu). Thus, our high erosion rates and erosional coefficients are likely from landslides triggered by more frequent extreme rainfall events rather than infrequent major earthquakes.

3.8 Connection among tectonics, climate, and erosion for the Himalaya

We observe a concave upward U-shaped trend between ^{10}Be-derived erosion rates and distance from major fault structures (MFT/MCT) for basins dominated by metasedimentary lithology, while those dominated by crystalline lithology show a generally decreasing trend. These spatial patterns indicate relatively high ^{10}Be-derived erosion rates close to the active major faults for basins dominated by metasedimentary lithology, which may suggest an overall tectonic control on erosion rates (Fig. 3.4a). Previous studies have observed similar concave upward U-shaped trends in million-year-timescale rock uplift rates inferred from low-temperature thermochronometers such as apatite fission track, zircon (U-Th)/He ages, and muscovite ^{40}Ar/^{39}Ar (Robert et al., 2009; Herman et al., 2013; Thiede and Ehlers, 2013; Godard et al., 2014). Conversely, the general decrease in ^{10}Be-derived erosion rates for basins dominated by crystalline lithology with varying distances from major fault structures (Fig. 3.4b) may be related to rock uplift being concentrated near the MCT. However, inflated erosion rates related to steep, deglaciated landscapes in the hinterland may obscure a clear trend between ^{10}Be-derived erosion rates and distance from major fault structures for these basins. We also observed similar spatial trends between k_{sn}-q and $Dist_{MFT}$/$Dist_{MCT}$, except for basins dominated by metasedimentary lithology close to the MFT (Fig. 3.4c,d). Overall, the range of K_{lp} is relatively constant (Fig. 3.4e,f). We find that K_{lp} values in metasedimentary lithology generally increase with increasing NEE for varying intervals of $Dist_{MFT}$, with the highest K_{lp} values found in tectonically active areas with extreme precipitation in the range front.

These findings may support quasi-equilibrium landscapes where tectonic uplift rates are balanced with erosion rates, and topography reflects erosional efficiency influenced by climatic and lithologic controls.

Significantly high erosional efficiency and erosion rates in relatively weak, metasedimentary rocks in the range front may indicate a link between climate-driven erosion and tectonics, which has implications for the large-scale evolution of the Himalaya. For example, the increasing rate of long-term erosion and crustal shortening toward the eastern range front may lead to the southward decrease in thrust belt width and the absence of several Himalayan-Tibetan lithologic units (Yin, 2006; Haproff et al., 2019, 2020). In addition, if Lesser Himalayan metasedimentary rocks eroded faster than Greater Himalayan crystalline rocks, this in turn predicts a higher likelihood of out-of-sequence thrusting in Lesser Himalayan rocks (Leturmy et al., 2000; Koyi et al., 2000; Hoth et al., 2006; Cruz et al., 2010). Indeed, the recent Nepal earthquake (M_w 7.8 2015 Gorkha earthquake) is considered to be the result of an out-of-sequence thrust located in Lesser Himalayan rocks (Mendoza et al., 2019). Our work may imply that climate-erosion-tectonic interactions potentially vary depending on lithology, which has general implications for the long-term dynamic evolution of an orogenic-wedge system.

However, it is also possible that some of our ^{10}Be-derived or landslide erosion rates may reflect transient signals from landscape changes rather than reflecting long-term tectonics. For example, some basins from central and eastern Nepal (ARU-11-12, ARU-12-13, TR-170311-02) tend to have abnormally high landslide-derived erosion rates, densities, and average failure rates (Fig. 3.5), which are significantly higher than millennial ^{10}Be-derived erosion rates of other basins residing along the MCT. This discrepancy may be attributed to a pulse of abundant landslides triggered by earthquakes in the area. Additionally, in the easternmost Himalaya, the spatial trend of thermochronologic ages gradually decreases from the range front to the hinterland, compared to millennial ^{10}Be-derived erosion rates (Fig. B2). ^{10}Be-derived erosion rates in the range front tend to be higher (4.6–7.5 mm/yr) than million-year exhumation rates inferred from thermochronologic ages (~3.5 mm/yr) (Salvi et al., 2020). Despite these rate differences, our topographic analyses based on channel and hillslope properties support topographic equilibrium over timescales necessary to generate the observed fluvial relief (i.e. ~100 kyr) (Fig. B8-10;

Appendix B). This observation indicates that tectonic perturbations may be longer than ~100 kyr, likely over million-year timescales, similar to the timescales expected for episodic and alternating slips between faults (e.g., Cruz et al. (2010); Haproff et al. (2020)).

Nevertheless, we observe high climate-driven erosional efficiencies and erosion rates in the relatively weak, metasedimentary rocks of the Himalayan range front, which is a robust observation regardless of our interpretation of erosion rates from steady or transient landscapes. The combination of separating basins by lithology and our new samples with high NEE values and threshold hillslopes may enable us to observe the strong influence of precipitation rates on erosion rates and efficiencies in our compilation. We acknowledge that other factors not incorporated in our analyses, such as the unique tectonic setting and fault kinematics or geometry, may also contribute to our observations. Future studies with more extensive datasets of low-temperature thermochronometers, ^{10}Be-derived erosion rates, fault geometries and kinematics, and long-term climate history will offer insight into the connections among tectonic, erosion, and climate over varying timescales.

3.9 Figures

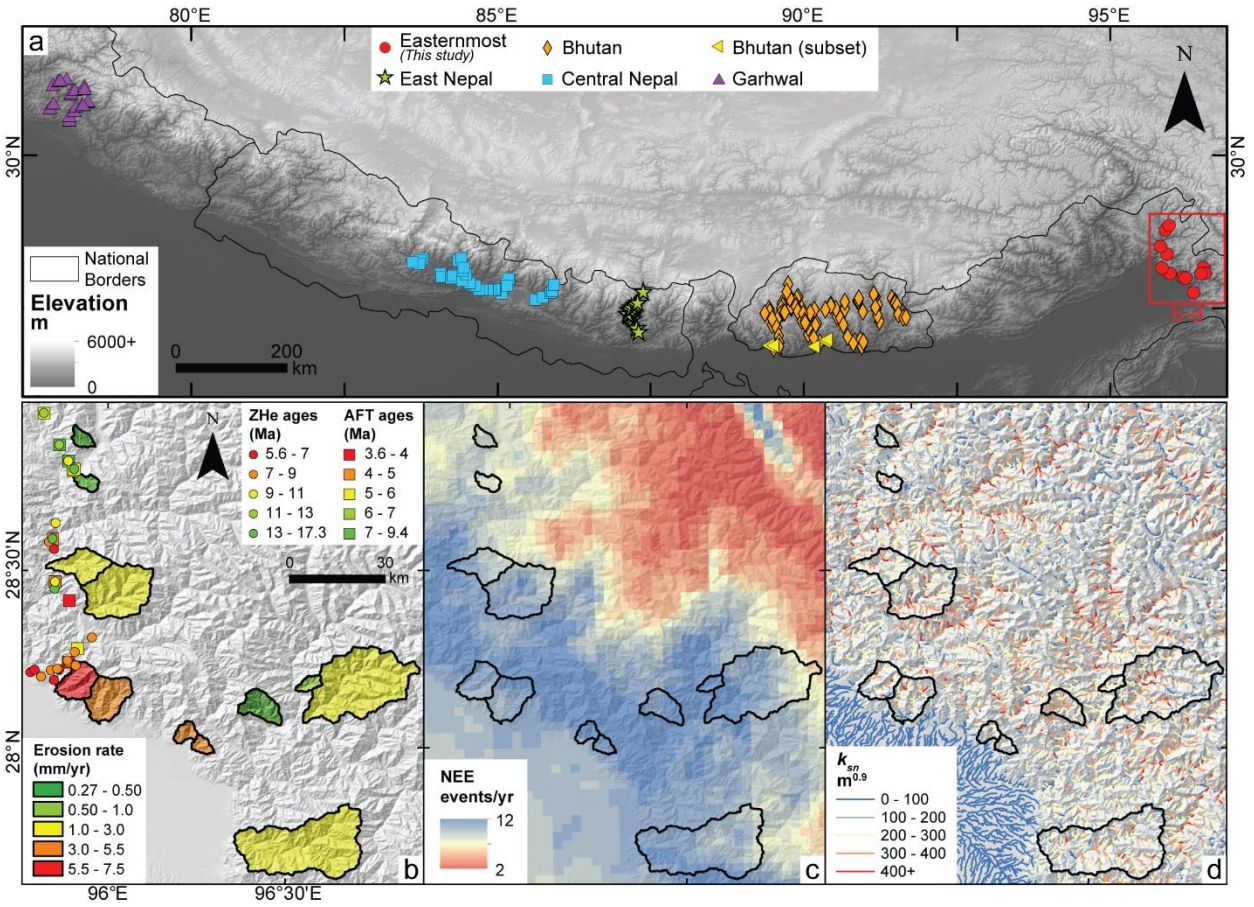

Fig. 3.1: Maps of our study area. a, elevation map with the locations of compiled basins across the Himalaya (n = 173). The white-outlined box indicates the easternmost Himalaya shown in b-d. **b**, hillshade map with our sampled basins (n = 12) colored by ^{10}Be-derived erosion rates (mm/yr) and the locations of zircon (U-Th)/He (ZHe, circles) ages from Haproff et al., (2020) and apatite fission track (AFT, squares) ages from Salvi et al., (2020). **c**, number of extreme rainfall events (NEE, events/yr) (Bookhagen and Burbank, 2010). **d**, channel steepness (k_{sn}) shown for 1 km-channel segments.

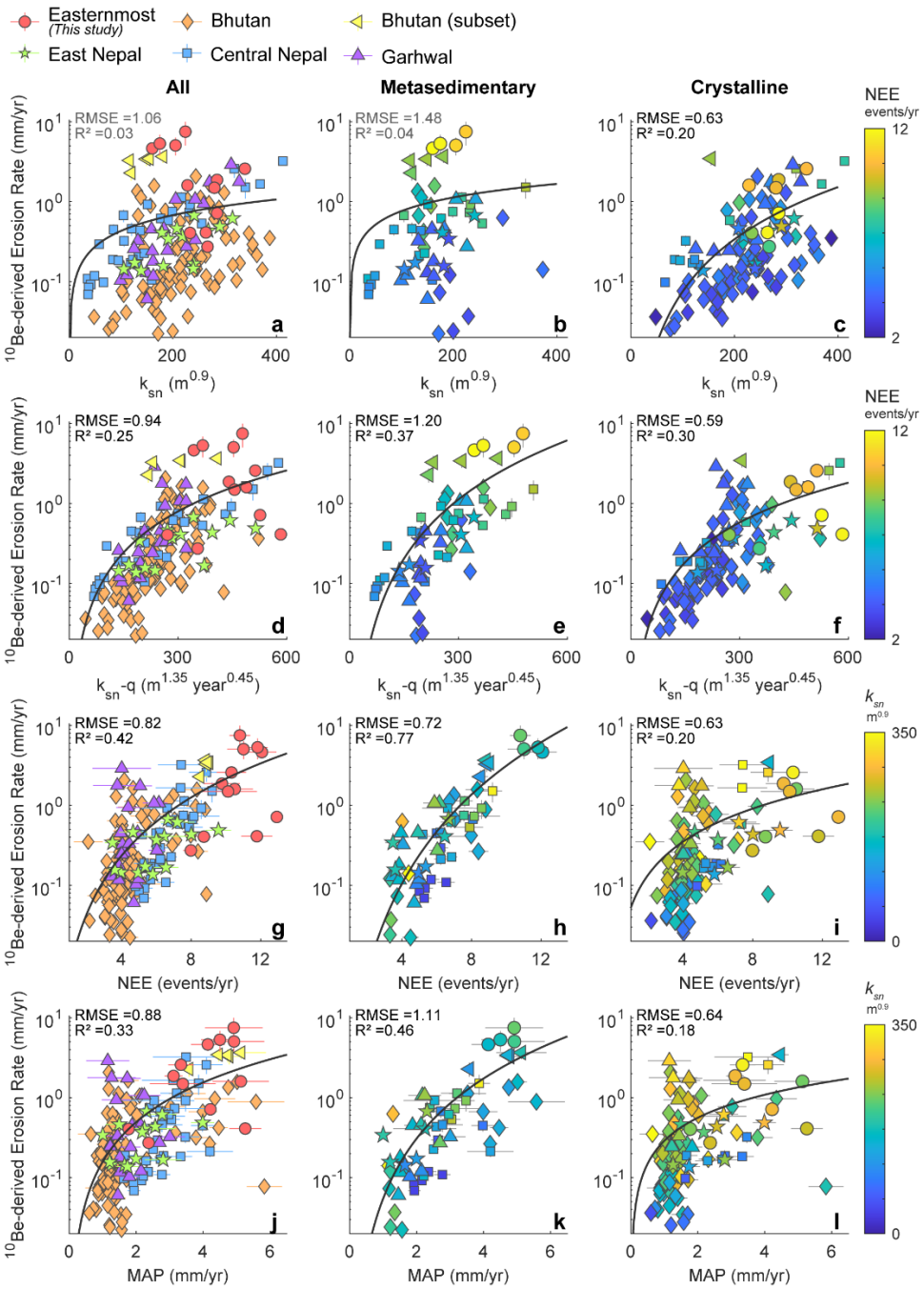

Fig. 3.2: Comparison between ^{10}Be-derived erosion rates and topographic and climatic metrics. a-c, channel steepness, k_{sn}. **d-f**, discharge-based channel steepness, k_{sn}-q. **g-i**, the number of extreme rainfall events (NEE). **j-l**, mean annual precipitation (MAP). The results for (**a, d, g, j**) all basins (n = 173) and subsets of basins dominated by (**b, e, h, k**) metasedimentary (n = 61) or (**c, f, i, l**) crystalline lithology (n = 112). Symbol shapes indicate the respective regions of sample locations. Symbol colors represent (**a, d, g, j**) respective regions, (**b, c, e, f**) NEE, and (**h, i, k, l**) k_{sn}. Power-law model fits are shown as black lines, with the corresponding values for root mean square errors (RMSE) and ordinary coefficients of determination (R^2). A lower RMSE and higher R^2 indicate a better fit. Values shown in gray indicate insignificant correlations ($p > 0.05$). Error bars are calculated from ±1σ uncertainties in ^{10}Be-derived

erosion rates, ±1σ ranges of NEE and MAP within basins, and ±1 standard errors for k_{sn} (mostly smaller than symbols).

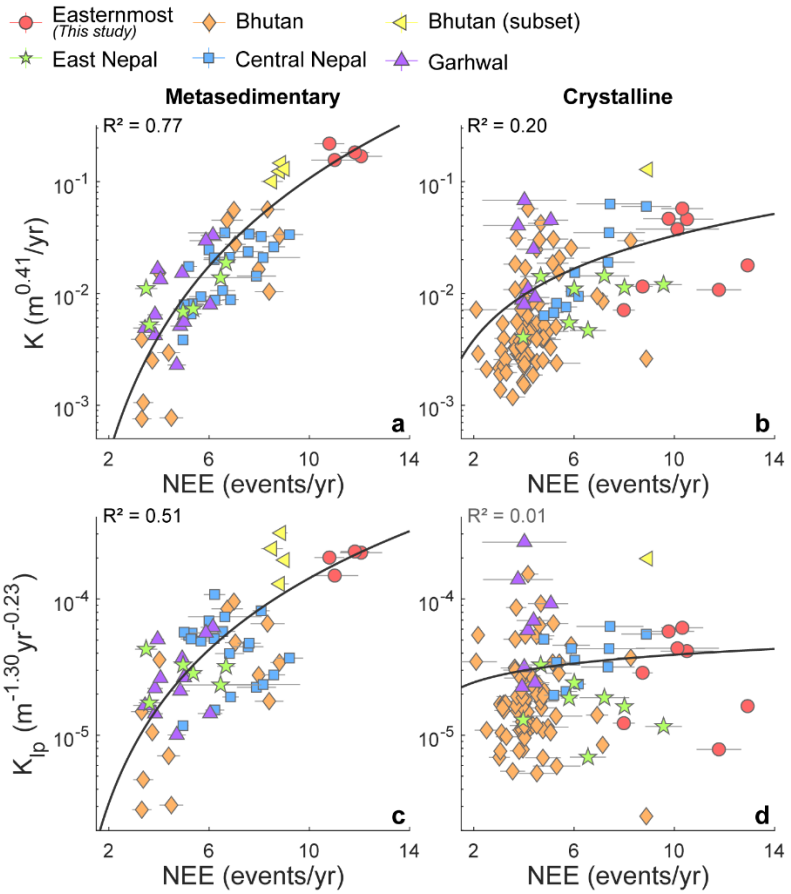

Fig. 3.3: Comparison between climatic metric and erosional efficiency coefficients. Extreme rainfall events (NEE) compared with (**a-b**) ordinary (K) and (**c-d**) modified (K_{lp}) erosional coefficients. K and K_{lp} were calculated based on relationships between ^{10}Be-derived erosion rates and k_{sn} and k_{sn}-q (see Eq. 1, 2). Results for basins dominated by (**a, c**) metasedimentary (n = 61) or (**b, d**) crystalline lithology (n = 112). Power-law model fits are shown as black lines, with the corresponding ordinary coefficients of determination (R^2). Black- and gray-colored values indicate statistically significant ($p < 0.05$) and insignificant correlations ($p > 0.05$) correlations, respectively. Error bars are calculated from ±1σ ranges of NEE and MAP within basins.

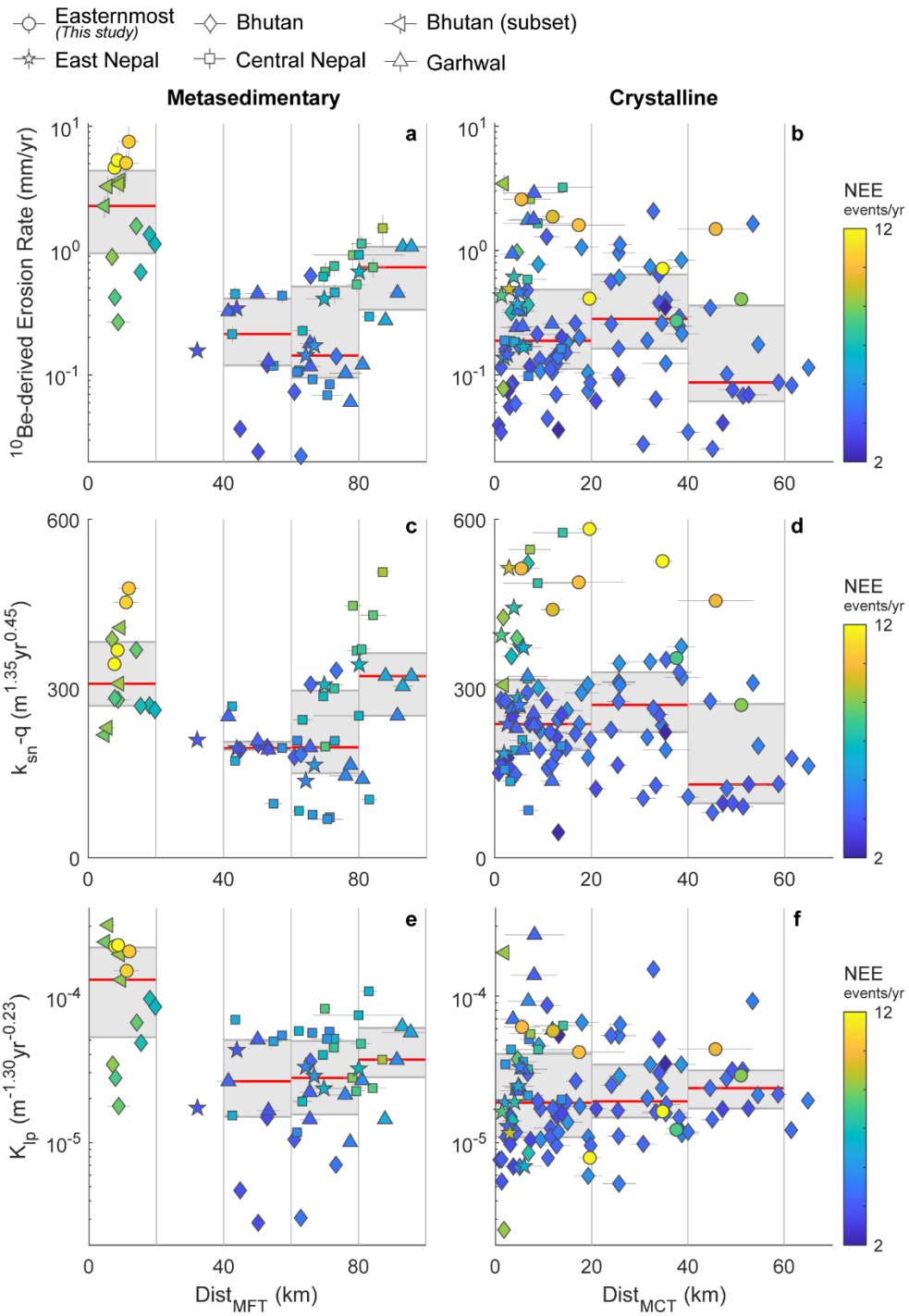

Fig. 3.4: Variations of erosion rates and efficiencies with proximity to major faults. **a-b**, ^{10}Be-derived erosion rates. **c-d**, ordinary (*K*) and **e-f**, modified (K_{lp}) erosional coefficients. Results from basins dominated by (**a, c, e**) metasedimentary or (**b, d,f**) crystalline lithology are compared with the distances to the Main Frontal Thrust ($Dist_{MFT}$) or Main Central Thrust ($Dist_{MCT}$), respectively. Red lines and gray shaded boxes indicate the median values and interquartile ranges, respectively, calculated from basins within 20-km intervals denoted by vertical gray lines. Symbol shapes indicate the regions of sample locations. Symbol colors indicate the number of extreme rainfall events (NEE).

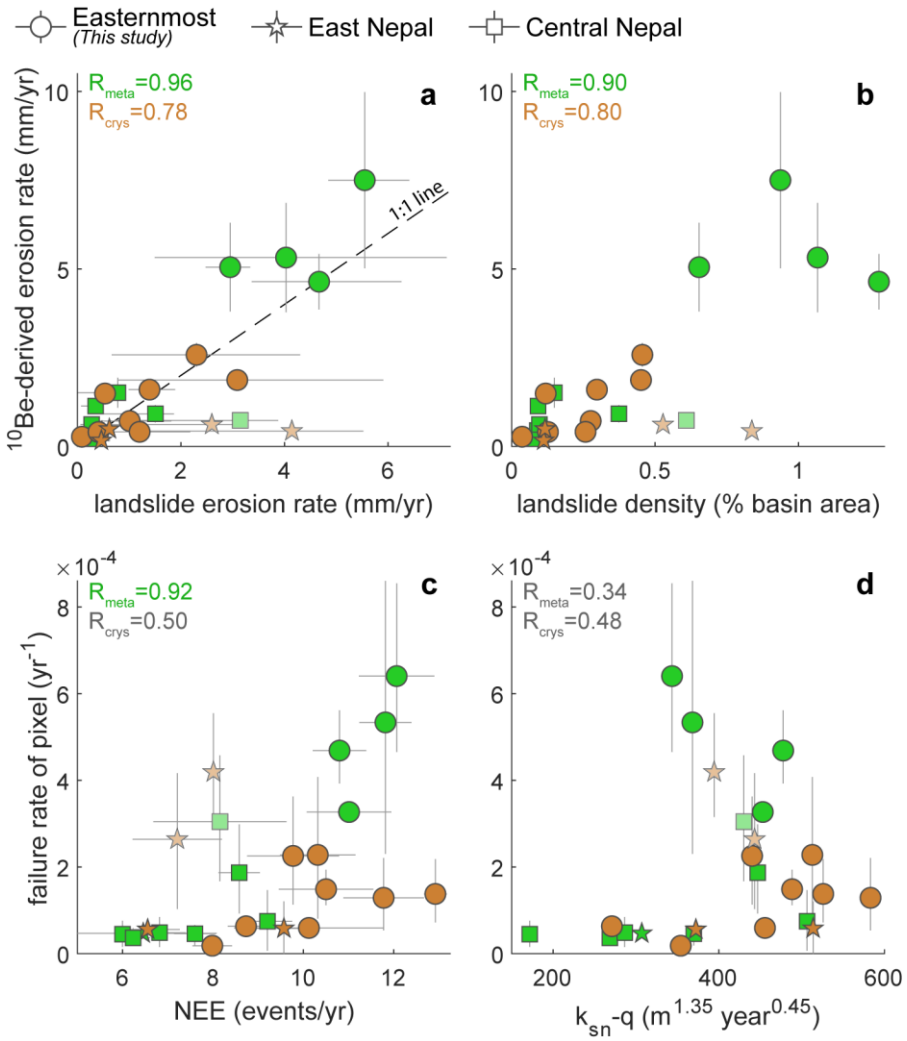

Fig. 3.5: Comparison among landslides, erosion rates, and environmental metrics. Basins with available landslide information are shown (n = 25) see Appendix B for details. Relationships between ^{10}Be-derived erosion rates and (**a**) landslide-derived erosion rates and (**b**) landslide density calculated over a 20-year interval. Relationships between average failure rates and basin-averaged (**c**) number of extreme rainfall events and (**d**) discharge-based channel steepness (k_{sn}-q). Symbol shapes indicate the regions of sample locations. Symbol colors indicate basins dominated by metasedimentary (green, n = 13) or crystalline (brown, n = 12) lithology. The linear correlation coefficients (R) are calculated for basins from each dominant lithologic group. Values in gray indicate no statistical significance (p > 0.05). Three basins shown with transparent symbols and one basin beyond the axis limit with high landslide erosion rates may indicate transient signals, which are excluded from the calculations. Error bars represent the ranges calculated from two consecutive ~10-year intervals for landslide erosion rates and average failure rates, ±1σ uncertainties in ^{10}Be-derived erosion rates, and ±1σ range of metrics within basins.

3.10 References

Abrahami, R., van der Beek, P., Huyghe, P., Hardwick, E., and Carcaillet, J., 2016, Decoupling of long-term exhumation and short-term erosion rates in the Sikkim Himalaya: Earth and Planetary Science Letters, v. 433, p. 76–88, doi:10.1016/j.epsl.2015.10.039.

Adams, B.A., Whipple, K.X., Forte, A.M., Heimsath, A.M., and Hodges, K. V, 2020, Climate controls on erosion in tectonically active landscapes: Science Advances, v. 6, p. 3166–3182.

Adams, B.A., Whipple, K.X., Hodges, K. V., and Heimsath, A.M., 2016, In situ development of high-elevation, low-relief landscapes via duplex deformation in the Eastern Himalayan hinterland, Bhutan: Journal of Geophysical Research: Earth Surface, v. 121, p. 294–319, doi:10.1002/2015JF003508.

Andermann, C., Bonnet, S., and Gloaguen, R., 2011, Evaluation of precipitation data sets along the Himalayan front: Geochemistry, Geophysics, Geosystems, v. 12, doi:10.1029/2011GC003513.

Attal, M., and Lavé, J., 2006, Changes of bedload characteristics along the Marsyandi River (central Nepal): Implications for understanding hillslope sediment supply, sediment load evolution along fluvial networks, and denudation in active orogenic belts: Special Paper of the Geological Society of America, v. 398, p. 143–171, doi:10.1130/2006.2398(09).

Baker, V.R., 1977, Stream-channel response to floods, with examples from central Texas: Geological Society of America Bulletin, v. 88, p. 1057–1071.

Balco, G., Stone, J.O., Lifton, N.A., and Dunai, T.J., 2008, A complete and easily accessible means of calculating surface exposure ages or erosion rates from ^{10}Be and ^{26}Al measurements: Quaternary Geochronology, v. 3, p. 174–195, doi:10.1016/j.quageo.2007.12.001.

Beaumont, C., Jamieson, R.A., Nguyen, M.H., and Lee, B., 2001, Himalayan tectonics explained by extrusion of a low-viscosity crustal channel coupled to focused surface denudation: Nature, v. 414, p. 738–742.

von Blanckenburg, F., 2005, The control mechanisms of erosion and weathering at basin scale from cosmogenic nuclides in river sediment: Earth and Planetary Science Letters, v. 237, p. 462–479, doi:10.1016/j.epsl.2005.06.030.

Bookhagen, B., and Burbank, D.W., 2010, Toward a complete Himalayan hydrological budget: Spatiotemporal distribution of snowmelt and rainfall and their impact on river discharge: Journal of Geophysical Research: Earth Surface, v. 115, doi:10.1029/2009JF001426.

Bookhagen, B., Thiede, R.C., and Strecker, M.R., 2005a, Abnormal monsoon years and their control on erosion and sediment flux in the high, arid northwest Himalaya: Earth and Planetary Science Letters, v. 231, p. 131–146, doi:10.1016/j.epsl.2004.11.014.

Bookhagen, B., Thiede, R.C., and Strecker, M.R., 2005b, Late Quaternary intensified monsoon phases control landscape evolution in the northwest Himalaya: Geology, v. 33, p. 149–152, doi:10.1130/G20982.1.

Burbank, D.W., Blythe, A.E., Putkonen, J., Pratt-Sitaula, B., Gabet, E., Oskin, M., Barros, A., and Ojha, T.P., 2003, Decoupling of erosion and precipitation in the Himalayas: Nature, v. 426, p. 652–655.

Burbank, D.W., Lelandt, J., Fielding, E., Anderson, R.S., Brozovic, N., Reidt, M.R., and Duncan, C., 1996, Bedrock incision, rock uplift and threshold hillslopes in the northwestern Himalayas: Nature, v. 379, p. 505–510.

Burgess, W.P., Yin, A., Dubey, C.S., Shen, Z.K., and Kelty, T.K., 2012, Holocene shortening across the main frontal thrust zone in the eastern Himalaya: Earth and Planetary Science Letters, v. 357–358, p. 152–167, doi:10.1016/j.epsl.2012.09.040.

Clarke, B.A., and Burbank, D.W., 2010, Bedrock fracturing, threshold hillslopes, and limits to the magnitude of bedrock landslides: Earth and Planetary Science Letters, v. 297, p. 577–586, doi:10.1016/j.epsl.2010.07.011.

Corbett, L.B., Bierman, P.R., and Rood, D.H., 2016, An approach for optimizing in situ cosmogenic ^{10}Be sample preparation: Quaternary Geochronology, v. 33, p. 24–34, doi:10.1016/j.quageo.2016.02.001.

Coudurier-Curveur, A., Tapponnier, P., Okal, E., Van der Woerd, J., Kali, E., Choudhury, S., Baruah, S., Etchebes, M., and Karakaş, C., 2020, A composite rupture model for the great 1950 Assam earthquake across the cusp of the East Himalayan Syntaxis: Earth and Planetary Science Letters, v. 531, doi:10.1016/j.epsl.2019.115928.

Cruz, L., Malinski, J., Wilson, A., Take, W.A., and Hilley, G., 2010, Erosional control of the kinematics and geometry of fold-and-thrust belts imaged in a physical and numerical sandbox: Journal of Geophysical Research: Solid Earth, v. 115, doi:10.1029/2010JB007472.

Dahlen, F.A., Suppe, J., and Davis, D., 1984, Mechanics of Fold-and-Thrust Belts and Accretionary Wedges: Cohesive Coulomb Theory: Journal of Geophysical Research, v. 89, p. 10087–10101, doi:10.1029/JB089iB12p10087.

Eppes, M.C., and Keanini, R., 2017, Mechanical weathering and rock erosion by climate-dependent subcritical cracking: Reviews of Geophysics, v. 55, p. 470–508, doi:10.1002/2017RG000557.

Eppes, M.C., Magi, B., Scheff, J., Warren, K., Ching, S., and Feng, T., 2020, Warmer, Wetter Climates Accelerate Mechanical Weathering in Field Data, Independent of Stress-Loading: Geophysical Research Letters, v. 47, doi:10.1029/2020GL089062.

Farr, T.G. et al., 2007, The Shuttle Radar Topography Mission: Reviews of Geophysics, v. 45, doi:10.1029/2005RG000183.

de Ferranti, J., 2021, Digital elevation data:, http://viewfinderpanoramas.org/dem3.html (accessed January 2022).

Godard, V., Bourlès, D.L., Spinabella, F., Burbank, D.W., Bookhagen, B., Fisher, G.B., Moulin, A., and Léanni, L., 2014, Dominance of tectonics over climate in Himalayan denudation: Geology, v. 42, p. 243–246, doi:10.1130/G35342.1.

Godard, V., Burbank, D.W., Bourls, D.L., Bookhagen, B., Braucher, R., and Fisher, G.B., 2012, Impact of glacial erosion on ^{10}Be concentrations in fluvial sediments of the Marsyandi catchment, central Nepal: Journal of Geophysical Research: Earth Surface, v. 117, doi:10.1029/2011JF002230.

Godard, V., Lavie, J., and Cattin, R., 2006, Numerical modelling of erosion processes in the Himalayas of Nepal: effects of spatial variations of rock strength and precipitation: Analogue and Numerical Modeling of Crustal-Scale Processes, v. 253, p. 341–358.

Graveleau, F., Malavieille, J., and Dominguez, S., 2012, Experimental modelling of orogenic wedges: A review: Tectonophysics, v. 538–540, p. 1–66, doi:10.1016/j.tecto.2012.01.027.

Grujic, D., Coutand, I., Bookhagen, B., Bonnet, S., Blythe, A., and Duncan, C., 2006, Climatic forcing of erosion, landscape, and tectonics in the Bhutan Himalayas: Geology, v. 34, p. 801–804, doi:10.1130/G22648.1.

Haproff, P.J., Odlum, M.L., Zuza, A. V., Yin, A., and Stockli, D.F., 2020, Structural and Thermochronologic Constraints on the Cenozoic Tectonic Development of the Northern Indo-Burma Ranges: Tectonics, v. 39, doi:10.1029/2020TC006231.

Haproff, P.J., Zuza, A. V., Yin, A., Harrison, T.M., Manning, C.E., Dubey, C.S., Ding, L., Wu, C., and Chen, J., 2019, Geologic framework of the northern Indo-Burma Ranges and lateral correlation of Himalayan-Tibetan lithologic units across the eastern Himalayan syntaxis: Geosphere, v. 15, p. 856–881, doi:10.1130/GES02054.1.

Herman, F., Seward, D., Valla, P.G., Carter, A., Kohn, B., Willett, S.D., and Ehlers, T.A., 2013, Worldwide acceleration of mountain erosion under a cooling climate: Nature, v. 504, p. 423–426, doi:10.1038/nature12877.

Hilley, G.E., Porder, S., Aron, F., Baden, C.W., Johnstone, S.A., Liu, F., Sare, R., Steelquist, A., and Young, H.H., 2019, Earth's topographic relief potentially limited by an upper bound on channel steepness: Nature Geoscience, v. 12, p. 828–832, doi:10.1038/s41561-019-0442-3.

Hilley, G.E., and Strecker, M.R., 2004, Steady state erosion of critical Coulomb wedges with applications to Taiwan and the Himalaya: Journal of Geophysical Research: Solid Earth, v. 109, doi:10.1029/2002jb002284.

Hoth, S., Adam, J., Kukowski, N., and Oncken, O., 2006, Influence of erosion on the kinematics of bivergent orogens: Results from scaled sandbox simulations: Special Paper of the Geological Society of America, v. 398, p. 201–225, doi:10.1130/2006.2398(12).

Jamshadali, V.H., Reji, M.J.K., Varikoden, H., and Vishnu, R., 2021, Spatial variability of south Asian summer monsoon extreme rainfall events and their association with global climate indices: Journal of Atmospheric and Solar-Terrestrial Physics, v. 221, p. 105708, doi:10.1016/j.jastp.2021.105708.

Jones, J.N., Boulton, S.J., Stokes, M., Bennett, G.L., and Whitworth, M.R.Z., 2021, 30-year record of Himalaya mass-wasting reveals landscape perturbations by extreme events: Nature Communications, v. 12, doi:10.1038/s41467-021-26964-8.

Kirby, E., and Whipple, K.X., 2012, Expression of active tectonics in erosional landscapes: Journal of Structural Geology, v. 44, p. 54–75, doi:10.1016/j.jsg.2012.07.009.

Koyi, H.A., Hessami, K., and Teixell, A., 2000, Epicenter distribution and magnitude of earthquakes in fold-thrust belts: Insights from sandbox models: Geophysical Research Letters, v. 27, p. 273–276, doi:10.1029/1999GL010833.

Kumar, S., Wesnousky, S.G., Rockwell, T.K., Briggs, R.W., Thakur, V.C., and Jayangondaperumal, R., 2006, Paleoseismic evidence of great surface rupture earthquakes along the Indian Himalaya: Journal of Geophysical Research: Solid Earth, v. 111, p. 3304, doi:10.1029/2004JB003309.

Larsen, I.J., and Montgomery, D.R., 2012, Landslide erosion coupled to tectonics and river incision: Nature Geoscience, v. 5, p. 468–473, doi:10.1038/ngeo1479.

Larsen, I.J., Montgomery, D.R., and Korup, O., 2010, Landslide erosion controlled by hillslope material: Nature Geoscience, v. 3, p. 247–251, doi:10.1038/ngeo776.

Lavé, J., and Avouac, J.P., 2000, Active folding of fluvial terraces across the Siwaliks Hills, Himalayas of central Nepal: Journal of Geophysical Research: Solid Earth, v. 105, p. 5735–5770, doi:10.1029/1999JB900292.

Leonard, J.S., Whipple, K.X., and Heimsath, A.M., 2023, Isolating climatic, tectonic, and lithologic controls on mountain landscape evolution: Science Advances, v. 9, p. 1–10, https://www.science.org.

Leturmy, P., Mugnier, J.L., Vinour, P., Baby, P., Colletta, B., and Chabron, E., 2000, Piggyback basin development above a thin-skinned thrust belt with two detachment levels as a function of interactions between tectonic and superficial mass transfer: the case of the Subandean Zone (Bolivia):, www.elsevier.com/locate/tecto.

Lupker, M. et al., 2017, ^{10}Be systematics in the Tsangpo-Brahmaputra catchment: The cosmogenic nuclide legacy of the eastern Himalayan syntaxis ETH Library Be systematics in the Tsangpo-Brahmaputra catchment: the cosmogenic nuclide legacy of the eastern Himalayan syntaxis: Earth Surf. Dynam, v. 5, p. 429–449, doi:10.3929/ethz-b-000192411.

Marder, E., and Gallen, S.F., 2023, Climate control on the relationship between erosion rate and fluvial topography: Geology, doi:10.1130/g50832.1.

Mendoza, M.M., Ghosh, A., Karplus, M.S., Klemperer, S.L., Sapkota, S.N., Adhikari, L.B., and Velasco, A., 2019, Duplex in the Main Himalayan Thrust illuminated by aftershocks of the 2015 M_w 7.8 Gorkha earthquake: Nature Geoscience, v. 12, p. 1018–1022, doi:10.1038/s41561-019-0474-8.

Molnar, P., and England, P., 1990, Late Cenozoic uplift of mountain ranges and global climate change: chicken or egg? Nature, v. 346, p. 29–34.

Montgomery, D.R., and Dietrich, W.E., 1994, A physically based model for the topographic control on shallow landsliding: Water Resources Research, v. 30.

Moon, S., Shelef, E., and Hilley, G.E., 2015, Recent topographic evolution and erosion of the deglaciated Washington Cascades inferred from a stochastic landscape evolution model: Journal of Geophysical Research: Earth Surface, v. 120, p. 856–876, doi:10.1002/2014JF003387.

Mukherjee, S., Joshi, R., Prasad, R.C., Vishvakarma, S.C.R., and Kumar, K., 2015, Summer monsoon rainfall trends in the Indian Himalayan region: Theoretical and Applied Climatology, v. 121, p. 789–802, doi:10.1007/s00704-014-1273-1.

Nishiizumi, K., Imamura, M., Caffee, M.W., Southon, J.R., Finkel, R.C., and McAninch, J., 2007, Absolute calibration of ^{10}Be AMS standards: Nuclear Instruments and Methods in Physics Research, Section B: Beam Interactions with Materials and Atoms, v. 258, p. 403–413, doi:10.1016/j.nimb.2007.01.297.

Olen, S.M., Bookhagen, B., Hoffmann, B., Sachse, D., Adhikari, D.P., and Strecker, M.R., 2015, Understanding erosion rates in the Himalayan orogen: A case study from the Arun Valley: Journal of Geophysical Research: Earth Surface, v. 120, p. 2080–2102, doi:10.1002/2014JF003410.

Olen, S.M., Bookhagen, B., and Strecker, M.R., 2016, Role of climate and vegetation density in modulating denudation rates in the Himalaya: Earth and Planetary Science Letters, v. 445, p. 57–67, doi:10.1016/j.epsl.2016.03.047.

Perron, J.T., and Royden, L., 2013, An integral approach to bedrock river profile analysis: Earth Surface Processes and Landforms, v. 38, p. 570–576, doi:10.1002/esp.3302.

Peruccacci, S., Brunetti, M.T., Gariano, S.L., Melillo, M., Rossi, M., and Guzzetti, F., 2017, Rainfall thresholds for possible landslide occurrence in Italy: Geomorphology, v. 290, p. 39–57, doi:10.1016/j.geomorph.2017.03.031.

Peruccacci, S., Brunetti, M.T., Luciani, S., Vennari, C., and Guzzetti, F., 2012, Lithological and seasonal control on rainfall thresholds for the possible initiation of landslides in central Italy: Geomorphology, v. 139–140, p. 79–90, doi:10.1016/j.geomorph.2011.10.005.

Portenga, E.W., and Bierman, P.R., 2011, Understanding Earth's eroding surface with ^{10}Be: GSA Today, v. 21, p. 4–10, doi:10.1130/G111A.1.

Portenga, E.W., Bierman, P.R., Duncan, C., Corbett, L.B., Kehrwald, N.M., and Rood, D.H., 2015, Erosion rates of the Bhutanese Himalaya determined using in situ-produced ^{10}Be: Geomorphology, v. 233, p. 112–126, doi:10.1016/j.geomorph.2014.09.027.

Robert, X., van der Beek, P., Braun, J., Perry, C., Dubille, M., and Mugnier, J.L., 2009, Assessing quaternary reactivation of the Main Central thrust zone (central Nepal Himalaya): New thermochronologic data and numerical modeling: Geology, v. 37, p. 731–734, doi:10.1130/G25736A.1.

Le Roux-Mallouf, R. et al., 2015, Evidence for a wide and gently dipping Main Himalayan Thrust in western Bhutan: Geophysical Research Letters, v. 42, p. 3257–3265, doi:10.1002/2015GL063767.

Salvi, D., Mathew, G., Kohn, B., Pande, K., and Borgohain, B., 2020, Thermochronological insights into the thermotectonic evolution of Mishmi hills across the Dibang Valley, NE Himalayan Syntaxis: Journal of Asian Earth Sciences, v. 190, doi:10.1016/j.jseaes.2019.104158.

Scherler, D., Bookhagen, B., and Strecker, M.R., 2014, Tectonic control on ^{10}Be-derived erosion rates in the Garhwal Himalaya, India: Journal of Geophysical Research: Earth Surface, v. 119, p. 83–105, doi:10.1002/2013JF002955.

Schwanghart, W., and Scherler, D., 2014, Short Communication: TopoToolbox 2 - MATLAB-based software for topographic analysis and modeling in Earth surface sciences: Earth Surface Dynamics, v. 2, p. 1–7, doi:10.5194/ESURF-2-1-2014.

Sklar, L.S., and Dietrich, W.E., 2004, A mechanistic model for river incision into bedrock by saltating bed load: Water Resources Research, v. 40, doi:10.1029/2003WR002496.

Sklar, L.S., and Dietrich, W.E., 2001, Sediment and rock strength controls on river incision into bedrock: Geology, v. 29, p. 1087–1090, http://pubs.geoscienceworld.org/gsa/geology/article-pdf/29/12/1087/3520001/i0091-7613-29-12-1087.pdf.

Stevens, V.L., and Avouac, J.P., 2015, Interseismic coupling on the main Himalayan thrust: Geophysical Research Letters, v. 42, p. 5828–5837, doi:10.1002/2015GL064845.

Thiede, R.C., and Ehlers, T.A., 2013, Large spatial and temporal variations in Himalayan denudation: Earth and Planetary Science Letters, v. 371–372, p. 278–293, doi:10.1016/j.epsl.2013.03.004.

Tucker, G.E., and Bras, R.L., 2000, A stochastic approach to modeling the role of rainfall variability in drainage basin evolution: Water Resources Research, v. 36, p. 1953–1964, doi:10.1029/2000WR900065.

Vance, D., Bickle, M., Ivy-Ochs, S., and Kubik, P.W., 2003, Erosion and exhumation in the Himalaya from cosmogenic isotope inventories of river sediments: Earth and Planetary Science Letters, v. 206, p. 273–288, doi:10.1016/S0012-821X(02)01102-0.

Varikoden, H., and Revadekar, J. V., 2020, On the extreme rainfall events during the southwest monsoon season in northeast regions of the Indian subcontinent: Meteorological Applications, v. 27, doi:10.1002/met.1822.

Wang, J., Jin, Z., Hilton, R.G., Zhang, F., Densmore, A.L., Li, G., and Joshua West, A., 2015, Controls on fluvial evacuation of sediment from earthquake-triggered landslides: Geology, v. 43, p. 115–118, doi:10.1130/G36157.1.

Whipple, K.X., 2009, The influence of climate on the tectonic evolution of mountain belts: Nature Geoscience, v. 2, p. 97–104, doi:10.1038/ngeo413.

Yatagai, A., Kamiguchi, K., Arakawa, O., Hamada, A., Yasutomi, N., and Kitoh, A., 2012, Aphrodite constructing a long-term daily gridded precipitation dataset for Asia based on a dense network of rain gauges: Bulletin of the American Meteorological Society, v. 93, p. 1401–1415, doi:10.1175/BAMS-D-11-00122.1.

Yin, A., 2006, Cenozoic tectonic evolution of the Himalayan orogen as constrained by along-strike variation of structural geometry, exhumation history, and foreland sedimentation: Earth-Science Reviews, v. 76, p. 1–131, doi:10.1016/j.earscirev.2005.05.004.

Chapter 4:

Patterns of low-temperature thermochronologic ages from the easternmost Himalaya

Note: This chapter is modified from Shao, K., Moon, S., Fosdick, J.C., Haproff, P.J., Odlum, M.L., Yin, A (in prep). Patterns of low-temperature thermochronologic ages from the easternmost Himalaya.

4.1 Introduction

The debate between the relative importance of climate and tectonic controls on long-term erosion rates has been explored across a variety of landscapes. Previous studies of the Himalaya have shown large along-strike variations in exposed geology and thrust belt width between the central and Northern Indo-Burma Ranges of the Arunachal Himalaya (Yin, 2006; Haproff et al., 2019). A primary difference is the lack of surface exposure and the surficial narrowing in width of the Greater Himalayan Crystalline Complex (GHC) and the Lesser Himalayan Sequence (LHS), respectively, in the Arunachal Himalaya at the far eastern end of the mountain range (hereafter, easternmost Himalaya). The absence of the GHC and minimal surface exposure of the LHS may be related to a greater magnitude of crustal shortening due to tectonics and climate-driven erosion in the region, which is potentially related to increased tectonics or precipitation. Estimates of horizontal shortening strain from previous studies range between ~78-86% in the range front of the easternmost Himalaya (Ningthoujam et al., 2014; Haproff et al., 2019; Salvi et al., 2020), which is generally greater than but comparable to the maximum of those from the central and western Himalaya. Additionally, previous studies investigating millennial erosion rates found especially high rates in the easternmost Himalaya (Shao et al., in review; Lupker et al., 2017), which has one of the highest precipitation magnitudes and variabilities in the Himalayan range.

Accurate quantification of the magnitude, distribution, and history of exhumation rates may offer insight into proposed fault geometries in the range front and the persistence of out-of-sequence faulting in

the hinterland. A balanced cross-section constructed by Haproff et al. (2020) displays a ramp-flat thrust in the range front with steep thrust geometries in the hinterland. Conversely, thermokinematic modeling by Salvi et al. (2020) suggests that more gradually dipping faults in the range front best fit reported low-temperature thermochronology ages. Additionally, a palinspastic reconstruction based on available zircon (U-Th-Sm)/He ages suggests the reactivation of the Lohit thrust in the hinterland (Haproff et al., 2020). However, this reconstruction of the Dibang Valley accounts for events until ~5 Ma and is limited by the lack of constraints from thermochronology ages sensitive to lower temperature systems. Unraveling fault geometry and activity on recent timescales may have further implications on crustal shortening estimates, landscape evolution, and natural hazard mitigation in tectonically active areas.

Here, we examine the magnitude and spatial distribution of million-year timescale cooling and inferred exhumation rates using apatite (U-Th-Sm)/He thermochronology of the easternmost Himalaya. We measured apatite (U-Th-Sm)/He ages in five samples from the range front into the hinterland near the Lohit thrust of the Dibang Valley. Using inverse thermal modeling incorporating previously reported zircon (U-Th-Sm)/He ages (Haproff et al., 2020), we determined plausible T-t cooling histories of range front and hinterland samples. These histories offer insight into the spatial distribution of exhumation compared to other Himalayan regions and potential links among climate, tectonics, and millennial erosion in the easternmost Himalaya.

4.2 Methods

We measured apatite (U-Th-Sm)/He (AHe) ages in five detrital and bedrock samples (16 single grains) collected along the range front to the hinterland of the Dibang Valley (detrital: aPH-1-14-13-5, aPH-1-3-13-11B, aPH-11-9-15-27; bedrock: aPH-1-8-13-8, aPH-1-8-13-1B) (Fig. 4.1, 4.2). These samples were selected to investigate exhumation patterns in the unconstrained range front as well as the persistence of out-of-sequence faulting on recent million-year timescales. Our sample rock types include phyllite from the Sewak unit, paragneiss from the Lalpani schist and Mayodia gneiss, and diorite and monzodiorite from the Western Lohit Plutonic Complex. We combine our measurements with four zircon

(U-Th-Sm)/He (ZHe) ages reported by Haproff et al. (2020) for further geological context of our study area. These AHe and ZHe measurements are obtained from the same samples except for aPH-11-9-15-27, which does not have a reported ZHe age.

Apatite crystals were separated from whole rock samples by crushing using a steel mortar and pestle at the University of California, Los Angeles. Crystals screened and selected for quality, crystal size, shape, and absence of inclusions were packed in Nb foil packets at the Basin Analysis & Helium Thermochronology Laboratory (BAHTL) at the University of Connecticut. There, radiogenic ^{4}He was extracted and measured by heating packets. Degassed sample aliquots were chemically dissolved and measured for U, Th, and Sm content by ICP-MS at the University of Colorado Thermochronology Research and Instrumentation Laboratory (TRaIL). Grain morphometric data, blank-corrected He concentrations, and U-Th measurements were used to calculate (U-Th-Sm)/He ages using an in-house data reduction MATLAB code at BAHTL (Ketcham et a., 2011). All AHe grain ages are reported at $\pm 1\sigma$ analytical uncertainties, which accounts for instrumental error (Table C1). The lab standard reproducibility is ~8% at BAHTL for the apatite (U-Th-Sm)/He age of the Durango ignimbrite emplacement of 31.1 ± 1.0 Ma (McDowell et al., 2005), which is consistent with typical lab reproducibility measurements. Additional details about AHe preparation and analytical methods can be found in Appendix Note C1.

We used the HeFTy thermal history modeling program v1.9.3 (Ketcham, 2005) to inverse model plausible T-t histories for our four AHe samples along with their respective ZHe ages reported by Haproff et al. (2020) (Ketcham, 2005). Zircon U-Pb ages for the same samples reported by Haproff et al. (2019) were included to create constraining points along the modeled T-t history. We used $\pm 2\sigma$ analytical uncertainties in our inverse modeling for all samples except for aPH-1-14-13-5, for which we were able to find acceptable T-t histories using $\pm 1\sigma$ analytical uncertainties. Additionally, the Monte-Carlo inversion iterations were run until 100 acceptable fits (goodness of fit value >0.05) were obtained for each sample. Closure temperature of apatite crystals, accounted for by HeFTy, is influenced by factors such as crystal size and cooling rate (Dodson, 1973). The closure temperature of apatite is commonly assumed to be

~70°C, but can vary between ~50-115°C for a cooling rate of 10°C/Myr (Wolf et al., 1996; Farley, 2000; Reiners and Farley, 2001; Ehlers and Farley, 2003; Reiners and Brandon, 2006; Shuster et al., 2006; Flowers et al., 2009). The uncorrected AHe and ZHe grain ages were corrected using the alpha-ejection correction method of Ketcham et al. (2011). Additionally, we conducted sensitivity tests to examine the impact of single-grain measurements on the robustness of plausible T-t histories. These tests were conducted by removing certain grains of differing ages or characteristics from the sample and observing deviations in recalculated plausible T-t histories. Further details regarding AHe and ZHe ages, HeFTy model parameters, and results of sensitivity tests can be found in Appendix Note C2.

4.3 Results: Measured (U-Th-Sm)/He ages and inferred T-t histories

Corrected, single grain AHe ages vary from 0.9 ± 0.2 Ma to 3.1 ± 0.7 Ma (aPH-1-3-13-11B) in the Sewak unit and Lalpani schist of the range front (n = 7) (Fig. 4.1, 4.2, 4.3; Table C1). Single grain AHe ages of the hinterland located on the hanging wall of the Lohit thrust (n = 7) vary from 3.1 ± 0.1 Ma (aPH-1-8-13-8) to 11.8 ± 2.0 Ma (aPH-1-8-13-1B) in the Western Lohit Plutonic Complex. Our samples generally display an increase in age with increasing distance from the Himalayan Main Frontal Thrust (MFT). Although grains from aPH-1-14-13-5 exhibit a large variation in effective uranium (eU = U + (0.235*Th)) concentration, they are consistent in AHe ages and equivalent spherical radius (R_S) (Fig. 4.3a,b). AHe ages from aPH-1-3-13-11B are inversely related to the R_S over consistent eU concentrations. Grains from aPH-11-9-15-27 are generally consistent in eU and R_S but display large variations in age. Because of the lack of T-t constraints and variations in ages, this sample was not included in HeFTy modeling. Additionally, grains from aPH-1-8-13-8 display relatively consistent ages, eU, and R_S. AHe ages from aPH-1-8-13-1B vary substantially for consistent eU and R_S with the oldest grain age having a low eU (5.77 ppm).

ZHe single grain ages reported by Haproff et al. (2020) vary between 5.7 ± 0.5 Ma (PH-1-14-13-5) to 9.3 ± 0.7 Ma (PH-1-3-13-11B) in the range front (n = 5) and from 5.3 ± 0.4 Ma (PH-1-8-13-8) to 11.1 ± 0.9 Ma (PH-1-8-13-1B) in the hinterland (n = 6) (Fig. 4.3c,d). ZHe single grain uncertainties represent

standard errors of 8% (±2σ) derived from the reproducibility of the Fish Canyon Tuff standard (Reiners et al., 2002). Sample PH-1-14-13-5 contains an anomalously old ZHe age with a substantially higher eU compared to that of the other sample grains. This grain will not be included in our HeFTy inverse model analyses. Additionally, ZHe ages from PH-1-3-13-11B (n = 3) positively correlate with large variations in eU over consistent R_S.

Our inverse thermal model results indicate rapid cooling along the Mishmi and Lalpani thrusts in the range front and concentrated cooling near the Lohit thrust, potentially until the present. Because of our AHe and ZHe age inputs, we focus our analyses and interpretations from HeFTy inverse modeled T-t histories up to ~10-5 Ma. HeFTy inverse model results constraining plausible T-t histories for sample aPH-1-14-13-5 located in the range front suggest steady, rapid cooling from ~130-150°C over the last 5 Ma (Fig. 4.4a). These T-t histories are consistent with a large variation in AHe eU over consistent ages, which suggests rapid cooling through the AHe partial retention zone.

Additionally, modeled T-t histories for sample aPH-1-3-13-11B in the range front suggest a potentially protracted cooling around the ZHe partial retention zone with more rapid cooling beginning between 1-2 Ma (Fig. 4.4b). Sensitivity tests indicate that the two youngest AHe grains constrain the existence and timing of the change in cooling rate (Fig. C1).

Modeled T-t histories for sample aPH-1-8-13-8 located on the hanging wall of the Lohit thrust suggest either gradual cooling from around ~150-200°C or more episodic periods of rapid and protracted cooling over the last 10 Ma (Fig. 4.4c). However, plausible T-t histories show large variations older than 4 Ma.

Last, modeled T-t histories for sample aPH-1-8-13-1B also located on the hanging wall of the Lohit thrust, ~8 km north of the previous sample aPH-1-8-13-8, suggest potential cooling until ~10-9 Ma at which the grains resided at near-surface temperatures until present (Fig. 4.4d). All modeled histories are generally consistent with their respective sensitivity tests indicating that these T-t histories are not strongly controlled by any single grain (Fig. C1).

4.4 Discussion

4.4.1 Inferred exhumation of the easternmost Himalayan range front and hinterland

Our results from the range front suggest especially high exhumation rates concentrated near the range front along the Lalpani thrust that may be associated with a ramp-flat fault geometry. Our findings are generally consistent with a palinspastic reconstruction between ~36-5 Ma of the Dibang Valley by Haproff et al. (2020) using ZHe and biotite $^{40}Ar/^{39}Ar$ ages. Haproff et al. (2020) inferred foreland in-sequence slip of the Mishmi and Lalpani thrusts beginning and potentially continuing through ~6-5 Ma and ~11-5 Ma, respectively. However, a lack of additional thermochronometers sensitive to lower temperature systems made it difficult to constrain movement along the fault at more recent timescales. Our inverted T-t histories for AHe sample aPH-1-14-13-5 indicate that slip along the Mishmi thrust led to steady, rapid exhumation over the last 5 Ma. Additionally, those of AHe sample aPH-1-3-13-11B indicate slow vertical exhumation between ~5-2 Ma with a drastic increase in exhumation rate beginning around ~2-1 Ma. The change in exhumation rate between these periods is consistent with a thrust ramp and bedding-parallel flat fault geometry reported by Haproff et al. (2019) where changes from relatively slow to rapid exhumation correspond to a transition from the flat to the ramp. Assuming a simplified geothermal gradient of 25°C/km, we estimate maximum exhumation rates of ~1 mm/yr over the last ~5 Ma and ~2.0-3.5 mm/yr over the last ~2-1 Ma for the Mishmi and Lalpani thrusts, respectively. Our exhumation rate estimates along the Lalpani thrust are lower than the estimated ~3.5-3.7 mm/yr rate over the last 40 Ma reported by Salvi et al. (2020) calculated using Pecube thermokinematic inverse modeling. This modeling incorporated a best-fit fault geometry and apatite fission track, ZHe, and biotite $^{40}Ar/^{39}Ar$ ages. Because a Pecube-derived temperature-depth profile reported by Salvi et al. (2020) displays geotherm deflection due to rock advection, our exhumation rates represent maximum estimates and characterization of the geothermal gradient requires careful attention. Nevertheless, our results suggest high, concentrated exhumation associated with a ramp-flat fault along the Lalpani thrust.

Our findings from samples in the hinterland suggest exhumation continues through more recent million-year to modern timescales with exhumation concentrated near the Lohit thrust. These results are

generally consistent with out-of-sequence thrusting of the Lohit thrust between ~11-6 Ma inferred by Haproff et al. (2020) using ZHe ages. Many plausible T-t histories for sample aPH-1-8-13-8 suggest rapid cooling and exhumation until ~5-2 Ma before continuing at a slower rate (Fig. 4.4c). Of these histories, certain scenarios indicate near deactivation of the fault by ~3-2 Ma. However, other plausible histories suggest steady exhumation rates over the last 10 Ma. Assuming a simplified geothermal gradient of 25°C/km, exhumation along the Lohit thrust could have reached ~0.5 mm/yr over the last Ma. Additional AHe grain measurements with differing eU or R_S characteristics may help elucidate protracted or rapid cooling near the AHe partial retention zone and thus, at recent timescales where cooling rates remain unclear. Nevertheless, earthquake occurrence data compiled between 1970-2023 and GPS velocities spanning 1999-2011 (Ge et al., 2015; Incorporated Research Institutions for Seismology, www.iris.edu) indicate modern tectonic activity in the hinterland near the Lohit thrust. Conversely, plausible T-t histories incorporating aPH-1-8-13-1B further north into the hinterland consistently indicate relatively slow exhumation ($\leq$0.15 mm/yr at 25°C/km) over the last ~8 Ma. This relatively inactive site indicates that potential exhumation may be localized near the Lohit thrust on recent timescales. Our findings allow us to better quantify and understand tectonic activity in the easternmost Himalaya on a timescale more relevant to modern topography and millennial erosion rates.

4.4.2 Comparison of exhumation with other Himalayan regions

Our inferred exhumation rates from the easternmost Himalayan range front are comparable to the highest estimated exhumation rates from the Greater Himalayan Sequence of other regions. Thiede and Ehlers (2013) estimated exhumation rates over the last ~10 Ma with a 1-D Monte Carlo thermal model using compiled apatite and zircon fission track and muscovite $^{40}Ar/^{39}Ar$ ages across the Himalaya. Their findings revealed high exhumation rates near western and central Nepal (~2.0-2.5 mm/yr) and especially high erosion rates near the Nanga Parbat and Namcha Barwa (~3.0 mm/yr) over the last 4 Ma (Bojar et al., 2005; Patel and Carter, 2009; Thiede and Ehlers, 2013). These rates are similar to our estimates of the exhumation rate along the Lalpani thrust over the last ~2-1 Ma. Additionally, the focus of vertical

exhumation in the easternmost Himalaya may differ from that of the rest of the mountain belt over recent million-year timescales. Previous studies from various regions along the Himalaya report high exhumation and Holocene slip rates focused along the Main Frontal and Central thrusts, which marks the southern boundary of the mountain belt and separates the Lesser and Greater Himalayan Sequences, respectively (Powers et al., 1998; Lavé and Avouac, 2000; Kirby and Whipple, 2001; Burbank et al., 2003; Godard et al., 2004; Bojar et al., 2005; Blythe et al., 2007; Srivastava and Misra, 2008; Robert et al., 2009; Srivastava et al., 2009; Thiede et al., 2009; Patel and Carter, 2009; Kumar et al., 2010; Burgess et al., 2012; Herman et al., 2013; Thiede and Ehlers, 2013).

Conversely, the distribution of exhumation in the easternmost Himalaya on recent million-year timescales appears to be unimodal with the highest rates near the Mishmi Thrust or Main Frontal Thrust equivalent. HeFTy thermal modeling of ZHe samples located in the Mayodia gneiss reported by Haproff et al. (2020) suggests exhumation rates along the Tidding thrust or likely Main Central thrust equivalent to be slower (~0-1 mm/yr) relative to those of our range front samples. This difference in location and distribution of concentrated exhumation may be related to the absence of lithological units (i.e. Greater and Tethyan Himalayan Sequences and Southern Gangdese Batholith) and narrower thrust belt in this study area compared to other Himalayan regions. However, further measurements are needed to elucidate recent tectonic activity around the Main Central thrust equivalents of the easternmost Himalaya. These measurements would include additional AHe or apatite fission track ages, which provide information on cooling rates in lower temperature systems than ZHe and thus, over more recent timescales. Nevertheless, the easternmost Himalaya provides a distinctive tectonic setting characterized by high vertical exhumation rates in the range front.

4.4.3 Comparison between spatial patterns of exhumation and millennial erosion rates in the easternmost Himalaya

Coinciding spatial distributions of tectonic activity, millennial erosion rates, and climate forcing suggest a potential link over geologic timescales, but differences in magnitude potentially support

episodic fault slip and relatively transient conditions. Previously reported basin-averaged, millennial erosion rates based on ^{10}Be from along the Dibang Valley correlate with the number of extreme rainfall events and exhibit high rates near the range front (5.0-7.5 mm/yr). These rates decrease rapidly in the hinterland (0.27-0.41 mm/yr) (Shao et al., in review; Bookhagen and Burbank, 2010) (Fig. 4.5). Likewise, our inferred exhumation rates peak in the range front followed by a similar decrease into the hinterland. These nearly overlapping peaks in inferred exhumation rate, millennial erosion rate, and extreme rainfall events in the range front suggest potential interactions among extreme climate, erosion, and tectonics in the easternmost Himalaya over geologic timescales. Although the magnitude of exhumation rates differs from that of millennial erosion rates, differences may be related to the short-term variability of millennial erosion rates in this region. Physical and numerical experiments suggest that the growth and adjustment of an orogenic wedge may occur through episodic slip along faults (Cruz et al., 2010). These brief episodes on geologic timescales may not be fully captured by the averaging effects of even low-temperature-sensitive thermochronometers, such as AHe, and subsequent thermal modeling. Conversely, the timescale captured by millennial erosion rates is likely relatively short compared to those of these episodes, which may explain modern topographic steady-state conditions (Shao et al., in review). Spatially coinciding zones of high degrees of rainfall, millennial erosion, and exhumation across a topographically steady-state landscape suggest a potential link between tectonics, climate, and erosion in the region.

4.5 Limitations and Future Work

Our findings contribute to an improved understanding of the spatial distribution and magnitude of exhumation in the easternmost Himalayan over recent million-year timescales. Additionally, our inferred exhumation rates provide geological context for rapid, unsustainable millennial erosion rates observed in our study area (Shao et al., in review). However, we acknowledge the need for additional AHe or apatite fission track samples sensitive to low-temperature systems across the active range front. Additional samples might be located in the Mayodia gneiss near the Demwe thrust, Lalpani schist on the Hunli

duplex, and the Tidding/Mayodia mélange complex near the Tidding thrust. Expanding out dataset may improve constraints on the timing and degree of activity along these various faults, which elucidates the zone of high exhumation in the range front and activity of the MCT equivalent in the region. Additionally, our simplified geothermal gradient requires better constraints, especially for the rapidly exhuming range front, for more accurate and reliable exhumation rate estimates. Future work will include Pecube thermokinematic modeling, which offers a better understanding of the geothermal gradient and subsurface temperature field that can be used alongside plausible T-t histories from our HeFTy thermal modeling (Braun, 2003). Furthermore, we plan to expand our analyses of plausible T-t histories to include thermal modeling by QTQt. Unlike HeFTy, which employs a Monte Carlo algorithm and statistical hypothesis tests that encounter issues when datasets are sufficiently large or precise, QTQt uses a Bayesian Markov Chain Monte Carlo algorithm that improves performance with increasing sample size (Gallagher, 2012; Vermeesch and Tian, 2014). By expanding our dataset along with additional thermal modeling, we can further assess the relationships among million-year exhumation rates, millennial erosion rates, and climate and tectonic forcing in the easternmost Himalaya.

4.6 Figures

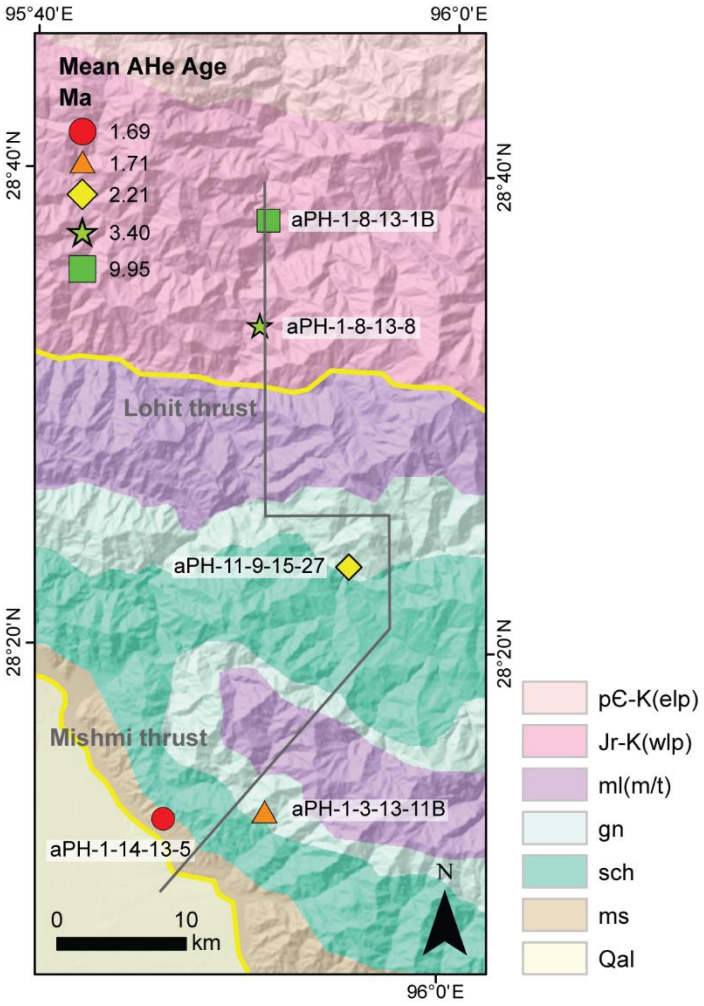

Fig. 4.1: Apatite (U-Th-Sm)/He (AHe) sample locations and mean ages. All ages displayed are average AHe ages except for aPH-11-9-15-27, which displays the lowest grain age. Symbol shapes correspond to different samples. The grey line represents the approximate location of the cross-section transect presented in Fig. 4.2. Lithologic boundaries and fault traces are reported in Haproff et al. (2019). Individual grain ages are reported in Table C1. Abbreviations: Qal – quaternary alluvium; ms – Sewak unit; sch – Lalpani schist; gn – Mayodia gneiss; ml(m/t) – Tidding/Mayodia mélange complex; Jr-K(wlp) – Western Lohit Plutonic Complex; pЄ-K(elp) – Eastern Lohit Plutonic Complex.

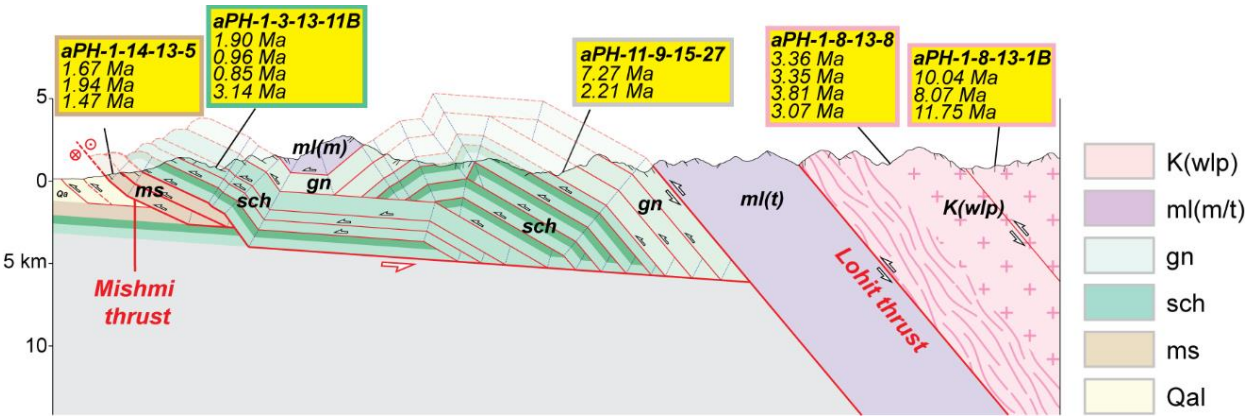

Fig. 4.2: Apatite (U-Th-Sm)/He (AHe) sample locations and grain ages in cross-sectional view. Corrected, individual grain ages and characteristics are reported in Table C1. Adapted from Haproff et al. (2020). Abbreviations: Qal – quaternary alluvium; ms – Sewak unit; sch – Lalpani schist; gn – Mayodia gneiss; ml(m/t) – Tidding/Mayodia mélange complex; K(wlp) – Western Lohit Plutonic Complex.

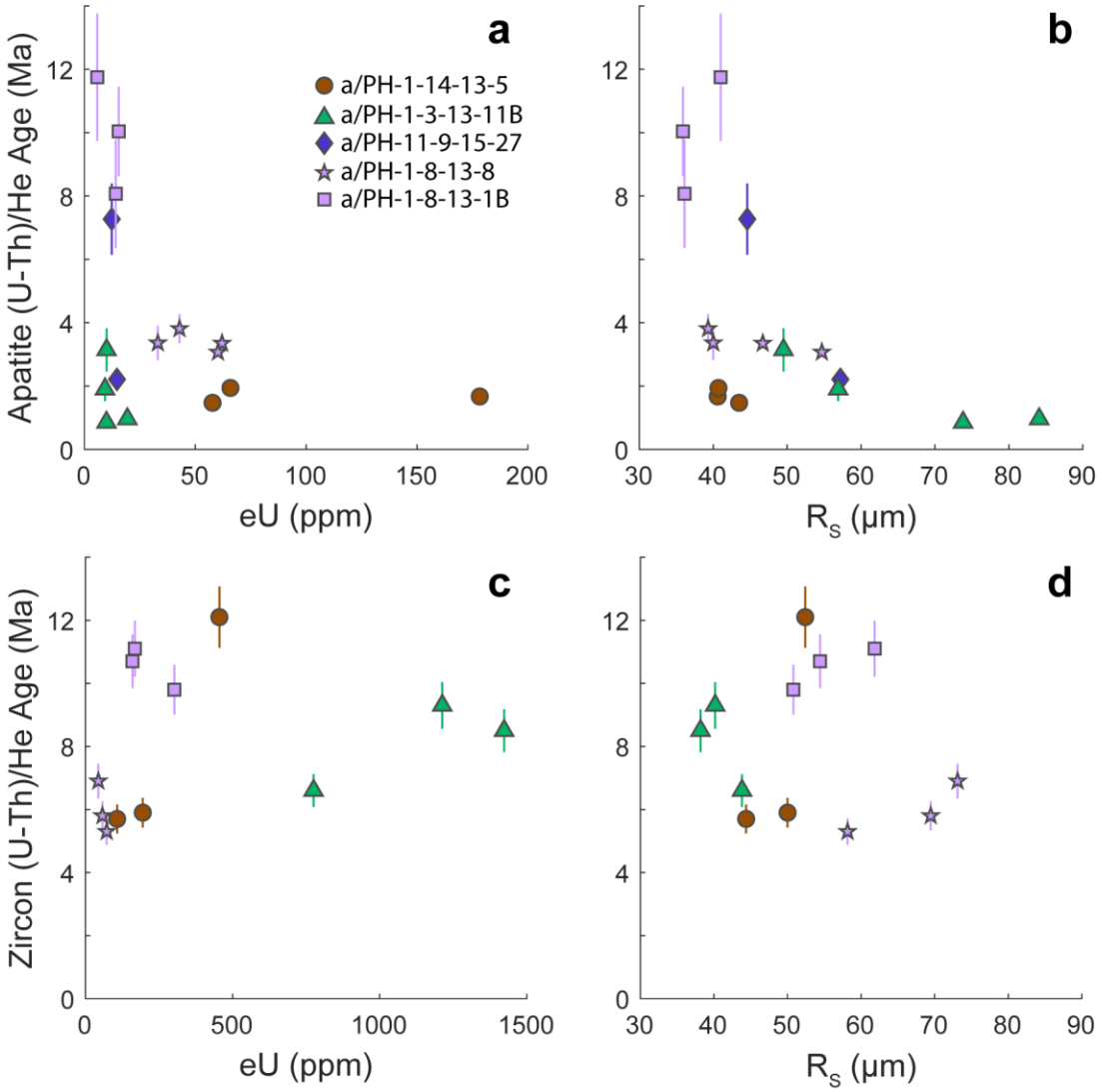

Fig. 4.3: Relationship between single grain apatite and zircon (U-Th-Sm)/He ages and effective uranium (eU) concentration and equivalent spherical radius (R_S). Zircon (U-Th-Sm)/He ages are reported by Haproff et al., (2020). Error bars show ±1σ analytical uncertainty for apatite grains and 8% standard errors (±2σ) based on reproducibility of the Fish Canyon Tuff standard (Reiners et al., 2002). Symbols and colors correspond to different samples with multiple grains per sample. Further details regarding grain measurements are presented in Table C1.

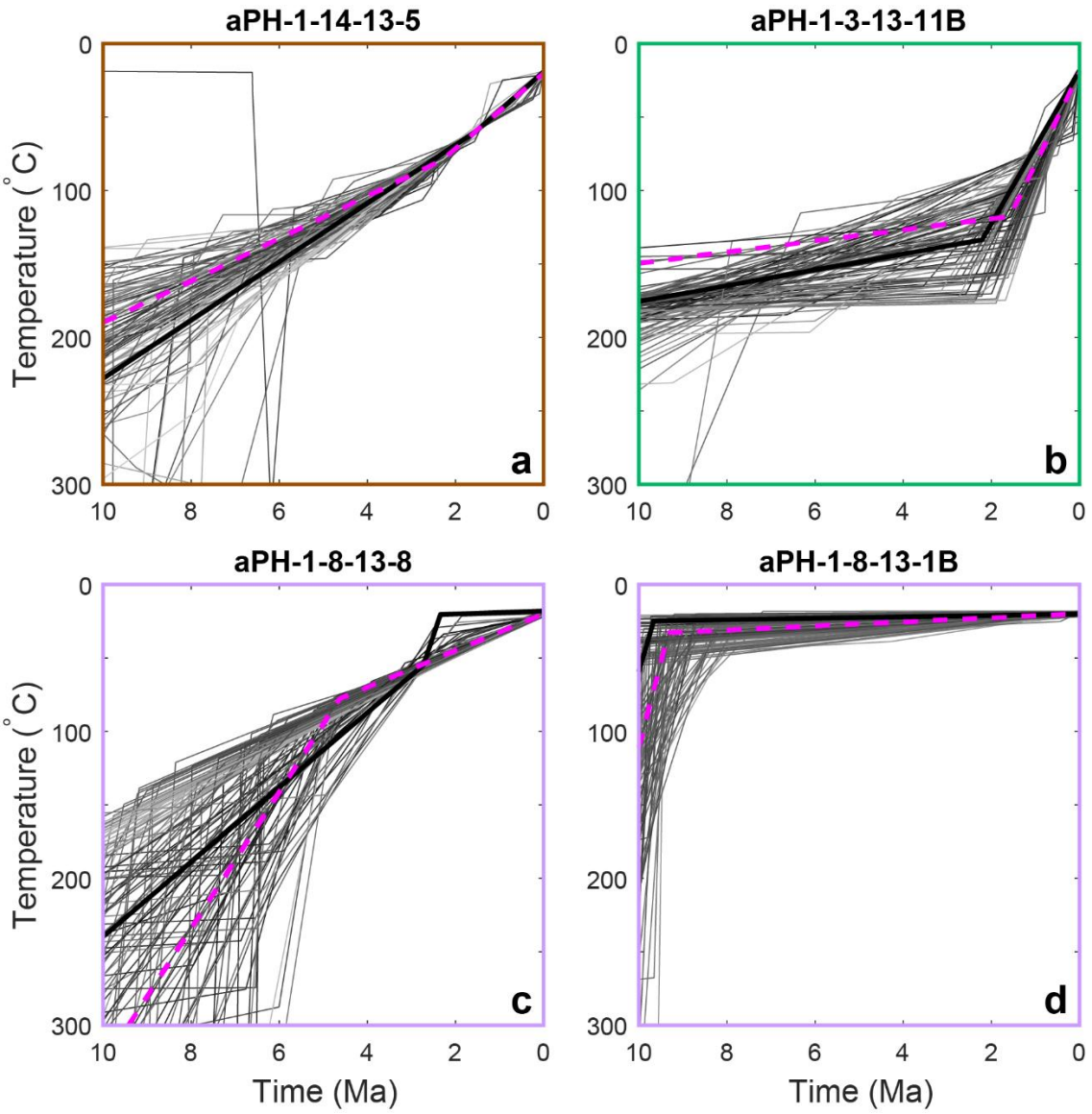

Fig. 4.4: HeFTy inverse-modeled T-t histories for our four apatite (U-Th-Sm)/He samples. Samples in brown (a) and green (b) borders are located in the Sewak unit and Lalpani schist near the range front, respectively. Those in purple border (c, d) are located in the hinterland north of the Lohit thrust in the Western Lohit Plutonic Complex. 100 acceptable fits (goodness of fit >0.05) were calculated for each sample and the scenario with the best goodness of fit value is marked in a thick, black line. Weighted mean paths are shown in magenta dashed lines. Weighted mean paths are our preferred path and were used to estimate exhumation rates displayed in Fig. 4.5. T-t paths are colored in grey with darker shades indicating higher goodness of fit than those with lighter shades.

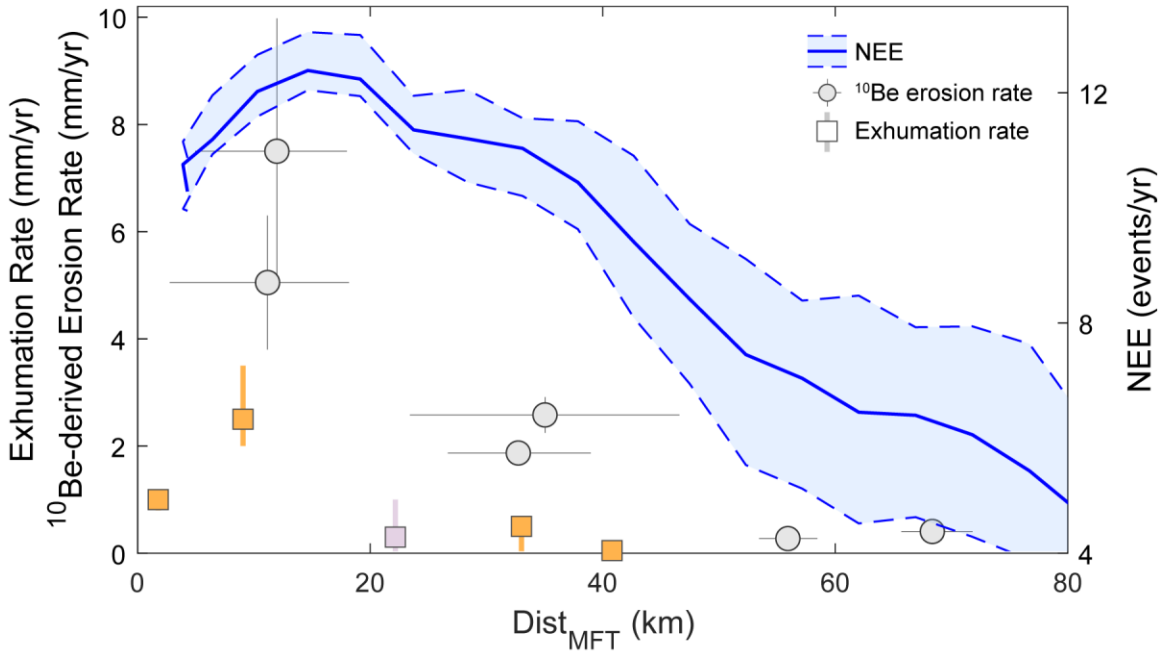

Fig. 4.5: Spatial trends of ^{10}Be-derived millennial erosion rates, inferred exhumation rates, and the number of extreme rainfall events (NEE) with distance from the Main Frontal Thrust (Dist$_{MFT}$). Exhumation rates are maximum estimates inferred from HeFTy inverse modeled T-t histories over the last 2-1 Ma assuming a simplified geothermal gradient of 25°C/km. Squares represent exhumation rates calculated using the weighted mean T-t history. Orange squares represent rates calculated for T-t histories reported in this study while the purple square represents the rate estimated using the preferred T-t history of ZHe sample PH-1-8-13-26 reported by Haproff et al. (2020). Exhumation rate error bars are inferred exhumation rate estimates based on the fastest and slowest cooling scenarios over the last ~2-1 Ma determined using HeFTy. ^{10}Be-derived millennial erosion rates (±1σ) are reported in Shao et al. (in review). NEE was extracted from an across-strike swath with a profile width of 100 km and 5 km transverse and longitudinal sampling distances (Bookhagen and Burbank, 2010). Blue-shaded areas represent ±1σ ranges in NEE across the width of the swath.

4.7 References

Blythe, A.E., Burbank, D.W., Carter, A., Schmidt, K., and Putkonen, J., 2007, Plio-Quaternary exhumation history of the central Nepalese Himalaya: 1. Apatite and zircon fission track and apatite [U-Th]/He analyses: Tectonics, v. 26, doi:10.1029/2006TC001990.

Bojar, A.V., Fritz, H., Nicolescu, S., Bregar, M., and Gupta, R.P., 2005, Timing and mechanisms of Central Himalayan exhumation: Discriminating between tectonic and erosion processes: Terra Nova, v. 17, p. 427–433, doi:10.1111/j.1365-3121.2005.00629.x.

Bookhagen, B., and Burbank, D.W., 2010, Toward a complete Himalayan hydrological budget: Spatiotemporal distribution of snowmelt and rainfall and their impact on river discharge: Journal of Geophysical Research: Earth Surface, v. 115, doi:10.1029/2009JF001426.

Braun, J., 2003, Pecube: A new finite-element code to solve the 3D heat transport equation including the effects of a time-varying, finite amplitude surface topography: Computers and Geosciences, v. 29, p. 787–794, doi:10.1016/S0098-3004(03)00052-9.

Burbank, D.W., Blythe, A.E., Putkonen, J., Pratt-Sitaula, B., Gabet, E., Oskin, M., Barros, A., and Ojha, T.P., 2003, Decoupling of erosion and precipitation in the Himalayas: Nature, v. 426, p. 652–655.

Burgess, W.P., Yin, A., Dubey, C.S., Shen, Z.K., and Kelty, T.K., 2012, Holocene shortening across the main frontal thrust zone in the eastern Himalaya: Earth and Planetary Science Letters, v. 357–358, p. 152–167, doi:10.1016/j.epsl.2012.09.040.

Cruz, L., Malinski, J., Wilson, A., Take, W.A., and Hilley, G., 2010, Erosional control of the kinematics and geometry of fold-and-thrust belts imaged in a physical and numerical sandbox: Journal of Geophysical Research: Solid Earth, v. 115, doi:10.1029/2010JB007472.

Dodson, M.I., 1973, Closure Temperature in Cooling Geochronological and Petrological Systems: Springer-Verlag.

Ehlers, T.A., and Farley, K.A., 2003, Apatite (U-Th)/He thermochronometry: methods and applications to problems in tectonic and surface processes: Earth and Planetary Science Letters, v. 206, p. 1–14, www.elsevier.com/locate/epsl.

Farley, K.A., 2000, Helium diffusion from apatite: General behavior as illustrated by Durango fluorapatite: Journal of Geophysical Research: Solid Earth, v. 105, p. 2903–2914, doi:10.1029/1999jb900348.

Flowers, R.M., Ketcham, R.A., Shuster, D.L., and Farley, K.A., 2009, Apatite (U-Th)/He thermochronometry using a radiation damage accumulation and annealing model: Geochimica et Cosmochimica Acta, v. 73, p. 2347–2365, doi:10.1016/j.gca.2009.01.015.

Gallagher, K., 2012, Transdimensional inverse thermal history modeling for quantitative thermochronology: Journal of Geophysical Research: Solid Earth, v. 117, doi:10.1029/2011JB008825.

Ge, W.P., Molnar, P., Shen, Z.K., and Li, Q., 2015, Present-day crustal thinning in the southern and northern Tibetan Plateau revealed by GPS measurements: Geophysical Research Letters, v. 42, p. 5227–5235, doi:10.1002/2015GL064347.

Godard, V., Cattin, R., and Lavé, J., 2004, Numerical modeling of mountain building: Interplay between erosion law and crustal rheology: Geophysical Research Letters, v. 31, p. 1–5, doi:10.1029/2004GL021006.

Haproff, P.J., Odlum, M.L., Zuza, A. V., Yin, A., and Stockli, D.F., 2020, Structural and Thermochronologic Constraints on the Cenozoic Tectonic Development of the Northern Indo-Burma Ranges: Tectonics, v. 39, doi:10.1029/2020TC006231.

Haproff, P.J., Zuza, A. V., Yin, A., Harrison, T.M., Manning, C.E., Dubey, C.S., Ding, L., Wu, C., and Chen, J., 2019, Geologic framework of the northern Indo-Burma Ranges and lateral correlation of Himalayan-Tibetan lithologic units across the eastern Himalayan syntaxis: Geosphere, v. 15, p. 856–881, doi:10.1130/GES02054.1.

Herman, F., Seward, D., Valla, P.G., Carter, A., Kohn, B., Willett, S.D., and Ehlers, T.A., 2013, Worldwide acceleration of mountain erosion under a cooling climate: Nature, v. 504, p. 423–426, doi:10.1038/nature12877.

Ketcham, R.A., 2005, Forward and inverse modeling of low-temperature thermochronometry data: Reviews in Mineralogy and Geochemistry, v. 58, p. 275–314, doi:10.2138/rmg.2005.58.11.

Ketcham, R.A., Gautheron, C., and Tassan-Got, L., 2011, Accounting for long alpha-particle stopping distances in (U-Th-Sm)/He geochronology: Refinement of the baseline case: Geochimica et Cosmochimica Acta, v. 75, p. 7779–7791, doi:10.1016/j.gca.2011.10.011.

Kirby, E., and Whipple, K., 2001, Quantifying differential rock-uplift rates via stream profile analysis:, https://pubs.geoscienceworld.org/gsa/geology/article-pdf/29/5/415/3521633/i0091-7613-29-5-415.pdf.

Kumar, S., Wesnousky, S.G., Jayangondaperumal, R., Nakata, T., Kumahara, Y., and Singh, V., 2010, Paleoseismological evidence of surface faulting along the northeastern Himalayan front, India: Timing, size, and spatial extent of great earthquakes: Journal of Geophysical Research: Solid Earth, v. 115, doi:10.1029/2009JB006789.

Lavé, J., and Avouac, J.P., 2000, Active folding of fluvial terraces across the Siwaliks Hills, Himalayas of central Nepal: Journal of Geophysical Research: Solid Earth, v. 105, p. 5735–5770, doi:10.1029/1999JB900292.

Lupker, M. et al., 2017, ^{10}Be systematics in the Tsangpo-Brahmaputra catchment: The cosmogenic nuclide legacy of the eastern Himalayan syntaxis ETH Library Be systematics in the Tsangpo-Brahmaputra catchment: the cosmogenic nuclide legacy of the eastern Himalayan syntaxis: Earth Surf. Dynam, v. 5, p. 429–449, doi:10.3929/ethz-b-000192411.

McDowell, F.W., McIntosh, W.C., and Farley, K.A., 2005, A precise 40Ar-39Ar reference age for the Durango apatite (U-Th)/He and fission-track dating standard: Chemical Geology, v. 214, p. 249–263, doi:10.1016/j.chemgeo.2004.10.002.

Ningthoujam, P.S., Dubey, C.S., Lolee, L.K., Shukla, D.P., Naorem, S.S., and Singh, S.K., 2014, Tectonic studies and crustal shortening across Easternmost Arunachal Himalaya: Journal of Asian Earth Sciences, v. 111, p. 339–349, doi:10.1016/j.jseaes.2015.07.003.

Patel, R.C., and Carter, A., 2009, Exhumation history of the higher Himalayan Crystalline along Dhauliganga-Goriganga river valleys, NW India: New constraints from fission track analysis: Tectonics, v. 28, doi:10.1029/2008TC002373.

Powers, P.M., Lillie, R.J., and Yeats, R.S., 1998, Structure and shortening of the Kangra and Dehra Dun reentrants, Sub-Himalaya, India: GSA Bulletin, v. 110, p. 1010–1027, http://pubs.geoscienceworld.org/gsa/gsabulletin/article-pdf/110/8/1010/3382932/i0016-7606-110-8-1010.pdf.

Reiners, P.W., and Brandon, M.T., 2006, Using thermochronology to understand orogenic erosion: Annual Review of Earth and Planetary Sciences, v. 34, p. 419–466, doi:10.1146/annurev.earth.34.031405.125202.

Reiners, P.W., and Farley, K.A., 2001, Influence of crystal size on apatite (U-Th)/He thermochronology: an example from the Bighorn Mountains, Wyoming: Earth and Planetary Science Letters, v. 188, p. 413–420, www.elsevier.com/locate/epsl.

Reiners, P.W., Farley, K.A., and Hickes, H.J., 2002, He diffusion and (U-Th)/He thermochronometry of zircon: initial results from Fish Canyon Tuff and Gold Butte: Tectonophysics, v. 349, p. 297–308, www.elsevier.com/locate/tecto.

Robert, X., van der Beek, P., Braun, J., Perry, C., Dubille, M., and Mugnier, J.L., 2009, Assessing quaternary reactivation of the Main Central thrust zone (central Nepal Himalaya): New thermochronologic data and numerical modeling: Geology, v. 37, p. 731–734, doi:10.1130/G25736A.1.

Salvi, D., Mathew, G., Kohn, B., Pande, K., and Borgohain, B., 2020, Thermochronological insights into the thermotectonic evolution of Mishmi hills across the Dibang Valley, NE Himalayan Syntaxis: Journal of Asian Earth Sciences, v. 190, doi:10.1016/j.jseaes.2019.104158.

Shao, K., Moon, S., Li, G.K., Haproff, P.J., Yin, A., Corbett, L.B., Bierman, P.R., Argueta, M.O., and Hidy, A.J. Climate-driven erosion varies with lithology across the Himalaya: In review at Nature Communications.

Shuster, D.L., Flowers, R.M., and Farley, K.A., 2006, The influence of natural radiation damage on helium diffusion kinetics in apatite: Earth and Planetary Science Letters, v. 249, p. 148–161, doi:10.1016/j.epsl.2006.07.028.

Srivastava, P., Bhakuni, S.S., Luirei, K., and Misra, D.K., 2009, Morpho-sedimentary records at the Brahmaputra River exit, NE Himalaya: Climate-tectonic interplay during the Late Pleistocene-Holocene: Journal of Quaternary Science, v. 24, p. 175–188, doi:10.1002/jqs.1190.

Srivastava, P., and Misra, D.K., 2008, Morpho-sedimentary records of active tectonics at the Kameng river exit, NE Himalaya: Geomorphology, v. 96, p. 187–198, doi:10.1016/j.geomorph.2007.07.019.

Thiede, R.C., and Ehlers, T.A., 2013, Large spatial and temporal variations in Himalayan denudation: Earth and Planetary Science Letters, v. 371–372, p. 278–293, doi:10.1016/j.epsl.2013.03.004.

Thiede, R.C., Ehlers, T.A., Bookhagen, B., and Strecker, M.R., 2009, Erosional variability along the northwest Himalaya: Journal of Geophysical Research: Earth Surface, v. 114, doi:10.1029/2008JF001010.

Vermeesch, P., and Tian, Y., 2014, Thermal history modelling: HeFTy vs. QTQt: Earth-Science Reviews, v. 139, p. 279–290, doi:10.1016/j.earscirev.2014.09.010.

Wolf, R.A., Farley, K.A., and Silver, L.T., 1996, Helium diffusion and low-temperature thermochronometry of apatite: Geochimica et Cosmochimica Acta, v. 60, p. 4231–4240, doi:10.1016/S0016-7037(96)00192-5.

Yin, A., 2006, Cenozoic tectonic evolution of the Himalayan orogen as constrained by along-strike variation of structural geometry, exhumation history, and foreland sedimentation: Earth-Science Reviews, v. 76, p. 1–131, doi:10.1016/j.earscirev.2005.05.004.

Chapter 5:

Synthesis

5.1 Summary of findings

This dissertation explores the controls of erosion over decadal and million-year timescales in the easternmost Himalaya and millennial timescales across the Himalaya. I address the need for 1) geological insights into the drivers of landslides over decadal timescales by an interpretable neural network, 2) a clear examination of climatic influences on millennial erosion rates and efficiency by separating for lithology across the Himalaya, and 3) further constraining of recent million-year timescale exhumation rates in the easternmost Himalaya.

Over decadal timescales, landslides appear to be driven by both strong climate-slope couplings and microclimates across three regions of the easternmost Himalaya with varying environmental conditions. Landslides contribute to sediment flux from mountains belts and pose a great natural hazard but are difficult to predict due to the numerous potential triggering factors as well as the shortcomings of current physical and statistical models. I mapped landslide occurrences using satellite imagery, which were ultimately used to train an interpretable superposable neural network (SNN), developed and applied by my colleague, to estimate landslide susceptibility. Model performance was similar to that of a state-of-the-art deep neural network. By exploiting the model's interpretable architecture, I directly observed the contribution of each input feature to landslide susceptibility and determined primary contributing features to landslide occurrence on a local scale. I determined the product of climate metrics and slope to be a ubiquitous top primary feature with hillslope aspect being a recurring primary feature component across all three regions. With future improvements in satellite imagery and digital elevation model resolution, these results can be further updated and refined.

Over millennial timescales, ^{10}Be-derived erosion rates from across the Himalaya correlate with the number of extreme rainfall events in basins dominated by metasedimentary lithology. Additionally,

especially high erosion rates and efficiencies influenced by climate and lithology of basins near the Main Frontal Thrust suggest a link among tectonics, climate, and erosion. ^{10}Be-derived erosion rates from the Himalaya have generally not displayed a correlation with climate metrics, which may be due to the confounding controls of lithology and topography. I measured and analyzed ^{10}Be-derived and landslide-derived erosion rates across 12 new basins in the easternmost Himalaya, a relatively unconstrained region of the mountain belt, to further explore their correlation with environmental metrics. I compiled 161 additional ^{10}Be-derived erosion rates from across the Himalaya and landslide inventories from 13 basins in Nepal and separated basins by dominant metasedimentary or crystalline (south or north of the Main Central Thrust, respectively) lithology. Climate metrics display a clear correlation with erosion rates from basins dominated by metasedimentary lithology that is absent in basins dominated by crystalline lithology. This correlation is tied to the differing responses of hillslope and fluvial erosional efficiency to climate depending on lithology. Landslide metrics for 25 basins from the easternmost and Nepal Himalaya suggest climate-induced landslides may be involved in facilitating efficient fluvial erosion and transport, resulting in high erosion rates and efficiencies in basins dominated by metasedimentary lithology. Although high erosional efficiency in relatively weak, metasedimentary rocks in the range front may support a link between climate-driven erosion and tectonics, erosion rate trends potentially matching that of tectonic forcing or landslide erosion rates reflecting transient signals need further consideration. Nevertheless, our observations of especially high erosional efficiency across the Himalayan range front are robust.

Over recent million-year timescales, concentrated exhumation of the easternmost Himalayan range front spatially coincides with high degrees of rainfall and millennial erosion rates. Although out-of-sequence faulting may have occurred on recent million-year timescales, the timing of fault activity in the easternmost Himalaya over this period has generally remained unconstrained. I measured five apatite (U-Th)/He sample ages from the Dibang Valley and estimate exhumation rates over the last ~2-1 Ma using HeFTy inverse thermal history modeling. My results indicate that exhumation in the range front is highest

along the Lalpani thrust while exhumation in the hinterland is concentrated near the Lohit thrust. These findings potentially support persistent out-of-sequence faulting of the Lohit thrust that continues until the present though at a lower rate than that of the range front. Additionally, high degrees of exhumation, rainfall, and millennial erosion may suggest a connection among tectonics, climate, and erosion in the range front. Further measurements within the active range front of thermochronometers sensitive to low-temperature systems such as apatite would increase the spatial and temporal resolution of current exhumation rate estimates. Additionally, better constraints on the geothermal gradient in the region would yield more accurate and reliable exhumation rate estimates.

My findings presented in this dissertation describe a continuous story of the spatial patterns and controls of short to long-term erosion for each examined timescale in the easternmost Himalaya. I show that a combination of precipitation and steep slope induced by tectonics is a primary factor triggering landslide occurrence over decadal timescales. Although these individual landslides and extreme rainfall events are episodic and ephemeral, recurring events may lead to altered channel properties, such as grain size distribution, whose effects accumulate to influence the erosivity of channels over millennial timescales. Over million-year timescales, this especially high, climate-driven erosional efficiency of relatively weak rocks may influence the evolution and growth of the orogenic wedge, resulting in a link between erosion-induced fault activity and tectonically-driven erosion. However, further investigation is necessary to understand whether processes observed over millennial timescales are representative of those operating over million-year timescales. Nevertheless, my findings indicate that investigating erosion on varying timescales is important to our understanding of the processes involved in landscape evolution shaping the world we see today.

APPENDIX A:

Landslide Susceptibility Modeling by Interpretable Neural Network

Note: This appendix is modified from Youssef, K.*, Shao, K.*, Moon, S., & Bouchard, L. S. (2023). Landslide susceptibility modeling by interpretable neural network. *Communications Earth & Environment*, 4(1), 162. (* co-first authors).

A.1 Appendix Note A1: Construction and Performance Assessments of Models

We evaluated the performance of the SNN compared to traditional approaches using several performance metrics including the area under the receiver operating characteristic curve (AUROC), accuracy, sensitivity (i.e., probability of detection, POD), specificity (i.e., probability of false detection, POFD), and POD-POFD following the literature. See for example (Prakash et al., 2020). AUROC is a cutoff-independent performance criteria while accuracy, POD, and POFD are cutoff-dependent. The AUROC is calculated as the area under a curve created by plotting the true positive rate against the false positive rate at various thresholds along a feature's range. AUROC ranges between 0 and 1, with 1 indicating a perfect classifier and 0.5 indicating a random model. After generating a threshold-modeled landslide map based within the ~30% testing partition using the optimal S_t threshold corresponding to the point closest to [0,1] on an ROC curve, accuracy is calculated as the fraction of landslide and non-landslide area correctly classified by the model relative to all studied areas. POD and POFD measure the proportion of landslide areas correctly classified relative to all observed landslide areas and the proportion of incorrectly classified landslide areas relative to all observed non-landslide areas, respectively.

We calculated these metrics for all 15 single features, a physically-based slope stability model (SHALSTAB), two statistical methods (logistic regression and likelihood ratios), and Level-1 and Level-

2 SNNs. First, we investigated each of the 15 single features as individual classifiers for landslide occurrences (Table A3). Second, we assessed the propensity of landslides using a topographic metric called the failure index. The failure index (*FI*) is the ratio of driving to resisting forces on a hillslope, which is the inverse of the factor-of-safety. *FI* is modified from SHALSTAB, which couples infinite slope stability and steady-state hydrology for a cohesionless material (Dietrich et al., 1995, 2001; Moon et al., 2011; Huang and Montgomery, 2014). Considering that landslides smaller than 100,000 m^2 (the upper bound for soil landslides found from global and Himalayan landslide compilations (Larsen et al., 2010; Larsen and Montgomery, 2012)) constitute >99% of landslides in number and ~80% of total landslide area, we assumed that most landslides in our inventory are soil landslides.

To calculate the *FI*, we first determined the spatial distribution of wetness (*W*), which represents the degree of subsurface saturation. *W* is calculated as the ratio between local hydraulic flux from a given steady-state precipitation relative to that of soil profile saturation (Montgomery and Dietrich, 1994):

$$W = \frac{h}{z} = \frac{qA}{bTsin\theta} \qquad Eq.\ 1$$

where h is the saturated height of the soil column (L), z is the total height of the soil column (L), q is the steady-state precipitation during a storm event (L/T), A is the drainage area (L^2) draining across the contour length b (L), T is the soil transmissivity when saturated (L^2/T), and θ is the local slope in degrees. W varies from 0 (unsaturated) to a capped value of 1 (fully saturated). We used the spatial distribution of *MAP* (Bookhagen and Burbank, 2010) to represent the steady-state precipitation, q. T may vary spatially depending on surface conditions such as depth of soil or weathered rock and hydraulic conductivity (Montgomery et al., 2002). However, we do not have field measurements to constrain the spatial variation of this value. Very high or low T values will result in spatially uniform wetness values of 0 or 1, respectively. Thus, we used a base value of 1×10^{-4} m^2/s for T following Moon et al. (2011), which allowed for a large spatial variation of wetness influenced by precipitation gradient across the area. We then calculated the spatial distribution of *FI* as:

$$FI = \frac{S}{S_0}\left(1 - W\frac{\rho_w}{\rho_s}\right)^{-1} \quad \textit{Eq. 2}$$

where S_0 is the threshold slope set at 45˚, S is the local slope, ρ_s is the wet bulk density of soil (2.0 g/cm^3), and ρ_w is the bulk density of water (1.0 g/cm^3). To examine whether the performance of *FI* is different when predicting all landslides vs soil landslides, we included the performance metric results for *FI* calculated using all landslides and soil landslides in Table A3. Third, we applied two statistical models, logistic regression and likelihood ratios, to assess landslide susceptibility. Logistic regression (hereafter, *LogR*) is based on a multivariate regression between a binary response of landslide occurrence and a set of predicting features that are continuous, discrete, or a combination of both types (Lee, 2005). To build these models, we considered only one curvature metric following (Lee, 2005), instead of using all four different curvatures. We selected $Curv_M$ to build the statistical models. In addition, we considered $\log_{10}$(drainage area) and $\log_{10}$(discharge) because of their inverse power-law relationships with landslide and debris flow incision (Stock and Dietrich, 2003, 2006). The relationship between features and landslide occurrence can be displayed as:

$$p = \frac{e^c}{e^c + 1} \quad \textit{Eq. 3}$$

where p is the probability of landslide occurrence that varies from 0 to 1 in an S-shaped curve, and c is the linear combination of features:

$$c = b_0 + b_1x_1 + b_2x_2 + \ldots + b_nx_n \quad \textit{Eq. 4}$$

where x_i (i = 1, 2, . . ., n) represents each feature, b_i represents the optimized coefficient, and b_0 represents the intercept of the model. Utilizing Eqs. 3 and 4, we obtained an extended expression for the *LogR* model relating the probability of landslide occurrence p and multiple features:

$$logit(p) = log\left(\frac{p}{1-p}\right) = b_0 + b_1x_1 + b_2x_2 + \ldots + b_nx_n \quad \textit{Eq. 5}$$

where log is the natural log. To determine any possible collinearity between features, we calculated the correlation coefficient (R) between all combinations of 12 features (Table A6). We observed maximum

absolute values of R = -0.828 (N-S), 0.717 (NW-SE), and 0.857 (E-W), which are below the threshold of 0.894 corresponding to a variance inflation factor of <5. R below this threshold indicate low collinearity between features (Stine, 1995; Kavzoglu et al., 2014) and thus we used all 12 features. We treated aspect as a discrete feature due to its nonlinear relation with landslide occurrences. The best-fit coefficient values are shown in Table A7.

Similar to the SNN, the *LogR* method provides information about the importance of variables through the best-fit coefficients. To compare those results, we determined top features that differentiate areas with and without threshold-modeled landslides for the N-S region based on the *LogR* output following similar procedures that we used for the SNN. The output of *LogR* ranges between 1.06×10^{-6} to 0.820. The threshold value (t) of 0.005 that corresponds to the point closest to [0,1] on an ROC curve (i.e., a perfect classifier) was used to classify landslide (*ld*) and non-landslide areas (*nld*) for the N-S region. We calculated $\Delta\overline{cn}_j$ as the difference between the average value of a feature multiplied by its respective coefficient for *ld* and *nld* areas, then divided by an adjusted threshold that was transformed from t (i.e., 0.005) from the *LogR* output according to the equation below:

$$\Delta\overline{cn}_i = \frac{\bar{c}_{i,ld} - \bar{c}_{i,nld}}{t_a} \; where \; t_a = \log\left(\frac{t}{1-t}\right) - b_0 \qquad Eq.\ 6$$

where $\bar{c}_{i,a}$ is the average feature (i) value multiplied by its respective coefficient for areas (a) of *ld* or *nld*, and t_a is the adjusted threshold value based on b_0, the overall intercept value determined by the *LogR* model and t, the threshold determined using the ROC curve (i.e., 0.005 for the N-S region). We transformed t to t_a and used it for normalization to enable the direct comparison of results between *LogR* and the SNN. For the SNN-determined primary features, we calculated $\Delta\overline{Sn}_j$ as $\Delta\bar{S}_j$ divided by the threshold that is used to classify landslides (i.e., 0.767 for SNN Level-2 and 0.399 for SNN Level-1 for the N-S region). The value of 1 in both $\overline{Sn}$ and $\overline{cn}$ represents the threshold susceptibility that classifies *ld* and *nld* areas. The results of the identified primary controls of landslides, which induce large differences in average susceptibility between *ld* and *nld* areas, in the N-S region from *LogR*, the SNN Level-1, and the SNN Level-2 are shown in Fig. A10. All methods identified climate-related factors (e.g., *MAP*, *NEE*,

Asp) as primary controls; however, only the SNN Level-2 was able to identify the importance of the composite feature *MAP***Slope*.

The likelihood ratio method uses the relationship between observed landslide occurrences and controlling feature ranges. Previous studies have quantified the ratio of the probability of landslide occurrences within a range of feature values to the probability of non-occurrences or all-occurrences and referred to it as the likelihood ratio, frequency ratio, or probability ratio (Lee, 2005; Akgun, 2012; Reichenbach et al., 2018). In this study, we calculated likelihood ratios (*LR*) as the ratio of the percentage of landslide pixels relative to total landslide pixels divided by the percentage of pixels relative to the total area for a specific range of feature values (Lee, 2005; Akgun, 2012). Landslide susceptibility for each pixel is calculated as the sum of the corresponding *LR* from each feature's value. A ratio of 1 and >1 indicates the average and above-average likelihood of landslide occurrence within the feature range compared to that of the study area. Conversely, values less than 1 indicate a below-average likelihood. In this study, we used all 15 single features with each feature's range divided into ten bins to calculate *LR* and landslide susceptibility. The first and last bins represent areas less than and greater than the 10^{th} and 90^{th} percentile of *LR*, respectively, with values between these bins split into eight equal bin ranges.

We determined 95% confidence intervals of mean AUROC by conducting a 10-fold cross-validation for all statistical and neural network models utilized in this study. We tested the trained model on 50% of the testing dataset that was selected randomly and uniformly. We then calculated the AUROC for each trial. This procedure was repeated 10 times for each method and the results were used to calculate the 95% confidence interval for the mean AUROC and $\pm 2\sigma$ range of AUROC from 10 validation tests (Table A4).

Our model assessments for the single features indicate that *MAP* [AUROC = 0.756 (N-S region)] and slope [AUROC = 0.696 (NW-SE), 0.760 (E-W)] are the highest performing single features. The SNN produces a ~19-22% average improvement in AUROC compared to a physically-based landslide model (e.g., failure index for all landslides or soil landslides). The physically-based model of *FI* produces slightly different AUROC when predicting all landslides vs. soil landslides, but both AUROC values

were lower than that of the SNN (Table A3). Additionally, the SNN produced an average of ~5% and ~8% increases in performance compared to the *LogR* and *LR* methods, respectively. Further investigation using performance metrics including the AUROC, accuracy, POD, POFD, and POD-POFD reveals that the SNN largely outperformed the tested statistical and physically-based models across all metrics (Table A3, A5).

Our implementation of *FI* can be improved by including additional model parameters (e.g., cohesion), calibrating parameters such as soil depth or transmissivity to account for landscape heterogeneities, performing parameter optimizations, or adopting probabilistic approaches in future studies (e.g., (Raia et al., 2014)). To properly calibrate model parameters, we need extensive field measurements, which are not currently available. Without field-calibrated model parameters, physically-based models often yield lower performance compared to data-driven models at a regional scale (e.g., (Yilmaz and Keskin, 2009)).

A.2 Appendix Note A2: Explanation of Aspect as a Microclimate Control

The SNN identified aspect, the direction of slope face, as another primary feature that influences landslide occurrences. Previous studies considered hillslope aspect preference in terms of: 1) vegetation activity that affects root cohesion (McGuire et al., 2016), or 2) the orientation of wind-driven rainfall. To examine vegetation activity across hillslope aspect, we calculated the normalized difference vegetation index (*NDVI*) following the USGS procedure (Ihlen and Zanter, 2019). We first converted Landsat 8 Level-1 Digital Numbers to top-of-atmosphere (TOA) reflectance. TOA reflectance eliminates the impact of different solar angles and illumination geometries and is calculated as:

$$\rho\lambda = \frac{M_\lambda Q_{cal} + A\rho}{cos(\theta_{SZ})} \qquad Eq.\ 7$$

where $\rho\lambda$ is the TOA reflectance, M_λ is the band-specific multiplicative rescaling factor from the Landsat 8 metadata, Q_{cal} are the standard product pixel values, $A\rho$ is the band-specific additive rescaling factor from the metadata, and θ_{SZ} is the local solar zenith angle.

We use the corrected bands 4 and 5 from Landsat 8 to calculate NDVI as:

$$NDVI = \frac{band5 - band4}{band5 + band4} \qquad Eq.\ 8$$

where bands 4 and 5 represent visible and near-infrared light reflected by vegetation, respectively. Healthy vegetation with high photosynthetic capacity absorbs a larger proportion of incident visible light while reflecting a greater portion of near-infrared light compared to sparse or unhealthy vegetation (Tucker et al., 1986). Therefore, an *NDVI* value close to 1 suggests a higher density of healthy vegetation and green leaves while a value near 0 might indicate unhealthy or no vegetation. We utilized Landsat 8 satellite imagery from October 2015, November 2017, and February 2018 ("United States Geological Survey EarthExplorer," 2020) for our analyses of *NDVI*. These months were selected to characterize *NDVI* values before and after the summer monsoon season, during which a large proportion of landslides are suspected to occur because of intense rainfall. We excluded summer months from our analyses because of the abundant cloud cover present in those images, which masks the visibility of the land surface.

NDVI plotted against aspect in our study areas shows a broad distribution of high values centered around values corresponding to south-facing slopes. Field observations indicate fast re-vegetation rates of landslide scars in the easternmost Himalayan region (Shao et al., in review; Larsen and Montgomery, 2012). These rates may in turn suggest high soil production rates especially for south-facing slopes that are exposed to enhanced moisture relative to north-facing slopes. Soil depth exceeding the steady-state depth has been linked with slope instability (Yu et al., 2019), which may provide a plausible mechanism for increased slope failure on south-facing slopes. However, improved understanding of soil production rates and subsurface weathering zones requires further investigation in this region.

Additionally, this *NDVI* distribution is different from the observed peak of S_{Asp} around 145° to 180° (Fig. A9). This result may imply that more landslides on south-facing slopes are likely due to orographic precipitation patterns caused by moisture delivery from the south rather than through the effects of vegetation. In fact, if vegetation root cohesion has a substantial impact on landslide stability, we would expect decreased landslide occurrences in south-facing slopes considering the increased *NDVI*. Previous

work has characterized the northward moisture transfer to this study area from the Bay of Bengal during monsoon seasons (Barros et al., 2004; Bookhagen and Burbank, 2010; Yang et al., 2018). Thus, we believe that the SNN-identified primary feature aspect supports the influence of aspect-related differences in microclimate (e.g., moisture availability) on landslide occurrences in this area.

A.3 Appendix Figures and Tables

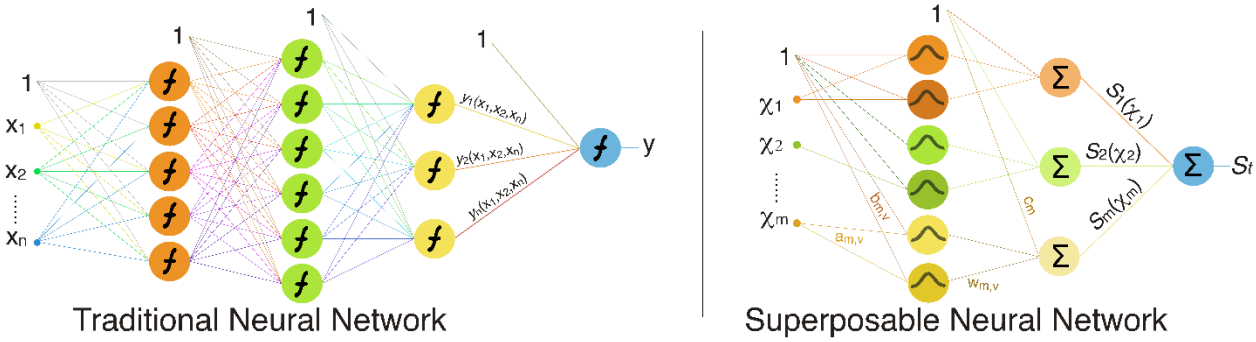

Fig. A1: Conventional DNN architecture vs SNN architecture. In a conventional DNN, features are interconnected and interdependencies are embedded in the network, making them virtually impossible to separate. In an SNN, features and feature interdependencies that contribute to the output are found in advance and explicitly added as independent inputs. Radial basis (Gaussian) activation functions are used in the SNN, where each neuron is connected to one input only. The x_1, x_2, ...x_n refers to a set of *n* original features, and χ_1, χ_2, ...χ_M refers to a set of M composite features. *y* and S_t refer to DNN and SNN outcomes of total susceptibility, respectively. The symbols in this figure are defined and explained in the main text, eq. (1).

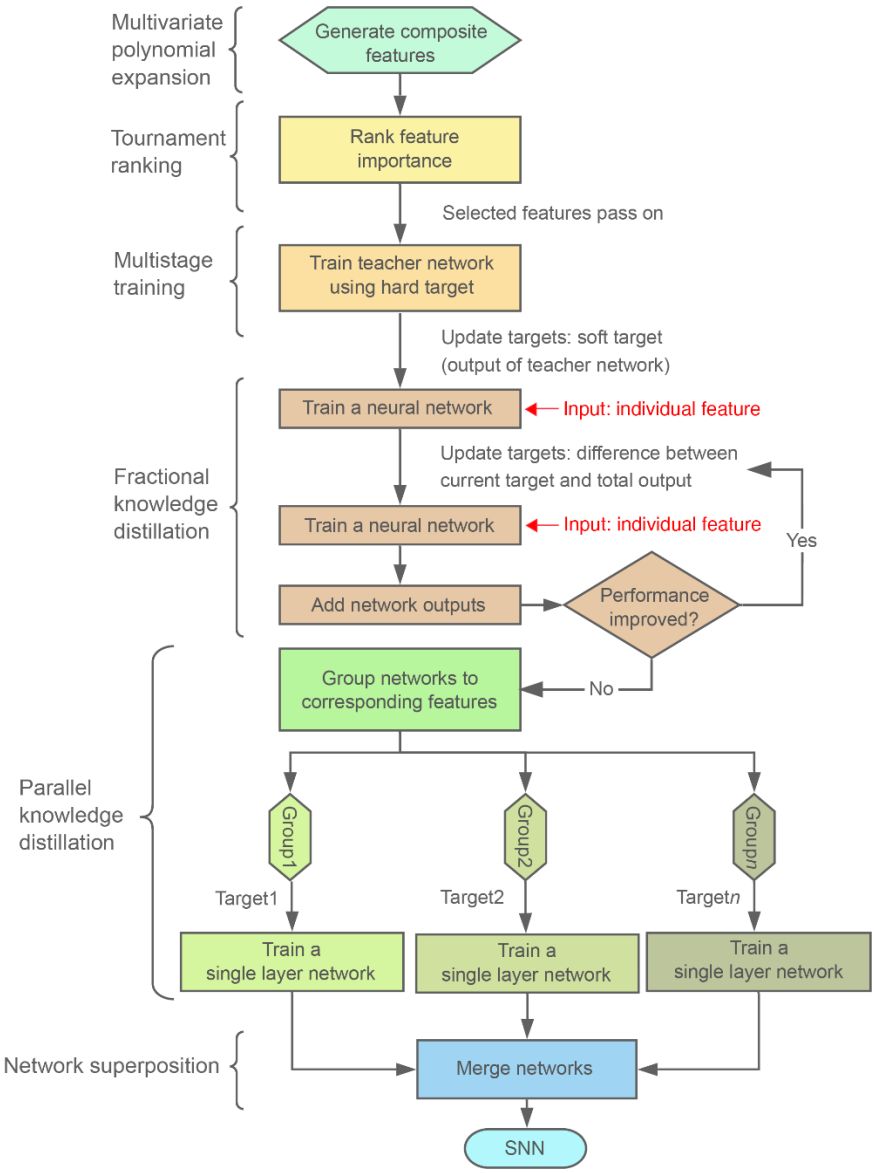

Fig. A2: Superposable neural network training flow diagram. The flow diagram shows the methods used in our study, which include the feature-selection model and multistage training. Our feature-selection model based on multivariate polynomial expansion and tournament ranking allows for the exploration of multiple combinations of parameters without relying on an expert's choices, precondition, or classification of input features and identify a set of optimal composite features that are relevant to the landslide susceptibility. Then, multiple steps of knowledge distillation are used to quantify each control's contribution to susceptibility (S_j, where j corresponds to single layer network). By superposing S_j, we create an additive, superposable neural network (SNN) model for total landslide susceptibility. The details of each methodology are explained in the Methods.

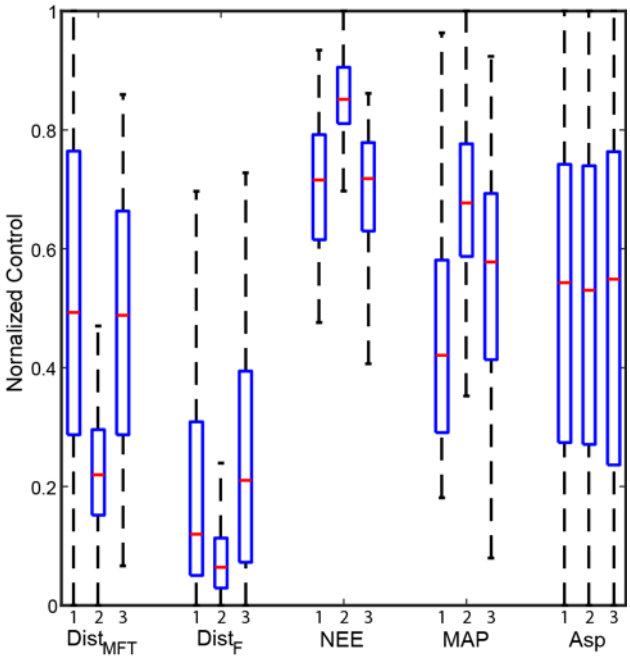

Fig. A3: **Comparison among the feature ranges of our three study regions.** Feature ranges of distance to the Main Frontal Thrust and suture zone ($Dist_{MFT}$), distance to all faults ($Dist_{F}$), number of extreme rainfall events (*NEE*), mean annual precipitation (*MAP*), and aspect (*Asp*), each normalized by the maximum feature value across all three regions. Red center lines represent the median and top and bottom ends of the box represent the 25th and 75th quartiles, respectively. The ends of the dashed lines extending from each side of the box plot represent 1.5 times the interquartile range or the minimum or maximum values. On the *x*-axis, 1, 2, and 3 correspond to the N-S (Dibang), NW-SE (range front), and E-W (Lohit) regions, respectively.

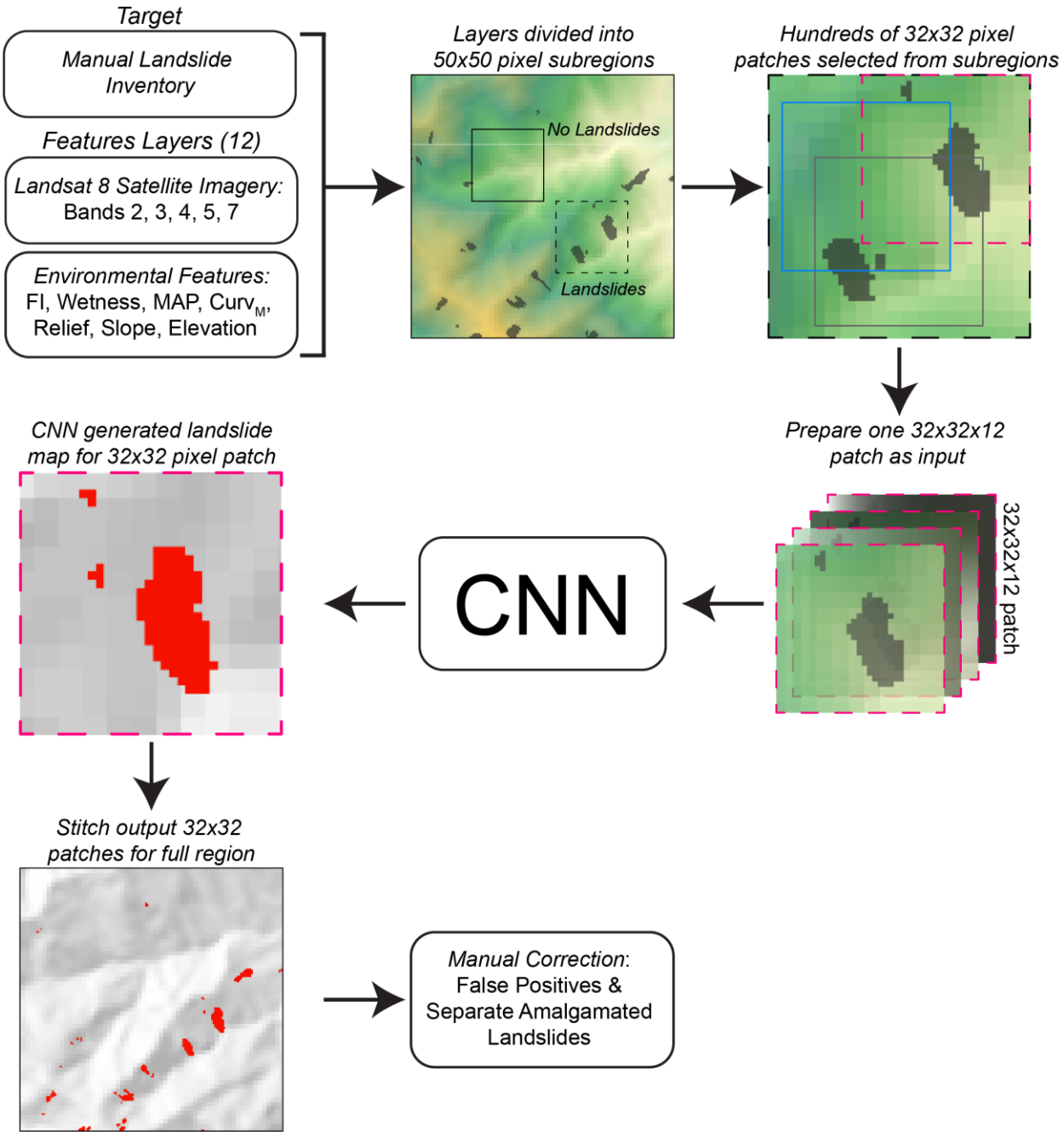

Fig. A4: **Flowchart detailing the semi-automatic landslide mapping procedure**.

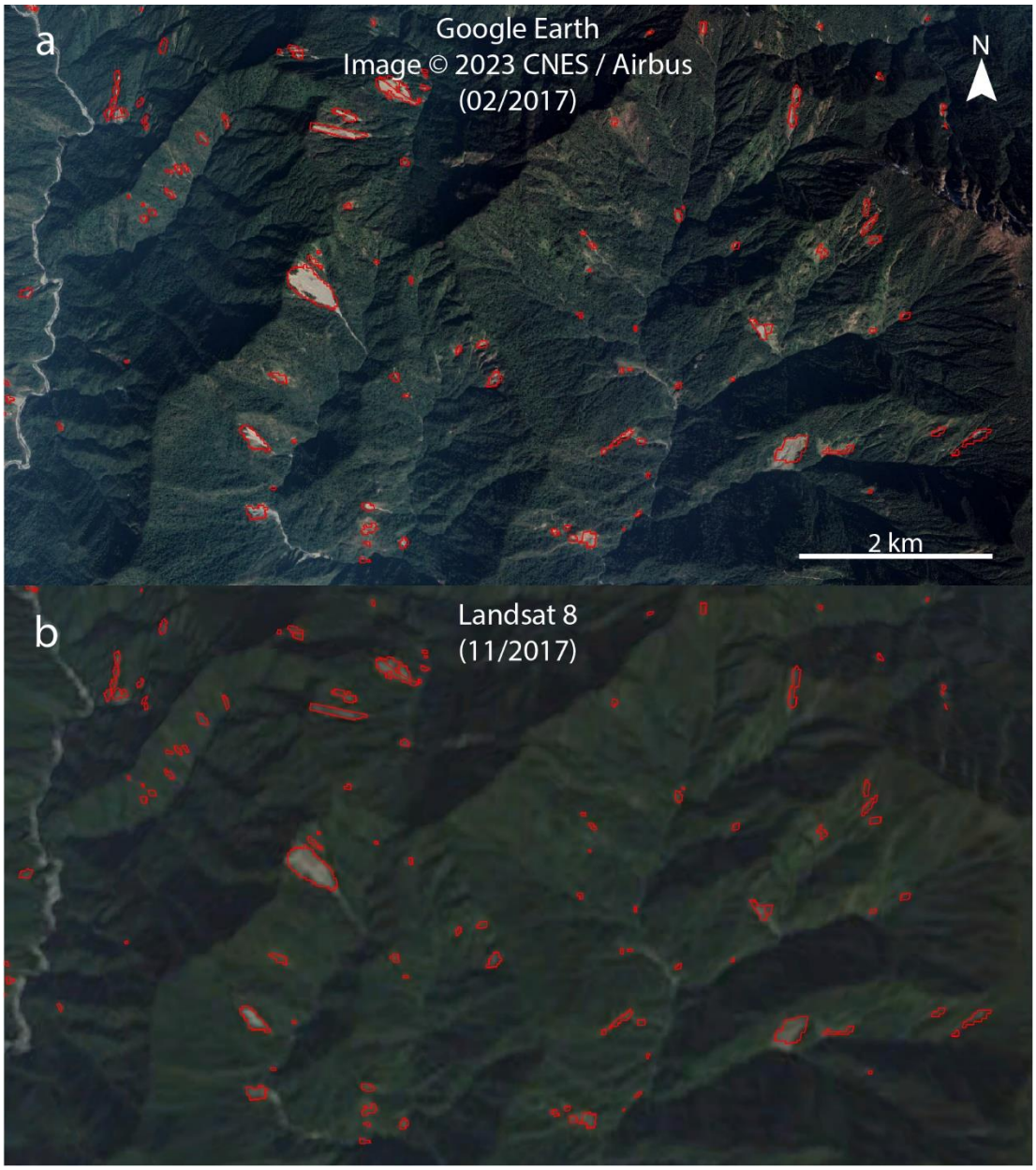

Fig. A5: **Examples of semi-automatically detected landslides.** Mapped landslide polygons from the N-S (Dibang) subregion are shown in red outlines with background images from (a) Google Earth and (b) Landsat 8. Landsat 8 natural imagery is composed of bands 2, 3, and 4, but landslide mapping is based on 5 bands (2, 3, 4, 5, 7) and 7 input features (see Methods).

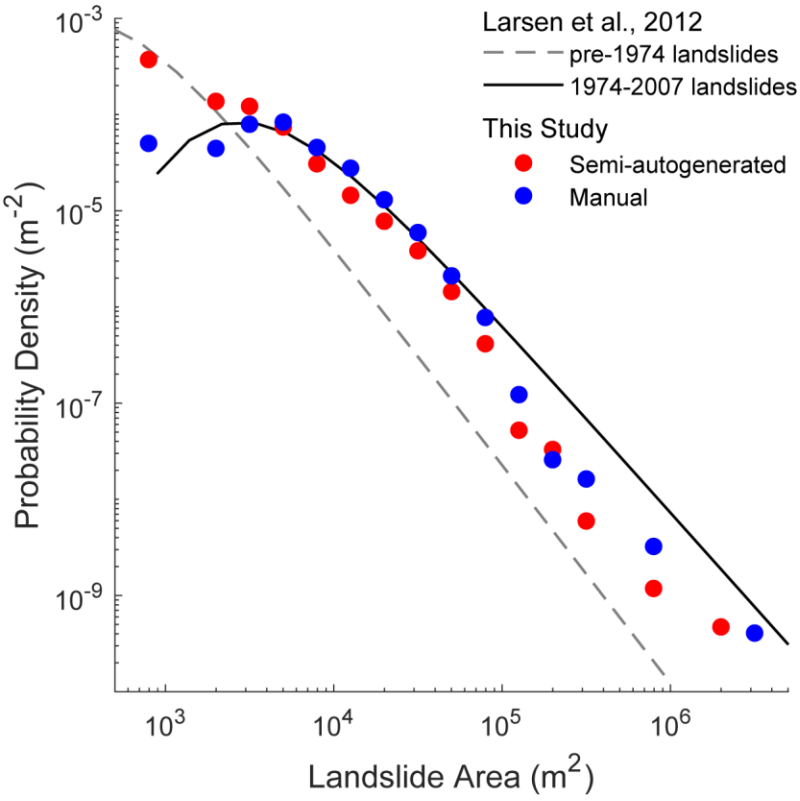

Fig. A6: **Landslide area versus probability density.** The manually and semi-automatically mapped landslides before 2017 from our site are shown in blue and red circles, respectively. For reference, the inverse-gamma fits of the pre-1974 (grey dashed line) and 1974-2007 (black solid line) landslides from the nearby Namche Barwa region in the eastern Himalaya (Larsen et al., 2010; Larsen and Montgomery, 2012) are shown.

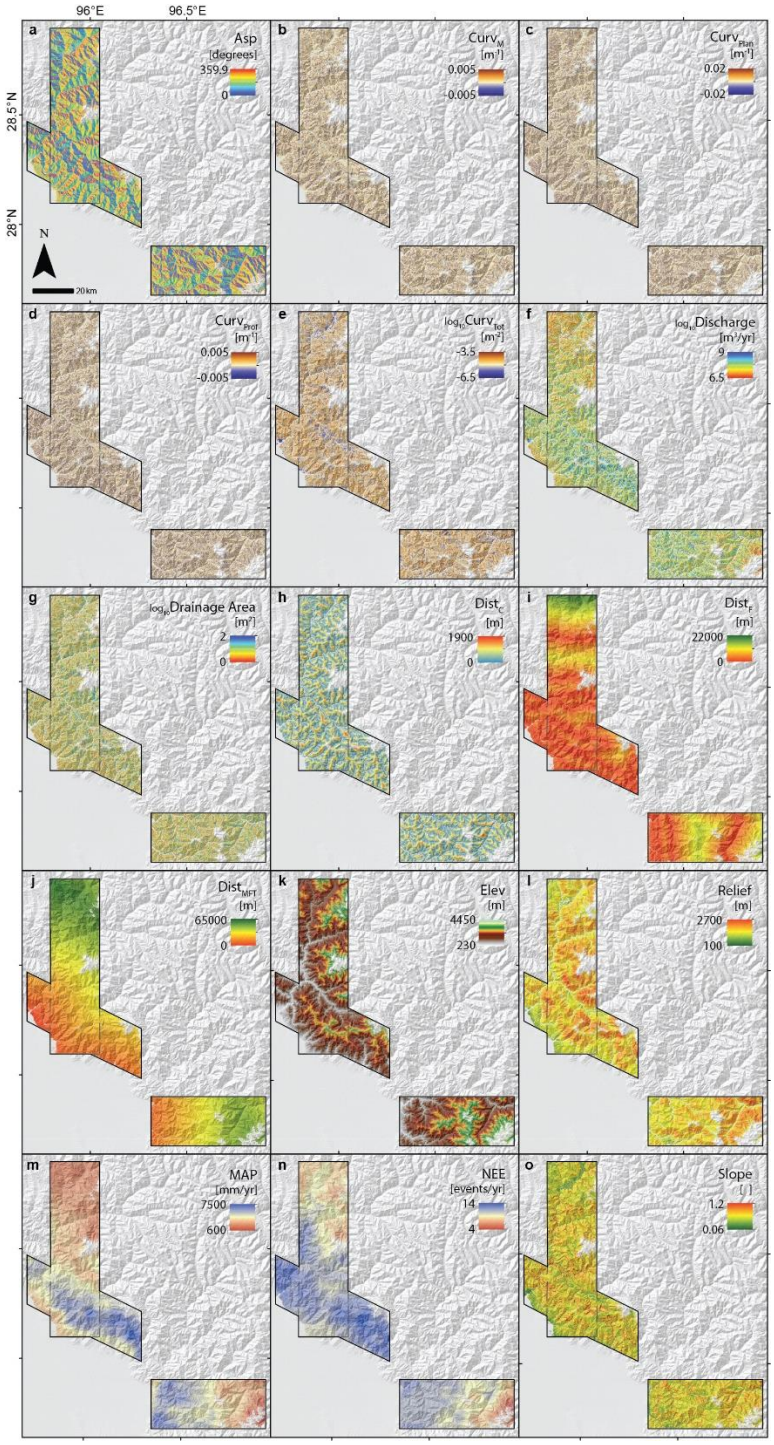

Fig. A7: **Spatial distribution of 15 features used in the superposable neural network model.** The 15 single features include (a) aspect (*Asp*), (b) mean curvature ($Curv_M$), (c) planform curvature ($Curv_{Plan}$), (d) profile curvature ($Curv_{Prof}$), (e) total curvature ($Curv_{Tot}$), (f) discharge, (g) drainage area, (h) distance to channel ($Dist_C$), (i) distance to faults ($Dist_F$), (j) distance to the Main Frontal Thrust and suture zone ($Dist_{MFT}$), (k) elevation (*Elev*), (l) local relief (*Relief*), (m) mean annual precipitation (*MAP*), (n) number of extreme rainfall events (*NEE*), and (o) slope. Dashed lines mark the overlapping area between the N-S (Dibang) and NW-SE (range front) regions. Features in (e, f, g) are displayed on logarithmic scales.

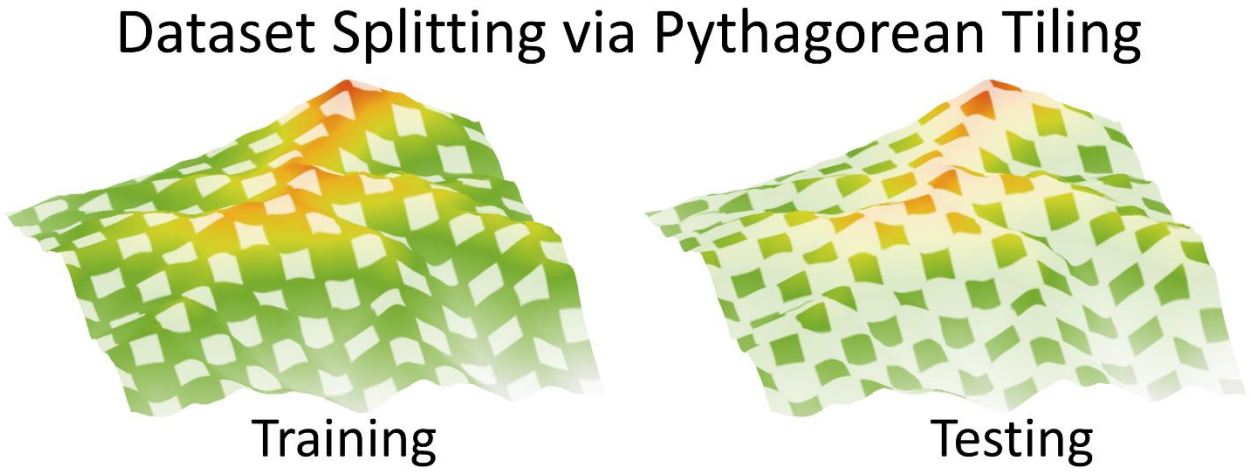

Fig. A8: Illustration of spatial data partitioning using Pythagorean tiling. Pythagorean tiling is used to divide data from the modeled region in a spatially representative manner that maintains variability between training and testing partitions. Using Pythagorean tiling, we generate a checkerboard-like pattern with a 70/30% square ratio, where bigger squares correspond to training and smaller squares correspond to testing.

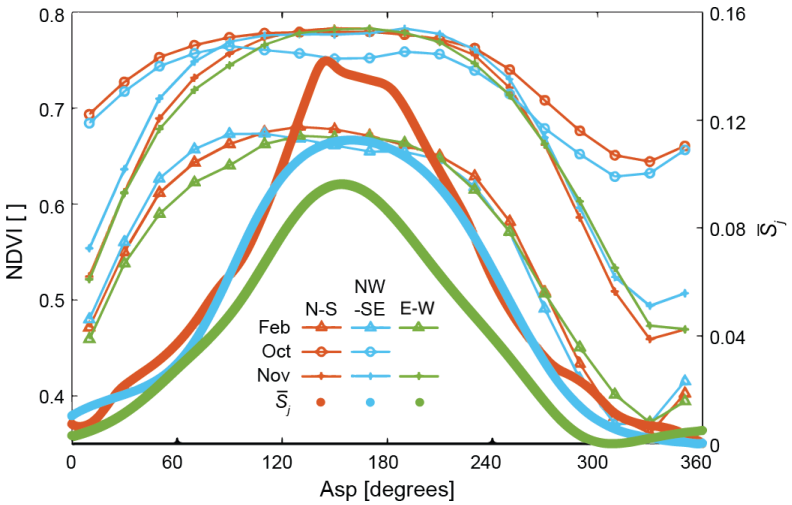

Fig. A9: **The relationship among aspect, normalized difference vegetation index, and S_{Asp}.** The normalized difference vegetation index (*NDVI*) is shown in thin lines and S_{Asp} from SNN Level-1 is shown in thick lines. Colors correspond to different regions while symbols shown as thin lines correspond to different times of measurement (October 2015, November 2017, and February 2018). Symbols on thin lines represent the averaged *NDVI* value for a 20° interval of aspect. N-S (Dibang), NW-SE (range front), E-W (Lohit).

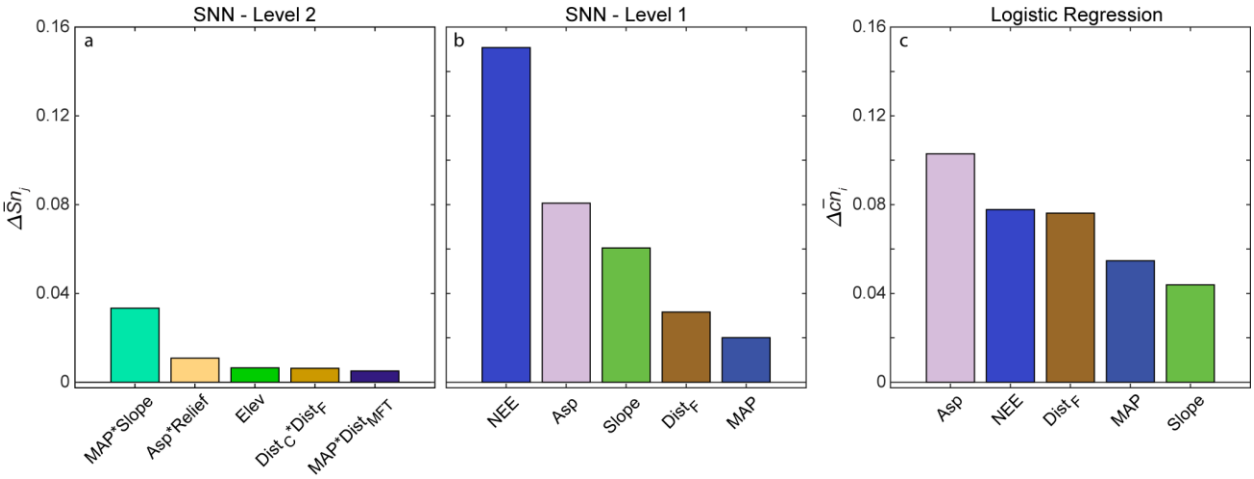

Fig. A10: **Bar charts representing $\Delta\overline{Sn}_j$ from different methods.** $\Delta\overline{Sn}_j$ from the (a) SNN Level-2 and (b) SNN Level-1 and $\Delta\overline{cn}_j$ for (c) logistic regression for the N-S region, arranged in descending order. Details on the calculations of $\Delta\overline{Sn}_j$ and $\Delta\overline{cn}_j$ are provided in Appendix Note 2. Features related to topography, aspect, climate, and geology are shown in green, pink, blue, and brown or combinations thereof, respectively. Mean annual precipitation (*MAP*), number of extreme rainfall events (*NEE*), aspect (*Asp*), elevation (*Elev)*, mean curvature ($Curv_M$), distances to channel ($Dist_C$), all faults ($Dist_F$), and the Main Frontal Thrust and suture zone ($Dist_{MFT}$), and local relief (*Relief*). The asterisk * indicates algebraic multiplication of two features.

Mapping Methods	N-S		NW-SE		E-W		Overall	
	Semi-automatically	Manually	Semi-automatically	Manually	Semi-automatically	Manually	Semi-automatically	Manually
Total Study Area (m^2)	2.09E+09		1.38E+09		1.34E+09		4.19E+09	
Number of Landslides	959	763	1536	1154	386	267	2289	1673
Total Landslide Area (m^2)	9.43E+06	1.24E+07	2.12E+07	2.46E+07	3.68E+06	4.07E+06	2.83E+07	3.31E+07
Areal Density	0.005	0.006	0.015	0.018	0.003	0.003	0.007	0.008
% of Total Landslide Area from Landslides with Area Greater than 10^5 m^2	12.2	16.2	21.6	29.2	9.7	11.1	19.7	25.8
Number of Landslides with Area >10^5 m^2	6	8	13	19	2	2	18	23
% of Total Landslide Area from Landslides with Area of 3600 m^2 (4 pixels) or Less	10.6	3.0	6.2	1.9	10.2	4.1	7.5	2.3

Table A1: Description of Landslide Inventory.

Name	Abbreviation	Units	N-S: Minimum	N-S: Maximum	NW-SE: Minimum	NW-SE: Maximum	E-W: Minimum	E-W: Maximum	Description	Reference
Aspect	Asp	Degrees	0	359.99	0	359.99	0	359.99	Aspect as the direction of slope faces. 0 and 180 represent north- and south-facing slopes, respectively.	Schwanghart and Scherler, 2014
Curvature (Mean)	$Curv_M$	m^{-1}	-0.012	0.010	-0.016	0.010	-0.011	0.009	Curvature for the average of principal curvatures.	
Curvature (Planform)	$Curv_{Plan}$	m^{-1}	-7.4	8.7	-7.4	4.8	-2.5	2.6	Curvature perpendicular to slope gradient.	Shary, 1995
Curvature (Profile)	$Curv_{Prof}$	m^{-1}	-0.037	0.034	-0.062	0.034	-0.047	0.030	Curvature in the direction of the greatest rate of change of slope gradient.	
Curvature (Total)	$Curv_{Tot}$	m^{-2}	4.2E-10	4.3E-03	1.9E-10	5.8E-03	4.6E-10	4.5E-03	Curvature of the surface itself instead of a line across the surface.	Wilson and Gallant, 2000
Discharge	Discharge	m^3/yr	1.2E+06	1.8E+13	2.4E+06	2.0E+13	5.4E+05	2.4E+13	Amount of water from upstream areas considering spatially varying mean annual precipitation. The calculation is based on a D8 flow direction.	Schwanghart and Scherler, 2014
Distance to Channel	$Dist_C$	m	0	1984	0	2079	0	1892	Distance to channel points defined as drainage area > 1 km^2.	
Drainage Area	Drainage Area	m^2	900	8.9E+09	900	9.4E+09	900	1.2E+10	Total area of upstream cells based on a D8 flow direction.	
Elevation	Elev	m	265	4249	229	4106	282	4446	Elevation acquired from a 90 m SRTM DEM.	USGS EarthExplorer
Fault Distance from All Faults	$Dist_F$	m	0	21831	0	7860	0	15892	Euclidean Distance from faults shown in the lithology map from Haproff et al. (2019).	Haproff et al., 2019
Fault Distance from Main Frontal Thrust or Suture Zone	$Dist_{MFT}$	m	0	66388	0	31213	4428.3	57076	Euclidean Distance from the main frontal thrust fault and suture shown in the Himalayan fault map from Taylor and Yin (2009).	Taylor and Yin, 2009
Local Relief	Relief	m	97	2772	268	2522	606	2533	Local relief calculated as an elevation range within a 2500m radius circular window.	Schwanghart and Scherler, 2014
Mean Annual Precipitation	MAP	mm/yr	1364	7253	2654	7529	600	6954	12 year-averaged (1998 - 2009) mean annual precipitation obtained from the Tropical Rainfall Measuring Mission (TRMM).	Bookhagen and Burbank, 2010
Number of Extreme Events	NEE	events/yr	6.8	13.2	9.9	14.1	3.8	12.2	12 year-averaged (1998 - 2009) annual number of extreme events obtained from TRMM.	
Slope	Slope	--	0.1	3.2	0.1	3.3	0.1	3.0	Slope calculated as the steepest descent gradient using D8 flow routing based on 90 m SRTM DEM.	Schwanghart and Scherler, 2014

Table A2: Description and Ranges of 15 Features.

Models / Features	Area Under the Curve		
	N-S	NW-SE	E-W
SNN			
Single - 1	0.864	0.826	0.878
Composite - 2	0.896	0.856	0.919
Multi-Stage Training Neural Network (MST)	0.927	0.912	0.922
Statistical Models			
Logistic Regression	0.869	0.795	0.880
Likelihood Ratio	0.841	0.792	0.835
Physical Models			
Failure Index	0.756	0.694	0.732
Failure Index (Area $<10^5$ m^2)	0.784	0.741	0.723
Wetness	0.575	*0.516*	*0.568*
Single Features			
Aspect	*0.553*	*0.546*	*0.588*
Curvature (Mean)	*0.554*	*0.534*	0.530
Curvature (Planform)	*0.537*	*0.528*	0.505
Curvature (Profile)	*0.528*	*0.515*	0.526
Curvature (Total)	0.568	0.573	0.611
Discharge	*0.504*	*0.503*	*0.505*
Distance to Channel	*0.505*	0.523	0.574
Drainage Area	*0.502*	*0.502*	*0.502*
Elevation	*0.589*	*0.513*	*0.624*
Fault Distance from All Faults	*0.700*	0.544	*0.661*
Fault Distance from Main Frontal Thrust or Suture Zone	*0.744*	*0.603*	*0.666*
Local Relief	0.571	0.525	*0.507*
Mean Annual Precipitation	0.756	*0.525*	0.598
Number of Extreme Events	0.744	0.585	0.627
Slope	0.698	0.696	0.760

Entries in italics have negative correlations with landslide propensity
AUROC of physical models and single features were normalized to be from 0 to 1
Based on 30% testing partition

Table A3: AUROC of Models and Single Features.

	N-S			
	MST	SNN	Logistic Regression	Likelihood Ratio
Mean	0.928	0.900	0.869	0.843
SE	0.05%	0.09%	0.24%	0.32%
σ	0.0014	0.0028	0.0008	0.0010
95% Confidence Interval of Mean				
CI +	0.929	0.902	0.871	0.845
CI -	0.927	0.898	0.867	0.841
±2σ Data Range				
Mean +2σ	0.930	0.906	0.874	0.850
Mean -2σ	0.925	0.894	0.864	0.837
	NW-SE			
	MST	SNN	Logistic Regression	Likelihood Ratio
Mean	0.911	0.860	0.794	0.792
SE	0.05%	0.11%	0.40%	0.35%
σ	0.0014	0.0034	0.0012	0.0011
95% Confidence Interval of Mean				
CI +	0.912	0.862	0.797	0.794
CI -	0.910	0.858	0.791	0.789
±2σ Data Range				
Mean +2σ	0.914	0.867	0.802	0.799
Mean -2σ	0.908	0.853	0.786	0.785
	E-W			
	MST	SNN	Logistic Regression	Likelihood Ratio
Mean	0.922	0.920	0.879	0.834
SE	0.14%	0.11%	0.50%	0.56%
σ	0.0044	0.0035	0.0016	0.0018
95% Confidence Interval of Mean				
CI +	0.926	0.923	0.882	0.838
CI -	0.919	0.917	0.875	0.830
±2σ Data Range				
Mean +2σ	0.931	0.927	0.889	0.845
Mean -2σ	0.914	0.913	0.869	0.823

*Based on 10-fold validation of randomly selecting 50% of the 30% testing partition

Table A4: Artificial Neural Network and Statistical Model Confidence Intervals.

	N-S				
	MST	SNN-L2	SNN-L1	LogR	LR
AUROC	0.927	0.896	0.864	0.869	0.841
Accuracy	0.841	0.792	0.757	0.766	0.723
True positive Rate/Sensitivity/POD	0.871	0.853	0.812	0.806	0.802
False Positive Rate/Specificity/POFD	0.165	0.208	0.244	0.234	0.277
POD - POFD	0.706	0.644	0.569	0.572	0.525
	NW-SE				
	MST	SNN-L2	SNN-L1	LogR	LR
AUROC	0.912	0.856	0.826	0.795	0.792
Accuracy	0.845	0.792	0.755	0.739	0.703
True positive Rate/Sensitivity/POD	0.824	0.777	0.755	0.694	0.730
False Positive Rate/Specificity/POFD	0.154	0.208	0.245	0.260	0.297
POD - POFD	0.670	0.569	0.510	0.434	0.433
	E-W				
	MST	SNN-L2	SNN-L1	LogR	LR
AUROC	0.922	0.919	0.878	0.880	0.835
Accuracy	0.821	0.838	0.779	0.812	0.768
True positive Rate/Sensitivity/POD	0.883	0.867	0.797	0.794	0.749
False Positive Rate/Specificity/POFD	0.182	0.162	0.221	0.188	0.232
POD - POFD	0.702	0.706	0.576	0.606	0.517

* Based on 30% testing partition

LogR = Logistical Regression; LR = Likelihood Ratio

Table A5: Performance Metrics for Models.

N-S Region Features	Asp	$Curv_M$	$Dist_C$	Elev	Log_{10} (Discharge)	Log_{10} (Drainage Area)	$Dist_F$	$Dist_{MFT}$	Relief	NEE	MAP	Slope
Asp	1											
$Curv_M$	-0.002	1										
$Dist_C$	-0.003	0.290	1									
Elev	0.004	0.154	0.390	1								
Log_{10}(Discharge)	0.009	-0.671	-0.327	-0.232	1							
Log_{10}(Drainage Area)	0.003	-0.581	-0.210	-0.104	0.696	1						
$Dist_F$	-0.016	0.001	-0.039	0.179	-0.168	-0.008	1					
$Dist_{MFT}$	-0.031	-0.001	-0.049	0.382	-0.206	0.005	0.684	1				
Relief	0.036	-0.002	0.045	0.365	0.072	0.041	-0.170	-0.032	1			
NEE	0.010	0.002	0.045	-0.349	0.213	0.009	-0.601	-0.792	0.131	1		
MAP	0.005	-0.00001	0.048	-0.183	0.246	0.007	-0.599	-0.828	0.159	0.802	1	
Slope	-0.015	0.414	0.205	0.167	-0.326	-0.238	-0.110	-0.070	0.311	0.124	0.111	1

NW-SE Region Features	Asp	$Curv_M$	$Dist_C$	Elev	Log_{10} (Discharge)	Log_{10} (Drainage Area)	$Dist_F$	$Dist_{MFT}$	Relief	NEE	MAP	Slope
Asp	1											
$Curv_M$	-0.002	1										
$Dist_C$	-0.028	0.272	1									
Elev	0.013	0.164	0.425	1								
Log_{10}(Discharge)	-0.013	-0.686	-0.332	-0.102	1							
Log_{10}(Drainage Area)	-0.007	-0.584	-0.199	-0.098	0.717	1						
$Dist_F$	0.030	0.0001	-0.006	0.165	0.049	0.024	1					
$Dist_{MFT}$	-0.041	-0.007	-0.008	0.432	0.120	0.054	0.366	1				
Relief	0.032	-0.005	0.018	0.463	0.103	0.048	0.112	0.351	1			
NEE	-0.013	0.003	0.016	0.124	0.037	-0.003	0.032	-0.128	0.177	1		
MAP	-0.024	-0.003	0.034	0.586	0.148	0.030	0.203	0.403	0.485	0.357	1	
Slope	0.023	0.410	0.141	0.188	-0.329	-0.230	0.011	0.053	0.296	0.108	0.168	1

E-W Region Features	Asp	$Curv_M$	$Dist_C$	Elev	Log_{10} (Discharge)	Log_{10} (Drainage Area)	$Dist_F$	$Dist_{MFT}$	Relief	NEE	MAP	Slope
Asp	1											
$Curv_M$	-0.001	1										
$Dist_C$	0.004	0.286	1									
Elev	0.005	0.120	0.336	1								
Log_{10}(Discharge)	0.000	-0.686	-0.342	-0.264	1							
Log_{10}(Drainage Area)	0.001	-0.595	-0.212	-0.068	0.707	1						
$Dist_F$	0.029	-0.001	0.013	0.501	-0.092	0.004	1					
$Dist_{MFT}$	-0.036	-0.009	0.018	0.636	-0.140	0.054	0.330	1				
Relief	-0.051	0.003	0.050	0.312	-0.061	0.040	0.137	0.537	1			
NEE	0.019	0.011	0.009	-0.601	0.194	-0.041	-0.348	-0.786	-0.421	1		
MAP	0.018	0.008	-0.021	-0.553	0.209	-0.042	-0.305	-0.835	-0.426	0.857	1	
Slope	-0.023	0.449	0.210	0.171	-0.421	-0.269	0.053	0.150	0.252	-0.135	-0.117	1

Table A6: Correlation Metrics Between Features (R-value).

Feature	Coefficient		
	N-S	NW-SE	E-W
Intercept	-13.33	-11.85	-7.09
Asp NE	0.728	0.984	2.166
Asp E	1.626	1.942	3.340
Asp SE	2.510	2.281	3.658
Asp S	2.476	2.264	3.783
Asp SW	2.062	2.104	2.811
Asp W	1.319	1.176	1.834
Asp NW	0.604	-0.286	-0.865
$Curv_M$	-280	-289	-225
Log_{10}(Discharge)	0.055	0.146	-0.092
$Dist_C$	2.25E-04	2.51E-04	1.12E-03
Log_{10}(Drainage Area)	0.008	-0.005	0.096
Elev	-4.48E-04	2.56E-04	-6.60E-04
$Dist_F$	-1.49E-04	1.38E-04	-2.88E-05
$Dist_{MFT}$	1.93E-06	-1.16E-04	-6.44E-05
Relief	3.96E-05	2.40E-05	4.96E-04
MAP	2.84E-04	1.03E-05	-1.84E-04
NEE	0.347	0.276	-0.120
Slope	2.383	2.925	3.617

Table A7: Logistic Regression Control Coefficients.

A.4 Appendix References

Akgun, A., 2012, A comparison of landslide susceptibility maps produced by logistic regression, multi-criteria decision, and likelihood ratio methods: A case study at İzmir, Turkey: Landslides, v. 9, p. 93–106, doi:10.1007/s10346-011-0283-7.

Barros, A.P., Kim, G., Williams, E., and Nesbitt, S.W., 2004, Probing orographic controls in the Himalayas during the monsoon using satellite imagery: Natural Hazards and Earth System Sciences, v. 4, p. 29–51.

Bookhagen, B., and Burbank, D.W., 2010, Toward a complete Himalayan hydrological budget: Spatiotemporal distribution of snowmelt and rainfall and their impact on river discharge: Journal of Geophysical Research: Earth Surface, v. 115, doi:10.1029/2009JF001426.

Dietrich, W.E., Bellugi, D., and Real de Asua, R., 2001, Validation of the Shallow Landslide Model, SHALSTAB, for forest management, *in* Land use and watersheds: human influence on hydrology and geomorphology in urban and forest areas, v. 2, p. 195–227, doi:10.1029/ws002p0195.

Dietrich, W.E., Reiss, R., Hsu, M.-L., and Montgomery, D.R., 1995, A Process-Based Model For Colluvial Soil Depth and Shallow Landsliding Using Digital Elevation Data: Hydrological Processes, v. 9, p. 383–400.

Huang, A.Y.L., and Montgomery, D.R., 2014, Topographic locations and size of earthquake- and typhoon-generated landslides, Tachia River, Taiwan: Earth Surface Processes and Landforms, v. 39, p. 414–418, doi:10.1002/esp.3510.

Ihlen, V., and Zanter, K., 2019, Landsat 8 (L8) Data Users Handbook.

Kavzoglu, T., Sahin, E.K., and Colkesen, I., 2014, Landslide susceptibility mapping using GIS-based multi-criteria decision analysis, support vector machines, and logistic regression: Landslides, v. 11, p. 425–439, doi:10.1007/s10346-013-0391-7.

Larsen, I.J., and Montgomery, D.R., 2012, Landslide erosion coupled to tectonics and river incision: Nature Geoscience, v. 5, p. 468–473, doi:10.1038/ngeo1479.

Larsen, I.J., Montgomery, D.R., and Korup, O., 2010, Landslide erosion controlled by hillslope material: Nature Geoscience, v. 3, p. 247–251, doi:10.1038/ngeo776.

Lee, S., 2005, Application of logistic regression model and its validation for landslide susceptibility mapping using GIS and remote sensing data: International Journal of Remote Sensing, v. 26, p. 1477–1491, doi:10.1080/01431160412331331012.

McGuire, L.A., Rengers, F.K., Kean, J.W., Coe, J.A., Mirus, B.B., Baum, R.L., and Godt, J.W., 2016, Elucidating the role of vegetation in the initiation of rainfall-induced shallow landslides: Insights from an extreme rainfall event in the Colorado Front Range: Geophysical Research Letters, v. 43, p. 9084–9092, doi:10.1002/2016GL070741.

Montgomery, D.R., and Dietrich, W.E., 1994, A physically based model for the topographic control on shallow landsliding: Water Resources Research, v. 30.

Montgomery, D.R., Dietrich, W.E., and Heffner, J.T., 2002, Piezometric response in shallow bedrock at CB1: Implications for runoff generation and landsliding: Water Resources Research, v. 38, p. 10-1-10–18, doi:10.1029/2002wr001429.

Moon, S., Page Chamberlain, C., Blisniuk, K., Levine, N., Rood, D.H., and Hilley, G.E., 2011, Climatic control of denudation in the deglaciated landscape of the Washington Cascades: Nature Geoscience, v. 4, p. 469–473, doi:10.1038/ngeo1159.

Prakash, N., Manconi, A., and Loew, S., 2020, Mapping landslides on EO data: Performance of deep learning models vs. Traditional machine learning models: Remote Sensing, v. 12, doi:10.3390/rs12030346.

Raia, S., Alvioli, M., Rossi, M., Baum, R.L., Godt, J.W., and Guzzetti, F., 2014, Improving predictive power of physically based rainfall-induced shallow landslide models: A probabilistic approach: Geoscientific Model Development, v. 7, p. 495–514, doi:10.5194/gmd-7-495-2014.

Reichenbach, P., Rossi, M., Malamud, B.D., Mihir, M., and Guzzetti, F., 2018, A review of statistically-based landslide susceptibility models: Earth-Science Reviews, v. 180, p. 60–91, doi:10.1016/j.earscirev.2018.03.001.

Shao, K., Moon, S., Li, G.K., Haproff, P.J., Yin, A., Corbett, L.B., Bierman, P.R., Argueta, M.O., and Hidy, A.J. Climate-driven erosion varies with lithology across the Himalaya: In review at Nature Communications.

Stine, R.A., 1995, Graphical interpretation of variance inflation factors: The American Statistician, v. 49, p. 53–56, doi:10.1080/00031305.1995.10476113.

Stock, J.D., and Dietrich, W.E., 2006, Erosion of steepland valleys by debris flows: Bulletin of the Geological Society of America, v. 118, p. 1125–1148, doi:10.1130/B25902.1.

Stock, J., and Dietrich, W.E., 2003, Valley incision by debris flows: Evidence of a topographic signature: Water Resources Research, v. 39, doi:10.1029/2001WR001057.

Tucker, C.J., Fungt, I.Y., Keeling, C.D., and Gammon, R.H., 1986, Relationship between atmospheric CO2 variations and a satellite-derived vegetation index: Nature, v. 319, p. 195–199.

United States Geological Survey EarthExplorer, 2020.

Yang, Y., Zhao, T., Ni, G., and Sun, T., 2018, Atmospheric rivers over the Bay of Bengal lead to northern Indian extreme rainfall: International Journal of Climatology, v. 38, p. 1010–1021, doi:10.1002/joc.5229.

Yilmaz, I., and Keskin, I., 2009, GIS based statistical and physical approaches to landslide susceptibility mapping (Sebinkarahisar, Turkey): Bulletin of Engineering Geology and the Environment, v. 68, p. 459–471, doi:10.1007/s10064-009-0188-z.

Yu, F., Hunt, A., Egli, M., and Raab, G., 2019, Comparison and Contrast in Soil Depth Evolution for Steady State and Stochastic Erosion Processes: Possible Implications for Landslide Prediction: Geochemistry, Geophysics, Geosystems, v. 20, p. 2886–2906, doi:10.1029/2018GC008125.

APPENDIX B:

Climate-driven erosional efficiency varies with lithology across the Himalaya

B.1 Appendix Note B1: Description of sample preparation

For 12 detrital sand samples collected from the easternmost Himalaya, we separated quartz through a series of physical and chemical procedures at the University of California, Los Angeles cosmogenic preparatory laboratory. We sieved samples for the 250-500 μm grain size fraction, except for sample AH18-13 from which we sieved the 250-710 μm grain size fraction because of the small sample size. Subsequently, we performed magnetic separation. Then, we treated samples with an 8 M nitric acid solution to dissolve carbonates and organic material. After the nitric acid bath, we etched samples at least four times in a hot 1% solution of hydrofluoric-nitric acid to dissolve all grains excluding quartz (Kohl and Nishiizumi, 1992). We also conducted mineral separation using lithium metatungstate heavy liquid to remove dense mineral phases (2.70 g/cm^3).

Quartz purity tests using Inductively Coupled Plasma Optical Emission Spectrometry and Be isolation were conducted at the National Science Foundation/University of Vermont Community Cosmogenic Facility (NSF/UVM CCF). We extracted pure Be from quartz samples at the NSF/UVM CCF following the methods detailed in (Corbett et al., 2016). Samples were prepared in two separate batches with three and two process blanks, respectively, in each batch. We dissolved a total of 14.12 to 44.05 g of quartz for each sample with 240 to 246 μg of ^{9}Be using an in-house made low-ratio beryl carrier with a concentration of 291 ppm Be (Table B2). Then, we digested samples in concentrated hydrofluoric acid and isolated Be using anion and cation exchange columns. Last, we precipitated the Be fractions as hydroxide gels for each sample, which were subsequently burned, homogenized with Nb powder, and packed into stainless steel cathodes for Accelerator Mass Spectrometry (AMS) measurements.

B.2 Appendix Note B2: Accelerator Mass Spectrometry analysis

$^{10}Be/^{9}Be$ ratios were measured by the AMS facility at Lawrence Livermore National Laboratory following Nishiizumi et al. (2007). Sample ratios were normalized to the primary standard 07KNSTD3110, which has an assumed ratio of 2.850×10^{-12}. We processed and analyzed the samples in two separate batches (November 2018 and January 2021). We assume sources of ^{10}Be in the full process blanks include the ^{10}Be carrier, machine blank, and chemical processing additions. $^{10}Be/^{9}Be$ ratios of the three full process blanks from the first batch are 3.8×10^{-16}, 4.0×10^{-16}, and 7.3×10^{-16}; $^{10}Be/^{9}Be$ ratios in the second batch were 9.6×10^{-16} and 5.97×10^{-15}. Considering the relative consistency among our four blanks (three from the first batch, and one from the second batch) and the long-term $^{10}Be/^{9}Be$ ratio of beryl carrier blanks at the NSF/UVM CCF (Corbett et al., 2016), we omitted the one higher blank from our calculations based on the assumption that it was contaminated. We used the average and standard deviation of the four remaining blanks, $6.2\pm2.8\times10^{-16}$, to correct the sample ratios from both batches. We conducted a sensitivity analysis based on a different blank correction scenario, which used blanks for their respective batches (5.0×10^{-16} for the 2018 batch and 9.6×10^{-16} for the 2021 batch) instead of our reported four sample average blank correction. The inferred erosion rates of our analyzed samples differ by ~0.25% to ~10% (Fig. B11; Table B2). The resulting differences in erosion rates do not affect the main results of this study (e.g., correlations between erosion rates and climatic, topographic, and lithologic controls).

Sample AH18-16 was prepared twice with 21.744 g and 44.054 g of quartz in the November 2018 and January 2021 batches, respectively. The $^{10}Be/^{9}Be$ ratio measured from the first batch was near the AMS detection limit and yielded large uncertainties. Therefore, we prepared AH18-16 again with approximately double the quartz mass to increase the $^{10}Be/^{9}Be$ ratio. The measured $^{10}Be/^{9}Be$ ratio of the second, higher-mass attempt was above the detection limit and had lower uncertainties than that of the first run. Therefore, we used the $^{10}Be/^{9}Be$ ratio measurement from the second batch in our analysis.

B.3 Appendix Note B3: ^{10}Be-derived erosion rate calculation

We converted blank-corrected ^{10}Be concentrations to millennial basin-averaged erosion rates using the CRONUS-Earth online calculator version 2.3 (Balco et al., 2008) following input calculations from Adams et al. (2020). We assumed no shielding correction and values for sample thickness (1 cm) and density (2.7 g/cm^3). We used time-independent scaling for spallogenic production from Stone (2000). Additionally, we calculated topographic metrics utilized in our erosion rate calculations, including basin-averaged latitude, longitude, and elevation, using TopoToolbox v2 (Schwanghart and Scherler, 2014).

B.4 Appendix Note B4: Compilation of ^{10}Be-derived erosion rates

We compiled ^{10}Be-derived erosion rates from a total of 178 across the Himalaya, 166 basins from previous studies (Godard et al., 2012, 2014; Scherler et al., 2014; Portenga et al., 2015; Le Roux-Mallouf et al., 2015; Olen et al., 2015; Adams et al., 2016, 2020) and 12 basins from this study. We adopted 32, 14, and 95 basins from the central Nepal, eastern Nepal, and Bhutan Himalaya, respectively, from Adams et al. (2020) and compiled 20 basins from the Garhwal Himalaya from Scherler et al. (2014). For the Bhutan Himalaya, they included 95 basins from Portenga et al. (2015), Le Roux-Mallouf et al. (2015), Adams et al. (2016), and Adams et al. (2020). Five basins (BT1106, BT1107, BT1116, BT1118, and BT1119) were designated as a separate "Bhutan (subset)" region within our compilation due to their abnormally high erosion rates. For the eastern Nepal Himalaya, from the originally compiled 15 basins, we selected 14 basins from Olen et al. (2015). We excluded a basin that was reported as having recent landslide influences and a denudation rate that likely does not represent the temporal average. For the central Nepal Himalaya, they compiled 32 basins from Godard et al. (2012) and Godard et al. (2014). For the Garhwal Himalaya, we compiled 20 basins from Scherler et al. (2014) with the exclusion of sample DS6-008, which was found to be a potential outlier because of its abnormally high erosion rate, and basins with drainage area >650 km^2. We recalculated ^{10}Be-derived erosion rates reported by Scherler et al. (2014) using the CRONUS-Earth online calculator version 2.3 to have consistent input values with those of Adams et al. (2020) (e.g., density, no shielding).

B.5 Appendix Note B5: Quantification of topographic, climatic, lithologic, and geologic controls

We calculated topographic variables including slope, channel steepness, local relief, and drainage area using a 90 m SRTM digital elevation model (DEM) for all compiled and measured basins consistently (Farr et al., 2007; de Ferranti, 2021). Although 30 m resolution DEMs are available, due to profound artifacts found in the steep mountains of our area in the easternmost Himalaya, we used a 90 m DEM to calculate topographic metrics, including slope, drainage area, local relief, and channel steepness (with and without correction for discharge variability).

We calculated slope as the steepest descent gradient in an 8-direction (D8) flow route. We calculated local relief as the range in elevation within 2.5 and 5 km radii circular windows. 2.5 and 5 km radii were used because these radii are generally consistent with the distance between ridges and valleys for our basins. Also, these length scales are consistent with previous studies in the Himalaya (e.g., Scherler et al. (2014)).

Mean annual precipitation (MAP) and the number of extreme rainfall events (NEE) were acquired from Bookhagen and Burbank (2010), which analyzed the 2B31 dataset from the Tropical Rainfall Measuring Mission (TRMM) spanning from January 1998 to December 2009. To calculate MAP, rainfall measurements were integrated over 90-min measurements over these 12 years. NEE was calculated as the number of days with measured daily rainfall above the 90^{th} percentile over the 12-year period for each pixel. Only rainy days with measured rainfall were included when calculating the 90^{th} percentile of daily rainfall. Both MAP and NEE from TRMM have an original resolution of ~5 km. These datasets were resampled and interpolated to 90 m resolution to be consistent with that of our DEM.

Using D8 flow directions of stream networks, we calculated drainage area as the number of upstream cells that contribute to each pixel in a 90 m DEM. We considered pixels with an upstream area >1 km^2 as streams. We also recalculated channel points, channel slope, and drainage area for basins in their respective regions to be consistent in our analysis. We calculated channel steepness (k_{sn}) using both the integral method based on χ (Perron and Royden, 2013) and the basin-averages of channel slope

normalized by drainage area (Wobus et al., 2006) from extracted channel points with drainage area >1 km^2. A drainage area >1 km^2 has been used in previous studies in the Himalaya (Scherler et al., 2014; Adams et al., 2020). According to the integral method, we calculated k_{sn} following Perron and Royden (2013):

$$z(x) = z(x_b) + \left(\frac{k_s}{{A_0}^{\theta}}\right)\chi \qquad Eq.\ 1$$

where z is elevation, x is horizontal distance, b is base level, A_0 is a reference drainage area set as 1 km^2, and $\chi = \int_{x_b}^{x} (\frac{A_0}{A(x)})^{\theta} dx$. We assumed a reference concavity value (θ) of 0.45, which has previously been applied to the study regions of our compiled dataset, when calculating channel steepness (Scherler et al., 2014; Olen et al., 2015; Adams et al., 2020). Both the integral and basin-averaged methods produced similar k_{sn} values (Table B1). We selected k_{sn} calculated using the integral method for our main analysis.

Similarly, basin-averaged, discharge-based channel steepness (k_{sn}-q) was calculated from the same channel points extracted for k_{sn} following Adams et al. (2020). We used the corresponding 90 m resolution DEM for the region to determine channel slope and drainage area along with the TRMM 2B31 dataset to calculate discharge. We calculated k_{sn}-q following Adams et al. (2020):

$$k_{sn} - q = Q^{\theta} \bullet S \qquad Eq.\ 2$$

where Q is discharge, θ is the reference concavity of 0.45, and S is the channel slope. We calculated k_{sn}-q for 1 km long channel segments. Basin-averaged k_{sn}-q was then calculated using all channel segments within each basin, which have upstream areas > 1 km^2.

Previous studies showed potential variations in rock strength from the Lesser Himalayan Sequence and Greater Himalayan Crystalline Complex (Attal and Lavé, 2006; Godard et al., 2006). Thus, we separated lithologic units as south and north of the Main Central Thrust (MCT) in the Garhwal, Nepal, and Bhutan Himalaya and Demwe thrust in the easternmost Himalaya. South of the MCT, lithologic units include the Sub- and Lesser Himalayan Sequences. North of the MCT, lithologic units include the Greater and Tethyan Himalayan Sequences (Yin, 2006; Haproff et al., 2019). We delineated the Himalayan Main Central Thrust (MCT) following Vannay et al. (2004) for the Garhwal Himalaya, Godard et al. (2014) for

the central Nepal Himalaya, Rai et al. (2021) for the eastern Nepal Himalaya, and Long et al. (2011) for the Bhutan Himalaya. In our study region of the easternmost Himalaya, we delineated the Demwe Thrust from the geologic map reported in Haproff et al. (2019). South of the Demwe Thrust, lithologic units include quaternary alluvium, the Tezu and Sewak units, and the Lalpani schist. These units are mainly sedimentary and metasedimentary lithologies and qualitatively equivalent to the Sub- and Lesser Himalayan Sequences. The metasedimentary lithologic units of the Dibang Valley reach further into the hinterland relative to that of the Lohit Valley (Haproff et al., 2019, 2020) (Fig. B3a). North of the Demwe Thrust, lithologic units include the Mayodia gneiss, Tidding/Mayodia mélange complex, and Lohit Plutonic Complexes. These units are crystalline lithologies and qualitatively similar to the Greater Himalayan Sequence.

For simplicity, we grouped lithologies south of the MCT and Demwe Thrust as sedimentary and metasedimentary lithologies (hereafter, metasedimentary lithology) and those north of the MCT and Demwe Thrust as crystalline lithology. We quantified areal extent of metasedimentary and crystalline lithology for each basin (Table B1). Then, we assigned a dominant lithology for each basin based on areal extent being >50%.

We calculated the geologic metrics of distance from the Main Frontal thrust (MFT) and MCT using fault traces delineated by Taylor and Yin (2009) for the MFT and the aforementioned studies of each region for the MCT. We calculated the Euclidean distance from the MFT or both faults using ArcGIS 10.6.

Based on assigned dominant lithology for each basin, we examined the linear and nonlinear relationships between topographic and climatic controls and ^{10}Be-derived erosion rates. We defined linear relationships as:

$$y = n_1 + n_2 x \qquad Eq.\ 3$$

where y is the predicted ^{10}Be-derived erosion rate, x is the control value (e.g., climatic and topographic variables), and n_1 and n_2 are the best-fit parameters. Additionally, we examined nonlinear relationships using power-law and exponential model fits. We defined power-law and exponential relationships as:

$$\text{power-law: } y = b_1 x^{b_2} \qquad Eq.\ 4$$

$$\text{exponential: } y = exp\,(k_1 x + k_2) \qquad Eq.\ 5$$

where b_1, b_2 and k_1, k_2 are the best-fit parameters. To examine the goodness of fit of each linear and nonlinear model, we calculated root mean square error (RMSE), which is an estimate of the standard deviation of the prediction errors (Table B5). We calculated RMSE by dividing the square root of the sum of squared errors by the degrees of freedom, which is the number of data points subtracted by the number of parameters. Best fit coefficients and performance metrics were calculated using all erosion rates as well as those for basins dominated by metasedimentary and crystalline lithologies separately (Table S5).

We investigated the intercorrelations among our examined climate and topographic metrics including NEE, MAP, k_{sn}, k_{sn}-q, and $Dist_{MFT}$/$Dist_{MCT}$ (Fig. B5). Climate metrics and k_{sn} do not appear to be correlated regardless of lithologic grouping. However, climate metrics are loosely, positively correlated with k_{sn}-q, which is expected since MAP is incorporated in its calculation as discharge. NEE for basins dominated by metasedimentary lithology exhibits a similar U-shaped pattern with respect to $Dist_{MFT}$ similar to those of ^{10}Be-derived erosion rates. For basins dominated by crystalline lithology, we do not observe a clear correlation between NEE and $Dist_{MCT}$. However, we do not rule out the possibility that NEE and $Dist_{MCT}$ are nonlinearly correlated. Additionally, we quantify intercorrelations between topographic and climate metrics using the variance inflation factor (VIF) calculated as (Stine, 1995; Kavzoglu et al., 2014):

$$VIF = \frac{1}{(1 - R^2)} \qquad Eq.\ 6$$

where R is the linear correlation coefficient. VIF values of 1 indicate the that the metrics are not correlated while a VIF > 5 to 10 indicates a linear correlation. With a highest VIF of 2.46 between NEE and k_{sn}-q, our examined topographic and climatic metrics are not linearly correlated.

B.6 Appendix Note B6: Description of ^{10}Be-derived erosion rates and quantified controls

We compared the means and distributions of ^{10}Be-derived erosion rates and quantified controls from basins dominated by metasedimentary (n = 61) and crystalline lithologies (n = 112). They span similar minimum and maximum ranges in value (Table B4). Mean ^{10}Be-derived erosion rates of basins dominated by metasedimentary lithology are higher than those of basins dominated by crystalline lithology (Table B4). To examine the distribution of these two groups from different lithologies, we conducted a two-sample Kolmogorov-Smirnov test (K-S test). The results indicated that the distributions of ^{10}Be-derived erosion rates from these two sets are not from the same probability distribution ($p_{\text{K-S test}} < 0.01$). Local relief, k_{sn}, and k_{sn}-q are lower in basins dominated by metasedimentary lithologies relative to those underlain by crystalline lithologies ($p_{\text{K-S test}} < 0.01$). On the other hand, MAP and NEE are higher in basins dominated by metasedimentary lithology than in basins dominated by crystalline lithology ($p_{\text{K-S test}} < 0.01$). Considering that many active faults are present near the range front with sedimentary and metasedimentary lithologies, the higher mean erosion rates from basins dominated by metasedimentary lithology are reasonable. For landscapes at equilibrium between uplift rates and erosion rates, higher erosion rates would lead to higher k_{sn}, k_{sn}-q, and local relief if climatic and lithologic controls on erosion are not significant. Higher MAP and NEE and lower k_{sn}, k_{sn}-q, and local relief despite higher erosion rates for basins dominated by metasedimentary lithology suggests the possibility of variations in topography due to lithologic and climatic influences (Kirby and Whipple, 2012; Hilley et al., 2019). Thus, we decide to separate basins by lithology and examine each group's climatic and topographic controls.

B.7 Appendix Note B7: Landslide mapping and analysis

We mapped landslides in the easternmost Himalaya using NASA's Landsat satellite imagery from December 23, 1997, December 16, 2006, and November 12, 2017, with bands 2, 3, and 4 for Landsat 8 and 1, 2, and 3 for Landsat 5 (Fig. B12) (https://earthexplorer.usgs.gov/). These Landsat 8 and 5 bands used in this study have resolutions of 30 m. These Landsat bands were used to generate natural color imagery to best identify landslides (Clark et al., 2016). Landslide inventory maps were generated by manually detecting the absence of vegetation due to landslides. High degrees of vegetation in the study

area allowed for the clear delineation of landslides. We eliminated alpine areas with bare bedrock where it is difficult to detect and assess landslide occurrences. Alpine areas were classified using spectral signatures representing snow cover in Landsat 8 imagery from February 2018. In addition, areas of slope gradient <0.06 were excluded in landslide mapping since these areas are unlikely to be scar regions of landslides (Parker et al., 2011). Landslide scars were mapped independently from landslide deposits based on their differences in spectral signature, shape, and down-sloping orientation.

We calculated total landslide volume for each examined basin using the following volume-area scaling relation reported in Larsen et al. (2010):

$$V = \alpha A^{\gamma} \qquad Eq.\ 6$$

where V is the landslide volume, A is the landslide scar area, and α and γ are empirically determined scaling parameters. We used $\alpha = 10^{-0.59}$ and $\gamma = 1.36$ following Larsen et al. (2010) who obtained these values based on mixed soil and bedrock inventories in the Himalaya comprising 428 landslides. We calculated landslide volumes for the 2006 and 2017 landslide inventories while accounting for fractional, overlapping landslides from 1997 and 2006, respectively. The difference in landslide volume across the ~10-year intervals was used to calculate landslide-derived sediment fluxes. By normalizing sediment flux by total basin area and averaging the normalized rates from the two consecutive ~10-year intervals, we calculated basin-averaged landslide-derived erosion rates over a 20-year interval.

Monsoon-induced landslides mapped in basins from central and eastern Nepal were reported by Jones et al. (2021). Landslides between 1989-1999 and 2004-2009 were mapped using Landsat 4/5 while those between 2013-2018 were mapped using Landsat 8. Landsat 4/5 and 8 have a spatial resolution of 30 x 30 m and 15 x 15 m (panchromatic imagery), respectively. Landslides were mapped using annual pre-post monsoon imagery with the minimum mappable landslide area being ~1000 m^2. Mapped landslides include scars, runout, and depositional areas and represent the maximum affected landslide area. To be consistent with mapping procedures from our inventory in the easternmost Himalaya, we adjust the polygons of landslides mapped with an aspect ratio >4. This aspect ratio was determined from a probability distribution function generated using the easternmost Himalayan landslide inventory.

Individual landslide volumes were calculated using the same procedure described above. We elected to only include landslides from 1989-2009 in our analyses for these regions to be consistent with our landslide inventory from the easternmost Himalaya. This time interval represents the 20-years before ^{10}Be samples reported in Godard et al. (2012, 2014) were collected.

We calculated average landslide density as the percent of pixels classified as landslides within each study basin between 1997 to 2017. Next, average landslide density (% of study area) was divided by the total mapping time interval (20 years) to obtain the average likelihood of an area (i.e., 900 m^2) in that basin to experience a landslide each year (average failure rate; yr^{-1}).

To characterize how landslides are distributed on landscapes, we analyzed the hillslope positions of each landslide relative to ridges and valleys following Meunier et al. (2008). The distance to a ridge is calculated as the steepest descent distance from the highest point of a mapped landslide to the nearest ridgeline, while distance to a channel is calculated as that of the lowest point of a mapped landslide to the nearest channel. These distances are then normalized by the total flow length of the hillslope that the landslide is located on. The normalized distances to a ridge and channel for a given landslide varies from 0 (closest) to 1 (furthest). We determined ridge points as channels of the inverted 90 m DEM. Ridge points were defined as points with a drainage area > 1 km^2 from an inverted DEM.

We investigated the size-frequency distribution of landslide scar areas using a probability density plot to assess the similarities with that of the nearby Namche Barwa region (Fig. B13). We calculated the probability density of a given landslide area in our inventory following Malamud et al. (2004):

$$p(A_L) = \frac{1}{N_{LT}} \frac{\delta N_L}{\delta A_L} \qquad Eq.\ 7$$

where A_L is landslide area, $p(A_L)$ is the probability density of the landslide area bin, N_{LT} is the total number of landslides in the inventory, δN_L is the number of landslides within the specified area bin between A_L and $A_L + \delta A_L$. We calculated the probability density functions of landslide areas for each inventory (1997, 2006, and 2017). We fitted the probability density distributions using an inverse-gamma function following Malamud et al. (2004):

$$p(A_{ls}; q, m, s) = \frac{1}{m\Gamma(q)}\left[\frac{m}{A_{ls} - s}\right]^{q+1} exp\ exp\ \left[-\frac{m}{A_{ls} - s}\right] \qquad Eq.\ 8$$

where A_{ls} are individual landslide areas, p is the probability density, and q, m, and s are the best-fit parameters of the inverse-gamma function. Best-fit parameters are as follows: 1997 (q = 2.42, m = 1.70 $\times 10^4$ m^2, s = 0 m^2, r^2 = 0.75), 2006 (q = 2.06, m = 1.56 $\times$ 10^4 m^2, s = 0 m^2, r^2 = 0.77), and 2017 (q = 2.19, m = 1.44 $\times$ 10^4 m^2, s = 0 m^2, r^2 = 0.75). The inverse-gamma function fit of landslides from our study basins displays a slightly thinner-tailed distribution compared to those of the pre-1974 and 1974-2007 landslide inventories mapped by Larsen and Montgomery (Larsen and Montgomery, 2012) from the nearby Namche Barwa region (e.g., q = 0.96 – 1.27). The probability density of our landslide sizes between ~$10^{3.3}$ and ~$10^{4.1}$ m^2 is more similar to that of the 1974-2007 inventory that used similar resolution Landsat satellite images (Larsen and Montgomery, 2012) (Fig. B13).

We acknowledge the limitations of our analyses in the easternmost Himalaya due to differences in the timescales that our landslide inventory and TRMM 2B31 precipitation datasets represent. The precipitation datasets are averaged spatially and temporally, not allowing for the direct relation between rainstorm events and the resulting landslides in our inventory. Additionally, our landslide inventory was mapped using post-failure spectral signatures of satellite imagery from three specific times (i.e., 1997, 2006, 2017 Landsat), which does not provide precise information regarding the specific timing of landslide events. However, TRMM datasets may capture a representative, spatial distribution of orographic precipitation over our timescales of concern. MAP and NEE from TRMM and APHRODITE datasets spanning 12 and 50 years display similar spatial patterns with high rates near the rangefront that decrease into the hinterland consistent with orographic precipitation (Bookhagen and Burbank, 2010; Andermann et al., 2011; Yatagai et al., 2012). Furthermore, landslides mapped at different times display similar distributions with more frequent occurrences in basins near the range front with less frequent occurrences for those in the hinterland. This similarity suggests that our landslide distributions may also be representative over the same timescale as the TRMM precipitation dataset.

B.8 Appendix Note B8: Topographic steady-state in the easternmost Himalaya

Channel profile and landslide position analyses suggest topographic steady-state conditions in the easternmost Himalaya. χ, which represents the steady-state elevation of a channel at a specific location, does not exhibit large differences across drainage divides, indicating relatively stationary conditions (Fig. B8) (Willett et al., 2014). Additionally, for our measured basins specifically, we find that distinct disequilibrium features (e.g., changes in channel steepness, knickpoints) are generally absent in most channel profiles (Fig. B9), and many landslides are driven by river incision (Fig. B10). These basin and landslide properties further suggest that channels and hillslopes are likely in equilibrium with underlying tectonics over timescales necessary to generate the observed fluvial relief.

B.9 Appendix Figures and Tables

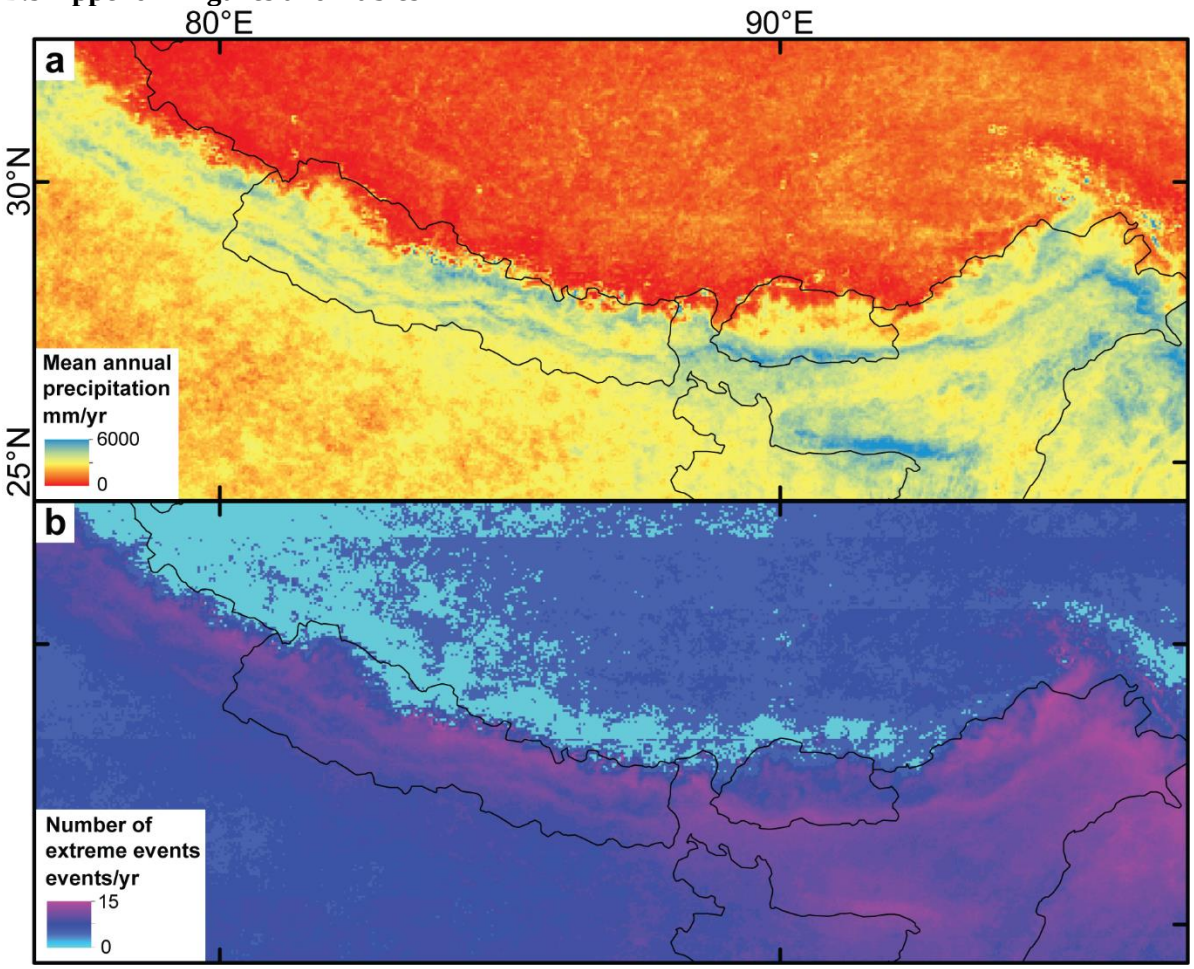

Fig. B1: Along-strike variations of climate metrics in the Himalaya. a, mean annual precipitation (MAP). **b**, number of extreme rainfall events (NEE). MAP and NEE were obtained from Bookhagen and Burbank (2010) who analyzed NASA's ~5 km-resolution Tropical Rainfall Measuring Mission 2B31 product.

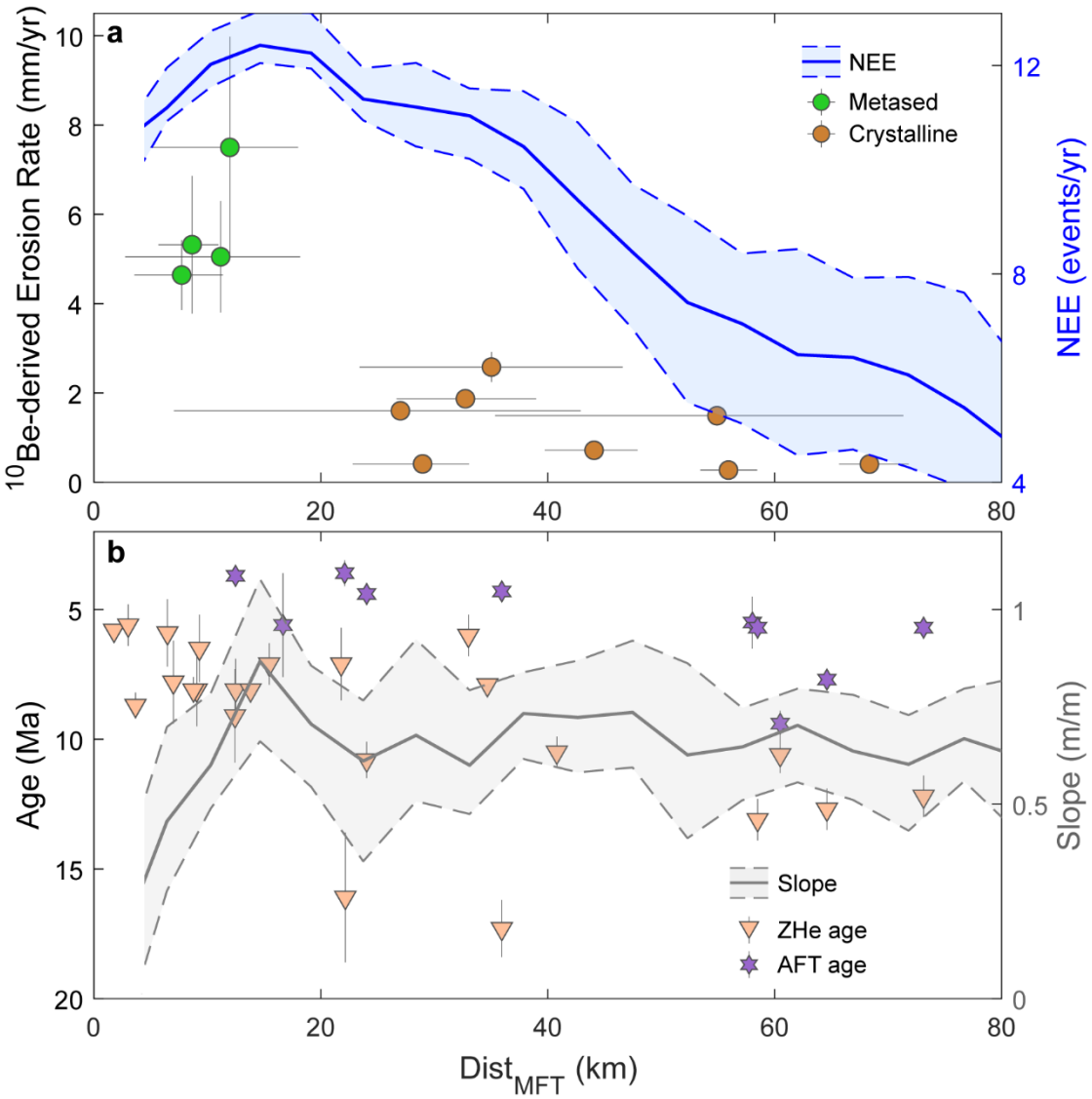

Fig. B2: Spatial patterns of erosion and low-temperature thermochronology ages in the easternmost Himalaya. Comparison between distance from the Main Frontal Thrust ($Dist_{MFT}$) and (**a**) ^{10}Be-derived erosion rates and number of extreme rainfall events (NEE) and (**b**) zircon (U-Th)/He (ZHe) ages (Haproff et al., 2020), apatite fission track (AFT) ages (Salvi et al., 2020), and slope. Thick lines and shaded areas represent mean ±1σ ranges in NEE (blue) and slope (gray) extracted from swaths that are 100 km wide at 5 km intervals longitudinally.

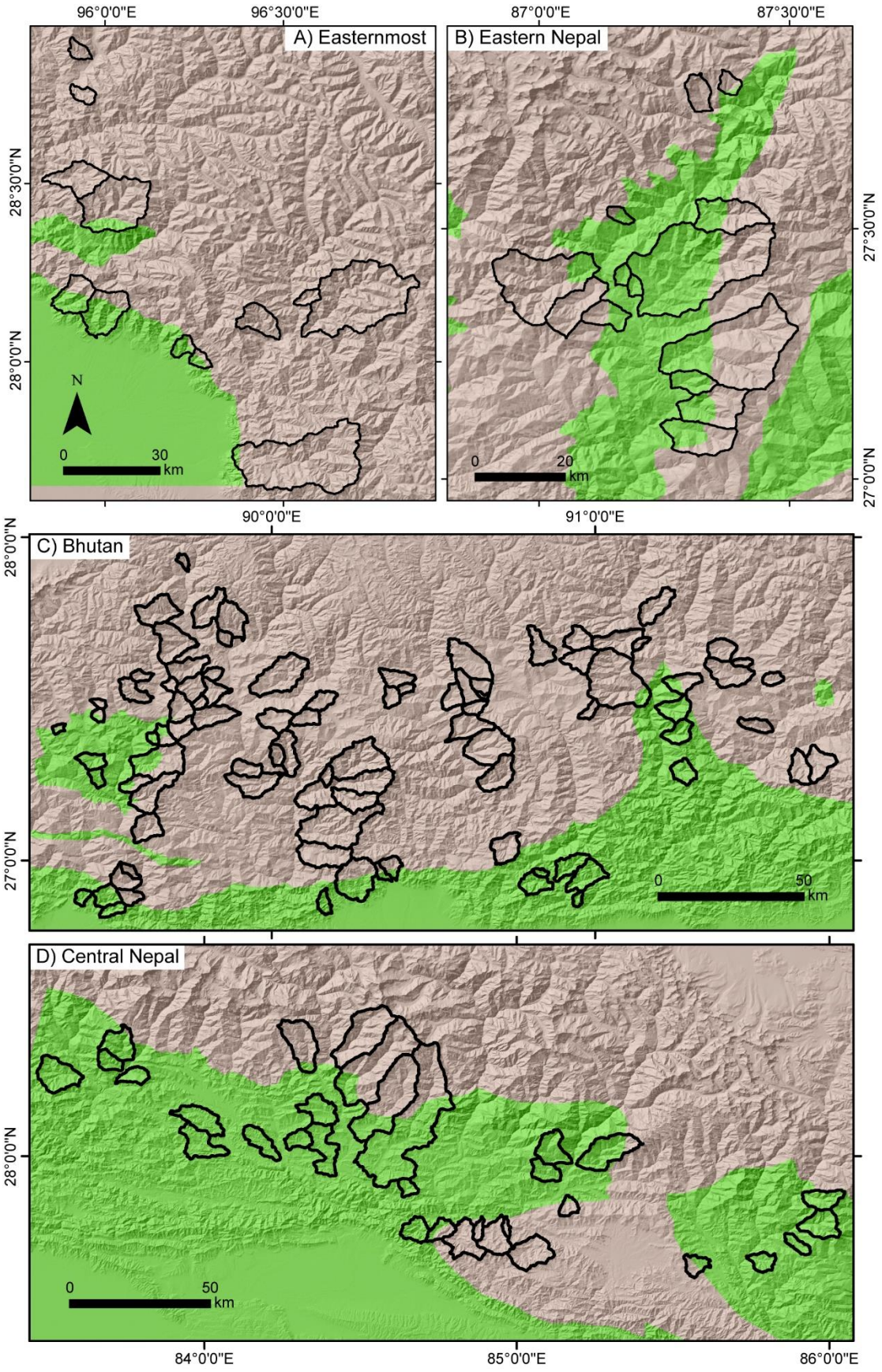
A) Easternmost
B) Eastern Nepal
C) Bhutan
D) Central Nepal
96°0'0"E
96°30'0"E
87°0'0"E
87°30'0"E
28°30'0"N
28°0'0"N
27°30'0"N
27°0'0"N
90°0'0"E
91°0'0"E
84°0'0"E
85°0'0"E
86°0'0"E
N
0
30
km
0
20
km
0
50
km
0
50
km

Fig. B3a: Simplified lithologic maps of the study areas in our compilation. Areas colored in green and brown consist of metasedimentary and crystalline lithologies, respectively. The delineation is based on the locations of Main Central Thrust (MCT) or locally known as the Demwe thrust. Basins sampled for ^{10}Be-derived erosion rates are shown in black polygons. Additional information on data sources, basin locations, erosion rate, and topographic and climatic metrics of our compilation can be found in Table B1. Further information on the lithologic maps used to categorize areas of metasedimentary and crystalline lithology in each study area can be found in Appendix B Note 5.

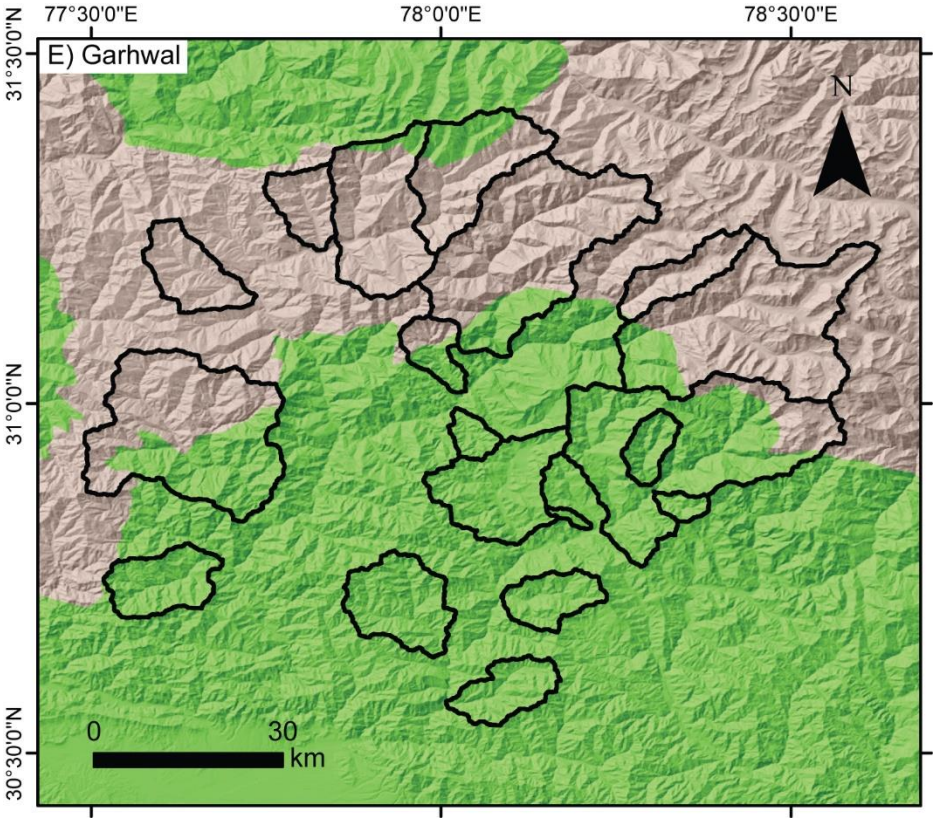

Fig. B3b: Simplified lithologic map of the Garhwal Himalaya study area. Areas colored in green and brown consist of metasedimentary and crystalline lithologies, respectively. The delineation is based on the locations of Main Central Thrust (MCT) or locally known as the Demwe thrust. Basins sampled for ^{10}Be-derived erosion rates are shown in black polygons. Additional information on data sources, basin locations, erosion rate, and topographic and climatic metrics of our compilation can be found in Table B1. Further information on the lithologic maps used to categorize areas of metasedimentary and crystalline lithology in each study area can be found in Appendix B Note 5.

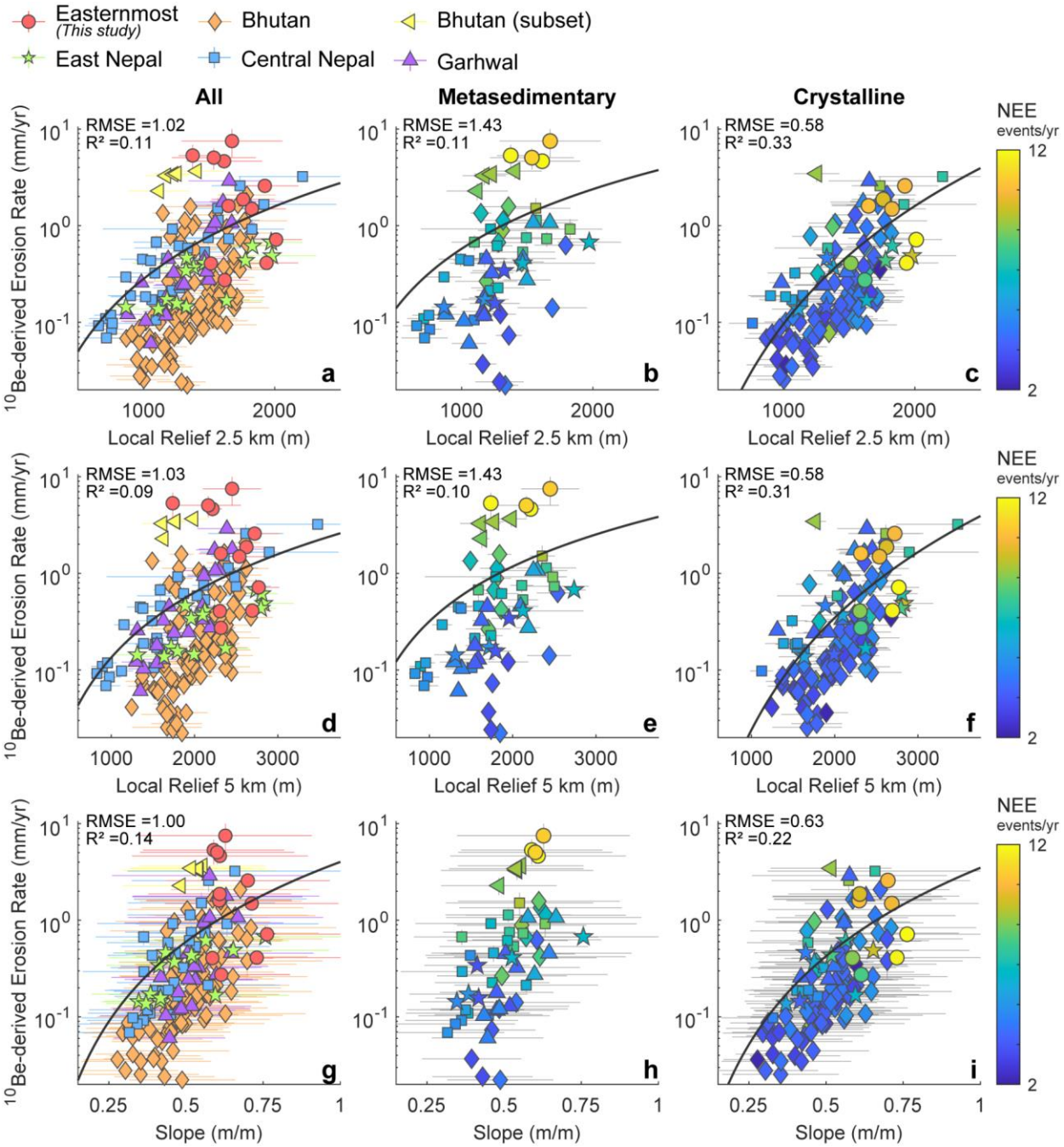

Fig. B4: Comparison between ^{10}Be-derived erosion rates and topographic metrics. **a-f**, local relief, calculated using (**a-c**) 2.5 km- and (**d-f**) 5 km-radius circular windows. **g-i**, slope. The details of symbol descriptions, power-law fits, and statistical measures are the same as Fig. 3.2. Error bars are calculated from ±1σ uncertainties in ^{10}Be-derived erosion rates and ±1σ range of metric values within basins.

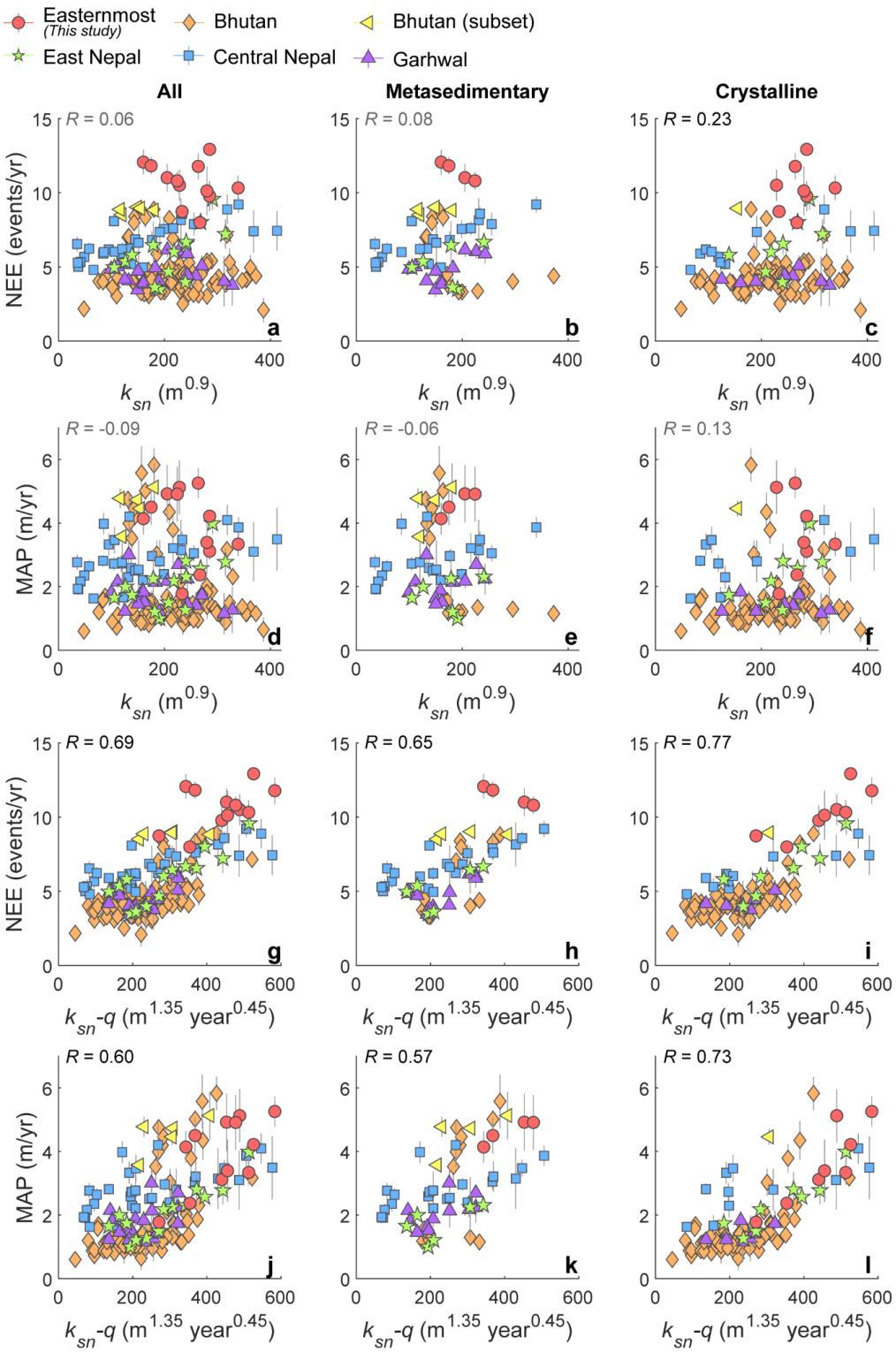

Fig. B5a: Comparison between topographic and climatic metrics across the Himalaya. These metrics include (**a-f**) channel steepness k_{sn}, (**g-l**) discharge-based channel steepness, k_{sn}-q, (**a-c, g-i**) the number of extreme rainfall events (NEE), and (**d-f, j-l**) mean annual precipitation (MAP). The results for (**a, d, g, j**) all basins (n = 173) and subsets of basins dominated by (**b, e, h, k**) metasedimentary (n = 61) or (**c, f, i, l**) crystalline lithology (n = 112). The linear correlation coefficients (R) are presented. Black- and gray-

colored values indicate statistically significant ($p < 0.05$) and insignificant ($p > 0.05$) correlations, respectively. Symbol shapes and colors indicate the respective study region. Error bars are calculated from ±1σ ranges of NEE and MAP within basins and ±1 standard errors for k_{sn} (mostly smaller than symbol sizes).

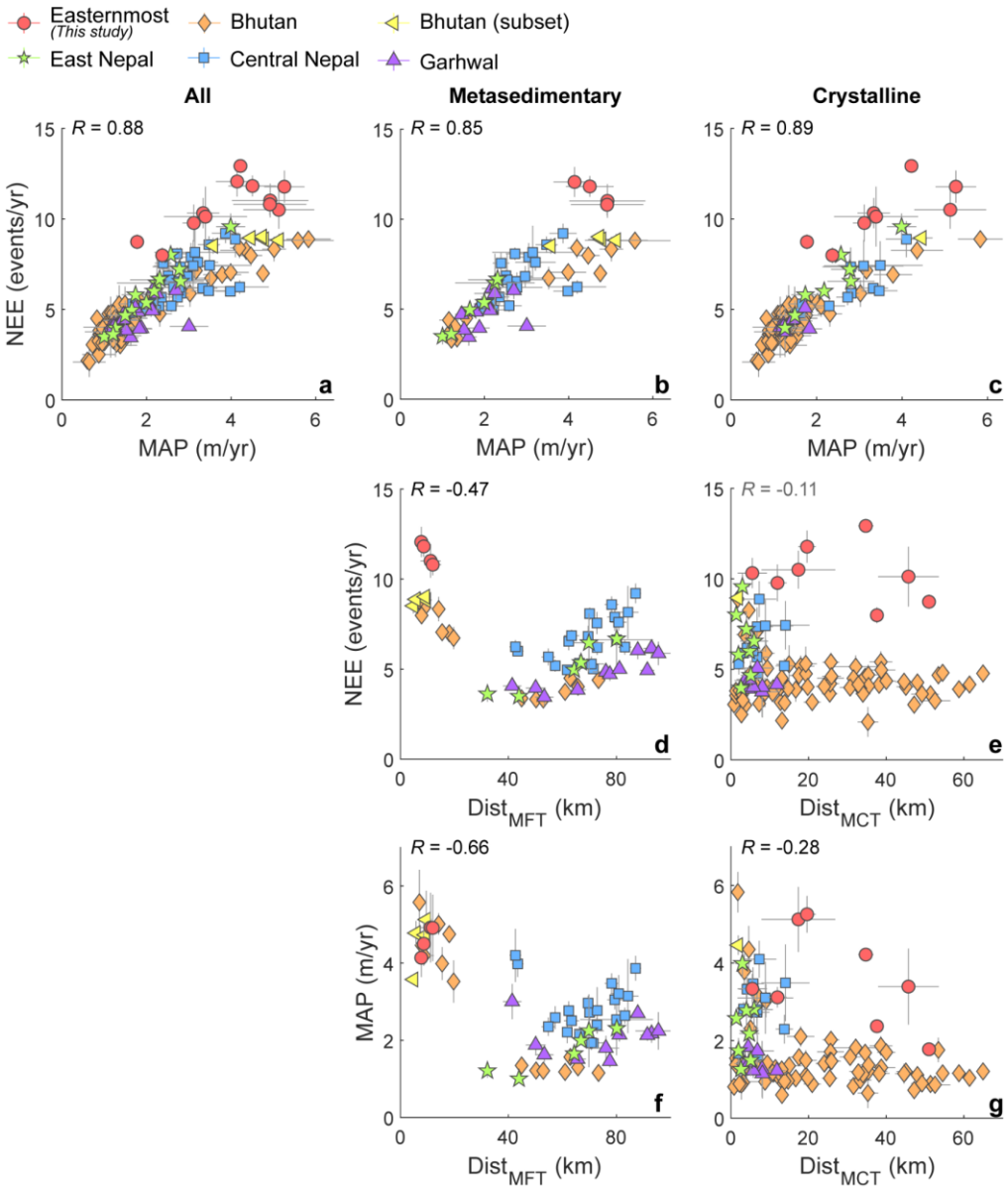

Fig. B5b: Comparison between geologic and climatic metrics across the Himalaya. These metrics include (**a-e**) the number of extreme rainfall events (NEE), (**a-c, f-g**) mean annual precipitation (MAP), and (**d-g**) distance to major faults. Results from (**a**) all basins and basins dominated by (**b, d, f**) metasedimentary or (**c, e, g**) crystalline lithology, which are compared with the distances to the Main Frontal Thrust ($Dist_{MFT}$) or Main Central Thrust ($Dist_{MCT}$), respectively. The linear correlation coefficients (R) are presented. Black- and gray-colored values indicate statistically significant ($p < 0.05$) and insignificant ($p > 0.05$) correlations, respectively. Symbol shapes and colors indicate the respective study region. Error bars are calculated from ±1σ ranges of NEE, MAP, and $Dist_{MFT}$ or $Dist_{MCT}$ values within basins.

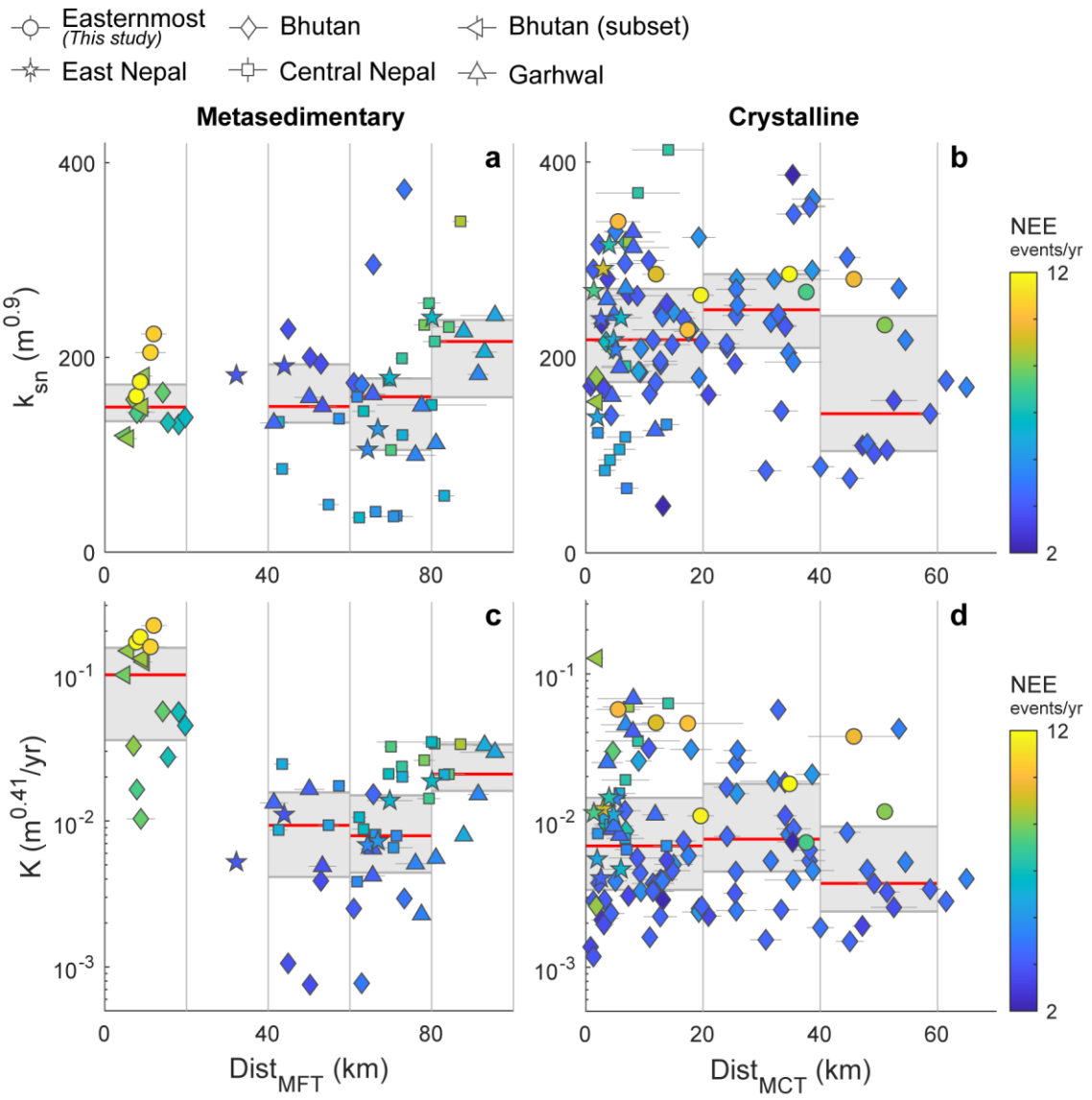

Fig. B6: Variations of erosional efficiencies with proximity to major faults. **a-b**, channel steepness k_{sn}. **c-d**, ordinary erosional efficiency (K). Results from basins dominated by (**a, c**) metasedimentary or (**b,d**) crystalline lithology are compared with the distances to the Main Frontal Thrust ($Dist_{MFT}$) or Main Central Thrust ($Dist_{MCT}$), respectively. Red lines and gray shaded boxes indicate the median values and interquartile ranges, respectively, calculated from basins within 20-km intervals denoted by vertical gray lines. Symbol shapes indicate the regions of sample locations. Symbol colors indicate the number of extreme rainfall events (NEE).

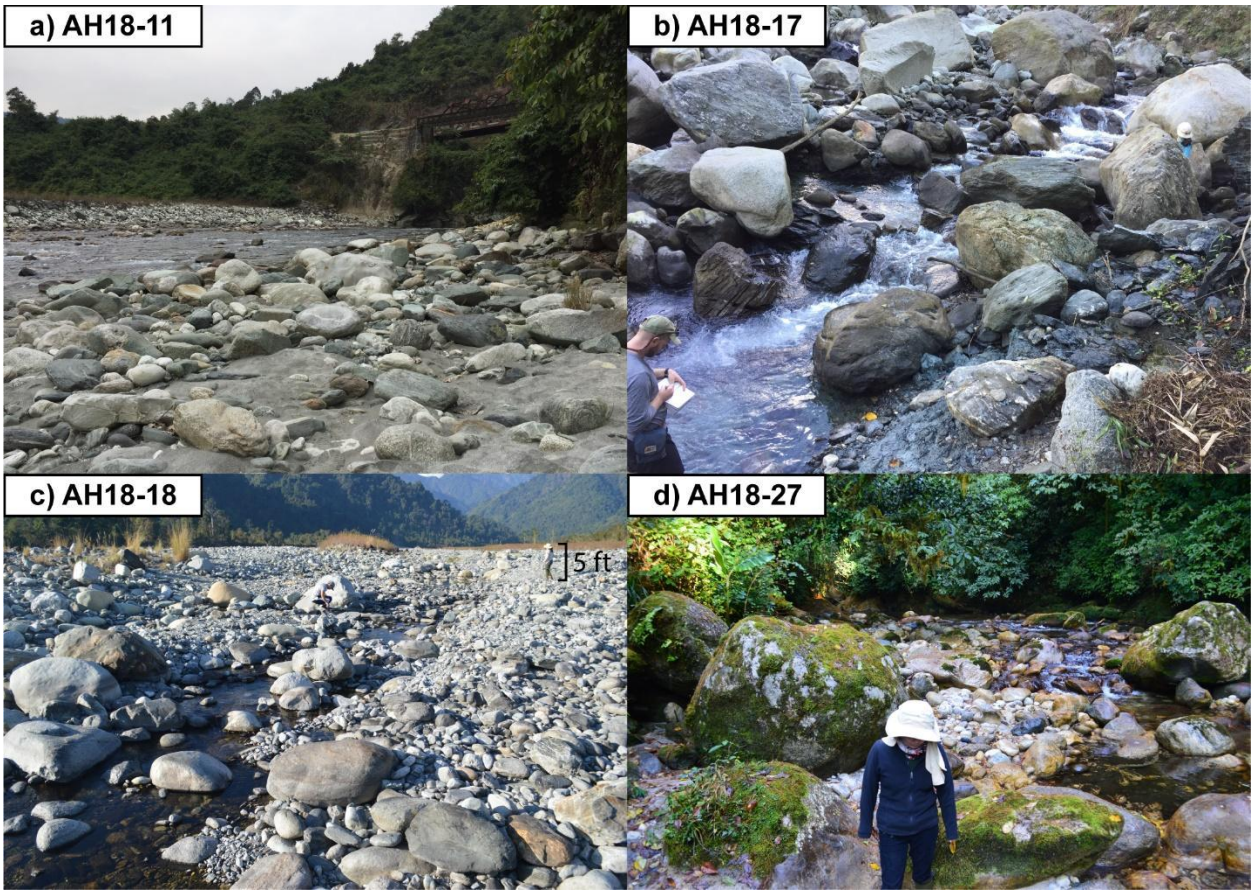

Fig. B7: Field photos of detrital sand sample locations at basin outlets. (**a**) AH18-11, (**b**) AH18-17, (**c**) AH18-18, (**d**) AH18-27. AH18-17 and AH18-18 are located near the rangefront while AH18-11 and AH18-27 are in the hinterland. People shown in the photos are 5-6 ft tall.

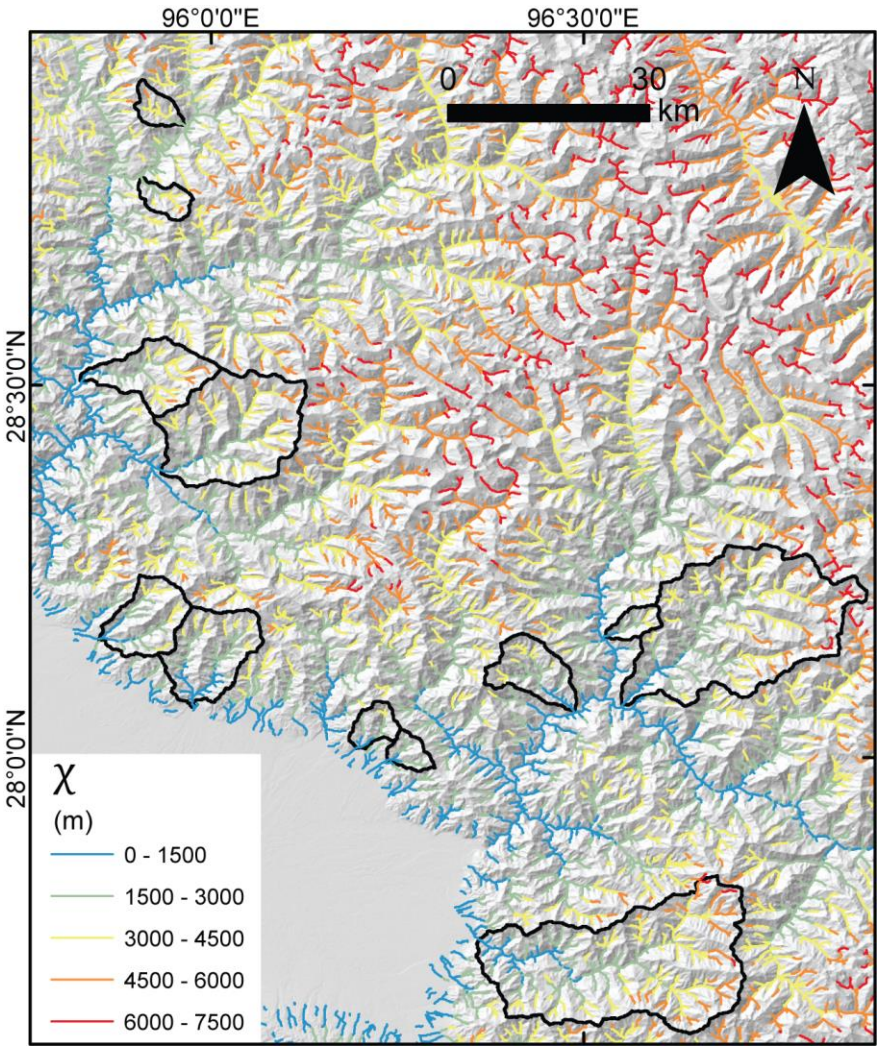

Fig. B8: Map of χ for the easternmost Himalaya. χ is calculated for 1 km long channel segments with > 1 km^2 upstream drainage area, at > 350 m elevation, and θ = 0.45. Study basins are delineated by a black border.

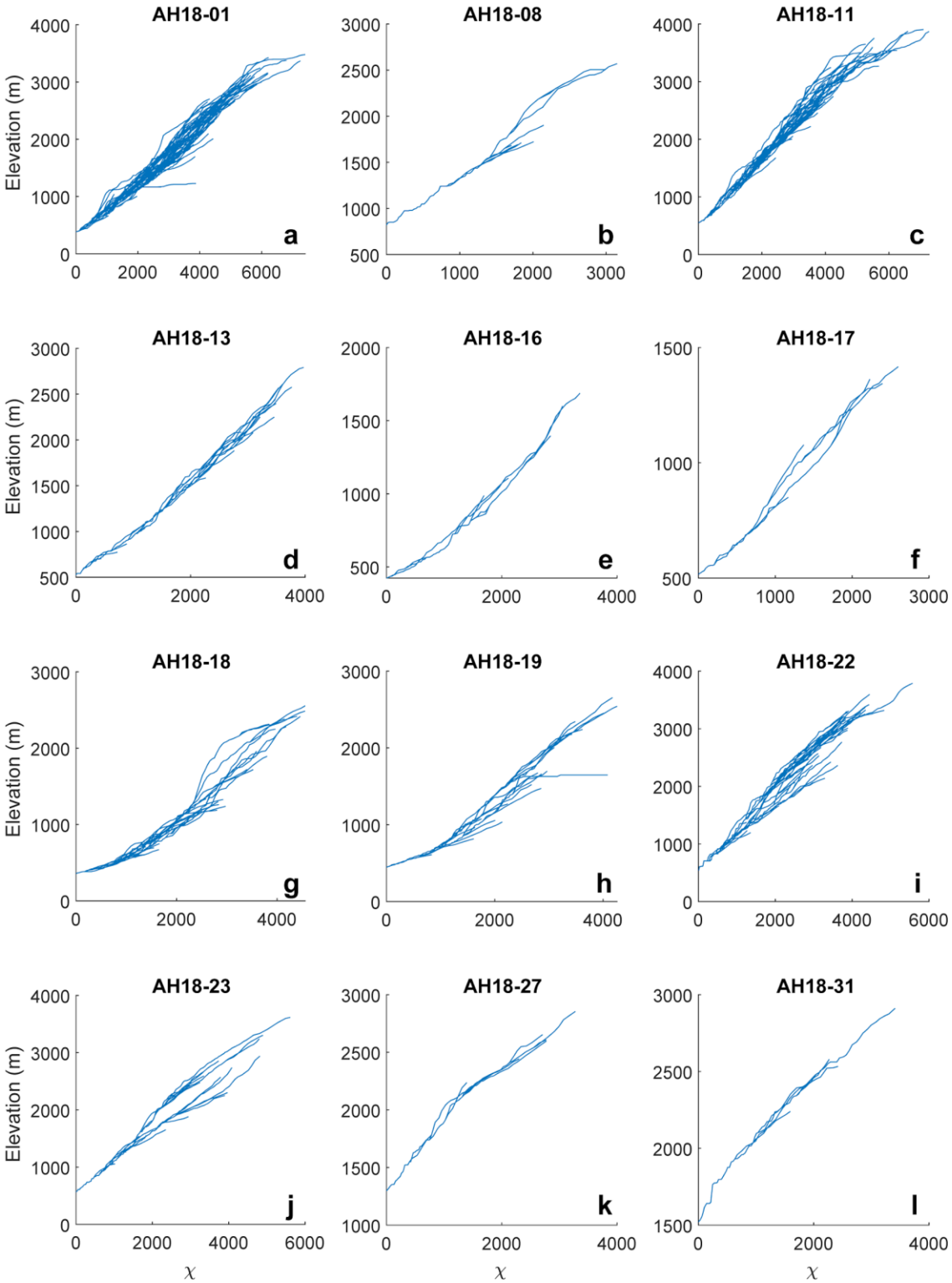

Fig. B9: Relationship between χ and elevation for our study basins in the easternmost Himalaya. Lines in blue indicate channel profiles where channel points have > 1 km^2 upstream drainage area. Most main channel profiles, except for AH18-08, 18, and 27, do not show differences in channel steepness in upstream and downstream portions.

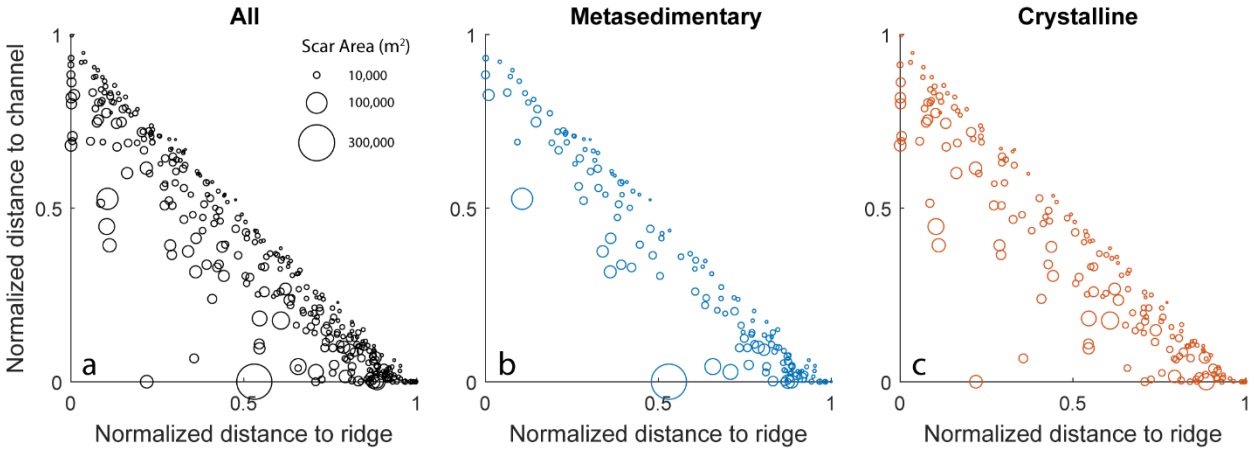

Fig. B10: Hillslope positions of landslides from in the easternmost Himalaya. Landslides are mapped from 2017 Landsat 8 imagery within 12 basins. Results from (**a**) all landslides and landslides from basins dominated by (**b**) metasedimentary or (**c**) crystalline lithology. The steepest descent distance was used to calculate the distance from the highest pixel to the nearest ridgeline (distance to ridge) as well as from the lowest pixel to the nearest channel (distance to channel) for each mapped landslide following Meunier et al. (2008). Distances were normalized by the landslide's respective total hillslope length. The size of circles linearly correlates with the size of mapped landslide scars.

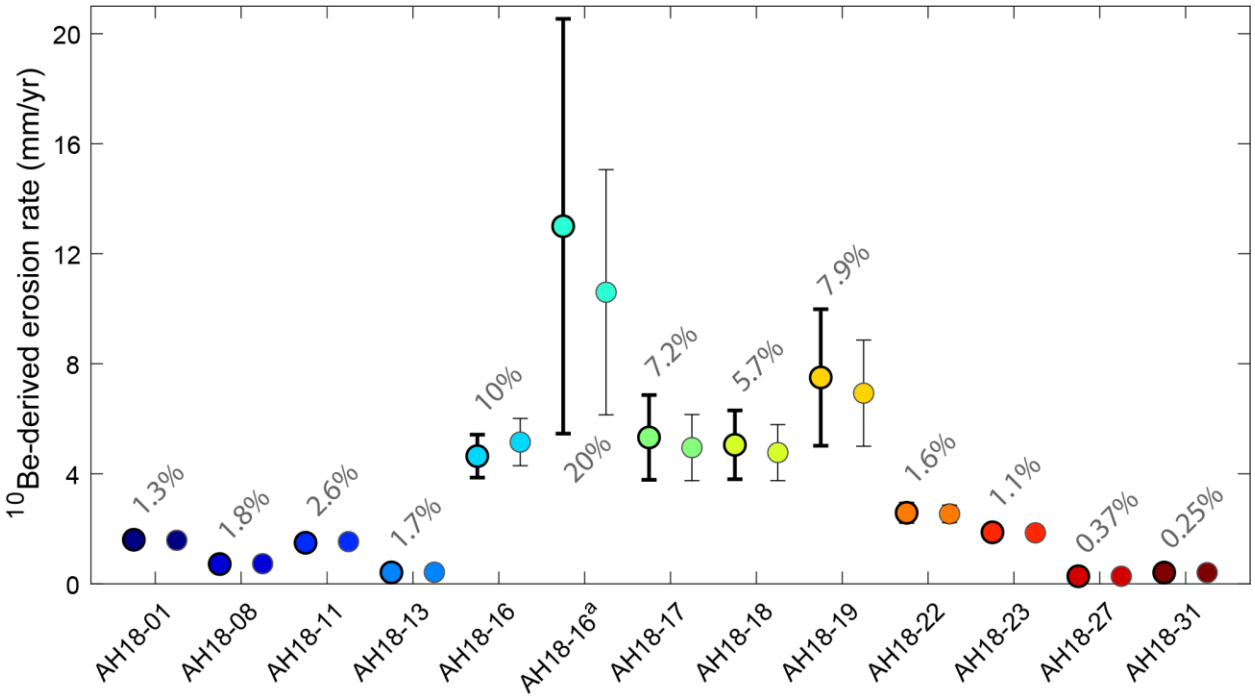

Fig. B11: ^{10}Be-derived erosion rates calculated using different blank scenarios. Results from samples in the easternmost Himalaya displayed in order of sample ID. Circles represent blank-corrected erosion rates and are shown with ±1σ error bars. Erosion rates in thick, black outline were calculated using the average of the four lowest blanks (^{10}Be/^{9}Be = 6.2×10^{-16}) from both sample batches. Points in thin, gray outline were calculated using the averaged blank for each batch on their respective samples (^{10}Be/^{9}Be = 5.0×10^{-16} for the 2018 batch, and 9.6×10^{-16} for the 2021 batch). Erosion rates are colored according to sample ID. Numbers in gray represent the percent difference between inferred erosion rates calculated using the different blank scenarios for each sample. AH18-16[a] was our first attempt at measuring ^{10}Be-derived erosion rate using ~20 g of quartz. AH18-16 was our second attempt using ~40 g of quartz, which we used in our analyses.

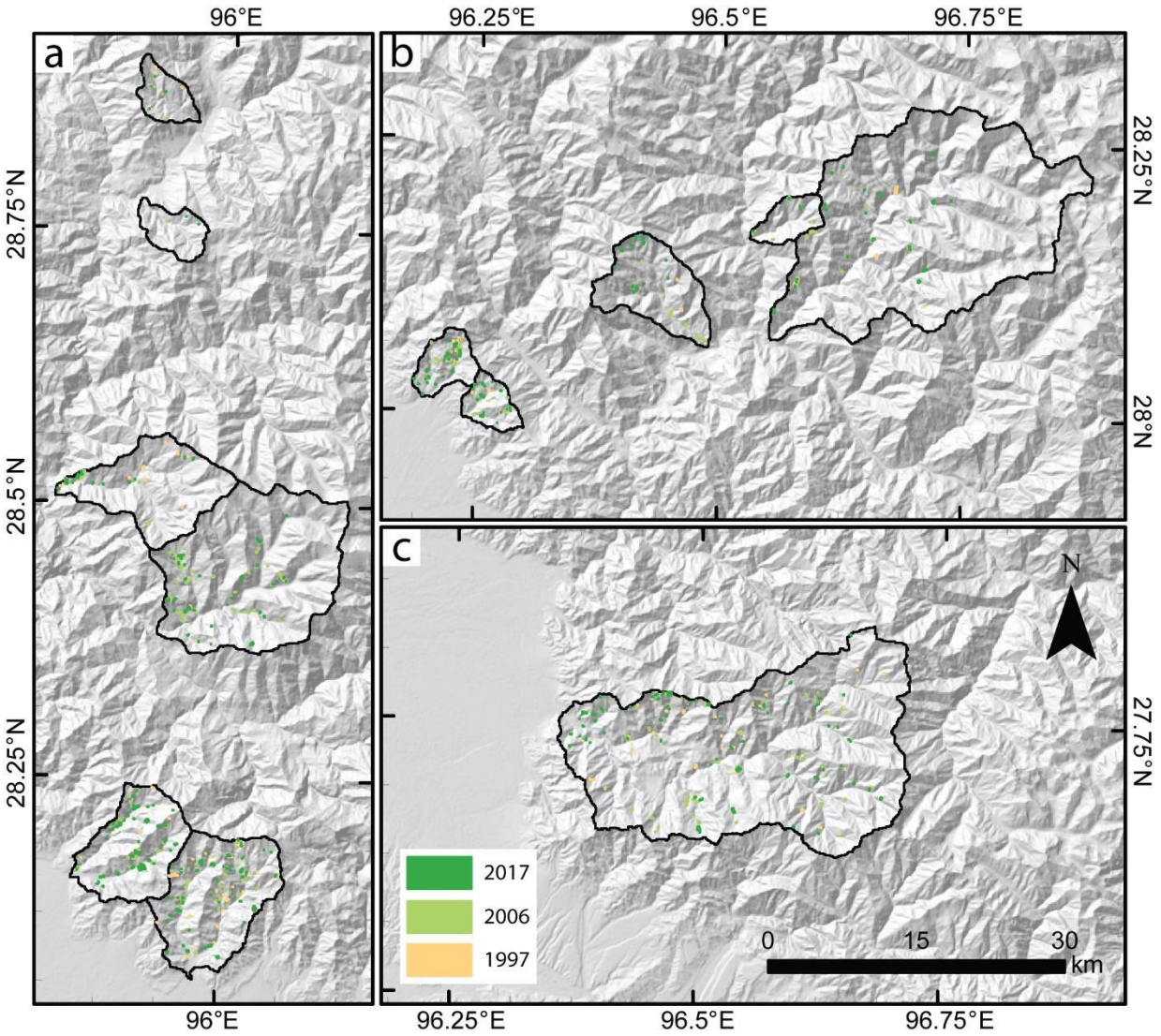

Fig. B12: Maps of landslides across studied basins in the easternmost Himalaya. Landslides from 1997, 2006, and 2017 are shown in their respective colors.

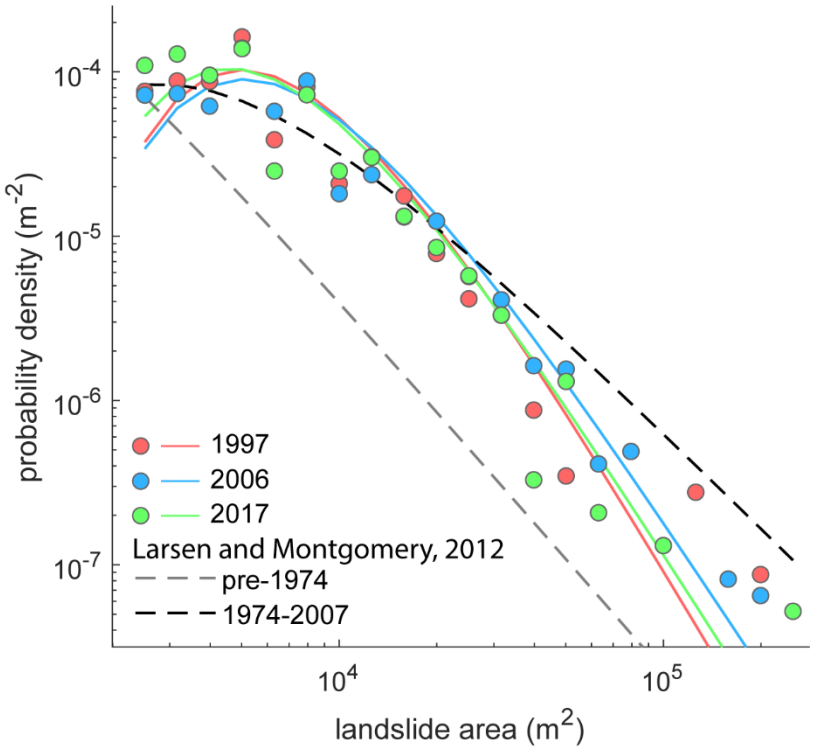

Fig. B13: Probability density as a function of landslide area. Curves indicate the best-fit inverse-gamma functions for the landslide area probability density distributions shown as points for the 1997 (red), 2006 (blue), and 2017 (green) inventories. We show best-fit inverse-gamma functions reported in Larsen and Montgomery (Larsen and Montgomery, 2012) for the pre-1974 and 1974-2007 landslide inventories from a nearby region of the eastern Himalaya in gray and black dashed lines, respectively.

Table B1: Basin-averaged topographic, climatic, and erosional variables

Sample	Reference	Sample Latitude (N)	Sample Longitude (E)	Latitude (N)	Longitude (E)	Drainage Area	Elevation		Local Relief (2.5 km radius)		Local Relief (5 km radius)		Slope (gradient)		Mean Annual Precipitation		Number of Extreme Rainfall Events	
							mean	± 1σ	mean	± 1σ	mean	± 1σ	mean	± 1σ	mean	± 1σ	mean	± 1σ
		◦	◦	◦	◦	km^2	m	m	m	m	m	m	--	--	m/yr	m/yr	events/yr	events/yr
AH18-01	This Study	27.7544	96.3605	27.7230	96.5569	527	2174	812	1634	277	2315	263	0.61	0.24	5.12	0.84	10.5	1.0
AH18-08	This Study	28.1625	96.5291	28.1802	96.5694	24	2154	623	1995	196	2770	246	0.76	0.25	4.22	0.13	12.9	0.3
AH18-11	This Study	28.0704	96.5521	28.1785	96.7093	473	2727	855	1813	258	2538	298	0.71	0.28	3.39	0.98	10.1	1.7
AH18-13	This Study	28.0624	96.4862	28.1152	96.4319	78	2087	737	1923	240	2693	233	0.73	0.28	5.26	0.47	11.8	0.9
AH18-16	This Study	28.0121	96.1957	28.0425	96.2190	30	1299	508	1604	290	2215	114	0.61	0.28	4.14	0.50	12.1	0.8
AH18-17	This Study	27.9961	96.2359	28.0062	96.2657	23	1310	360	1366	108	1737	73	0.59	0.23	4.50	0.57	11.8	0.6
AH18-18	This Study	28.0660	95.9778	28.1410	95.9988	128	1566	690	1525	319	2164	392	0.60	0.25	4.92	0.90	11.0	0.9
AH18-19	This Study	28.1599	95.8489	28.1851	95.9149	92	1697	704	1661	385	2450	349	0.63	0.28	4.91	0.86	10.8	0.6
AH18-22	This Study	28.3859	95.9328	28.4405	96.0292	252	2653	828	1910	256	2721	298	0.70	0.27	3.34	0.38	10.3	0.8
AH18-23	This Study	28.5059	95.8261	28.5141	95.9265	108	2382	801	1745	238	2623	311	0.61	0.23	3.12	0.26	9.8	1.0
AH18-27	This Study	28.7780	95.9056	28.7493	95.9391	27	2551	456	1606	177	2316	171	0.61	0.22	2.37	0.11	8.0	0.4
AH18-31	This Study	28.8492	95.9638	28.8723	95.9266	26	2648	426	1500	128	2303	171	0.59	0.20	1.78	0.14	8.7	0.4
123	Portenga et al., 2015	27.2479	90.2088	27.3099	90.2687	156	2878	752	1822	197	2549	222	0.71	0.28	1.86	0.25	5.4	0.6
126	Portenga et al., 2015	27.2271	90.1696	27.2627	90.1709	19	2095	416	1553	126	2205	131	0.65	0.24	1.69	0.18	4.6	0.4
127	Portenga et al., 2015	27.2237	90.1846	27.1889	90.2560	75	2581	652	1620	141	2304	169	0.61	0.20	2.02	0.16	5.4	0.5
131	Portenga et al., 2015	27.0796	90.0754	27.1080	90.1990	238	1921	758	1392	204	2051	303	0.55	0.21	2.11	0.26	5.2	0.6
134	Portenga et al., 2015	27.1837	90.0721	27.2500	90.2431	443	2515	863	1736	243	2426	284	0.67	0.26	1.82	0.24	5.1	0.6
137	Portenga et al., 2015	27.2670	90.0420	27.3368	90.0508	65	2064	685	1609	182	2238	264	0.70	0.25	1.13	0.19	3.7	0.5
139	Portenga et al., 2015	27.2704	90.0371	27.2393	89.9465	90	1968	548	1388	168	2068	203	0.56	0.18	1.41	0.06	4.1	0.2
140	Portenga et al., 2015	27.4554	89.9029	27.4481	89.8166	73	2473	545	1407	142	1986	153	0.50	0.19	1.29	0.08	3.9	0.4
144	Portenga et al., 2015	27.5063	89.9620	27.5721	90.0270	147	2609	511	1305	176	1885	136	0.53	0.24	1.21	0.20	4.7	0.6
152	Portenga et al., 2015	27.6813	89.9106	27.7460	89.8755	83	3235	746	1539	304	2385	293	0.56	0.23	1.15	0.23	4.1	0.3
237	Portenga et al., 2015	27.6687	89.7738	27.6761	89.6929	108	2909	672	1630	232	2442	363	0.56	0.21	1.71	0.31	4.5	0.7
17	Portenga et al., 2015	27.5295	89.8771	27.5238	89.7831	114	2387	485	1229	175	1867	195	0.45	0.19	1.13	0.10	4.0	0.1
20	Portenga et al., 2015	27.5079	89.7921	27.4876	89.7785	15	2752	342	1312	102	1904	138	0.47	0.17	1.32	0.05	4.0	0.0
23	Portenga et al., 2015	27.4737	90.1679	27.4942	90.1538	41	3275	250	1002	206	1669	417	0.35	0.19	1.20	0.11	4.0	0.2
2	Roux-Mallouf et al., 2015	27.7212	89.7580	27.7777	89.8031	76	3443	740	1590	317	2449	330	0.55	0.23	1.30	0.15	5.0	0.8
12	Roux-Mallouf et al., 2015	27.1884	89.5642	27.2099	89.6286	95	3624	609	1327	353	1970	248	0.50	0.25	1.38	0.40	3.0	0.4
13	Roux-Mallouf et al., 2015	27.0551	89.5922	27.1023	89.6139	66	3145	525	1559	249	2287	345	0.57	0.24	2.31	0.28	4.8	0.7
22	Roux-Mallouf et al., 2015	27.6821	89.9107	27.7461	89.8754	83	3239	742	1540	304	2386	293	0.56	0.23	1.15	0.23	4.1	0.3
27	Roux-Mallouf et al., 2015	27.6340	89.8009	27.5944	89.7372	69	2589	602	1492	240	2140	221	0.52	0.22	1.57	0.21	4.7	0.7
30	Roux-Mallouf et al., 2015	27.5761	89.6356	27.5710	89.5948	18	3558	465	1513	133	2108	110	0.53	0.20	1.01	0.23	3.2	0.4
35	Roux-Mallouf et al., 2015	27.5447	89.6587	27.5436	89.6887	16	3185	300	1212	83	1641	129	0.46	0.18	1.15	0.15	4.0	0.2
38	Roux-Mallouf et al., 2015	27.5041	89.6331	27.5236	89.5716	49	3727	550	1312	232	1920	175	0.49	0.22	1.29	0.12	3.1	0.3
51	Roux-Mallouf et al., 2015	27.4961	89.4382	27.4868	89.4672	10	3113	330	1358	156	1909	32	0.46	0.16	0.92	0.08	3.7	0.3
56	Roux-Mallouf et al., 2015	27.4449	89.4431	27.4502	89.4650	14	3105	303	1202	87	1620	97	0.40	0.15	0.81	0.04	3.1	0.2
62	Roux-Mallouf et al., 2015	27.4223	89.3622	27.4090	89.3411	9	3333	348	1360	99	1757	76	0.46	0.14	1.18	0.04	3.7	0.3
65	Roux-Mallouf et al., 2015	27.4232	89.6468	27.3856	89.6691	30	3190	426	1222	150	1793	160	0.42	0.16	1.55	0.33	3.6	0.5
73	Roux-Mallouf et al., 2015	27.3945	89.6169	27.3783	89.6339	12	3059	314	1333	97	1848	47	0.49	0.17	1.56	0.09	4.5	0.5
77	Roux-Mallouf et al., 2015	27.3195	89.5654	27.3062	89.6537	141	3531	534	1265	221	1860	235	0.45	0.17	0.87	0.39	2.5	0.5
88	Roux-Mallouf et al., 2015	27.2338	89.4833	27.2577	89.4605	23	3234	315	1160	104	1711	99	0.39	0.16	1.35	0.19	3.4	0.4
90	Roux-Mallouf et al., 2015	27.2342	89.5296	27.2385	89.5771	36	3360	530	1478	204	2182	185	0.49	0.22	1.37	0.11	3.8	0.4
96	Roux-Mallouf et al., 2015	27.6624	89.8858	27.6885	89.8558	19	2375	422	1576	161	2360	179	0.55	0.19	0.83	0.03	4.5	0.4
104	Roux-Mallouf et al., 2015	26.9413	89.5953	26.9406	89.5431	47	1958	480	1373	183	2111	199	0.46	0.19	4.35	0.61	8.3	0.5
106	Roux-Mallouf et al., 2015	26.9540	89.5979	26.9688	89.5618	16	2180	575	1654	230	2425	149	0.47	0.19	3.17	0.15	7.1	0.2
112	Roux-Mallouf et al., 2015	26.8794	89.5971	26.8892	89.5618	30	1567	348	1346	132	1774	71	0.45	0.19	5.83	0.52	8.9	0.3

Table B1: Basin-averaged topographic, climatic, and erosional variables (cont 1)

Sample	Reference	Channel Steepness (integral)		Channel Steepness (basin averaged)	Discharge-based Channel Steepness	Distance from Main Frontal Thrust		Distance from Main Central Thrust		Erosional Coefficient (K) n = 0.65	Modified Erosional Coefficient (K_{lp}) n = 1.71	Metasedimentary Lithology	Crystalline Lithology	Erosion Rate[a]	
		mean	± 1σ	mean	mean	mean	± 1σ	mean	± 1σ					mean	± 1σ
		$m^{0.9}$	$m^{0.9}$	$m^{0.9}$	($m^{1.35}year^{-0.45}$)	km	km	km	km	$m^{0.41}/yr$	$m^{-1.30}yr^{-0.23}$ (*10^4)	%	%	mm/yr	mm/yr
AH18-01	This Study	228	0.9	238	488	--	--	17	9	0.0460	0.414	2	98	1.60	0.18
AH18-08	This Study	285	5.2	273	526	8	2	--	--	0.1682	2.191	0	100	0.72	0.06
AH18-11	This Study	280	1.1	268	456	9	1	--	--	0.1822	2.232	0	100	1.49	0.14
AH18-13	This Study	264	1.8	274	583	11	4	--	--	0.1559	1.487	0	100	0.41	0.04
AH18-16	This Study	160	3.2	176	344	12	3	--	--	0.2184	2.018	82	18	4.64	0.78
AH18-17	This Study	175	2.7	182	368	--	--	6	4	0.0573	0.615	56	44	5.3	1.5
AH18-18	This Study	205	3.4	213	453	--	--	12	2	0.0465	0.578	72	28	5.1	1.3
AH18-19	This Study	224	3.7	224	478	--	--	38	1	0.0071	0.122	59	41	7.5	2.5
AH18-22	This Study	339	2.1	299	513	--	--	51	2	0.0115	0.287	16	84	2.58	0.33
AH18-23	This Study	285	3.0	262	440	--	--	35	2	0.0178	0.163	0	100	1.87	0.22
AH18-27	This Study	267	4.9	239	354	--	--	46	8	0.0375	0.434	0	100	0.27	0.02
AH18-31	This Study	233	4.2	204	271	--	--	20	2	0.0108	0.079	0	100	0.41	0.03
123	Portenga et al., 2015	289	2.0	285	375	--	--	39	3	0.0207	0.341	0	100	*0.84*	*0.07*
126	Portenga et al., 2015	205	2.7	191	235	--	--	35	2	0.0081	0.235	0	100	*0.26*	*0.02*
127	Portenga et al., 2015	280	1.4	253	345	--	--	26	2	0.0153	0.285	0	100	*0.61*	*0.05*
131	Portenga et al., 2015	229	1.1	207	292	--	--	18	4	0.0306	0.662	0	100	*1.06*	*0.09*
134	Portenga et al., 2015	280	1.0	268	348	--	--	32	6	0.0186	0.341	0	100	*0.74*	*0.07*
137	Portenga et al., 2015	233	1.6	236	254	--	--	34	2	0.0182	0.506	0	100	*0.64*	*0.06*
139	Portenga et al., 2015	210	1.0	194	226	--	--	24	2	0.0078	0.247	0	100	*0.26*	*0.02*
140	Portenga et al., 2015	217	1.4	197	221	--	--	11	4	0.0037	0.125	0	100	*0.13*	*0.01*
144	Portenga et al., 2015	195	1.3	175	191	--	--	35	5	0.0039	0.158	0	100	*0.12*	*0.01*
152	Portenga et al., 2015	355	5.6	297	329	--	--	38	3	0.0053	0.125	0	100	*0.25*	*0.02*
237	Portenga et al., 2015	270	1.8	257	312	--	--	26	3	0.0024	0.052	0	100	*0.09*	*0.01*
17	Portenga et al., 2015	193	1.3	171	184	--	--	13	3	0.0040	0.169	0	100	*0.12*	*0.01*
20	Portenga et al., 2015	185	4.1	168	191	--	--	9	1	0.0044	0.171	0	100	*0.13*	*0.01*
23	Portenga et al., 2015	76	1.3	75	80	--	--	45	2	0.0015	0.144	0	100	*0.025*	*0.002*
2	Roux-Mallouf et al., 2015	362	4.9	284	320	--	--	39	4	0.0046	0.114	0	100	*0.21*	*0.02*
12	Roux-Mallouf et al., 2015	280	3.9	225	252	--	--	4	2	0.0022	0.069	4	96	*0.09*	*0.01*
13	Roux-Mallouf et al., 2015	329	5.9	264	379	--	--	5	2	0.0039	0.068	0	100	*0.17*	*0.02*
22	Roux-Mallouf et al., 2015	354	5.6	297	329	--	--	38	3	0.0063	0.148	0	100	*0.29*	*0.03*
27	Roux-Mallouf et al., 2015	227	2.2	196	237	--	--	18	3	0.0058	0.177	0	100	*0.20*	*0.02*
30	Roux-Mallouf et al., 2015	246	1.7	228	215	--	--	13	1	0.0039	0.152	0	100	*0.14*	*0.01*
35	Roux-Mallouf et al., 2015	163	2.1	148	159	--	--	11	1	0.0016	0.079	0	100	*0.045*	*0.004*
38	Roux-Mallouf et al., 2015	264	4.7	215	237	--	--	7	2	0.0031	0.104	0	100	*0.12*	*0.01*
51	Roux-Mallouf et al., 2015	168	1.9	159	155	--	--	3	1	0.0029	0.150	0	100	*0.08*	*0.01*
56	Roux-Mallouf et al., 2015	171	3.2	166	150	--	--	1	1	0.0014	0.076	47	53	*0.039*	*0.003*
62	Roux-Mallouf et al., 2015	174	2.4	167	179	61	1	--	--	0.0025	0.105	53	47	*0.07*	*0.01*
65	Roux-Mallouf et al., 2015	176	2.2	148	170	--	--	1	1	0.0012	0.054	49	51	*0.035*	*0.003*
73	Roux-Mallouf et al., 2015	172	2.4	151	184	63	1	--	--	0.0008	0.031	99	1	*0.022*	*0.002*
77	Roux-Mallouf et al., 2015	235	1.4	200	177	--	--	3	2	0.0021	0.109	39	61	*0.07*	*0.01*
88	Roux-Mallouf et al., 2015	229	5.5	171	191	45	2	--	--	0.0011	0.047	100	0	*0.037*	*0.003*
90	Roux-Mallouf et al., 2015	290	4.9	241	280	--	--	1	1	0.0028	0.077	39	61	*0.11*	*0.01*
96	Roux-Mallouf et al., 2015	236	4.0	235	214	--	--	32	1	0.0053	0.200	0	100	*0.19*	*0.02*
104	Roux-Mallouf et al., 2015	209	2.0	205	389	--	--	5	2	0.0296	0.371	0	100	*0.97*	*0.13*
106	Roux-Mallouf et al., 2015	318	3.4	311	522	--	--	7	1	0.0085	0.085	0	100	*0.37*	*0.04*
112	Roux-Mallouf et al., 2015	180	2.8	191	426	--	--	2	1	0.0026	0.025	7	93	*0.08*	*0.01*

Table B1: Basin-averaged topographic, climatic, and erosional variables (cont 2)

Sample	Reference	Sample Latitude (N)	Sample Longitude (E)	Latitude (N)	Longitude (E)	Drainage Area	Elevation		Local Relief (2.5 km radius)		Local Relief (5 km radius)		Slope (gradient)		Mean Annual Precipitation		Number of Extreme Rainfall Events	
							mean	± 1σ	mean	± 1σ	mean	± 1σ	mean	± 1σ	mean	± 1σ	mean	± 1σ
		°	°	°	°	km^2	m	m	m	m	m	m	--	--	m/yr	m/yr	events/yr	events/yr
113	Roux-Mallouf et al., 2015	27.5908	89.8508	27.5780	89.8194	20	2023	330	1199	144	1737	130	0.38	0.14	1.10	0.09	4.8	0.3
116	Roux-Mallouf et al., 2015	27.5302	89.7987	27.5345	89.7548	55	2575	399	1241	188	1916	186	0.47	0.20	1.11	0.07	4.0	0.1
336	Roux-Mallouf et al., 2015	27.8944	89.7424	27.9259	89.7276	13	3551	565	1719	240	2356	104	0.59	0.25	1.76	0.32	4.7	0.5
BT0901	Adams et al., 2016	27.3674	90.5366	27.4152	90.6072	80	2869	592	1500	167	2303	212	0.55	0.21	1.15	0.26	4.3	0.4
BT0902	Adams et al., 2016	27.3345	90.5939	27.3523	90.6710	133	2867	777	1694	226	2540	266	0.56	0.19	1.37	0.15	4.1	0.2
BT0903	Adams et al., 2016	27.4906	90.5250	27.5060	90.5599	42	3089	378	1335	168	2016	225	0.45	0.17	1.16	0.12	4.8	0.4
BT0904	Adams et al., 2016	27.4978	90.6606	27.5329	90.6034	48	3484	293	869	166	1380	184	0.30	0.13	0.88	0.09	3.6	0.4
BT0905	Adams et al., 2016	27.5125	90.6586	27.5417	90.6482	27	3416	267	950	136	1245	52	0.33	0.12	0.72	0.07	3.0	0.2
BT0906	Adams et al., 2016	27.4945	90.6655	27.4733	90.6271	26	3451	312	1017	163	1507	194	0.37	0.16	1.11	0.08	4.3	0.4
BT0907	Adams et al., 2016	27.4952	90.6687	27.5194	90.6233	106	3433	303	913	178	1364	191	0.32	0.14	0.90	0.16	3.6	0.6
BT0909	Adams et al., 2016	27.6245	90.8772	27.6562	90.8304	65	3579	402	1087	130	1512	123	0.43	0.19	0.98	0.16	3.9	0.2
BT0910	Adams et al., 2016	27.6205	90.8906	27.6227	90.9536	58	3615	310	969	155	1524	191	0.33	0.13	0.88	0.11	3.2	0.4
BT0912	Adams et al., 2016	27.6647	90.9020	27.6842	90.9484	50	3822	315	1122	136	1650	175	0.45	0.19	1.03	0.08	3.7	0.5
BT0922	Adams et al., 2016	27.6105	90.6715	27.6176	90.6090	114	3585	379	1047	166	1599	235	0.35	0.15	0.86	0.21	3.3	0.5
BT0926	Adams et al., 2016	27.4780	91.1858	27.4686	91.2472	59	2685	594	1691	265	2439	262	0.54	0.21	1.15	0.23	4.4	0.5
BT0928	Adams et al., 2016	27.5583	91.2089	27.5515	91.2701	53	2679	590	1705	194	2430	243	0.58	0.18	0.89	0.07	3.8	0.3
BT0929	Adams et al., 2016	27.6876	91.1702	27.6722	91.1382	13	2222	419	1528	189	2387	277	0.63	0.26	1.41	0.02	5.1	0.2
BT0931	Adams et al., 2016	27.7149	91.1502	27.6769	91.0726	90	2770	661	1712	208	2361	170	0.65	0.26	1.35	0.17	5.3	1.1
BT0973	Adams et al., 2016	27.4403	90.9638	27.4645	90.9831	20	3778	122	1018	300	1900	260	0.28	0.11	0.60	0.08	2.2	0.2
BT0993	Adams et al., 2016	27.5256	89.8671	27.5238	89.7821	113	2399	475	1234	169	1872	192	0.45	0.19	1.13	0.10	4.0	0.1
BT0994	Adams et al., 2016	27.6685	89.7700	27.6762	89.6924	108	2918	665	1633	230	2448	356	0.56	0.21	1.71	0.31	4.5	0.7
BT0995	Adams et al., 2016	27.4560	89.9034	27.4481	89.8166	73	2473	545	1407	142	1986	153	0.50	0.19	1.29	0.08	3.9	0.4
BT0996	Adams et al., 2016	27.2976	89.9664	27.2838	89.9219	41	1950	451	1495	159	2236	221	0.53	0.19	1.48	0.05	4.2	0.4
BT0998	Adams et al., 2016	27.2674	90.0473	27.3371	90.0508	65	2070	681	1610	181	2241	261	0.70	0.24	1.13	0.19	3.7	0.5
BT09108	Adams et al., 2016	27.4318	89.6818	27.4100	89.7198	42	3214	327	1157	175	1745	144	0.42	0.16	1.40	0.28	3.3	0.4
BT1021	Adams et al., 2016	27.7267	91.1479	27.7858	91.1862	72	3117	726	1562	232	2370	161	0.57	0.25	1.49	0.26	5.3	0.9
BT1036	Adams et al., 2016	27.3294	89.4823	27.3086	89.4448	37	3145	400	1289	185	1740	91	0.43	0.16	1.22	0.11	3.3	0.4
BT1042	Adams et al., 2016	27.4264	90.1042	27.4419	90.1070	39	3367	273	1063	214	1670	310	0.35	0.19	1.70	0.20	4.4	0.4
BT1043	Adams et al., 2016	27.4145	89.9948	27.4357	90.0126	61	3016	260	971	227	1785	304	0.30	0.17	1.58	0.15	4.0	0.1
BT1044	Adams et al., 2016	27.7681	89.7247	27.7714	89.6472	89	3715	703	1733	230	2676	261	0.60	0.26	0.65	0.39	2.1	0.8
BT1111	Adams et al., 2016	27.2942	90.0119	27.3277	90.0166	26	2027	560	1788	218	2611	182	0.68	0.22	1.18	0.07	4.2	0.4
BT1112	Adams et al., 2016	27.2677	90.0211	27.2388	89.9452	89	1985	534	1392	166	2074	199	0.56	0.18	1.41	0.05	4.1	0.2
BT1135	Adams et al., 2016	27.2286	90.6428	27.2660	90.6992	85	2406	658	1770	324	2621	268	0.66	0.26	1.47	0.18	4.6	0.5
BT1142	Adams et al., 2016	27.5601	90.4426	27.5652	90.3849	45	2869	337	1070	99	1632	175	0.44	0.16	1.21	0.07	4.8	0.5
BT1143	Adams et al., 2016	27.5407	90.4425	27.5326	90.4141	14	2765	331	1274	112	1722	47	0.49	0.16	1.04	0.03	4.2	0.3
BT1145	Adams et al., 2016	27.2887	91.2326	27.2751	91.2733	45	2056	360	1294	120	1945	243	0.48	0.19	1.21	0.11	3.3	0.4
BT1146	Adams et al., 2016	27.3851	91.2036	27.3964	91.2588	49	2320	597	1793	239	2541	252	0.61	0.21	1.30	0.13	4.0	0.1
BT1147	Adams et al., 2016	27.5164	91.1712	27.5565	91.0628	275	2673	644	1646	228	2284	179	0.60	0.23	0.94	0.17	3.7	0.8
BT1148	Adams et al., 2016	27.6641	91.4376	27.6524	91.3905	52	3052	509	1483	192	2192	167	0.45	0.16	1.03	0.20	3.9	0.7
BT1149	Adams et al., 2016	27.6193	91.4854	27.6127	91.4550	14	2672	416	1456	154	2072	131	0.48	0.17	1.04	0.07	4.0	0.1
BT1150	Adams et al., 2016	27.5843	91.4904	27.5810	91.4106	95	2934	515	1435	141	1997	119	0.50	0.17	0.97	0.16	3.9	0.2
BT1151	Adams et al., 2016	27.5541	91.5215	27.5627	91.5484	22	2685	425	1573	190	2368	165	0.52	0.15	1.25	0.05	4.5	0.4
BT1152	Adams et al., 2016	27.4015	91.5484	27.4194	91.4979	35	2135	621	1665	189	2339	151	0.59	0.22	0.95	0.16	3.1	0.3
BT1153	Adams et al., 2016	27.3447	91.6238	27.2844	91.6335	56	2522	682	1688	146	2466	202	0.54	0.24	1.30	0.07	4.1	0.5
BT1154	Adams et al., 2016	27.3579	91.6721	27.3008	91.6921	66	2610	640	1547	179	2357	210	0.50	0.19	1.18	0.05	3.7	0.4
BT1161	Adams et al., 2016	27.4755	90.3502	27.5070	90.3703	29	3065	234	970	81	1377	88	0.31	0.12	1.16	0.10	3.9	0.2

Table B1: Basin-averaged topographic, climatic, and erosional variables (cont 3)

Sample	Reference	Channel Steepness (integral)		Channel Steepness (basin averaged)	Discharge-based Channel Steepness	Distance from Main Frontal Thrust		Distance from Main Central Thrust		Erosional Coefficient (K) n = 0.65	Modified Erosional Coefficient (K_{tp}) n = 1.71	Metasedimentary Lithology	Crystalline Lithology	Erosion Rate[a]	
		mean	± 1σ	mean	mean	mean	± 1σ	mean	± 1σ					mean	± 1σ
		$m^{0.9}$	$m^{0.9}$	$m^{0.9}$	($m^{1.35}year^{-0.45}$)	km	km	km	km	$m^{0.41}/yr$	$m^{-1.30}yr^{-0.23}$ (*10^4)	%	%	mm/yr	mm/yr
113	Roux-Mallouf et al., 2015	179	1.4	167	177	--	--	19	1	0.0025	0.109	0	100	*0.07*	*0.01*
116	Roux-Mallouf et al., 2015	174	1.9	157	166	--	--	12	2	0.0036	0.171	0	100	*0.11*	*0.01*
336	Roux-Mallouf et al., 2015	271	9.4	251	310	--	--	53	1	0.0423	0.924	0	100	*1.64*	*0.20*
BT0901	Adams et al., 2016	302	3.7	257	278	--	--	45	2	0.0083	0.235	0	100	*0.35*	*0.05*
BT0902	Adams et al., 2016	347	3.3	298	351	--	--	35	3	0.0088	0.183	0	100	*0.40*	*0.05*
BT0903	Adams et al., 2016	218	2.9	190	198	--	--	55	1	0.0052	0.211	0	100	*0.18*	*0.02*
BT0904	Adams et al., 2016	105	0.8	96	91	--	--	51	2	0.0033	0.312	0	100	*0.07*	*0.01*
BT0905	Adams et al., 2016	110	3.4	114	97	--	--	47	2	0.0019	0.169	0	100	*0.041*	*0.004*
BT0906	Adams et al., 2016	112	1.7	116	123	--	--	48	2	0.0046	0.274	0	100	*0.10*	*0.01*
BT0907	Adams et al., 2016	101	1.2	101	97	--	--	49	3	0.0037	0.312	0	100	*0.08*	*0.01*
BT0909	Adams et al., 2016	145	2.0	128	128	--	--	33	3	0.0025	0.162	0	100	*0.06*	*0.01*
BT0910	Adams et al., 2016	162	2.1	130	122	--	--	21	2	0.0022	0.170	0	100	*0.06*	*0.01*
BT0912	Adams et al., 2016	194	2.4	163	164	--	--	25	2	0.0032	0.166	0	100	*0.10*	*0.01*
BT0922	Adams et al., 2016	156	1.6	138	130	--	--	53	4	0.0026	0.171	0	100	*0.07*	*0.01*
BT0926	Adams et al., 2016	373	5.1	303	332	73	2	--	--	0.0029	0.071	97	3	*0.14*	*0.01*
BT0928	Adams et al., 2016	316	4.2	291	278	--	--	2	2	0.0037	0.109	41	59	*0.16*	*0.01*
BT0929	Adams et al., 2016	209	3.8	192	225	--	--	9	1	0.0033	0.105	0	100	*0.11*	*0.01*
BT0931	Adams et al., 2016	246	1.5	234	261	--	--	15	3	0.0050	0.138	0	100	*0.18*	*0.02*
BT0973	Adams et al., 2016	48	0.6	57	45	--	--	13	1	0.0029	0.543	0	100	*0.056*	*0.003*
BT0993	Adams et al., 2016	196	1.4	171	184	--	--	13	3	0.0022	0.096	0	100	*0.07*	*0.01*
BT0994	Adams et al., 2016	270	1.9	257	311	--	--	26	3	0.0247	0.536	0	100	*0.96*	*0.12*
BT0995	Adams et al., 2016	218	1.3	198	223	--	--	11	4	0.0033	0.110	0	100	*0.11*	*0.01*
BT0996	Adams et al., 2016	243	3.7	233	277	--	--	26	2	0.0045	0.111	0	100	*0.16*	*0.02*
BT0998	Adams et al., 2016	232	1.7	236	254	--	--	34	2	0.0108	0.300	0	100	*0.38*	*0.14*
BT09108	Adams et al., 2016	168	2.2	145	159	--	--	3	2	0.0020	0.097	3	97	*0.06*	*0.01*
BT1021	Adams et al., 2016	323	3.1	265	307	--	--	19	3	0.0024	0.059	0	100	*0.10*	*0.01*
BT1036	Adams et al., 2016	200	2.1	186	201	50	1	--	--	0.0008	0.028	100	0	*0.024*	*0.002*
BT1042	Adams et al., 2016	88	1.6	86	108	--	--	40	2	0.0019	0.118	0	100	*0.035*	*0.004*
BT1043	Adams et al., 2016	84	3.5	84	106	--	--	31	3	0.0015	0.098	0	100	*0.028*	*0.004*
BT1044	Adams et al., 2016	387	5.5	298	223	--	--	35	3	0.0072	0.346	0	100	*0.35*	*0.04*
BT1111	Adams et al., 2016	244	0.9	244	265	--	--	33	1	0.0571	1.525	0	100	*2.08*	*0.31*
BT1112	Adams et al., 2016	214	1.2	194	227	--	--	24	2	0.0169	0.538	0	100	*0.56*	*0.05*
BT1135	Adams et al., 2016	253	3.1	259	307	--	--	26	2	0.0301	0.641	0	100	*1.12*	*0.12*
BT1142	Adams et al., 2016	170	1.9	148	163	--	--	65	1	0.0040	0.194	0	100	*0.11*	*0.01*
BT1143	Adams et al., 2016	176	2.0	172	176	--	--	61	1	0.0028	0.122	0	100	*0.08*	*0.01*
BT1145	Adams et al., 2016	193	2.1	180	196	53	2	--	--	0.0039	0.149	100	0	*0.12*	*0.01*
BT1146	Adams et al., 2016	295	3.2	270	307	66	2	--	--	0.0152	0.358	100	0	*0.63*	*0.06*
BT1147	Adams et al., 2016	263	1.3	244	234	--	--	9	5	0.0056	0.192	8	92	*0.21*	*0.02*
BT1148	Adams et al., 2016	240	1.7	229	220	--	--	17	2	0.0073	0.263	0	100	*0.26*	*0.02*
BT1149	Adams et al., 2016	215	1.0	210	209	--	--	20	1	0.0026	0.095	0	100	*0.09*	*0.01*
BT1150	Adams et al., 2016	213	0.8	201	195	--	--	15	3	0.0046	0.189	0	100	*0.15*	*0.01*
BT1151	Adams et al., 2016	242	3.2	221	245	--	--	13	2	0.0039	0.118	0	100	*0.14*	*0.01*
BT1152	Adams et al., 2016	255	2.2	249	254	--	--	14	1	0.0054	0.158	0	100	*0.20*	*0.02*
BT1153	Adams et al., 2016	296	3.3	260	293	--	--	7	3	0.0117	0.298	0	100	*0.48*	*0.05*
BT1154	Adams et al., 2016	299	3.2	259	280	--	--	11	3	0.0312	0.865	0	100	*1.29*	*0.14*
BT1161	Adams et al., 2016	142	3.1	122	131	--	--	59	2	0.0034	0.213	0	100	*0.09*	*0.01*

Table B1: Basin-averaged topographic, climatic, and erosional variables (cont 4)

Sample	Reference	Sample Latitude (N)	Sample Longitude (E)	Latitude (N)	Longitude (E)	Drainage Area	Elevation		Local Relief (2.5 km radius)		Local Relief (5 km radius)		Slope (gradient)		Mean Annual Precipitation		Number of Extreme Rainfall Events	
							mean	± 1σ	mean	± 1σ	mean	± 1σ	mean	± 1σ	mean	± 1σ	mean	± 1σ
		°	°	°	°	km^2	m	m	m	m	m	m	--	--	m/yr	m/yr	events/yr	events/yr
BT1162	Adams et al., 2016	27.4343	89.6853	27.4715	89.7177	56	3127	297	1070	139	1559	142	0.41	0.15	1.33	0.24	4.0	0.6
BT09103	Adams et al., 2020	26.9439	90.2612	26.9439	90.2612	137	1225	506	1188	237	1707	271	0.49	0.21	4.19	0.22	8.4	0.6
BT1108	Adams et al., 2020	26.8481	89.5093	26.8481	89.5093	26	1171	451	1310	184	1805	175	0.56	0.21	5.58	0.84	8.8	0.4
BT1114	Adams et al., 2020	27.0179	90.1611	27.0179	90.1611	110	1500	461	1204	139	1697	158	0.44	0.18	3.03	0.43	5.9	0.7
BT1125	Adams et al., 2020	27.0388	90.7233	27.0388	90.7233	67	1775	394	1260	168	1814	169	0.48	0.20	3.79	0.45	6.9	0.4
BT1127	Adams et al., 2020	26.9629	90.8313	26.9629	90.8313	10	867	270	1147	79	1491	107	0.62	0.26	4.75	0.06	7.0	0.1
BT1128	Adams et al., 2020	26.9859	90.9220	26.9859	90.9220	53	1104	434	1315	197	1813	203	0.63	0.26	3.52	0.55	6.7	0.6
BT1129	Adams et al., 2020	26.9286	90.8129	26.9286	90.8129	51	1175	404	1357	210	1842	142	0.61	0.26	5.02	0.28	8.3	0.7
BT1131	Adams et al., 2020	26.8809	90.9461	26.8809	90.9461	12	950	341	1458	168	1862	17	0.62	0.28	4.46	0.27	8.0	0.1
BT1133	Adams et al., 2020	26.9528	90.9732	26.9528	90.9732	75	1112	389	1281	198	1775	164	0.57	0.23	3.99	0.43	7.0	0.4
BT1106	Adams et al., 2020	26.8886	89.4149	26.8886	89.4149	19	814	297	1118	233	1629	92	0.48	0.19	3.58	0.12	8.5	0.4
BT1107	Adams et al., 2020	26.8898	89.4910	26.8898	89.4910	48	1316	443	1406	205	1984	183	0.55	0.20	5.13	0.75	8.8	0.3
BT1116	Adams et al., 2020	26.8690	90.1626	26.8690	90.1626	25	981	309	1172	164	1613	243	0.54	0.25	4.78	0.31	8.9	0.3
BT1118	Adams et al., 2020	26.9624	90.3412	26.9624	90.3412	16	1272	395	1228	130	1773	121	0.54	0.22	4.73	0.11	9.0	0.0
BT1119	Adams et al., 2020	26.9826	90.3698	26.9826	90.3698	33	1291	385	1252	173	1767	130	0.52	0.20	4.46	0.25	8.9	0.2
ARU-11-03	Olen et al., 2015	27.3261	87.2027	27.4263	87.3166	387	1538	871	1464	553	2123	728	0.53	0.27	2.25	0.95	6.5	1.6
ARU-11-04	Olen et al., 2015	27.3655	87.1802	27.3846	87.1913	11	765	199	865	95	1312	251	0.35	0.12	1.65	0.14	5.0	0.0
ARU-11-05	Olen et al., 2015	27.3868	87.1535	27.4074	87.1668	12	873	276	1179	178	1717	160	0.38	0.19	1.99	0.11	5.4	0.3
ARU-11-06	Olen et al., 2015	27.3921	87.1332	27.3450	87.0721	74	1614	680	1380	277	2095	373	0.46	0.17	2.18	0.12	6.0	0.1
ARU-11-07	Olen et al., 2015	27.4203	87.1214	27.3945	87.0037	206	1984	723	1633	279	2371	287	0.59	0.24	2.81	0.55	6.6	0.7
ARU-11-18	Olen et al., 2015	27.3234	87.1813	27.3269	87.1342	40	997	373	1113	202	1635	304	0.37	0.13	1.74	0.33	5.8	0.3
ARU-11-20	Olen et al., 2015	27.2161	87.2416	27.2606	87.3910	314	1743	671	1328	216	1888	290	0.43	0.17	1.49	0.41	4.7	0.8
ARU-11-22	Olen et al., 2015	27.1824	87.2643	27.1943	87.3066	35	1172	448	1323	242	1958	213	0.41	0.17	1.00	0.07	3.5	0.4
ARU-11-23	Olen et al., 2015	27.1494	87.2759	27.1437	87.3504	90	1489	649	1326	277	1994	296	0.41	0.18	1.26	0.18	4.0	0.1
ARU-11-24	Olen et al., 2015	27.1181	87.2533	27.0835	87.3192	84	1292	491	1253	190	1795	188	0.42	0.14	1.21	0.18	3.6	0.4
ARU-11-12	Olen et al., 2015	27.5149	87.1890	27.5271	87.1605	13	1746	553	1972	241	2737	140	0.76	0.33	2.31	0.15	6.7	0.4
ARU-12-02	Olen et al., 2015	27.5525	87.3140	27.5262	87.3770	82	2448	736	1979	336	2830	354	0.65	0.31	3.99	0.34	9.6	0.7
ARU-12-12	Olen et al., 2015	27.7359	87.3450	27.7709	87.3185	32	2787	635	1829	177	2806	189	0.56	0.27	2.78	0.44	7.2	1.0
ARU-12-13	Olen et al., 2015	27.7698	87.3732	27.7896	87.3801	17	3070	427	1777	172	2797	190	0.52	0.20	2.57	0.06	8.0	0.1
KP-090311-01	Godard et al., 2014	27.7469	85.0659	27.6908	85.0449	111	1486	408	1143	180	1637	126	0.47	0.20	2.29	0.37	5.2	0.4
KP-090311-02	Godard et al., 2014	27.8074	84.9673	27.7728	84.9660	12	905	219	900	170	1387	222	0.40	0.17	2.81	0.18	5.9	0.2
KP-090311-03	Godard et al., 2014	27.8113	84.9506	27.7370	84.9306	88	1248	477	1063	248	1546	230	0.42	0.17	2.73	0.27	5.7	0.4
KP-090311-04	Godard et al., 2014	27.8054	84.8893	27.7624	84.8770	19	958	337	1015	265	1527	239	0.42	0.16	3.33	0.34	6.2	0.3
KP-090311-05	Godard et al., 2014	27.8031	84.8336	27.7293	84.8322	99	1116	429	1086	209	1490	182	0.49	0.24	3.47	0.42	6.0	0.2
KP-090311-06	Godard et al., 2014	27.8012	84.7514	27.7629	84.7576	46	899	275	992	167	1349	161	0.52	0.21	3.98	0.34	6.0	0.1
KP-090311-07	Godard et al., 2014	27.8046	84.6938	27.7638	84.6764	56	1095	346	1217	100	1544	82	0.57	0.23	4.20	0.69	6.2	0.4
KP-090311-08	Godard et al., 2014	27.8716	84.6338	27.9007	84.6498	27	924	258	1054	115	1380	53	0.39	0.15	2.59	0.30	5.2	0.3
KP-160311-09	Godard et al., 2014	28.0669	84.0604	28.1181	83.9884	93	862	212	711	127	893	131	0.38	0.20	2.77	0.24	6.5	0.5
KP-160311-10	Godard et al., 2014	28.0129	84.0781	28.0412	83.9873	97	869	243	750	125	954	114	0.38	0.19	2.35	0.24	5.7	0.5
KP-160311-11	Godard et al., 2014	27.9887	84.2389	28.0460	84.1809	66	677	208	657	105	827	75	0.36	0.18	2.16	0.20	5.3	0.5
KP-160311-12	Godard et al., 2014	28.0291	84.2637	28.0535	84.3026	42	676	195	756	93	976	141	0.34	0.19	1.92	0.10	5.0	0.1
PO-140311-01	Godard et al., 2014	28.3110	83.7725	28.3580	83.7277	87	2406	556	1465	247	2122	182	0.53	0.24	3.05	0.25	7.9	0.8
PO-150311-02	Godard et al., 2014	28.2755	83.7355	28.3042	83.6957	41	1897	470	1493	193	2110	137	0.52	0.21	2.39	0.20	7.6	0.6
PO-150311-03a	Godard et al., 2014	28.2318	83.7149	28.2577	83.7762	41	1523	334	1097	173	1587	79	0.36	0.16	2.72	0.21	8.1	0.3
PO-150311-05	Godard et al., 2014	28.2535	83.6132	28.2609	83.5295	116	1708	394	1277	203	1738	140	0.46	0.19	2.51	0.15	6.9	0.3
TR-170311-01	Godard et al., 2014	27.9214	85.1358	27.9520	85.0903	53	1245	376	1175	158	1590	197	0.47	0.20	2.77	0.60	6.2	0.4

Table B1: Basin-averaged topographic, climatic, and erosional variables (cont 5)

Sample	Reference	Channel Steepness (integral)		Channel Steepness (basin averaged)	Discharge-based Channel Steepness	Distance from Main Frontal Thrust		Distance from Main Central Thrust		Erosional Coefficient (K) n = 0.65	Modified Erosional Coefficient (K_{tp}) n = 1.71	Metasedimentary Lithology	Crystalline Lithology	Erosion Rate[a]	
		mean	± 1σ	mean	mean	mean	± 1σ	mean	± 1σ					mean	± 1σ
		$m^{0.9}$	$m^{0.9}$	$m^{0.9}$	($m^{1.35}year^{-0.45}$)	km	km	km	km	$m^{0.41}/yr$	$m^{-1.30}yr^{-0.23}$ (*10^4)	%	%	mm/yr	mm/yr
BT1162	Adams et al., 2016	141	1.5	134	148	--	--	4	2	0.0023	0.117	3	97	*0.06*	*0.01*
BT09103	Adams et al., 2020	144	2.3	146	280	9	3	--	--	0.0103	0.178	53	47	*0.27*	*0.03*
BT1108	Adams et al., 2020	157	3.9	170	388	7	2	--	--	0.0327	0.342	100	0	*0.89*	*0.11*
BT1114	Adams et al., 2020	186	1.6	179	301	--	--	9	2	0.0255	0.458	0	100	*0.77*	*0.08*
BT1125	Adams et al., 2020	216	2.0	193	357	--	--	3	2	0.0095	0.140	4	96	*0.32*	*0.03*
BT1127	Adams et al., 2020	131	1.5	134	270	18	1	--	--	0.0557	0.957	100	0	*1.35*	*0.17*
BT1128	Adams et al., 2020	138	1.5	153	262	20	2	--	--	0.0451	0.847	100	0	*1.13*	*0.12*
BT1129	Adams et al., 2020	164	4.0	179	369	14	2	--	--	0.0563	0.660	100	0	*1.58*	*0.23*
BT1131	Adams et al., 2020	143	2.8	147	283	8	1	--	--	0.0164	0.276	100	0	*0.42*	*0.04*
BT1133	Adams et al., 2020	133	2.4	147	269	15	2	--	--	0.0274	0.479	100	0	*0.67*	*0.08*
BT1106	Adams et al., 2020	120	2.7	122	218	5	2	--	--	0.1002	2.344	100	0	*2.28*	*0.46*
BT1107	Adams et al., 2020	181	3.1	196	408	10	2	--	--	0.1230	1.292	92	8	*3.67*	*0.63*
BT1116	Adams et al., 2020	117	1.3	113	231	6	2	--	--	0.1464	3.054	100	0	*3.28*	*0.67*
BT1118	Adams et al., 2020	149	3.3	155	309	9	2	--	--	0.1298	1.933	59	41	*3.41*	*0.62*
BT1119	Adams et al., 2020	155	2.8	158	306	--	--	2	1	0.1281	1.980	27	73	*3.45*	*0.62*
ARU-11-03	Olen et al., 2015	179	3.4	196	307.0	70	6	--	--	0.0138	0.234	69	31	*0.41*	*0.03*
ARU-11-04	Olen et al., 2015	105	6.0	110	136.3	64	1	--	--	0.0068	0.328	100	0	*0.14*	*0.01*
ARU-11-05	Olen et al., 2015	126	1.4	122	164.6	67	1	--	--	0.0073	0.285	100	0	*0.17*	*0.01*
ARU-11-06	Olen et al., 2015	218	1.9	202	283.5	--	--	5	3	0.0110	0.242	2	98	*0.37*	*0.03*
ARU-11-07	Olen et al., 2015	240	1.1	234	372.3	--	--	6	4	0.0047	0.069	15	85	*0.17*	*0.01*
ARU-11-18	Olen et al., 2015	139	2.2	137	184.2	--	--	2	1	0.0055	0.187	46	54	*0.14*	*0.01*
ARU-11-20	Olen et al., 2015	208	1.0	218	270.8	--	--	5	3	0.0142	0.328	25	75	*0.46*	*0.04*
ARU-11-22	Olen et al., 2015	191	1.8	190	193.9	44	1	--	--	0.0110	0.428	93	7	*0.34*	*0.03*
ARU-11-23	Olen et al., 2015	239	4.9	208	236.9	--	--	3	2	0.0040	0.129	43	57	*0.15*	*0.01*
ARU-11-24	Olen et al., 2015	182	1.2	187	209.0	32	2	--	--	0.0052	0.173	50	50	*0.16*	*0.01*
ARU-11-12	Olen et al., 2015	241	4.1	232	342.7	80	1	--	--	0.0187	0.320	62	38	*0.67*	*0.05*
ARU-12-02	Olen et al., 2015	291	3.2	279	513.9	--	--	3	2	0.0120	0.116	46	54	*0.49*	*0.04*
ARU-12-12	Olen et al., 2015	315	3.2	292	443.2	--	--	4	1	0.0144	0.188	0	100	*0.62*	*0.06*
ARU-12-13	Olen et al., 2015	268	3.6	259	394.4	--	--	1	1	0.0113	0.162	20	80	*0.43*	*0.04*
KP-090311-01	Godard et al., 2014	131	1.8	136	198	--	--	14	2	0.0067	0.196	0	100	*0.16*	*0.02*
KP-090311-02	Godard et al., 2014	84	1.5	85	136	--	--	3	2	0.0104	0.433	4	96	*0.19*	*0.02*
KP-090311-03	Godard et al., 2014	119	2.2	128	197	--	--	7	3	0.0075	0.209	1	99	*0.17*	*0.02*
KP-090311-04	Godard et al., 2014	95	3.0	108	191	--	--	4	2	0.0094	0.237	2	98	*0.18*	*0.02*
KP-090311-05	Godard et al., 2014	106	1.9	120	209	--	--	6	3	0.0154	0.356	1	99	*0.32*	*0.05*
KP-090311-06	Godard et al., 2014	85	1.5	92	172	43	2	--	--	0.0245	0.691	52	48	*0.45*	*0.07*
KP-090311-07	Godard et al., 2014	134	2.3	147	268	43	2	--	--	0.0087	0.153	100	0	*0.21*	*0.03*
KP-090311-08	Godard et al., 2014	137	1.3	130	194	57	2	--	--	0.0174	0.540	100	0	*0.43*	*0.06*
KP-160311-09	Godard et al., 2014	35	0.7	52	83	62	2	--	--	0.0106	0.578	100	0	*0.11*	*0.01*
KP-160311-10	Godard et al., 2014	49	1.8	65	96	55	3	--	--	0.0093	0.491	100	0	*0.12*	*0.01*
KP-160311-11	Godard et al., 2014	41	0.9	53	77	66	2	--	--	0.0081	0.562	100	0	*0.09*	*0.01*
KP-160311-12	Godard et al., 2014	37	1.3	53	72	71	2	--	--	0.0079	0.571	100	0	*0.08*	*0.01*
PO-140311-01	Godard et al., 2014	256	3.1	222	367	79	3	--	--	0.0143	0.225	93	7	*0.53*	*0.07*
PO-150311-02	Godard et al., 2014	199	2.4	200	300	73	2	--	--	0.0236	0.446	100	0	*0.75*	*0.12*
PO-150311-03a	Godard et al., 2014	105	2.1	124	197	70	2	--	--	0.0323	0.820	100	0	*0.67*	*0.12*
PO-150311-05	Godard et al., 2014	145	1.6	163	245	63	3	--	--	0.0088	0.191	100	0	*0.23*	*0.03*
TR-170311-01	Godard et al., 2014	120	2.0	126	208	73	2	--	--	0.0201	0.511	100	0	*0.46*	*0.09*

Table B1: Basin-averaged topographic, climatic, and erosional variables (cont 6)

Sample	Reference	Sample Latitude (N)	Sample Longitude (E)	Latitude (N)	Longitude (E)	Drainage Area	Elevation		Local Relief (2.5 km radius)		Local Relief (5 km radius)		Slope (gradient)		Mean Annual Precipitation		Number of Extreme Rainfall Events	
							mean	± 1σ	mean	± 1σ	mean	± 1σ	mean	± 1σ	mean	± 1σ	mean	± 1σ
		°	°	°	°	km^2	m	m	m	m	m	m	--	--	m/yr	m/yr	events/yr	events/yr
TR-170311-02	Godard et al., 2014	27.9758	85.1907	28.0159	85.2903	147	2147	864	1648	371	2500	412	0.56	0.22	3.15	0.96	8.2	1.5
TR-170311-03	Godard et al., 2014	27.9828	85.1756	28.0221	85.1128	86	1921	656	1569	316	2404	359	0.51	0.20	3.21	0.48	7.6	0.5
TR-170311-04	Godard et al., 2014	27.8657	85.1541	27.8380	85.1656	30	1144	361	1147	242	1554	99	0.44	0.19	1.66	0.33	5.3	0.6
EK-180311-01	Godard et al., 2014	27.6441	85.6173	27.6523	85.5726	41	1243	255	762	180	1124	140	0.33	0.17	1.63	0.12	4.8	0.3
EK-180311-02	Godard et al., 2014	27.6773	85.7347	27.6627	85.7860	42	1520	325	1095	111	1512	108	0.45	0.17	2.21	0.29	5.0	0.2
EK-180311-03	Godard et al., 2014	27.7532	85.8597	27.7180	85.8972	30	1725	415	1270	117	1868	204	0.51	0.20	2.97	0.19	6.8	0.6
EK-180311-04	Godard et al., 2014	27.7783	85.8961	27.7812	85.9730	91	2221	662	1826	245	2481	159	0.63	0.30	3.48	0.26	8.6	0.5
EK-180311-05	Godard et al., 2014	27.8819	85.9152	27.8633	85.9782	68	2853	577	1565	264	2355	153	0.55	0.24	3.87	0.32	9.2	0.5
NEP003	Godard et al., 2012	27.9066	84.5397	28.1049	84.6551	610	1469	1078	1220	531	1798	853	0.46	0.24	2.54	0.93	6.6	1.5
NEP030	Godard et al., 2012	27.9546	84.4188	28.0264	84.3810	110	727	214	717	176	936	171	0.32	0.18	1.93	0.19	5.3	0.4
NEP080	Godard et al., 2012	28.0595	84.4842	28.1824	84.5911	309	1820	977	1336	405	2031	721	0.44	0.20	2.80	0.66	7.4	1.1
NEP099	Godard et al., 2012	28.1131	84.4262	28.1470	84.3691	83	957	247	865	135	1153	120	0.36	0.20	2.64	0.21	6.2	0.4
NIB-975-02	Godard et al., 2012	28.2818	84.3550	28.3620	84.3093	136	2605	916	1735	216	2615	450	0.57	0.25	4.10	0.48	8.9	1.0
NEP118a	Godard et al., 2012	28.3233	84.4068	28.3892	84.5105	215	3464	1218	2212	489	3477	738	0.66	0.35	3.49	0.99	7.4	1.3
NIB-975-44a	Godard et al., 2012	28.1680	84.4483	28.2931	84.5480	352	2907	1553	1917	553	2896	832	0.61	0.28	3.10	0.93	7.4	1.4
DS7-048	Scherler et al., 2014	30.5734	78.0073	30.5896	78.0936	100	1808	421	1188	157	1695	164	0.50	0.18	1.88	0.24	3.9	0.3
DS7-049	Scherler et al., 2014	30.6416	78.0069	30.7142	77.9417	169	1839	439	1162	163	1585	198	0.52	0.19	1.62	0.19	3.4	0.5
DS6-AR3	Scherler et al., 2014	30.7222	78.0880	30.7211	78.1582	89	1882	377	1171	115	1547	114	0.48	0.18	1.51	0.10	3.8	0.3
DS7-051	Scherler et al., 2014	30.7222	78.0871	30.7211	78.1582	89	1881	378	1171	115	1547	114	0.48	0.18	1.51	0.10	3.8	0.3
DS7-061	Scherler et al., 2014	30.7998	78.1120	30.8794	78.0849	210	1893	332	1017	188	1387	186	0.43	0.21	1.80	0.32	4.8	0.4
DS7-045	Scherler et al., 2014	30.8203	78.2074	30.8371	78.1838	9	1829	311	1057	132	1349	16	0.45	0.18	1.46	0.16	4.7	0.4
DS7-044	Scherler et al., 2014	30.8729	78.3037	30.8536	78.3448	25	2538	440	1497	181	2186	144	0.60	0.24	2.70	0.11	6.0	0.5
DS6-006	Scherler et al., 2014	30.8882	78.3054	30.9380	78.2986	56	2745	536	1672	177	2296	211	0.67	0.28	2.17	0.24	6.2	0.5
DS7-077	Scherler et al., 2014	30.7767	77.6870	30.7444	77.6014	128	1703	370	1230	164	1626	111	0.54	0.20	3.00	0.46	4.1	0.2
DS7-072	Scherler et al., 2014	30.8494	77.7447	30.9583	77.6384	513	2125	484	1287	212	1754	212	0.53	0.20	1.83	0.30	3.9	0.3
DS7-062	Scherler et al., 2014	30.9909	78.0196	30.9530	78.0450	36	1724	240	879	113	1293	169	0.48	0.22	2.15	0.18	5.0	0.0
DS7-066	Scherler et al., 2014	31.0196	78.0354	31.0768	77.9904	66	2271	540	1468	251	2095	212	0.65	0.27	2.13	0.15	4.9	0.2
DS6-081	Scherler et al., 2014	31.0690	78.0982	31.2230	78.1246	535	3295	809	1606	250	2240	223	0.60	0.28	1.73	0.40	5.1	0.7
DS6-080A	Scherler et al., 2014	31.1373	78.2527	31.1856	78.3445	102	4142	735	1785	278	2452	400	0.63	0.30	1.27	0.72	3.8	1.4
DS6-023C	Scherler et al., 2014	31.0821	78.2536	31.1084	78.4370	549	4283	801	1653	311	2388	357	0.58	0.32	1.15	0.64	4.0	1.7
DS7-088	Scherler et al., 2014	31.1536	77.7363	31.1879	77.6428	123	2290	312	983	93	1312	91	0.42	0.16	1.23	0.15	4.2	0.3
DS7-086	Scherler et al., 2014	31.2195	77.8293	31.2849	77.8062	88	2701	504	1309	219	1928	299	0.51	0.21	1.22	0.18	4.0	0.1
DS6-088	Scherler et al., 2014	31.2524	77.9604	31.3358	78.0393	231	3740	649	1517	207	2113	195	0.56	0.26	1.41	0.43	4.4	0.7
DS7-055	Scherler et al., 2014	30.8202	78.2290	30.9345	78.3505	647	2975	863	1546	302	2249	408	0.58	0.27	2.24	0.49	5.9	0.6
DS6-094	Scherler et al., 2014	31.2263	77.8527	31.2995	77.9692	516	3314	744	1483	218	2092	221	0.53	0.24	1.44	0.33	4.4	0.6

[a] Italicized entries were reported in Adams et al. (2020).

Table B1: Basin-averaged topographic, climatic, and erosional variables (cont 7)

Sample	Reference	Channel Steepness (integral)		Channel Steepness (basin averaged)	Discharge-based Channel Steepness	Distance from Main Frontal Thrust		Distance from Main Central Thrust		Erosional Coefficient (K) n = 0.65	Modified Erosional Coefficient (K_{tp}) n = 1.71	Metasedimentary Lithology	Crystalline Lithology	Erosion Rate[a]	
		mean	± 1σ	mean	mean	mean	± 1σ	mean	± 1σ					mean	± 1σ
		$m^{0.9}$	$m^{0.9}$	$m^{0.9}$	($m^{1.35}year^{-0.45}$)	km	km	km	km	$m^{0.41}/yr$	$m^{-1.30}yr^{-0.23}$ (*10^4)	%	%	mm/yr	mm/yr
TR-170311-02	Godard et al., 2014	231	2.7	243	430	84	4	--	--	0.0209	0.236	84	16	*0.73*	*0.13*
TR-170311-03	Godard et al., 2014	216	2.8	214	370	81	3	--	--	0.0339	0.474	100	0	*1.14*	*0.18*
TR-170311-04	Godard et al., 2014	123	2.1	132	156	--	--	2	1	0.0082	0.343	18	82	*0.19*	*0.02*
EK-180311-01	Godard et al., 2014	66	2.0	69	84	--	--	7	2	0.0063	0.507	0	100	*0.10*	*0.01*
EK-180311-02	Godard et al., 2014	160	1.8	147	208	62	2	--	--	0.0038	0.117	100	0	*0.11*	*0.01*
EK-180311-03	Godard et al., 2014	177	1.1	177	286	69	1	--	--	0.0210	0.398	100	0	*0.62*	*0.10*
EK-180311-04	Godard et al., 2014	233	2.3	255	447	78	3	--	--	0.0261	0.277	100	0	*0.92*	*0.25*
EK-180311-05	Godard et al., 2014	340	5.5	276	507	87	2	--	--	0.0336	0.368	68	32	*1.51*	*0.42*
NEP003	Godard et al., 2012	151	2.7	154	252	80	13	--	--	0.0348	0.740	69	31	*0.92*	*0.09*
NEP030	Godard et al., 2012	37	0.7	50	68	71	5	--	--	0.0066	0.510	100	0	*0.07*	*0.01*
NEP080	Godard et al., 2012	191	3.1	188	317	--	--	7	4	0.0190	0.317	29	71	*0.59*	*0.06*
NEP099	Godard et al., 2012	58	1.7	67	103	83	2	--	--	0.0208	1.078	100	0	*0.29*	*0.03*
NIB-975-02	Godard et al., 2012	318	2.7	294	547	--	--	7	4	0.0598	0.552	11	89	*2.58*	*0.61*
NEP118a	Godard et al., 2012	412	2.2	356	576	--	--	14	6	0.0630	0.629	0	100	*3.22*	*0.34*
NIB-975-44a	Godard et al., 2012	368	4.2	307	487	--	--	9	7	0.0349	0.432	18	82	*1.66*	*0.16*
DS7-048	Scherler et al., 2014	159	1.6	159	207	50	4	--	--	0.0165	0.505	100	0	0.45	0.04
DS7-049	Scherler et al., 2014	150	1.7	154	191	53	3	--	--	0.0049	0.165	100	0	0.13	0.01
DS6-AR3	Scherler et al., 2014	162	1.4	163	196	66	3	--	--	0.0042	0.144	100	0	0.12	0.01
DS7-051	Scherler et al., 2014	162	1.4	163	196	66	3	--	--	0.0064	0.220	100	0	0.18	0.01
DS7-061	Scherler et al., 2014	99	1.6	111	145	76	5	--	--	0.0051	0.212	100	0	0.10	0.01
DS7-045	Scherler et al., 2014	150	1.6	143	164	78	1	--	--	0.0023	0.100	100	0	0.06	0.01
DS7-044	Scherler et al., 2014	226	2.6	206	322	88	1	--	--	0.0079	0.144	100	0	0.27	0.02
DS6-006	Scherler et al., 2014	205	2.3	212	304	93	3	--	--	0.0330	0.621	100	0	1.07	0.09
DS7-077	Scherler et al., 2014	133	1.4	152	251	41	3	--	--	0.0133	0.262	100	0	0.32	0.03
DS7-072	Scherler et al., 2014	160	0.8	175	230	--	--	4	3	0.0087	0.226	43	57	0.24	0.02
DS7-062	Scherler et al., 2014	112	1.4	101	140	81	2	--	--	0.0056	0.266	100	0	0.12	0.01
DS7-066	Scherler et al., 2014	183	1.9	178	252	91	3	--	--	0.0152	0.365	55	45	0.46	0.04
DS6-081	Scherler et al., 2014	271	0.9	257	322	--	--	7	4	0.0451	0.924	15	85	1.75	0.15
DS6-080A	Scherler et al., 2014	328	5.4	257	256	--	--	8	5	0.0404	1.390	1	99	1.78	0.15
DS6-023C	Scherler et al., 2014	313	1.9	228	235	--	--	8	6	0.0680	2.619	14	86	2.90	0.25
DS7-088	Scherler et al., 2014	125	0.9	123	136	--	--	12	2	0.0110	0.589	0	100	0.26	0.02
DS7-086	Scherler et al., 2014	190	1.5	172	191	--	--	6	3	0.0080	0.315	0	100	0.25	0.02
DS6-088	Scherler et al., 2014	259	1.6	240	264	--	--	4	3	0.0249	0.694	29	71	0.94	0.08
DS7-055	Scherler et al., 2014	243	1.6	225	322	96	9	--	--	0.0296	0.564	88	12	1.07	0.09
DS6-094	Scherler et al., 2014	243	0.8	232	266	--	--	5	3	0.0092	0.243	9	91	0.33	0.03

[a] Italicized entries were reported in Adams et al. (2020).

Table B2: Erosion rates and cosmogenic concentrations

Sample Name	Year Analyzed	Quartz Mass (g)	Mass of ^{9}Be Added (µg)	AMS Cathode Number	Uncorrected ^{10}Be/^{9}Be Ratio[a] ($*10^{-15}$)		Background-Corrected ^{10}Be/^{9}Be Ratio[b] ($*10^{-15}$)		^{10}Be Concentration (atoms g^{-1}) ($*10^{3}$)		Erosion Rate[b] (mm/yr)		Erosion Rate[c] (mm/yr)	
						± 1σ		± 1σ		± 1σ		± 1σ		± 1σ
AH18-01	2018	22.1	241	BE45311	9.25	0.61	8.63	0.67	6.29	0.49	**1.60**	**0.18**	1.58	0.17
AH18-08	2021	22.3	243	BE49162	19.68	0.73	19.06	0.78	13.89	0.57	**0.72**	**0.06**	0.73	0.06
AH18-11	2021	22.0	243	BE49163	13.20	0.54	12.58	0.60	9.27	0.45	**1.49**	**0.14**	1.53	0.14
AH18-13	2021	14.1	241	BE49164	21.00	0.68	20.38	0.74	23.26	0.84	**0.41**	**0.04**	0.42	0.04
AH18-16	2021	44.1	246	BE49165	4.10	0.44	3.49	0.52	1.30	0.19	**4.64**	**0.78**	5.15	0.86
AH18-16[e]	2018	21.7	242	BE45312	1.27	0.25	0.65	0.38	0.48	0.28	13.00	7.54	10.60	4.46
AH18-17	2018	21.9	242	BE45313	2.16	0.33	1.54	0.43	1.14	0.32	**5.32**	**1.54**	4.95	1.20
AH18-18	2018	22.1	242	BE45315	2.53	0.35	1.92	0.45	1.40	0.33	**5.05**	**1.25**	4.77	1.02
AH18-19	2018	22.4	241	BE45316	2.04	0.36	1.42	0.46	1.02	0.33	**7.50**	**2.48**	6.93	1.93
AH18-22	2018	21.9	241	BE45317	7.65	0.66	7.04	0.72	5.16	0.53	**2.58**	**0.33**	2.54	0.32
AH18-23	2018	21.9	241	BE45318	8.91	0.65	8.29	0.71	6.12	0.52	**1.87**	**0.22**	1.85	0.21
AH18-27	2018	22.1	241	BE45319	63.74	1.76	63.12	1.79	46.06	1.30	**0.27**	**0.02**	0.27	0.02
AH18-31	2018	21.8	240	BE45321	45.33	1.32	44.71	1.35	32.85	1.00	**0.41**	**0.03**	0.41	0.03

[a] Isotopic analysis was conducted at Lawrence Livermore National Laboratory; ratios were normalized against standard 07KNSTD3110 with an assumed ratio of 2850 x 10^{-15} (Nishiizumi et al., 2007).

[b] ^{10}Be concentration and uncertainty shown was calculated using the average of the blanks from both 2018 and 2021 batches ($6.2*10^{-16}$).

[c] Erosion rate was calculated with the blank correction using blanks from each batch ($5.0*10^{-16}$ for 2018 batch and $9.6*10^{-16}$ for 2021 batch).

[e] Duplicate sample was not included in analyses.

Erosion rates and uncertainties in bold were used in analyses.

Table B3: Landslide-derived erosion rates and characteristics

Sample ID	Landslide Volume		Landslide Count	Landslide-derived Erosion Rate	Total Landslide Area	Landslide Density	Average Failure Rate		
Unit	m^3		--	mm/yr	km^2	% basin area	10^{-4} yr^{-1}		
Easternmost Himalayas									
Time interval	1997-2006	2006-2017	1997-2017	1997-2017			1997-2006	2006-2017	1997-2017
AH18-01	8653651	5540706	144	1.4	1.51	0.30	1.94	1.12	1.49
AH18-08	389574	92153	10	1.0	0.07	0.28	2.18	0.72	1.38
AH18-11	1090095	2409859	29	0.53	0.39	0.12	0.43	0.73	0.59
AH18-13	1405427	316321	19	1.2	0.18	0.26	2.21	0.54	1.29
AH18-16	1674459	1100790	51	4.7	0.38	1.28	8.54	4.65	6.40
AH18-17	1505191	384935	37	4.0	0.25	1.07	9.04	2.30	5.33
AH18-18	2856585	4708407	89	3.0	0.84	0.65	3.21	3.32	3.27
AH18-19	5302594	4898568	81	5.5	0.86	0.94	5.61	3.93	4.69
AH18-22	7490110	1408202	73	2.3	0.88	0.46	4.07	0.81	2.28
AH18-23	5146837	831108	23	3.1	0.44	0.45	3.63	1.13	2.25
AH18-27	23898	23861	3	0.09	0.01	0.04	0.18	0.18	0.18
AH18-31	155062	47965	6	0.41	0.03	0.13	0.88	0.43	0.63
Eastern Nepal Himalayas									
Time interval	1989-1999	1999-2009	1989-2009	1989-2009			1989-1999	1999-2009	1989-2009
ARU-11-3	1835636	1833681	22	0.47	0.36	0.09	0.49	0.47	0.47
ARU-11-7	1206459	695976	25	0.46	0.23	0.11	0.76	0.42	0.56
ARU-11-12	1212253	1411467	16	10	0.26	1.96	8.92	10.43	9.78
ARU-12-2	1014697	0	15	0.62	0.10	0.12	1.21	0.00	0.58
ARU-12-12	270310	1368391	11	2.6	0.17	0.53	1.03	4.16	2.64
ARU-12-13	457063	913927	10	4.1	0.14	0.84	3.15	5.55	4.19
Central Nepal Himalayas									
Time interval	1989-1999	1999-2009	1989-2009	1989-2009			1989-1999	1999-2009	1989-2009
KP-090311-06	85242	248347	6	0.36	0.04	0.09	0.16	0.76	0.45
KP-090311-07	81764	198881	8	0.25	0.04	0.07	0.23	0.58	0.36
TR-170311-02	2147158	7075186	71	3.1	0.89	0.61	1.67	4.57	3.05
TR-170311-03	484075	121544	9	0.35	0.08	0.09	0.66	0.19	0.46
EK-180311-03	35829	128285	7	0.28	0.03	0.10	0.15	0.84	0.48
EK-180311-04	650797	2076408	35	1.5	0.34	0.37	0.92	2.98	1.87
EK-180311-05	17643	1040191	5	0.78	0.10	0.15	0.07	1.46	0.75

Table B4: Compilation statistics of erosion rate and controls

		Mean			± 1σ			Minimum			Maximum		
Metric	**Unit**	**All**	**Metasedimentary**	**Crystalline**	**All**	**Metasedimentary**	**Crystalline**	**All**	**Metasedimentary**	**Crystalline**	**All**	**Metasedimentary**	**Crystalline**
Erosion Rate	mm/yr	0.67	0.96	0.50	1.06	1.46	0.70	0.02	0.02	0.03	7.50	7.50	3.45
Channel Steepness (k_{sn})	$m^{0.9}/yr$	202	165	223	78	66	76	35	35	48	412	373	412
Dicharged-Based Channel Steepness (k_{sn}-q)	$m^{1.35}yr^{-0.45}$	258	254	261	110	101	116	45	68	45	583	507	583
Number of Extreme Rainfall Events	events/yr	5.5	6.3	5.1	2.2	2.2	2.0	2.1	3.3	2.1	12.9	12.1	12.9
Mean Annual Precipitation	m/yr	2.15	2.74	1.82	1.22	1.23	1.08	0.60	1.00	0.60	5.83	5.58	5.83
Local Relief (2.5 km)	m	1368	1280	1419	293	278	290	657	657	762	2212	1972	2212
Local Relief (5 km)	m	1972	1788	2077	446	426	423	827	827	1124	3477	2737	3477
Slope	m/m	0.51	0.51	0.51	0.10	0.09	0.11	0.28	0.32	0.28	0.76	0.76	0.76

Table B5: Model Coefficients and RMSE for relationships between erosion rates and controls

	All (n = 173)							Metasedimentary Lithology (n = 61)							Crystalline Lithology (n = 112)						
	k_{sn}	k_{sn}-q	NEE	MAP	Local Relief (2.5 km)	Local Relief (5 km)	Slope	k_{sn}	k_{sn}-q	NEE	MAP	Local Relief (2.5 km)	Local Relief (5 km)	Slope	k_{sn}	k_{sn}-q	NEE	MAP	Local Relief (2.5 km)	Local Relief (5 km)	Slope
Linear[a]																					
n_1	0.20	-0.57	**-1.02**	-0.39	-0.93	-0.68	-1.48	0.36	-1.15	**-2.44**	-1.23	-1.31	-1.02	-2.48	-0.37	**-0.37**	-0.29	-0.01	-1.27	-1.23	-1.11
n_2	2.31E-03	4.79E-03	**3.04E-01**	4.88E-01	1.17E-03	6.83E-04	4.21E+00	3.76E-03	8.32E-03	**5.35E-01**	7.83E-01	1.79E-03	1.12E-03	6.82E+00	3.92E-03	**3.34E-03**	1.55E-01	2.80E-01	1.24E-03	8.34E-04	3.16E+00
RMSE (mm/yr)	1.06	0.93	**0.85**	0.89	1.02	1.03	0.99	1.49	1.23	**0.95**	1.15	1.42	1.43	1.37	0.64	**0.59**	0.63	0.64	0.61	0.61	0.62
R^2	0.03	0.25	**0.38**	0.31	0.10	0.08	0.16	0.03	0.34	**0.61**	0.42	0.12	0.11	0.18	0.18	**0.30**	0.20	0.18	0.27	0.25	0.22
p-value	0.03	0.00	**0.00**	0.00	0.00	0.00	0.00	0.20	0.00	**0.00**	0.00	0.01	0.01	0.00	0.00	**0.00**	0.00	0.00	0.00	0.00	0.00
Power-Law[b]					[e]	[e]								[f]					[d,e]	[d,e]	
b_1	2.12E-02	4.74E-05	**8.10E-03**	1.58E-01	9.36E-09	2.58E-08	4.02E+00	5.66E-02	9.35E-07	**6.06E-04**	5.46E-02	4.18E-07	7.09E-07	--	3.39E-06	**4.69E-05**	5.24E-02	2.89E-01	6.94E-14	6.29E-14	3.49E+00
b_2	0.65	1.71	**2.43**	1.65	2.49	2.24	2.74	0.56	2.45	**3.71**	2.50	2.05	1.88	--	2.17	**1.65**	1.37	0.96	4.05	3.86	3.04
RMSE (mm/yr)	1.06	0.94	**0.82**	0.88	1.02	1.03	1.00	1.48	1.20	**0.72**	1.11	1.43	1.43	--	0.63	**0.59**	0.63	0.64	0.58	0.58	0.63
R^2	0.03	0.25	**0.42**	0.33	0.11	0.09	0.14	0.04	0.37	**0.77**	0.46	0.11	0.10	--	0.20	**0.30**	0.20	0.18	0.33	0.31	0.22
Log-transformed																					
R^2	0.13	**0.48**	0.42	0.37	0.27	0.21	0.40	0.09	0.46	**0.64**	0.56	0.24	0.23	0.37	0.33	**0.53**	0.29	0.26	0.44	0.39	0.46
p-value	0.00	**0.00**	0.00	0.00	0.00	0.00	0.00	0.02	0.00	**0.00**	0.00	0.00	0.00	0.00	0.00	**0.00**	0.00	0.00	0.00	0.00	0.00
Exponential[c]																					
k_1	3.23E-03	4.65E-03	**2.80E-01**	4.76E-01	1.62E-03	1.00E-03	4.56E+00	2.44E-03	6.89E-03	**3.95E-01**	6.28E-01	1.35E-03	9.20E-04	4.63E+00	7.99E-03	4.65E-03	1.76E-01	3.12E-01	**2.53E-03**	1.48E-03	5.07E+00
k_2	-1.09	-1.71	**-2.13**	-1.59	-2.73	-2.48	-2.79	-0.43	-2.01	**-2.90**	-2.05	-1.79	-1.72	-2.42	-2.66	-2.04	-1.64	-1.30	**-4.56**	-3.96	-3.39
RMSE (mm/yr)	1.06	0.95	**0.84**	0.90	1.02	1.03	1.01	1.50	1.21	**0.76**	1.14	1.44	1.44	1.40	0.63	0.60	0.65	0.66	**0.58**	0.59	0.63
Other																					
MSWD (y-uncertainty)	541.86	289.32	302.66	478.94	408.02	456.18	**279.17**	2382.05	694.70	**200.86**	**202.33**	1898.12	1798.86	805.08	182.64	163.93	247.96	418.07	**136.22**	172.08	**133.95**
±σ	0.11	0.11	**0.11**	0.11	0.11	0.11	0.11	0.18	0.18	**0.18**	**0.18**	0.18	0.18	0.18	0.13	0.13	0.13	0.13	**0.13**	0.13	**0.13**
MSWD (all uncertainty)	--	--	21.21	16.99	5.59	14.62	0.51	--	--	13.58	11.48	5.35	19.25	0.37	--	--	28.24	20.02	4.04	7.81	0.44
±σ	--	--	0.11	0.11	0.11	0.11	0.11	--	--	0.18	0.18	0.18	0.18	0.18	--	--	0.13	0.13	0.13	0.13	0.13
χ^2 **(power-law) (30%)**	322.13	111.08	85.08	164.97	197.06	225.68	155.34	1175.47	144.73	28.65	56.05	896.54	848.51	--	59.78	49.15	113.43	155.66	39.21	51.19	54.49
χ^2 **(power-law)**	3450.82	1181.91	871.32	1580.59	2144.89	2368.43	1715.78	13213.27	1534.13	283.41	465.57	10023.87	9529.36	1.00E+04	625.86	512.07	1109.04	1450.42	433.28	531.73	594.96
Spearman's ρ	0.36	**0.74**	0.62	0.59	0.56	0.50	0.67	0.29	0.77	**0.79**	0.74	0.53	0.53	0.67	0.60	**0.76**	0.54	0.53	**0.70**	0.66	0.70
p-value	9E-07	**9E-31**	6E-20	1E-17	2E-15	3E-12	5E-24	3E-02	4E-13	**4E-14**	8E-12	1E-05	1E-05	3E-09	0E+00	**0E+00**	8E-10	4E-09	**0E+00**	0E+00	0E+00
Kendall's τ	0.25	**0.54**	0.45	0.42	0.38	0.34	0.48	0.19	0.57	**0.60**	0.54	0.37	0.36	0.47	0.43	**0.57**	0.38	0.37	**0.51**	0.47	0.51
p-value	1E-06	**7E-26**	1E-18	2E-16	7E-14	3E-11	2E-20	3E-02	9E-11	**8E-12**	8E-10	2E-05	4E-05	9E-08	2E-11	**8E-19**	2E-09	6E-09	**2E-15**	2E-13	1E-15

Bolded entries are best correlated with erosion rate for each correlation method.

[a] Linear model: $y = n_1 + n_2 x$

[b] Power-Law model: $y = b_1 x^{b2}$

[c] Exponential model: $y = \exp(k_1 x + k_2)$

[d] Rank deficient.

[e] Jacobian at the solution is ill-conditioned.

[f] Fitting failed to converge.

B.10 Appendix References

Adams, B.A., Whipple, K.X., Forte, A.M., Heimsath, A.M., and Hodges, K. V, 2020, Climate controls on erosion in tectonically active landscapes: Science Advances, v. 6, p. 3166–3182.

Adams, B.A., Whipple, K.X., Hodges, K. V., and Heimsath, A.M., 2016, In situ development of high-elevation, low-relief landscapes via duplex deformation in the Eastern Himalayan hinterland, Bhutan: Journal of Geophysical Research: Earth Surface, v. 121, p. 294–319, doi:10.1002/2015JF003508.

Attal, M., and Lavé, J., 2006, Changes of bedload characteristics along the Marsyandi River (central Nepal): Implications for understanding hillslope sediment supply, sediment load evolution along fluvial networks, and denudation in active orogenic belts: Special Paper of the Geological Society of America, v. 398, p. 143–171, doi:10.1130/2006.2398(09).

Balco, G., Stone, J.O., Lifton, N.A., and Dunai, T.J., 2008, A complete and easily accessible means of calculating surface exposure ages or erosion rates from ^{10}Be and ^{26}Al measurements: Quaternary Geochronology, v. 3, p. 174–195, doi:10.1016/j.quageo.2007.12.001.

Bookhagen, B., and Burbank, D.W., 2010, Toward a complete Himalayan hydrological budget: Spatiotemporal distribution of snowmelt and rainfall and their impact on river discharge: Journal of Geophysical Research: Earth Surface, v. 115, doi:10.1029/2009JF001426.

Clark, K.E. et al., 2016, Storm-triggered landslides in the Peruvian Andes and implications for topography, carbon cycles, and biodiversity: Earth Surface Dynamics, v. 4, p. 47–70, doi:10.5194/esurf-4-47-2016.

Corbett, L.B., Bierman, P.R., and Rood, D.H., 2016, An approach for optimizing in situ cosmogenic ^{10}Be sample preparation: Quaternary Geochronology, v. 33, p. 24–34, doi:10.1016/j.quageo.2016.02.001.

Farr, T.G. et al., 2007, The Shuttle Radar Topography Mission: Reviews of Geophysics, v. 45, doi:10.1029/2005RG000183.

de Ferranti, J., 2021, Digital elevation data:, http://viewfinderpanoramas.org/dem3.html (accessed January 2022).

Godard, V., Bourlès, D.L., Spinabella, F., Burbank, D.W., Bookhagen, B., Fisher, G.B., Moulin, A., and Léanni, L., 2014, Dominance of tectonics over climate in Himalayan denudation: Geology, v. 42, p. 243–246, doi:10.1130/G35342.1.

Godard, V., Burbank, D.W., Bourls, D.L., Bookhagen, B., Braucher, R., and Fisher, G.B., 2012, Impact of glacial erosion on ^{10}Be concentrations in fluvial sediments of the Marsyandi catchment, central Nepal: Journal of Geophysical Research: Earth Surface, v. 117, doi:10.1029/2011JF002230.

Godard, V., Lavie, J., and Cattin, R., 2006, Numerical modelling of erosion processes in the Himalayas of Nepal: effects of spatial variations of rock strength and precipitation: Analogue and Numerical Modeling of Crustal-Scale Processes, v. 253, p. 341–358.

Haproff, P.J., Odlum, M.L., Zuza, A. V., Yin, A., and Stockli, D.F., 2020, Structural and Thermochronologic Constraints on the Cenozoic Tectonic Development of the Northern Indo-Burma Ranges: Tectonics, v. 39, doi:10.1029/2020TC006231.

Haproff, P.J., Zuza, A. V., Yin, A., Harrison, T.M., Manning, C.E., Dubey, C.S., Ding, L., Wu, C., and Chen, J., 2019, Geologic framework of the northern Indo-Burma Ranges and lateral correlation of Himalayan-Tibetan lithologic units across the eastern Himalayan syntaxis: Geosphere, v. 15, p. 856–881, doi:10.1130/GES02054.1.

Hilley, G.E., Porder, S., Aron, F., Baden, C.W., Johnstone, S.A., Liu, F., Sare, R., Steelquist, A., and Young, H.H., 2019, Earth's topographic relief potentially limited by an upper bound on channel steepness: Nature Geoscience, v. 12, p. 828–832, doi:10.1038/s41561-019-0442-3.

Jones, J.N., Boulton, S.J., Stokes, M., Bennett, G.L., and Whitworth, M.R.Z., 2021, 30-year record of Himalaya mass-wasting reveals landscape perturbations by extreme events: Nature Communications, v. 12, doi:10.1038/s41467-021-26964-8.

Kavzoglu, T., Sahin, E.K., and Colkesen, I., 2014, Landslide susceptibility mapping using GIS-based multi-criteria decision analysis, support vector machines, and logistic regression: Landslides, v. 11, p. 425–439, doi:10.1007/s10346-013-0391-7.

Kirby, E., and Whipple, K.X., 2012, Expression of active tectonics in erosional landscapes: Journal of Structural Geology, v. 44, p. 54–75, doi:10.1016/j.jsg.2012.07.009.

Kohl, C.P., and Nishiizumi, K., 1992, Scientific Comment Chemical isolation of quartz for measurement of in-situ-produced cosmogenic nuclides: Geochimica et Cosmochimica Acta, v. 56, p. 3583–3587.

Larsen, I.J., and Montgomery, D.R., 2012, Landslide erosion coupled to tectonics and river incision: Nature Geoscience, v. 5, p. 468–473, doi:10.1038/ngeo1479.

Larsen, I.J., Montgomery, D.R., and Korup, O., 2010, Landslide erosion controlled by hillslope material: Nature Geoscience, v. 3, p. 247–251, doi:10.1038/ngeo776.

Long, S., McQuarrie, N., Tobgay, T., and Grujic, D., 2011, Geometry and crustal shortening of the Himalayan fold-thrust belt, eastern and central Bhutan: Bulletin of the Geological Society of America, v. 123, p. 1427–1447, doi:10.1130/B30203.1.

Malamud, B.D., Turcotte, D.L., Guzzetti, F., and Reichenbach, P., 2004, Landslide inventories and their statistical properties: Earth Surface Processes and Landforms, v. 29, p. 687–711, doi:10.1002/esp.1064.

Meunier, P., Hovius, N., and Haines, J.A., 2008, Topographic site effects and the location of earthquake induced landslides: Earth and Planetary Science Letters, v. 275, p. 221–232, doi:10.1016/j.epsl.2008.07.020.

Nishiizumi, K., Imamura, M., Caffee, M.W., Southon, J.R., Finkel, R.C., and McAninch, J., 2007, Absolute calibration of ^{10}Be AMS standards: Nuclear Instruments and Methods in Physics Research, Section B: Beam Interactions with Materials and Atoms, v. 258, p. 403–413, doi:10.1016/j.nimb.2007.01.297.

Olen, S.M., Bookhagen, B., Hoffmann, B., Sachse, D., Adhikari, D.P., and Strecker, M.R., 2015, Understanding erosion rates in the Himalayan orogen: A case study from the Arun Valley: Journal of Geophysical Research: Earth Surface, v. 120, p. 2080–2102, doi:10.1002/2014JF003410.

Parker, R.N., Densmore, A.L., Rosser, N.J., De Michele, M., Li, Y., Huang, R., Whadcoat, S., and Petley, D.N., 2011, Mass wasting triggered by the 2008 Wenchuan earthquake is greater than orogenic growth: Nature Geoscience, v. 4, p. 449–452, doi:10.1038/ngeo1154.

Perron, J.T., and Royden, L., 2013, An integral approach to bedrock river profile analysis: Earth Surface Processes and Landforms, v. 38, p. 570–576, doi:10.1002/esp.3302.

Portenga, E.W., Bierman, P.R., Duncan, C., Corbett, L.B., Kehrwald, N.M., and Rood, D.H., 2015, Erosion rates of the Bhutanese Himalaya determined using in situ-produced ^{10}Be: Geomorphology, v. 233, p. 112–126, doi:10.1016/j.geomorph.2014.09.027.

Rai, L.K., Yoshida, K., and Kuritani, T., 2021, Reconstruction of the exhumation history of the eastern Nepal Himalaya based on provenance changes: Sedimentary Geology, v. 420, doi:10.1016/j.sedgeo.2021.105920.

Le Roux-Mallouf, R. et al., 2015, Evidence for a wide and gently dipping Main Himalayan Thrust in western Bhutan: Geophysical Research Letters, v. 42, p. 3257–3265, doi:10.1002/2015GL063767.

Scherler, D., Bookhagen, B., and Strecker, M.R., 2014, Tectonic control on ^{10}Be-derived erosion rates in the Garhwal Himalaya, India: Journal of Geophysical Research: Earth Surface, v. 119, p. 83–105, doi:10.1002/2013JF002955.

Schwanghart, W., and Scherler, D., 2014, Short Communication: TopoToolbox 2 - MATLAB-based software for topographic analysis and modeling in Earth surface sciences: Earth Surface Dynamics, v. 2, p. 1–7, doi:10.5194/ESURF-2-1-2014.

Stine, R.A., 1995, Graphical interpretation of variance inflation factors: The American Statistician, v. 49, p. 53–56, doi:10.1080/00031305.1995.10476113.

Stone, J.O., 2000, Air pressure and cosmogenic isotope production: Journal of Geophysical Research: Solid Earth, v. 105, p. 23753–23759, doi:10.1029/2000jb900181.

Taylor, M., and Yin, A., 2009, Active structures of the Himalayan-Tibetan orogen and their relationships to earthquake distribution, contemporary strain field, and Cenozoic volcanism: Geosphere, v. 5, p. 199–214, doi:10.1130/GES00217.1.

Vannay, J.C., Grasemann, B., Rahn, M., Frank, W., Carter, A., Baudraz, V., and Cosca, M., 2004, Miocene to Holocene exhumation of metamorphic crustal wedges in the NW Himalaya: Evidence for tectonic extrusion coupled to fluvial erosion: Tectonics, v. 23, doi:10.1029/2002TC001429.

Willett, S.D., McCoy, S.W., Taylor Perron, J., Goren, L., and Chen, C.Y., 2014, Dynamic reorganization of River Basins: Science, v. 343, doi:10.1126/science.1248765.

Wobus, C., Whipple, K.X., Kirby, E., Snyder, N., Johnson, J., Spyropolou, K., Crosby, B., and Sheehan, D., 2006, Tectonics from topography: Procedures, promise, and pitfalls: Special Paper of the Geological Society of America, v. 398, p. 55–74, doi:10.1130/2006.2398(04).

Yin, A., 2006, Cenozoic tectonic evolution of the Himalayan orogen as constrained by along-strike variation of structural geometry, exhumation history, and foreland sedimentation: Earth-Science Reviews, v. 76, p. 1–131, doi:10.1016/j.earscirev.2005.05.004.

APPENDIX C:

Patterns of low-temperature thermochronologic ages from the easternmost Himalaya

C.1 Appendix Note C1: Apatite (U-Th-Sm)/He preparation and analytical methods

Apatite crystals from samples were hand-picked, screened, and photographed under ethyl alcohol using a Leica M165 binocular microscope equipped with a calibrated digital camera at 120x magnification and cross-polarized light. From these high-resolution images, crystal size measurements of selected grains were collected, which were used to determine crystal mass and alpha-ejection correction factors required to calculate derived (U-Th-Sm)/He data (Farley et al., 1996; Hourigan et al., 2005). Individual crystals were then transferred into 1 mm diameter Nb foil packets for stable heating during gas extraction.

Nb packets containing the mineral aliquots were loaded into the He gas extraction line and pumped down to high vacuum (<10-8 torr). Packets were then heated with a diode laser at 1000°C for 3 minutes for the extraction of radiogenic ^{4}He. Sample gas was spiked with ~7 ncc of pure ^{3}He, cleaned using two SAES getters and cryogenic purification, and analyzed on a Balzers PrismaPlus QME 220 quadrupole mass spectrometer. This gas extraction and measurement procedure was repeated at least once to ensure complete mineral degassing to <1% re-extract gas volume. Aliquot ^{4}He gas concentrations were calculated from these data.

Degassed aliquots were shipped to the University of Colorado Thermochronology Research and Instrumentation Laboratory (TRaIL) for chemical dissolution and U-Th-Sm measurement. At TRaIL, apatite crystals, still enclosed in the Nb tubes, were placed in 1.5 mL Cetac vials, spiked with a ^{235}U – ^{230}Th – ^{145}Nd tracer in HNO_3, capped, and baked in a lab oven at 80°C for 2 hours. Once the crystals were dissolved, they were diluted with 1 mL of doubly-deionized water, and taken to the ICP-MS lab for

analysis. Sample solutions, along with normal solutions and blanks, were analyzed for U, Th, and Sm content using a Thermo Element 2 magnetic sector mass spectrometer equipped with a Teflon spray chamber and platinum cones.

U and Th measurements from TRaIL were combined with blank-corrected He concentrations and associated grain morphometric data to calculate (U-Th)/He dates using in-house data reduction MATLAB code. Crystal morphometrics, crystal mass, and alpha ejection correction parameter, F_T, were calculated following Ketcham et al. (2011) for mean alpha stopping distances and mineral densities for hexagonal (apatite) geometries. F_T was calculated for each parent isotope and applied separately in the age equation outlined by Ketcham et al. (2011). The reported equivalent spherical radius was derived from a surface-area/volume equivalent sphere.

For instrument calibration and data quality-control, Durango fluorapatite mineral standards were analyzed alongside these samples. The analysis of these standards yielded a weighted mean age of 32.1 ± 0.2 Ma (n = 4) (±1σ).

C.2 Appendix Note C2: HeFTy thermal model assumptions, constraints, and parameters

HeFTy inverse modeled T-t histories were calculated based on RDAAM for apatite and ZRDAAM for zircon grains (Flowers et al., 2009; Guenthner et al., 2013) with stopping distances and age alpha corrections based on Ketcham et al. (2011). Models were run with an assumed 20°C surface temperature. Paths between constraints were set to be monotonic consistent (2E). All inverse models were run until 100 acceptable fits were found.

aPH-1-14-13-5: (0 good fits, 100 acceptable fits, 56723 paths attempted)

Grains included in modeling:

Apatite (U-Th)/He grains	Zircon (U-Th)/He grains (Haproff et al., 2020)
aPH-1-14-13-5_1	PH-1-14-13-5_1
aPH-1-14-13-5_2	PH-1-14-13-5_3

aPH-1-14-13-5_3	PH-1-14-13-5_4

Assumptions	Description and data source
~27 ± 1 Ma depositional age of protolith at surface temperature.	Detrital zircon U-Pb date reported by Haproff et al. (2019).
Low-grade metamorphism at 300-450°C between ~27-4 Ma.	Approximate temperature range for metamorphism of phyllite.

aPH-1-3-13-11B: (0 good fits, 100 acceptable fits, 97752 paths attempted)

Grains included in modeling:

Apatite (U-Th)/He grains	Zircon (U-Th)/He grains (Haproff et al. 2020)
aPH-1-3-13-11B_1 aPH-1-3-13-11B_2 aPH-1-3-13-11B_3 aPH-1-3-13-11B_4	PH-1-3-13-11B_1 PH-1-3-13-11B_2 PH-1-3-13-11B_3

Assumptions	Description and data source
~525 ± 3 Ma depositional age of protolith at surface temperature	Detrital zircon U-Pb date reported by Haproff et al. (2019).
High-grade metamorphism at 550-700°C between ~525-15 Ma.	Approximate temperature range for metamorphism of paragneiss.

aPH-1-8-13-8: (14 good fits, 100 acceptable fits, 50926 paths attempted)

Grains included in modeling:

Apatite (U-Th)/He grains	Zircon (U-Th)/He grains (Haproff et al. 2020)
aPH-1-8-13-8_2 aPH-1-8-13-8_3 aPH-1-8-13-8_4 aPH-1-8-13-8_5	PH-1-8-13-8_1 PH-1-8-13-8_2 PH-1-8-13-8_3

Assumptions	Description and data source

~115 ± 13 Ma crystallization age at 550-600°C.	Zircon U-Pb date reported by Haproff et al. (2019). Approximate temperature of crystallization for diorite.

aPH-1-8-13-1B: (1 good fit, 100 acceptable fits, 125380 paths attempted)

Grains included in modeling:

Apatite (U-Th)/He grains	Zircon (U-Th)/He grains (Haproff et al. 2020)
aPH-1-8-13-1B_1 aPH-1-8-13-1B_4 aPH-1-8-13-1B_5	PH-1-8-13-1B_1 PH-1-8-13-1B_2 PH-1-8-13-1B_3

Assumptions	Description and data source
~96.3 ± 3 Ma crystallization age at 550-600°C.	Zircon U-Pb date reported by Haproff et al. (2019). Approximate temperature of crystallization for monzodiorite.

C.3 Appendix Figures and Tables

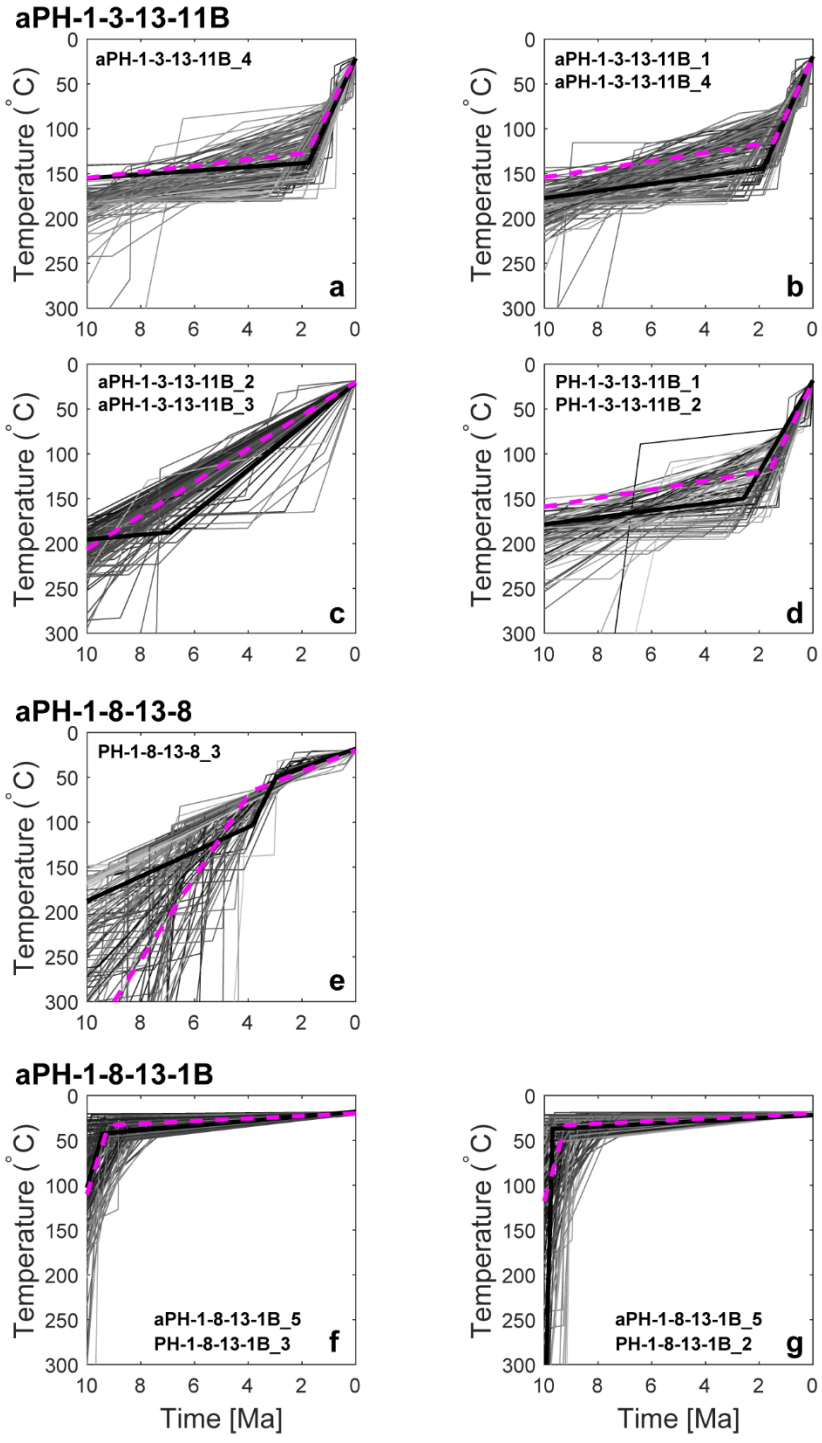

Fig. C1: HeFTy inverse-modeled sensitivity tests. Excluded grains for each test are shown at the top left or bottom center of the plot. 100 acceptable fits (goodness of fit >0.05) were calculated for each sample and the scenario with the best goodness of fit value is marked in a thick, black line. Weighted mean paths are shown in magenta dashed lines. Weighted mean paths are our preferred path. T-t paths are colored in grey with darker shades indicating a higher goodness of fit than those with lighter shades.

Table C1: Apatite grain properties and ages

Apatite Grain Information							He Data				
Aliquot Name	Latitude (°)	Longitude (°)	Elevation (m)	Rock Type	Rs (μm)[a]	Mass (μg)[b]	4He (ncc)	4He error (ncc)	4He measured (mol)	4He err (mol)	He (nmol/g)
aPH-1-14-13-5_1	28.2114	95.7807	417	Phyllite	40.6	1.34	0.0320	0.0015	1.429E-15	6.596E-17	0.82
aPH-1-14-13-5_3					40.7	1.58	0.0161	0.0015	7.173E-16	6.795E-17	0.43
aPH-1-14-13-5_4					43.5	2.10	0.0149	0.0015	6.627E-16	6.645E-17	0.36
aPH-11-9-15-27_2	28.3919	95.9231	629	Paragneiss	44.6	1.71	0.0130	0.0020	5.796E-16	8.901E-17	0.25
aPH-11-9-15-27_5					57.2	3.93	0.0119	0.0008	5.301E-16	3.464E-17	0.12
aPH-1-3-13-11B_1	28.2195	95.8615	1810	Paragneiss	56.9	4.59	0.0074	0.0015	3.314E-16	6.608E-17	0.06
aPH-1-3-13-11B_2					84.1	10.91	0.0205	0.0015	9.124E-16	6.560E-17	0.07
aPH-1-3-13-11B_3					73.8	10.04	0.0084	0.0015	3.728E-16	6.737E-17	0.04
aPH-1-3-13-11B_4					49.5	2.55	0.0070	0.0015	3.137E-16	6.572E-17	0.11
aPH-1-8-13-1B_1	28.6329	95.8523	798	Monzodiorite	35.9	1.28	0.0150	0.0021	6.705E-16	9.154E-17	0.50
aPH-1-8-13-1B_4					36.1	1.16	0.0099	0.0021	4.407E-16	9.170E-17	0.32
aPH-1-8-13-1B_5					41.0	1.63	0.0090	0.0015	4.000E-16	6.507E-17	0.23
aPH-1-8-13-8_2	28.5597	95.8478	736	Diorite	40.0	1.47	0.0130	0.0021	5.796E-16	9.304E-17	0.32
aPH-1-8-13-8_3					46.7	2.77	0.0491	0.0021	2.190E-15	9.518E-17	0.76
aPH-1-8-13-8_4					39.3	1.37	0.0175	0.0020	7.824E-16	8.932E-17	0.46
aPH-1-8-13-8_5					54.7	4.84	0.0812	0.0010	3.622E-15	4.523E-17	0.84

[a]Rs was derived from the radius of a surface-area/volume equivalent sphere.

[b]Mass of the crystal calculated based on grain dimensions, mineral densities, and voluime equations in Ketcham et al. (2011).

Laboratory standard Durango apatite analyzed with these samples yielded weighted mean age of 32.1 ± 0.24 Ma (n = 4) 1sigma.

Table C1: Apatite grain properties and ages (cont 1)

Apatite Grain I	U+Th+Sm Data (TRaIL)											Age Data					
Aliquot Name	U (ng)	±	Th (ng)	±	Sm (ng)	±	U (ppm)	Th (ppm)	Sm (ppm)	Th/U	eU[c]	F_T[d]	Measured Date (Ma)	Measured Uncertainty 1σ (Ma)	Corrected Date (Ma)[e]	Analytical Uncertainy 1σ (Ma)	Uncertainty based on Reproducibility of standard 1σ (Ma)
aPH-1-14-13-5_1	0.2211	0.0041	0.0792	0.0021	0.0387	0.0015	164.48	58.86	28.81	0.358	178.31	0.6458	1.1	0.1	**1.7**	**0.1**	**0.1**
aPH-1-14-13-5_3	0.0721	0.0018	0.1367	0.0034	0.0196	0.0017	45.56	86.37	12.41	1.896	65.86	0.6542	1.3	0.1	**1.9**	**0.2**	**0.2**
aPH-1-14-13-5_4	0.0775	0.0016	0.1867	0.0028	0.0225	0.0015	36.90	88.84	10.72	2.407	57.78	0.6855	1.0	0.1	**1.5**	**0.1**	**0.1**
aPH-11-9-15-27_2	0.0186	0.0006	0.0108	0.0002	0.0317	0.0015	10.85	6.31	18.48	0.581	12.33	0.6759	5.0	0.8	**7.3**	**1.1**	**0.6**
aPH-11-9-15-27_5	0.0577	0.0009	0.0000	0.0000	0.0757	0.0016	14.68	0.00	19.25	0.000	14.68	0.7490	1.7	0.1	**2.2**	**0.1**	**0.2**
aPH-1-3-13-11B_1	0.0421	0.0006	0.0023	0.0001	0.0131	0.0015	9.17	0.51	2.85	0.055	9.29	0.7436	1.4	0.3	**1.9**	**0.4**	**0.2**
aPH-1-3-13-11B_2	0.1999	0.0030	0.0483	0.0010	0.0521	0.0019	18.33	4.43	4.77	0.241	19.37	0.8267	0.8	0.1	**1.0**	**0.1**	**0.1**
aPH-1-3-13-11B_3	0.0978	0.0026	0.0086	0.0002	0.0125	0.0014	9.74	0.85	1.24	0.088	9.94	0.8029	0.7	0.1	**0.9**	**0.2**	**0.1**
aPH-1-3-13-11B_4	0.0251	0.0014	0.0014	0.0001	0.0021	0.0014	9.86	0.55	0.81	0.055	9.99	0.7122	2.3	0.5	**3.1**	**0.7**	**0.3**
aPH-1-8-13-1B_1	0.0177	0.0007	0.0090	0.0004	0.0019	0.0015	13.82	7.07	1.47	0.512	15.49	0.6109	6.3	0.9	**10.0**	**1.4**	**0.8**
aPH-1-8-13-1B_4	0.0142	0.0006	0.0094	0.0003	0.0008	0.0014	12.24	8.13	0.68	0.664	14.15	0.6049	5.0	1.1	**8.1**	**1.7**	**0.6**
aPH-1-8-13-1B_5	0.0091	0.0005	0.0011	0.0001	0.0004	0.0015	5.61	0.69	0.22	0.124	5.77	0.6561	7.9	1.4	**11.8**	**2.0**	**0.9**
aPH-1-8-13-8_2	0.0430	0.0010	0.0245	0.0014	0.0109	0.0015	29.20	16.64	7.39	0.570	33.11	0.6405	2.2	0.4	**3.4**	**0.5**	**0.3**
aPH-1-8-13-8_3	0.1433	0.0030	0.1212	0.0055	0.0212	0.0015	51.78	43.77	7.66	0.845	62.07	0.6954	2.4	0.1	**3.4**	**0.2**	**0.3**
aPH-1-8-13-8_4	0.0511	0.0021	0.0322	0.0014	0.0127	0.0015	37.36	23.53	9.29	0.630	42.89	0.6349	2.5	0.3	**3.8**	**0.5**	**0.3**
aPH-1-8-13-8_5	0.2435	0.0068	0.2046	0.0052	0.0431	0.0018	50.30	42.23	8.90	0.840	60.22	0.7419	2.3	0.1	**3.1**	**0.1**	**0.2**

[c] eU is effective uranium concentration, weights U and Th for their a productivity, computed as (U + (0.235 * Th)).

[d] FT calculated using α-correction equations of Ketcham et al. (2011).

[e] Corrected date using F_T

Laboratory standard Durango apatite analyzed with these samples yielded weighted mean age of 32.1 ± 0.24 Ma (n = 4) 1sigma.

C.4 Appendix References

Farley, K.A., Wolf, R.A., and Silver, L.T., 1996, The effects of long alpha-stopping distances on (U-Th)/He ages: Geochimica et Cosmochimica Acta, v. 60, p. 4223–4229, doi:10.1016/S0016-7037(96)00193-7.

Flowers, R.M., Ketcham, R.A., Shuster, D.L., and Farley, K.A., 2009, Apatite (U-Th)/He thermochronometry using a radiation damage accumulation and annealing model: Geochimica et Cosmochimica Acta, v. 73, p. 2347–2365, doi:10.1016/j.gca.2009.01.015.

Guenthner, W.R., Reiners, P.W., Ketcham, R.A., Nasdala, L., and Giester, G., 2013, Helium diffusion in natural zircon: radiation damage, anisotropy, and the interpretation of zircon (U-TH)/He thermochronology: American Journal of Science, v. 313, p. 145–198, doi:10.2475/03.2013.01.

Haproff, P.J., Odlum, M.L., Zuza, A. V., Yin, A., and Stockli, D.F., 2020, Structural and Thermochronologic Constraints on the Cenozoic Tectonic Development of the Northern Indo-Burma Ranges: Tectonics, v. 39, doi:10.1029/2020TC006231.

Hourigan, J.K., Reiners, P.W., and Brandon, M.T., 2005, U-Th zonation-dependent alpha-ejection in (U-Th)/He chronometry: Geochimica et Cosmochimica Acta, v. 69, p. 3349–3365, doi:10.1016/j.gca.2005.01.024.

Ketcham, R.A., Gautheron, C., and Tassan-Got, L., 2011, Accounting for long alpha-particle stopping distances in (U-Th-Sm)/He geochronology: Refinement of the baseline case: Geochimica et Cosmochimica Acta, v. 75, p. 7779–7791, doi:10.1016/j.gca.2011.10.011.